

Università degli Studi Roma Tre

Doctoral Thesis

Strongly correlated electron materials: A core level photoelectron spectroscopy investigation

Candidate:
Valerio Lollobrigida

Supervisor:
Dr. Francesco Offi

Coordinator:
Prof. Roberto Raimondi

Tesi sottomessa per il riconoscimento del titolo di Dottore di Ricerca

presso la

Scuola Dottorale in Matematica e Fisica
XXVIII Ciclo

January 2016

"Il dono di sapienza è il primo dono dello Spirito Santo, il più saporoso, il più acuto, il più penetrante, perché ci mette in comunicazione diretta con Dio e i suoi misteri."

Madre Trinidad de la Santa Madre Iglesia

Contents

Contents **IV**

List of Figures **VII**

List of Tables **XIII**

Abbreviations **XV**

Introduction **1**

1 Photoelectron spectroscopy on transition-metal systems **5**
1.1 Strongly correlated *d*-systems 5
1.2 Core level satellite lines 10
1.2.1 Kotani-Toyazawa model 11
1.2.2 Gunnarson-Schönhammer theory 13
1.2.3 Cluster model and nonlocal screening effects 15
1.2.4 Dynamical mean-field theory and quasi-particle states 16
1.3 HAXPES 19
1.3.1 Information depth in HAXPES 22
1.3.2 Bulk-only well-screened peaks in HAXPES 24
1.3.3 Local and nonlocal screening channels 27
1.4 Investigated systems 29
1.4.1 $Ga_{1-x}Mn_xAs$ 29
1.4.2 $La_{1-x}Sr_xMnO_3$ 31
1.4.3 RuO_2 36
1.4.4 TiO_2 38

2 Experimental methods **43**
2.1 Synchrotron radiation 43
2.2 Experimental setups for HAXPES at synchrotrons 47
2.2.1 GALAXIES beamline 47
2.2.2 I09 beamline 51
2.3 Experimental aspects 52

3 Experimental results **59**
3.1 $Ga_{0.87}Mn_{0.13}As$ 59
3.2 $La_{0.65}Sr_{0.35}MnO_3$ 65
3.3 A 4*d* system: RuO_2 73

3.4 $TiO_{2-\delta}$ 75

4 Discussion **85**
4.1 Surface characterisation 87
4.2 Well-screened satellites in $3d$ and $4d$ compounds 88
4.3 Depth dependent valence change and metallicity in manganites 96
4.4 Charge-transfer satellites in TiO_2 99

5 Perspectives **103**
5.1 Time-resolved HAXPES on $La_{1-x}Sr_xMnO_3$ 104
5.2 TOF spectrometers for time-resolved HAXPES 107
5.2.1 Linear time-of-flight spectrometer 109
5.2.2 Spherical reflector based time-of-flight spectrometer 112
5.2.3 Comparison 117

Conclusions **119**

Bibliography **123**

Acknowledgements **135**

List of Figures

1.1 Fermi level electronic structure of metals, semiconductor and insulators . 5
1.2 Electronic phase diagram in the plane of doping concentration x and temperature for distorted perovskite $La_{1-x}Sr_xMnO_3$ 6
1.3 Resistivity of $La_{1-x}Sr_xMnO_3$ crystals as a function of the temperature for different concentration levels x 7
1.4 Electron DOS for a band metal, a weakly correlated metal, a strongly correlated metal and a Mott-Hubbard insulator 8
1.5 Density of states for a (a) Mott-Hubbard and (b) charge-transfer insulator 10
1.6 Photoemission spectrum displaying adiabatic and shake-up/shake-off peaks 10
1.7 Pictorial representation of final states associated to main and charge-transfer satellite peak in the Kotani-Toyazawa model 12
1.8 Experimental and theoretical (Gunnarson-Schönhammer model) spectra of Ce $3d_{5/2}$, Th $4f_{7/2}$ and Ti $2p_{3/2}$ core levels 14
1.9 Experimental Ni $2p$ spectrum compared with NiO_6 and Ni_7O_{36} cluster calculations 16
1.10 Ru $3d$ soft X-ray photoemission spectra from different ruthenates 17
1.11 Electron configurations contributing to the core levels spectra of ruthenates 18
1.12 Photoionisation cross-section of Ti, Mn and Ru in the 1-30 keV photon energy range 20
1.13 Schematic representation of a photoelectron spectroscopy experiment from a solid sample 22
1.14 Inelastic mean free path (IMFP) for 41 elemental solids calculated with the TPP-2M algorithm 23
1.15 a) HAXPES spectra from $V_{1.98}Cr_{0.02}O_3$ in the paramagnetic metallic and antiferromagnetic insulating phase and b) spectrum in the paramagnetic metallic compared with calculations. c) Experimental spectra in the hard and soft X-ray regime and d) calculations for the Cu $2p$ core level of $Bi_2Sr_2CaCu_2O_{8+\delta}$ 24
1.16 Soft and hard X-ray Cu $2p_{3/2}$ spectra at 70 K from a $Nd_{1.85}Ce_{0.15}CuO_4$ sample 26
1.17 (a) Mn_8 cluster with cubic symmetry used for the calculations of the Mn $2p$ core level in $La_{1-x}Sr_xMnO_3$. (b) Mn $2p_{3/2}$ spectrum from $La_{1-x}Sr_xMnO_3$ in the ferromagnetic phase as a function of the Sr concentration and then of the number of e_g electrons in the Mn_8 cluster. Adapted from [33]. . . . 28
1.18 Zinc-blende crystal structure for $Ga_{1-x}Mn_xAs$ 29
1.19 a) Hard and soft X-ray Mn $2p$ spectra from $Ga_{0.95}Mn_{0.05}As$ compared with b) results of cluster calculations 31
1.20 a) Perovskite-type structure of manganites and b) shape of the five d orbitals 32

1.21 a) Fine structure of Mn ion $3d$ levels and b) pictorial density of states of $La_{2/3}Sr_{1/3}MnO_3$ . . . 33
1.22 Pictorial representation of tensile strain ($\delta > 0$), strain relaxation ($\delta = 0$) and compressive strain ($\delta < 0$) in epitaxial growth . . . 34
1.23 Mn $2p$ HAXPES spectra from $La_{1-x}Sr_xMnO_3$ as a function of the doping compared with MnO_6 cluster calculation results . . . 35
1.24 Rutile unit cell for RuO_2: the Ru atoms are in grey and the O atoms are in red. The three main crystallographic directions (a, b, c) are indicated. Adapted from [66]. . . . 36
1.25 (a) Comparison of experimental (solid lines) and theoretical (dotted lines) Ru $3d$ spectrum of RuO_2, where calculations are performed considering screening from quasiparticle levels at E_F. Screened and unscreened peaks are indicated by the letters "s" and "u", respectively. Adapted from [34]. (b) Calculated Ru $3d$ spectra for a Ru_4 cluster (shown in the inset) for three different orbital occupations, considering both local and nonlocal screening mechanism. These spectra are obtained without considering spin-orbit coupling (see text). Adapted from [33]. . . . 37
1.26 Anatase TiO_2 crystal and schematic lattice structure . . . 39
1.27 Ti $2p$ experimental spectrum from rutile TiO_2 and fitting with six Gaussians 40
1.28 Ti $1s$ and Ti $2p$ core level photoemission spectra in the hard X-ray regime 41

2.1 Schematic map of the third generation synchrotron radiation facility SOLEIL, showing the linac, the booster, the storage ring and the beamlines; for each beamline is indicated whether the light is produced by a bending magnet or an insertion device (wiggler or undulator). Adapted from [85]. 44
2.2 Electron trajectory between the poles of an insertion device . . . 45
2.3 Brilliance of undulators and bending magnets at the SOLEIL synchrotron 46
2.4 Schematic layout of the GALAXIES beemline of the SOLEIL synchrotron 47
2.5 Geometry of the four-bounce crystal monochromator in use at the GALAXIES beamline . . . 48
2.6 Polar plot of the angular distribution of photoelectrons from free atoms . 50
2.7 Geometry of an HAXPES experiment at the GALAXIES beamline . . . 50
2.8 Schematic layout of the I09 beamline of the Diamond synchrotron . . . 51
2.9 Picture of the I09 HAXPES UHV chamber showing the head of the manipulator and the nose of the analyser lens . . . 53
2.10 Fitting of Au $4f$ spectrum from the Au foil in electrical contact with the anatase TiO_2 samples at 6900 eV photon energy . . . 54
2.11 Fermi edge of the Au foil in electrical contact with the $Ga_{0.87}Mn_{0.13}As$ sample at a nominal photon energy of 800 eV measured at room temperature 55

3.1 Survey spectra of the $Ga_{0.87}Mn_{0.13}As$ sample at 800 and 5940 eV nominal photon energy . . . 60
3.2 As and Ga $3d$ spectra from $Ga_{0.87}Mn_{0.13}As$ as a function of the photon energy . . . 60
3.3 a) Mn $2p$ spectra from $Ga_{0.87}Mn_{0.13}As$ as a function of the photon energy compared with b) cluster calculations . . . 62
3.4 Fitting of the Mn $2p$ spectrum from $Ga_{0.87}Mn_{0.13}As$ at 5940 eV photon energy . . . 63

3.5 Attenuation of the well-screened peak as a function of the mean escape depth on the Mn $2p_{3/2}$ photoelectrons and exponential fitting 64
3.6 Energy separation between extra and main peak 65
3.7 (Left panel) Survey spectra measured on the three manganite thin films at $T = 200$ K and $\hbar\omega = 5940$ eV 66
3.8 a) Mn $2p$ spectra from three differently strained manganites films and b) photon energy dependence of the Mn $2p$ spectrum for the sample grown on LSAT (strain relaxed) measured at $T = 200$ K 67
3.9 Mn $2p_{3/2}$ spectra from the three manganite films at $\hbar\omega = 5940$ eV and $T = 200$ K 68
3.10 Fitting of the Mn $2p_{3/2}$ spectrum from the strain relaxed sample measured at $T = 200$ K with a photon energy of $\hbar\omega = 5940$ eV. Six Gaussian and a integral background have been used to reproduce the lineshape. 68
3.11 Attenuation of the Mn $2p_{3/2}$ extra-peak of strain relaxed and strain compressed manganites as a function of the mean escape depth and exponential fittings 69
3.12 Mn $3s$ spectra from the three manganite films measured at $\hbar\omega = 5940$ eV and $T = 200$ K 70
3.13 Mn $3s$ spectra from the strain relaxed (a) and compressive strained (b) sample at $\hbar\omega = 5940$ eV and $\hbar\omega = 2500$ eV 71
3.14 Fitting of the Mn $3s$ spectrum from the strain relaxed sample at 2500 eV photon energy 72
3.15 Valence band HAXPES spectrum measured at $\hbar\omega = 5940$ eV and $T = 200$ K on the three manganite films and b) photon energy dependence for the strain relaxed sample 73
3.16 Comparison of the survey spectrum measured at 5940 eV photon energy on the two ruthenates. The curves have been normalised to the intensity of the O $1s$ peak. 74
3.17 Photon energy dependence of the Ru $3d$ core level spectrum measured on the two ruthenates. The curves have been normalised to the intensity of the screened Ru $3d_{3/2}$ line after subtraction of a Tougaard background. . 75
3.18 Photon energy dependence of the valence band measured on the two ruthenates. The solid line curves are the spectra acquired on the sample grown on $SrTiO_3$, while for the specimen grown on TiO_2, small open circles are used. 76
3.19 Survey spectra from the $P(O_2) = 10$ Pa sample and the $P(O_2) = 10^{-3}$ Pa sample measured at $\hbar\omega = 6900$ eV 76
3.20 Survey spectra from the $P(O_2) = 10$ Pa sample and the $P(O_2) = 10^{-3}$ Pa sample measured at $\hbar\omega = 2500$ eV 77
3.21 Comparison of the Ti $1s$ acquired at 6900 eV photon energy from the two anatase TiO_2 specimens 78
3.22 Ti $1s$ spectrum at 6900 eV photon energy and Ti $2p$ spectra at $\hbar\omega = 6900$ eV and $\hbar\omega = 2500$ eV from the $P(O_2) = 10^{-3}$ Pa sample 79
3.23 Fitting of the Ti $1s$ spectrum measured at $\hbar\omega = 6900$ eV from the $P(O_2) = 10^{-3}$ Pa sample 80
3.24 Fitting of the Ti $2p$ lineshape acquired at 6900 eV photon energy from the $P(O_2) = 10^{-3}$ Pa sample. 81
3.25 Fitting of the Ti $2p$ lineshape acquired at 2500 eV photon energy from the $P(O_2) = 10^{-3}$ Pa sample 82

3.26 a) Valence band spectra of the anatase TiO_2 sample grown with $P(O_2) = 10^{-3}$ Pa at 6900 and 2500 eV photon energy and b) schematic electronic structure around the Fermi level 82

4.1 $10 \times 10\,\mu m^2$ AFM images of the $Ga_{1-x}Mn_xAs$ sample surface of the (a) as-received and (b) etched sample. Figures courtesy of dr. M. Cavallini. . 87
4.2 Attenuation of the Mn $2p_{3/2}$ extra peak from $Ga_{0.87}Mn_{0.13}As$ as a function of the probing depth as obtained from two different fitting procedures of the Mn $2p_{3/2}$ spectra 91
4.3 Stack of unit cells of $Ga_{0.87}Mn_{0.13}As$ compared with the thickness of the attenuating layer 91
4.4 Photon energy dependence of the Mn $2p$ peak measured from a) $Ga_{0.87}Mn_{0.13}As$ at room temperature and b) strain relaxed $La_{0.65}Sr_{0.35}MnO_3$ at $T = 200$ K 93
4.5 Attenuation of the extra-peak of the Mn $2p_{3/2}$ line for strain relaxed (black squares) and strain compressed (red circles) $La_{1-x}Sr_xMnO_3$ thin films. For the strain tensile sample, only the value corresponding to an excitation energy of $\hbar\omega = 5940$ eV is shown (blue triangles). The exponential fitting and the resulting parameters for the strain relaxed and strain compressed specimens are also displayed. 94
4.6 Photon energy dependence of the valence band of the strain relaxed manganite film. 97

5.1 Time scale of some chemical and physical processes compared with the typical time scales of XFEL and third generation light sources. Adapted from [119]. 103
5.2 Schematic representation of a conventional a) and time-resolved b) photoelectron spectroscopy experiment 104
5.3 Comparison of the Mn $2p_{3/2}$ spectra from strain relaxed $La_{0.65}Sr_{0.35}MnO_3$ thin film measured at a 100 ps delay from the pump pulse (red curve) and without laser pumping (black curve). Each experimental spectra, has been reproduced as the sum of four Gaussian profiles. At the bottom the difference between both the experimental and fitting curves is shown. 105
5.4 Intensity of the extra-peak of the Mn $2p_{3/2}$ spectrum from a strain relaxed $La_{0.65}Sr_{0.35}MnO_3$ sample as a function of the delay between pump and probe pulses. The blue stripe indicates the value of the intensity of the extra-peak for the spectra measured without pump. 106
5.5 Time structure of the radiation at the EXFEL 108
5.6 Schematic cross-section of the cylindrical retarding lens 109
5.7 a) Transmission curve and b) average time-of-flight as a function of the electron kinetic energy for the cylindrical lens. 110
5.8 Resolving power of the cylindrical lens obtained considering only the time resolution of the detector and including the time spread of electrons with same kinetic energy 111
5.9 3D view of the spherical mirror 113
5.10 Values of differential energy resolution (F, left axis) and energy resolution (ΔE, right axis) as a function of the outer electrode radius for different values of the ratio between the radii of the hemispheres. Adapted from [128]. 114
5.11 Cross-section of the spherical mirror with electron trajectories 115

5.12 Positions at the pupil plane of 4900 and 5020 eV kinetic energy electrons 115
5.13 a) Transmission and b) average time-of-flight (left axis) and differential energy resolution (right axis) as a function of the electron kinetic energy for the spherical mirror 116
5.14 Time structure of photoelectron bunches produced by EXFEL photon pulses as detected in the cylindrical lens and spherical mirror 118

List of Tables

1.1 Number of e_g electrons in a Mn_8 cluster with effective MnO_6 units for different hole doping. Values taken from [33]. 28

2.1 Values of O_2 partial pressure during deposition of the two TiO_2 samples. A lower values of pressure implies a higher concentration of oxygen vacancies, which act as charge carriers. 53
2.2 Substrate, lattice mismatch (and associated strain type), substrate temperature and O_3 pressure during deposition of the three $La_{0.65}Sr_{0.35}MnO_3$ samples which have been studied in this thesis work. 56
2.3 Substrate and crystallographic orientation of the two RuO_2 thin films under investigation. 56

3.1 A and B fitting parameters of the attenuation curves for the Mn $2p_{3/2}$ extra-peak of relaxed and compressive strained manganites 69
3.2 Exchange splitting of the Mn $3s$ peaks and Mn valence for the three manganite films 71
3.3 Energy separation and area ratio between satellites and main peak in the Ti $1s$ spectra from the two anatase samples 81

4.1 Elemental composition of the $Ga_{1-x}Mn_xAs$ and strain relaxed $La_{1-x}Sr_xMnO_3$ samples as a function of the photon energy 88
4.2 Fitting parameters of the peaks reproducing the Mn $2p_{3/2}$ spectra from $Ga_{0.87}Mn_{0.13}As$ 92
4.3 Fitting parameters of the peaks reproducing the Mn $2p_{3/2}$ spectrum at $T = 200$ K from tensile strained $La_{0.65}Sr_{0.35}MnO_3$ 95
4.4 Fitting parameters of the peaks reproducing the Mn $2p_{3/2}$ spectra at $T = 200$ K from strain relaxed $La_{0.65}Sr_{0.35}MnO_3$ 95
4.5 Fitting parameters of the peaks reproducing the Mn $2p_{3/2}$ spectra at $T = 200$ K from compressive strained $La_{0.65}Sr_{0.35}MnO_3$ 96
4.6 Fitting parameters of the peaks reproducing the Mn $3s$ spectrum at $T =$ 200 K from tensile strained $La_{0.65}Sr_{0.35}MnO_3$ 97
4.7 Fitting parameters of the peaks reproducing the Mn $3s$ spectra at $T = 200$ K from strain relaxed $La_{0.65}Sr_{0.35}MnO_3$ 98
4.8 Fitting parameters of the peaks reproducing the Mn $3s$ spectra at $T = 200$ K from compressive strained $La_{0.65}Sr_{0.35}MnO_3$ 98
4.9 Fitting parameters of the peaks reproducing the Ti $1s$ spectrum at $\hbar\omega =$ 6900 eV from $P(O_2) = 10$ Pa anatase TiO_2 100
4.10 Fitting parameters of the peaks reproducing the Ti $1s$ spectrum at $\hbar\omega =$ 6900 eV from $P(O_2) = 10^{-3}$ Pa anatase TiO_2 100

4.11 Fitting parameters of the peaks reproducing the Ti $2p$ spectra at $\hbar\omega =$ 2500 eV and $\hbar\omega = 6900$ eV from $P(O_2) = 10$ Pa anatase TiO_2 100
4.12 Fitting parameters of the peaks reproducing the Ti $2p$ spectra at $\hbar\omega =$ 2500 eV and $\hbar\omega = 6900$ eV from $P(O_2) = 10^{-3}$ Pa anatase TiO_2 101

5.1 Potential values of the six electrodes of the cylindrical lens for electron kinetic energies around 10000 eV 109

Abbreviations

AES	**A**uger **E**lectron **S**pectroscopy
AFI	**A**nti**F**erromagnetic **I**nsulator
BCT	**B**ody-**C**entered **T**etragonal
CCD	**C**harged-**C**oupled **D**evice
CI	**C**onfiguration **I**nteraction
CMR	**C**olossal **M**agneto**R**esistance
CT	**C**harge **T**ransfer
DCM	**D**ouble **C**rystal **M**onochromator
DMFT	**D**ynamical **M**ean-**F**ield **T**heory
DMS	**D**iluted **M**agnetic **S**emiconductor
DOS	**D**ensity **O**f **S**tates
EAL	**E**ffective **A**ttenuation **L**ength
EXFEL	**E**uropean **X**-ray **F**ree **E**lectron **L**aser
FWHM	**F**ull **W**idth at **H**alf **M**aximum
HDA	**H**emispherical **D**eflection **A**nalyser
HAXPES	**HA**rd **X**-ray **P**hotoelectron **S**pectroscopy
HRM	**H**igh-**R**esolution **M**onochromator
HRTEM	**H**igh-**R**esolution **T**ransmission **E**lectron **M**icroscope
ID	**I**nformation **D**epth
IMFP	**I**nelastic **M**ean **F**ree **P**ath
LHB	**L**ower **H**ubbard **B**and
LAO	**LaAlO**$_3$
LSAT	**La**$_{0.18}$**Sr**$_{0.82}$**Al**$_{0.59}$**Ta**$_{0.41}$**O**$_3$
LTMBE	**L**ow-**T**emperature **M**olecular **B**eam **E**pitaxy
MBE	**M**olecular **B**eam **E**pitaxy

MCP	**M**icro**C**hannel **P**late
MED	**M**ean **E**scape **D**epth
MH	**M**ott-**H**ubbard
MIT	**M**etal-**I**nsulator **T**ransition
PES	**P**hoto**e**lectron **S**pectroscopy
PLD	**P**ulsed **L**aser **D**eposition
PM	**P**aramagnetic **M**etal
RF	**R**adio-**F**requency
RIXS	**R**esonant **I**nelastic **X**-ray **S**cattering
SLAO	**S**r**L**a**A**l$\mathbf{O}_4$
STO	**S**r**T**i$\mathbf{O}_3$
TM	**T**ransition **M**etal
TMO	**T**ransition **M**etal **O**xide
tr-PES	**t**ime-**r**esolved **P**hoto**E**lectron **S**pectroscopy
TOF	**T**ime-**O**f-**F**light
UHB	**U**pper **H**ubbard **B**and
UPS	**U**ltraviolet **P**hotoelectron **S**pectroscopy
VOLPE	**VO**lume sensitive **P**hoto**E**mission **S**pectroscopy
XFEL	**X**-ray **F**ree **E**lectron **L**aser
XPS	**X**-ray **P**hotoelectron **S**pectroscopy

Introduction

One of the most fascinating challenges in modern solid state physics, both from a theoretical and an experimental point of view, is the comprehension of electron correlation and how it can affect the macroscopic properties of materials. Effects of electron correlation are extremely important in materials with open d and f electron shells, where electrons are confined in narrow orbitals and the interaction between the electrons internal degrees of freedom are enhanced. In fact these systems are known to display some of the most intriguing phenomena in condensed matter physics, such as:

- huge changes in the resistivity passing the metal-insulator transition in vanadium oxide or upon application of a magnetic field in manganites;
- considerable volume changes across phase transitions in actinides and lanthanides;
- high superconductivity transition temperatures (above liquid nitrogen temperatures) in copper-oxygen planes based materials.

The possibility to exploit these properties to realise devices has driven many theoretical and experimental efforts directed to understand how to describe these phenomena and how to control them by manipulating external parameters such as temperature, doping, etc.

From the experimental point of view, one of the techniques of choice that in the last decades has been extensively applied to the problem of comprehending electron-electron interaction is photoelectron spectroscopy (PES) [1]. For example from the interpretation of satellite structures in the valence band spectrum of NiO, it was first identified the charge-transfer character of the insulating gap of this oxide, helping establish the difference between Mott and charge-transfer insulators [2]. On the other hand, important information on the correlated nature of electrons can also be gained by studying the fine structure of core level spectra, as in the case of the copper dihalides [3].

For a correct interpretation of PES data, it is necessary to consider the N-body nature of atoms, molecule and solids. Usually the description of the photoemission process is based on a number of assumptions, among which one of the most important is the so-called *sudden approximation*, where it is assumed that the photoexcitation is fast with respect to the motion of the remaining $N-1$ electrons (which are sometimes called *passive* electrons). In this limit, it is possible to show that the photo-ionisation cross section is the product of a one-electron matrix element (for the electron which is being

photoemitted) with a $N-1$ overlap integral between the ionic wave function in the final state and a representation of the initial-state passive electrons. However, since electrons interact with each other, after the ejection of the photoelectron, the system will try to minimise its energy by rearranging its remaining $N-1$ electrons to *screen* the positive charge of the photohole: especially for strongly correlated materials, there will be several ways to do this, and then there will different final states over which the representation of the initial-state passive electrons can be projected. This different final states can be identified as satellite structures in core level spectra accompanying the so-called *main line*. The energy positions and the intensity of the satellites can then yield an insight on the nature of the correlation between electrons in the systems [1, 4].

Over the last decade, thanks to advances in the development of beamlines based at synchrotron radiation facilities, PES has been successfully extended to hard X-ray regime ($\hbar\omega > 2$ keV). This hard X-ray photoelectron spectroscopy (HAXPES) has the advantage with respect to conventional PES, to provide information on the chemical states of atoms with real bulk sensitivity (information depth up to 15-20 nm when the electron kinetic energy is ≥ 5 keV). This becomes particularly important when trying to probe bulk electronic properties of strongly correlated systems. In fact for these systems the intrinsic surface sensitivity of standard PES becomes a limitation, since effects occurring at surfaces such as structural distortion, stoichiometry changes, strong reactivity to external agents and major atomic and/or electronic reconstruction can severely influence electron correlation [5].

One of the most important results obtained through HAXPES, has been the identification of a completely new class of low binding energy satellite features, which have been named *extra-peaks*, which are particularly intense and resolved in the $2p$ core level spectra of $3d$ transition metal oxides [6] and more recently in diluted magnetic semiconductors [7]. These features were already known in the soft X-ray (more surface sensitive) spectra of $4d$ and $4f$ based systems, but not in $3d$ based materials. Several experiments have proved how these peaks are connected to the conduction and magnetic properties: for example in manganites such features are seen in the metallic phase and disappear when the systems goes into the insulating phase. Furthermore they are not detectable when low energy electrons are employed, suggesting that the electronic screening (hence the correlation between electrons) is different at the surface and the bulk of materials. The fact that these structures can be seen only when determined conditions are achieved, has led to question whether they could be used as a spectroscopic "fingerprint" of the metallic character in systems close to the metal-insulator transition and/or to evaluate the quality of samples produced for device implementation. Related to this issue, it would be important to know whether such peaks appear gradually or suddenly at a certain probing depth (i. e., when a certain electron kinetic energy is achieved) and also to put some constraints on the values of this "critical thickness" on different class of materials.

We have addressed this issue to some extent in this thesis work by exploiting the broad photon energy range achievable at the I09 beamline of the Diamond synchrotron radiation facility (Didcot, United Kingdom). In particular, we have studied the photon energy dependence of a low binding energy peak in the photoemission spectrum of Mn

$2p$ in both $Ga_{1-x}Mn_xAs$ (emblematic representative of the class of diluted magnetic semiconductors) and $La_{1-x}Sr_xMnO_3$ (distorted perovskite material known to display colossal magnetoresistance). This study has highlighted how in both systems, the contribution of the extra-peak to the total amplitude of the Mn $2p$ core level spectrum is significantly reduced when the energy of the probing photons is reduced. This behaviour has been interpreted by assuming the existence of a layer of material close to the surface where the screening channel associated to the extra-peak is suppressed with respect to the bulk. This slab in which the extra-peak is absent attenuates the signal coming from the "substrate": by considering a simple exponential attenuation of the intensity of the satellite, an estimation of the thickness of this layer can be obtained. This type of analysis has revealed that in manganites the attenuating layer is significantly thicker with respect to $Ga_{1-x}Mn_xAs$.

We have cited earlier that $4d$ systems display well screened features in the core level spectra already in the soft X-ray regime. As example of this class of compounds, rutile RuO_2 samples have also been investigated with HAXPES. The Ru $3d$ spectrum of this system (and of ruthenates in general) show a strong well screened peak which is more intense of the poorly screened one, already at conventional photon energies. We will show however that also these structures evolve as a function of the kinetic energy.

Furthermore, one of the most straightforward advantages of HAXPES is that it gives the possibility to probe deep core levels, such as the $1s$ of transition metal elements, which are not accessible in the photon energy range exploited in conventional PES. In general the lineshape of these core levels is expected to be simpler, given the absence of effects such as spin-orbit splitting and the reduction of exchange splitting due to the small superposition with valence orbitals and can give additional information on the screening processes which are associated to satellite features in photoemission spectra. In particular, it can be expected that the presence of a core-hole in the $1s$ orbital has weaker influence on the $3d$ states with respect to the case of a $2p$ photohole. As a representative system we have characterised at the GALAXIES beamline of the SOLEIL light source (Saint-Aubin, France), the $1s$ and $2p$ core level spectra of anatase TiO_2, a material which is considered particularly promising for photocatalytic applications, revealing in the case of the $1s$ a couple of satellite features which can be related to electronic charge moving from the $2p$ ligand levels to the crystal-field split $3d$ levels of the metal atom.

Due to the importance that HAXPES has gained in the ten years since its first development, there are already plans to extend this technique to the *time domain*. By exploiting the unique characteristics of the light produced at X-ray free electron lasers (XFELs), especially the very short duration on the pulses (tens of fs), it should be possible to use HAXPES to extract dynamical information at the time scales typical of electronic processes [8]. This will require a huge effort to realise spectrometers able to detect in a pulse-by-pulse fashion, high intensity photoelectron beams with good time (< 1 ns) and energy (~ 100 meV) resolution. We have addressed this issue by studying through electron trajectory simulations the behaviour of two different types of time-of-flight (TOF) electron spectrometers suitable for time-resolved HAXPES at the European X-ray Free Electron Laser (EXFEL), a fourth generation synchrotron radiation light source which is currently under construction at Hamburg, Germany.

This thesis work is organised as follows: in Chapter 1 the role of satellite structures in photoemission spectra in revealing the strongly correlated nature of $3d$ electrons in transition metal compounds is presented, with a particular emphasis on the contribution of HAXPES to the argument. In Chapter 2 a brief introduction on synchrotron radiation, which is one of the fundamental ingredients to perform HAXPES experiments, is given and the experimental stations where the data for this thesis have been acquired are described. The results of the work are presented in Chapter 3: core level spectra of $Ga_{0.87}Mn_{0.13}As$, $La_{0.65}Sr_{0.35}MnO_3$ films with different strains, RuO_2 films with different crystallographic orientation and TiO_2 samples with different oxygen vacancy concentration are studied through HAXPES. These results are then discussed in more detail in Chapter 4. Finally in Chapter 5, preliminary data obtained by time-resolved HAXPES on $La_{1-x}Sr_xMnO_3$ are briefly shown and the results of electron trajectory simulations for two different time-of-flight spectrometers suitable for HAXPES experiments at pulsed source like the EXFEL are presented and discussed.

Chapter 1

Photoelectron spectroscopy on transition-metal systems

1.1 Strongly correlated *d*-systems

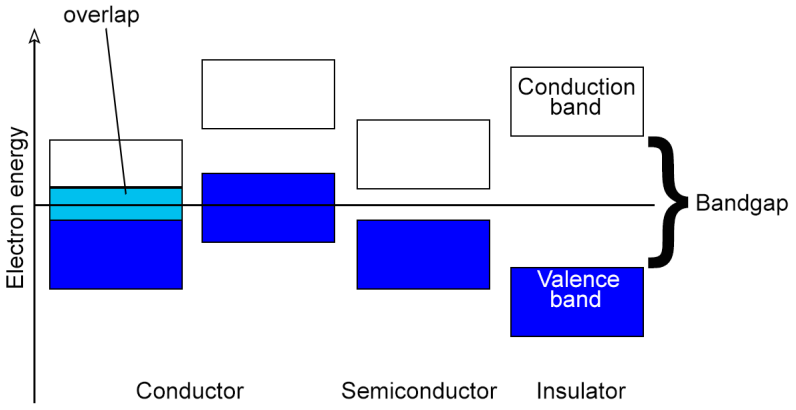


FIGURE 1.1: Schematic representation of the electronic structure around the Fermi level of metals, semiconductors and insulators as expected from band theory.

With the advent of quantum mechanics in the first decades of the 20th century, the description of noninteracting or weakly interacting electrons in a periodic crystal lattice led to band theory and to the first discrimination between metal and insulators (semiconductors) based on the filling of the electronic band at absolute zero temperature [9–11]. If the highest occupied band (*valence band*) is completely filled, then the Fermi level lies in the gap between this band and the lowest unoccupied band (*conduction band*) and we have an insulator, as in the case of Al_2O_3. If the gap is so small that electrons can be thermally excited to the lowest empty band we have a semiconductor, as Si for example. On the other hand if the highest occupied band is only partially filled as in the case of

Cu, then the Fermi level lies inside this band and the system is a metal. A metallic system can also arise when the valence and conduction bands overlap, as in the case of Mg. This is schematically represented in Fig. 1.1, where the valence and conduction bands are represented by rectangles, along with the position of the Fermi level (solid horizontal line). This approach, which can describe the physical properties of many materials, is however not adequate to account for materials like transition metal oxides (TMO) as NiO for example, describing them as metals while experiments proved them to be poor conductors if not insulators [12]. Indeed in these systems, characterised by atoms with partially filled d or f electron shells, the electrons are closely confined in these orbitals and then experience strong Coulomb repulsion. Furthermore, they can also interact through their spin and orbital angular momenta: this interplay among various degrees of freedom can lead to rich phase diagrams, where small changes in external parameters such as temperature, pressure or doping can cause significant variations of macroscopic properties. In Fig. 1.2 for example the electronic phase diagram in the plane of doping

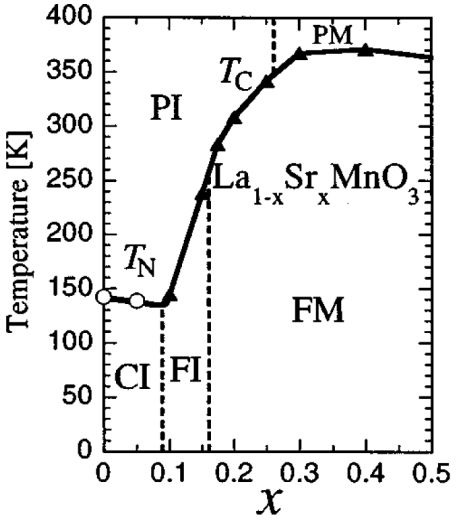


FIGURE 1.2: Electronic phase diagram in the plane of doping concentration x and temperature for distorted perovskite $La_{1-x}Sr_xMnO_3$. Various states are possible: CI, spin-canted insulating; FI, ferromagnetic insulating; FM, ferromagnetic metallic; PI paramagnetic insulating; PM paramagnetic metallic. Adapted from [13].

concentration x and temperature for distorted perovskite $La_{1-x}Sr_xMnO_3$ is reported. We see that for $x < 0.15$ exists a temperature at which the material undergoes a transition from the paramagnetic insulating (PI) to the spin-canted insulating (CI) phase, although for $x > 0.10$ this spin-ordered phase is almost ferromagnetic. Increasing more the doping a full ferromagnetic phase is reached, with the Curie temperature increasing strongly with the doping concentration, until saturation is reached around $x = 0.3$.

One of the most known consequence of electron correlation is the metal-insulator transition (MIT) [13], which occurs for example in transition metal oxides with open-shells, where resistivity can change as a function of external parameters in some cases over several orders of magnitude. In Fig. 1.3 the dependence from temperature of the resistivity in crystals of $La_{1-x}Sr_xMnO_3$ with different doping levels is reported. The arrows

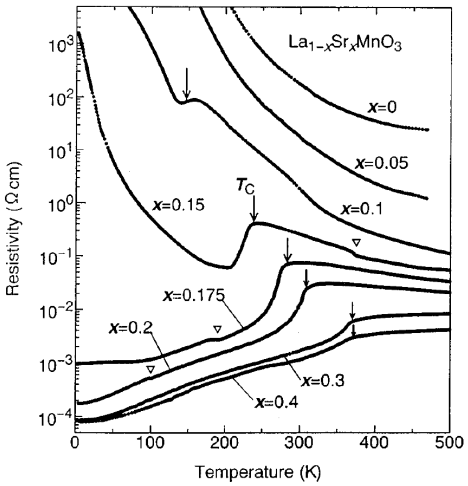


FIGURE 1.3: Resistivity of $La_{1-x}Sr_xMnO_3$ crystals as a function of the temperature for different concentration levels x. The Curie temperature of the manganites is represented by the arrows, while the structural transition temperature is represented by the triangles. Adapted by [13].

indicate the Curie temperature of the system and triangles the critical temperature for a rhombohedral-orthorhombic structural transition. Band theory, which considers only the interaction of a single electron with the average potential of the nuclei and other electrons, is simply not adequate to describe the insulating state and its fluctuations to the metallic state, as the role of correlated electrons is prominent in this phenomenon. The insulating state is called *Mott insulator* after Mott, who first developed a theoretical framework to describe the connection between electron correlation and such state [14, 15]. He described the systems as a lattice with one orbital on each site: in absence of correlation, a single band would arise by the superposition of all electron orbitals. However, when two electron reside on the same lattice site, they would feel a strong repulsion, which would split the band in two. The lower band would be formed by those electrons which reside alone on a lattice site, while the upper band would be made up by those electrons which occupy a site where an electron is already present. If all sites would host just one electron, only the lower band would be full and the system would result an insulator. Understanding the transition between Mott insulators and metals, proved to be more difficult, but the first results were achieved with the so-called *Hubbard model* [16]. In this approach, only electron orbitals near the Fermi level are considered, which can be sufficient when describing low energy and low temperature properties and when few (or in some cases only one) bands are involved. For a single band close to the Fermi level, the Hubbard Hamiltonian reads

$$H_H = \sum_{\langle ij\rangle,\sigma} t_{ij}(c^\dagger_{i\sigma}c_{j\sigma} + c^\dagger_{j\sigma}c_{i\sigma}) + U\sum_i \left(n_{i\uparrow} - \frac{1}{2}\right)\left(n_{i\downarrow} - \frac{1}{2}\right) - \mu\sum_{i\sigma} n_{i\sigma}, \qquad (1.1)$$

where t_{ij} is the matrix element describing the *hopping* of an electron with spin σ from an orbital on site i to one on the site j, $c^\dagger_{i\sigma}(c_{i\sigma})$ represents the creation (annihilation) operator of an electron on the site i having spin σ, U is the local Coulomb interaction between two electrons occupying the same lattice site, $n_{i\uparrow} \equiv c^\dagger_{i\uparrow}c_{i\uparrow}$ ($n_{i\downarrow} \equiv c^\dagger_{i\downarrow}c_{i\downarrow}$) is the

number operator of spin "up" ("down") electrons and μ is the chemical potential. t_{ij} represents the kinetic energy of electrons which hop between atoms, while the electron interaction energy is accounted for by the U parameter. These two terms are in competition, since the first favours the delocalisation of the electrons, while the second has a minimum when electrons are localised on different lattice sites. t_{ij} determines the bandwidth W: the U/W ratio, along with other parameters such as the temperature T and the doping or number of electrons, determine the properties of the systems in the framework of the Hubbard model. One of the most important questions, is how the spectral function (and consequently the density of states) varies as a function of the U/W ratio. This is pictorially represented in Fig. 1.4, which reports the density

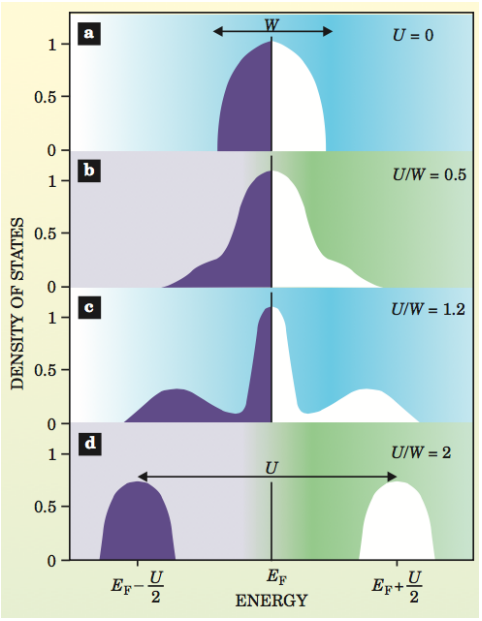


FIGURE 1.4: (a) Electron DOS for a metallic system in the case of entirely independent electrons ($U = 0$). (b) DOS in the weakly correlated regime ($U/W = 0.5$). Electrons can be described as quasi-particles whose DOS resembles the one for free-electrons. (c) DOS for strong correlated metals ($U/W = 1.2$), characterised by the quasi-particle peak at the Fermi level and the Hubbard bands. (d) DOS for a Mott-Hubbard insulator ($U/W = 2$), where electron interactions have caused the quasi-particle peak to disappear. Adapted from [17].

of states (DOS) of electrons in a material for different values of the U/W ratio; in this picture the occupied bands are violet, the un-occupied bands are white:

- (a) $U = 0$, is the case of delocalised electrons, where the DOS is assumed to be an half-ellipse, with the Fermi level in the middle, as in the case of a metal;
- (b) $U/W = 0.5$, is the case of a weakly-correlated metal, when electrons can be described in terms of quasi-particles (electrons "dressed" by the interaction);
- (c) $U/W = 1.2$, is the case of a strongly-correlated metal, where the DOS exhibits a quasi-particle peak at the Fermi edge and the two Hubbard bands due to local excitations broadened by the hopping of electrons to another atom;

- (d) $U/W = 2$, is the case of a Mott-Hubbard insulator, where the electron interactions are sufficiently strong to suppress the quasi-particle peak, whose spectral weight is distributed between the two Hubbard bands. The lower band is a simply occupied band (electron with one spin projection) and the upper band can be occupied by electrons with both spin projections.

Actually, the Hubbard model considers only electrons in s orbitals, while the MIT is mostly known in d-electron systems, namely transition metal (TM) compounds. In line with the above presented model one would expect that the gap is formed as a consequence of the splitting of the d band into an upper and a lower Hubbard band. The separation between the bands could be the on-site Coulomb interaction U we introduced in Eq. 1.1 and the only possible excitations across the gap should be of the type $(d^n)_i + (d^n)_j \rightarrow (d^{n-1})_i + (d^{n+1})_j$, meaning that in the initial state there are n electrons in the two d orbitals centered around two different lattice sites i and j while in the final state we have $n-1$ electrons on the site i and $n+1$ in the site j (an electron has passed from the lattice site i to j). However, photoelectron spectroscopy results showed that in some transition-metal oxides like NiO [2, 18], the smallest possible excitation involves $p-d$ charge transfer, $(d^n)_i + (d^n)_j \rightarrow (d^n\underline{L})_i + (d^{n+1})_j$, where $\underline{L}$ indicates a hole in the ligand L (in this case the oxygen orbital which bridges two d orbitals). In this case in fact the oxygen p band is found between the two Hubbard bands, so that the $p-d$ charge transfer energy $\Delta < U$. This kind of difference in the nature of the energy gap has brought Zaanen *et al.* [19] to separate insulators in two types:

- if the gap is formed between the occupied Hubbard lower d band (if this band is occupied, it means that there is one electron per site) and the empty upper Hubbard d band $\Rightarrow$ *Mott-Hubbard* insulators (V_2O_3, Ti_2O_3, Cr_2O_3);
- if the p level is close to the Fermi level, the ligand p band lies in between the Hubbard d bands, so the gap is of $p-d$ type $\Rightarrow$ *charge-transfer* insulators (NiO, FeO, $LaMnO_3$).

This separation can be better explained in Fig. 1.5, where a schematic energy-band diagram is reported for (a) Mott-Hubbard and (b) charge-transfer insulators; for both types of insulators, the energy-band diagram in a single-electron picture is also represented.

The results on the valence band NiO, helped establish photoelectron spectroscopy as one of the major tools in understanding the electronic structure of correlated TM, in particular thanks to the study of the variation in position and intensity of satellites structures accompanying the main features [2, 18]. Satellites peaks are also found in photoemission spectra of core-levels [3], in particular in the hard X-ray regime, whose higher bulk sensitivity with respect to conventional photoelectron spectroscopy helped identifying screening channels which are evidently suppressed at the surface [6, 7, 21, 22]. Some details on the spectral line shapes and the proposed mechanisms for the appearance of these satellites will be the subject of Sec. 1.2.

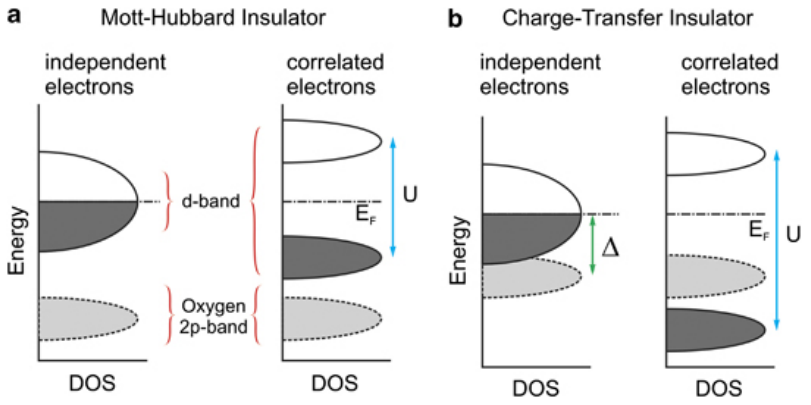


FIGURE 1.5: (a) Pictorial representation of Mott-Hubbard insulator density of states in a single electron picture and correlated electron model (left and right side, respectively). (b) Pictorial representation of charge-transfer insulator density of states in a single electron picture and correlated electron model (left and right side, respectively). The lower Hubbard d band is in dark gray, the upper Hubbard d band is in white, the p band is in light gray. E_F is the Fermi level (dotted-dashed line), U is the on-site d Coulomb interaction and Δ is the $p-d$ charge-transfer energy. Adapted from [20].

1.2 Core level satellite lines

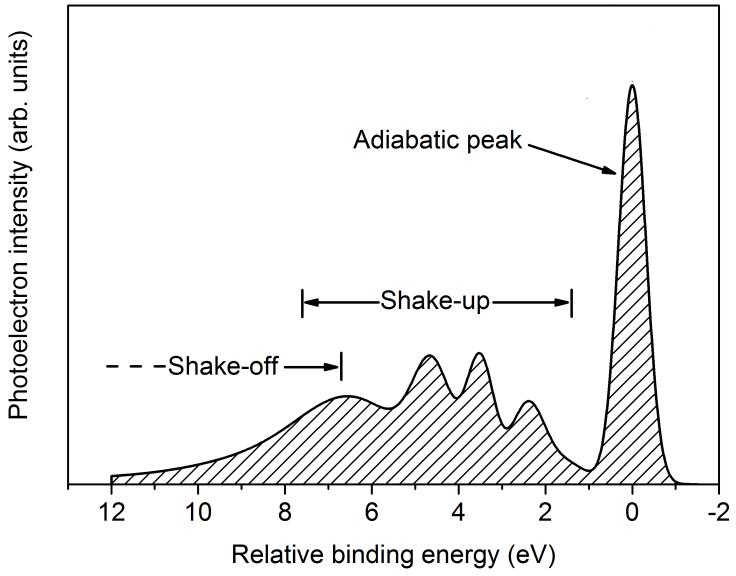


FIGURE 1.6: Schematic photoemission spectrum reporting the adiabatic peak along with shake-up and shake-off satellite structures.

The presence of satellite lines in photoemission spectra is due to the many-body nature of atoms: during the photoemission process, after the photoexcitation, the system can project over various different final states, because the wave-functions of the initial and final states are different [4]. In order to excite these states, energy must be provided, so

that these transitions are identified in a spectrum by features at lower kinetic energies with respect to the peak associated to the ground state (which is also called *adiabatic peak*, see also Fig. 1.6). If such transitions involve a final bound state, then the associated peak is called a *shake-up* peak; on the other hand if a continuum state is interested, the satellites structures are identified as *shake-off*. As these structures are created during the photoemission process, they are sometimes called *intrinsic*. In solids however, as the photoelectrons must travel through a volume containing other electrons before leaving the material, they can excite these other electrons by giving them part of their energy and then observed with a lower kinetic energy than expected. On the other hand, part of the electrons will travel through the solid without losing any energy: these photoelectrons will form the so-called *no-loss* line, while those which underwent collisions inside the material will be distributed in an *inelastic tail*. Usually this tail is formed by broad discrete peaks and a continue feature-less part. These structures are usually called *extrinsic*, because they arise following energy-loss events suffered by the photoelectron on their way to the surface.

We will now give a basic description of intrinsic satellites in the simple case of open shell solids (containing $3d$, $4d$, $5d$, $4f$ o $5f$ elements), following the approach of Hüfner [1]. For this class of systems the analysis of satellite lines is made "simple" by the fact that their d- or f-electrons are quite localised also in metals. In first approximation, this allows to use a simple molecular orbital approach, in which the d or f part of the system is described by one orbital and the ligand or valence band by another. A more accurate approach consists in representing the solids by means of clusters; although this neglects the intrinsic "infinite" nature of a solid, by using ligand field or configuration interaction theory, the energy levels of solids can be calculated with a high degree of accuracy. Another approach, based on a modified version of the Anderson Hamiltonian, which describes the interaction of localised and extended states, has also been intensively used to understand the nature of excitation spectra of solids characterised by localised electrons. With the extension of photoelectron spectroscopies to the hard X-ray regime, new features in core-level spectra of strongly correlated systems have been identified, whose theoretical description as combination of local and nonlocal screening or as consequence of screening from coherent or doping induced states at and near the Fermi level is still under debate.

1.2.1 Kotani-Toyazawa model

It was Kotani and Toyazawa that first presented an explanation for the appearance of satellite lines in the core level spectra of open d- and f-shell systems: they attributed it to the existence of different screening channels after the formation of a core level hole [23, 24], idea which was then validated with experiments on Ni metal [25]. The Kotani-Toyazawa model is described pictorially in Fig. 1.7, for a metal in the top panel and for an insulator in the bottom panel. The fundamental ingredients are the reorganisation of the electronic structure after the creation of a core-hole in the photoemission process and the transfer of electronic charge to screen such photohole. The metal is simply represented by:

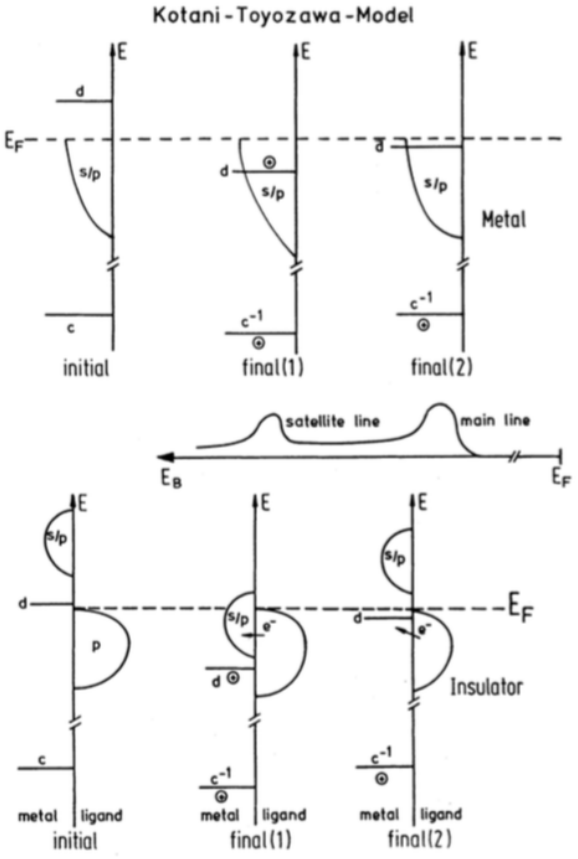


FIGURE 1.7: Pictorial representation of photoemission from a metal (upper panel) and an insulator (lower panel) in the framework of the Kotani-Toyazawa model. Adapted from [1].

- a core level (c) where the photohole is created;
- a partially occupied s/p band;
- an unoccupied d (f) level,

while the insulator is formed by a ligand/metal pair, where:

- the ligand has
  - a p band,
- and the metal ion
  - a core level (c) where the photohole is created;
  - an unoccupied d (f) level (close to the Fermi level, E_F);
  - an unoccupied s/p band.

Both systems present an unoccupied (and quite localised) d (f) level, which in the photoemission process is pulled below the Fermi level, forming along with the photohole

in the core level, a two-hole state. In the case of the metal, in order to minimise the energy of the system, this two-hole state can project over two possible final states:

- one where the two holes are screened by the delocalised s/p band ⇒ **satellite line**, (final state "final (1)" in top panel of Fig. 1.7);
- one where charge is transferred from the s/p band to the d level, which now screens the photohole ⇒ **main line**, ("final (2)" in bottom panel of Fig. 1.7).

Given its localised nature, the d level will be more efficient in screening the photohole than the extended s/p band and for these reason this second state will have a lower binding energy than the first state. Also in the case of the insulator, after the creation of a photohole in the metal ion core level, we have two possible screening scenarios:

- both the metal ion s/p band and d level are pulled below the Fermi level and charge is transferred from the ligand p band to the metal ion s/p band ⇒ **satellite line**, ("final (1)" in the bottom panel of Fig. 1.7);
- only the d level is pulled down the Fermi level and screens the photohole with the charge received by the ligand p band ⇒ **main line**, ("final (2)" in the bottom panel of Fig. 1.7).

For both metal and insulator, "final (1)" and "final (2)" states correspond to satellite and main line, respectively.

In order to quantitatively apply this model, in principle band structure calculations for the one-hole final state are needed. However, this situation can be simplified for insulators by representing the solids with one metal ion surrounded by a cluster of ligands, which in turn allows a molecular-orbital configuration interaction approach to be used. Finally, the valence orbitals can be described in terms of one metal orbital and one ligand orbital, whose interaction gives rise to two molecular orbitals [26]. In this simple version of a cluster approach, the metal s/p band is missing and cannot then be populated in order to screen the photohole as described above; however this band has a strong delocalised character, which means that following its overlap with the ligand p band, there will be not much charge accumulated around the metal ion (where the photohole is). For this reason the screening channel which gives rise to the satellite line in Fig. 1.7 is often referred to in the literature as *non-local screening*.

1.2.2 Gunnarson-Schönhammer theory

We have seen how features in core-level photoemission spectra can be understood in terms of screening of the core photohole by electrons occupying orbitals centered on the ionised atom. The shape of the photoemission line is related to the coupling between the screening electron and the other occupied, delocalised levels in the initial state. Initially developed to interpret photoemission spectra from Ce ($4f$) compounds, the

Gunnarson-Schönhammer theory was one of the first attempts to directly incorporate correlation effects between electrons in narrow bands [27]. It can be used to derive both core and valence spectra at zero temperature. The essential points of the model can

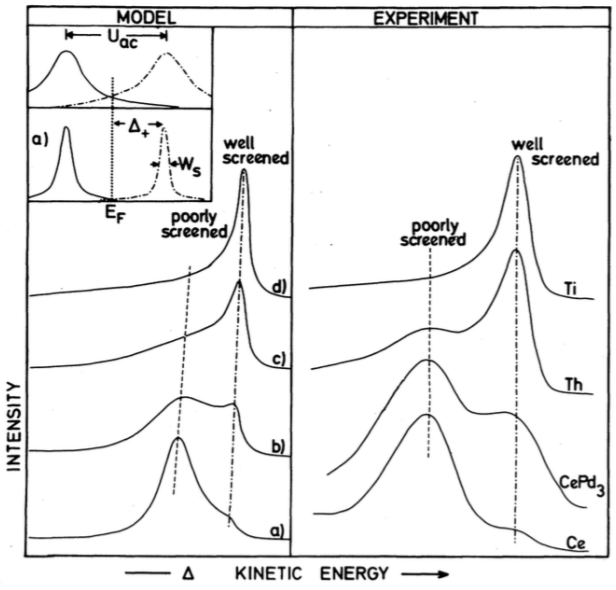


FIGURE 1.8: Comparison of photoemission spectra from core levels of metals (Ce $3d_{5/2}$, Th $4f_{7/2}$ and Ti $2p_{3/2}$) with theoretical results obtained by applying the Gunnarson-Schönhammer model of screening in photoemission. Adapted from [28].

be discussed by looking at Fig. 1.8. The role of a screening orbital is determined by its relative position with respect to the Fermi level (Δ_+ in the inset of Fig. 1.8) and on the degree of coupling with the occupied levels, expressed in terms of the width of the screening level (W_S in the inset of Fig. 1.8). After the creation of a photohole, the energy of screening level is decreased by an amount U_{ac} (see the inset of Fig. 1.8) and will pass below the Fermi level: then the final state with the minimum total energy will be the one in which an electron is transferred from level around the Fermi level to the screening orbital. The peaks associated to such states are called *well-screened*[1], and their intensity reflects the coupling of the screening level with the occupied states in the initial configuration. We note by looking at the left panel of Fig. 1.8 that by changing the value of the W_S/Δ_+ ratio, the peak shape changes from a situation in which most of the intensity is in the poorly screened peak (curve (a) in Fig. 1.8), to one in which most of the spectral weight has shifted to the well-screened peak. (curve (d) in Fig. 1.8). These calculations are compared to XPS spectra of Ce $3d_{5/2}$, Th $4f_{7/2}$ and Ti $2p_{3/2}$ from Ce, $CePd_3$, Th and Ti. In the case of metallic Ce, the Ce atoms have a $[Xe]4f^1(5d6s)^3$ configuration, while configurations with one more electron in the $4f$ ($4f^2$) have a distance $\Delta_+ = 3 - 7$ eV from the Fermi level (in the absence of a core-hole). When a core-hole is formed, the $4f^2$ configuration can pass the Fermi level so that charge can be transferred in the $4f$ orbitals and screen the core-hole. From the Gunnarsson-Schönhammer model it results that the $4f^2$ levels of Ce have a width of

[1]Please note that in contrast with what seen in the case of the Kotani-Toyazawa model, in this case it is called satellite the peak associated to transition to the ground state (the well-screened peak).

about $W_S = 0.1 - 1.0$ eV, which is quite less than Δ_+. This means that in the initial state they are poorly hybridised with the delocalised levels. This situation corresponds the weakly coupled limit of the Gunnarsson-Schönhammer model, and in fact in the experimental spectra (Ce and $CePd_3$ in the right panel of Fig. 1.8) most of the intensity is in the poorly screened peak. For Ti on the other hand, it is known that the $3d$ orbital are quite localised and that the d^{n+1} levels are close to the Fermi level. This means that these levels will be hybridised with the delocalised occupied orbitals, and this situation corresponds to the strongly coupled limit of the model, as confirmed by the fact that in the experimental spectrum most of the spectral weight is in the well-screened peak. These results we just illustrated, date as far as 1980 [28], however they represented the first case in which it was demonstrated how the trend of intensity in the two peaks is related to the degree of localisation of the orbitals involved in the screening. It led the authors to suggest that "one could even use XPS line shapes to set up a scale of degree of localisation of such screening orbitals".

1.2.3 Cluster model and nonlocal screening effects

In the framework of the Gunnarson-Schöhnammer theory we illustrated earlier, most calculations are limited to a single transition metal ion or a small cluster of ligands surrounding a central metal ion. In the case of NiO for example a NiO_6 cluster was used [29], whose results for the Ni $2p$ spectrum is illustrated in the right panel of Fig. 1.9 (in the inset the NiO_6 is represented). With this method three peaks are obtained:

- the most intense peak at 0 eV relative energy is associated to a final state with main character $3d^9\underline{L}$;
- the peak around 6 eV (the one in the middle) is instead related to a $3d^{10}\underline{L}^2$ final state;
- finally the peak at highest energies is the one associated to the final state where the hole in the $2p$ core level is left unscreened, which means a $3d^8L$ configuration.

In the left panel of Fig. 1.9, curve (a) represents the experimental Ni $2p$ spectrum measured from a NiO single crystal. It can immediately be noticed that there is an intense feature at 0 eV relative energy, along with a less intense peak at around 2 eV: this second peak is not reproduced in the cluster calculations reported in the right panel. It was proposed that the extra-peak in the experimental spectrum could be accounted for by including more metal ions in the cluster calculations [30]. In particular a Ni_7O_{36} cluster was used, formed by a central Ni atom surrounded by six NiO_6 clusters (see the inset of the left panel of Fig. 1.9). In order to not include all the valence holes of this cluster (it would have resulted in a fourteen particle problem), the holes of the NiO_6 clusters have been frozen on the Ni atom, except for that cluster whose central atom contains the core hole. The resultant spectrum is the (b) curve in the left panel of Fig. 1.9. It can be seen that an extra-peak on the high binding energy side of the main peak appears, as a result of the screening by an electron which does not come from one of the

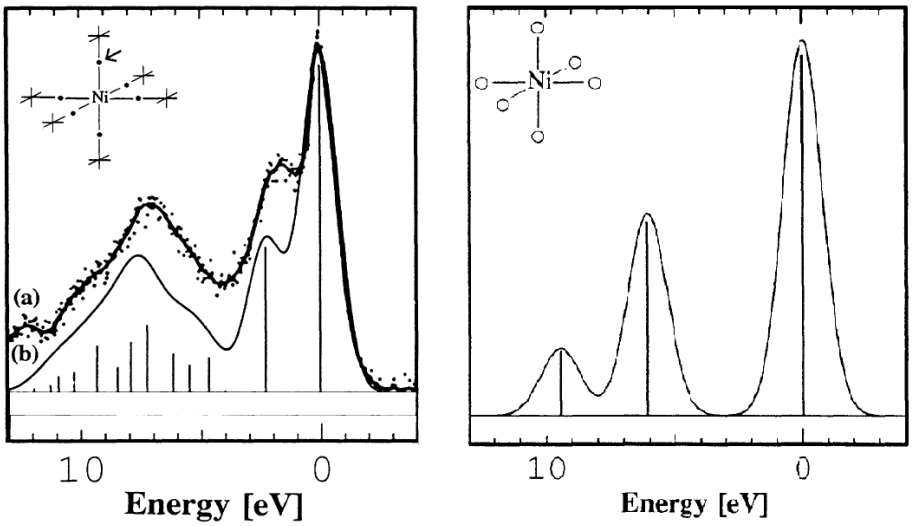


FIGURE 1.9: Left panel: comparison of experimental Ni $2p$ spectrum from a NiO single crystal (a) and the results from calculations with a Ni_7O_{36} cluster (b); the doubly peaked main line is due to nonlocal screening. The cluster is sketched in the inset of the picture. Right panel: Ni $2p$ spectrum calculated for a NiO_6 cluster, sketched in the inset. It can clearly be seen that the calculation fails to reproduce the double peaked structure of the main line. Adapted from [30].

O orbitals around the Ni ion with the core hole, but from a neighbouring NiO_6 cluster. Thus the local configuration of the NiO_6 unit containing the core-hole has mainly $\underline{2p}3d^9$ character. Overall, the spectrum shows good agreement with the measurements, which led to propose [30] "that the doubly peaked main line is intrinsic for bulk NiO" and is not due to defects, as it was previously suggested [31].

As we will be discussing later, nonlocal screening has also been used to explain the presence of low-binding energy features in high-resolution hard X-ray photoelectron spectroscopy on cuprates, manganites and ruthenates [32, 33]. It was also demonstrated how these features can be very sensitive to external parameters such as temperature and doping, not to mention changes in orbital occupation and orbital and/or spin ordering.

1.2.4 Dynamical mean-field theory and quasi-particle states

A different screening mechanism was proposed in the case of Mott-Hubbard systems, able to explain the Ru $3d$ spectra of various ruthenates, which have interesting properties related to the correlation among $4d$ electrons [34]. As illustrated in Fig. 1.10, the $3d$ spectrum is formed by the spin-orbit doublet (splitting of about 4 eV), each peak of which can be roughly separated in two components, which in a charge-transfer scheme can be called the "screened" ("s" in Fig. 1.10) and "un-screened" peak ("u" in Fig. 1.10). It can be seen that in the insulating $Y_2Ru_2O_7$ compound the s peak is absent and becomes more and more important for more metallic systems. Charge-transfer mechanism as in the Gunnarsonn-Schönhammer theory alone is not able to explain these kind of satellites, but some attempts were made by adding a nonlocal screening

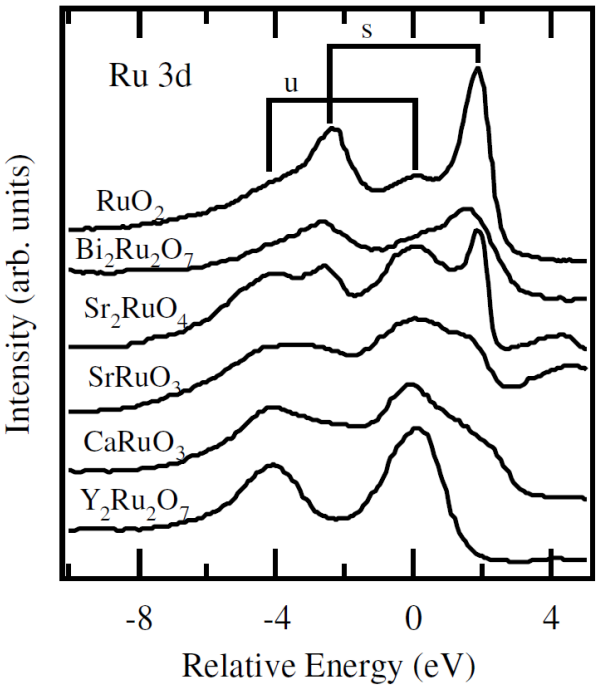


FIGURE 1.10: Ru 3*d* photoemission spectra measured on various ruthenates. s and u indicate the screened and un-screened components, respectively, for the spin-orbit doublet. Adapted from [34].

channel [32, 33]. It was also proposed that these satellite structures may be related to the screening of the core-hole by quasi-particles on the Fermi surface [34] coexisting with the Hubbard bands. This result was obtained by applying dynamical mean-field theory (DMFT) [17] to a single-band Hubbard model including a core-hole potential. DMFT is a technique which allows to map a many-body lattice problem to a single-site problem with effective parameters. One of its major achievement has been the description of the MIT in terms of the change of the ratio between the on-site Coulomb interaction of conduction electrons and the bandwidth W, as it was illustrated in Fig. 1.4. In [34] the origin of the two peaks which can be seen in Fig. 1.10 is investigated by calculating the eigenvalues and eigenvectors of initial and final states for a four-site model. Three energy levels in the conduction band were considered, representing a lower Hubbard band (LHB) a coherent peak (CP) and a upper Hubbard band (UHB); when the core-hole is formed, an impurity level at the core-hole site is considered as well. Then in the final state there are three possible valence electron configurations, which are schematically illustrated in Fig. 1.11.

- panel a) represents the d^1 configuration, where there is a hole in the core-level and the associated impurity level is sketched as a dashed line;
- panel b) is the $d^2\underline{C}$ final state, where an electron has been moved from the coherent peak at the Fermi level to screen the d core-hole;

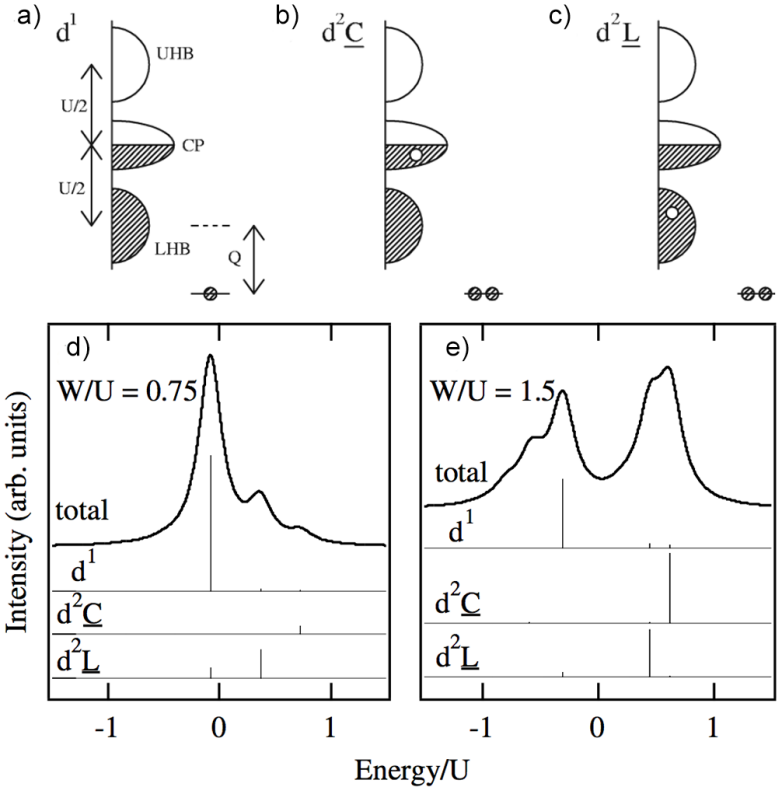


FIGURE 1.11: Pictorial representation of the three main valence electron configurations contributing to the core level spectra of ruthenates. Adapted from [34].

- panel c) is the $d^2\underline{L}$ configuration, analogue to the previous case, with the only difference that the electron screening the core-hole comes from the lower Hubbard band,

where d is the impurity level, C is the coherent peak at the Fermi level and L is the lower Hubbard band. In panel d) and e) are represented two core-level spectra calculated for the four-site model with a W/U ratio of 0.75 (narrow band case) and 1.5 (wide-band case), respectively. It can immediately be seen that in the narrow band case, the spectrum is dominated by the unscreened peak, which originated mainly from the d^1 configuration, as it can be seen by the bar diagram in the panel d) of Fig. 1.11. In the wide-band case the core level spectra present along with the d^1 peak, another structure at low binding energies is visible, which originates from the $d^2\underline{C}$ and $d^2\underline{L}$ configurations (so actually there are two screening channels). These calculated spectra can help us understand the relationship between the W/U ratio and the two peak structures which are observed in Fig. 1.10. Materials which are Mott insulators are characterised by a small value of the W/U ratio: in these systems the configuration $d^2\underline{C}$ is absent both in the ground and final state of the photoemission process and the unscreened peak (mainly d^1 configuration) becomes dominant, while the screened peak due to the $d^2\underline{L}$ configuration can be seen close to the screened feature. The $d^2\underline{L}$ configuration represents the case in which there is a hole in the lower Hubbard band, whose shape is reflected in a extra linewidth broadening of the core-level peak. For a metallic system the W/U

ratio is higher and $d^2\underline{C}$ configuration can now take part to the screening of the core hole created in the photoemission process. It is associated to a sharp *shake-down* satellite peak at lower binding energy, whose intensity increases with the weight of the coherent peak at the Fermi level.

1.3 HAXPES

In the previous section we have seen how the electronic structure of strongly correlated materials can be investigated by examining the details of the core level lines in photoelectron spectroscopy. Established since the mid-1950s as one of the major techniques for the characterisation of surface and bulk properties in a variety of materials, it has found a renewed interest thanks to the extension towards high photon energies, hence high electron kinetic energies. As a matter of fact, in the early stages of photoelectron spectroscopy, hard X-ray sources based on Mo Kα ($\hbar\omega = 17479$ eV) or Cu Kα ($\hbar\omega = 8047$ eV) were used. Later, the quest for higher energy resolution led to the use of X-ray sources based on the Mg Kα ($\hbar\omega = 1253.6$ eV) and Al Kα ($\hbar\omega = 1486.7$ eV), often in combination with a crystal monochromator to reduce the photon bandwidth [35]. However, with the advent of synchrotron radiation facilities, it was demonstrated that core level photoelectron spectroscopy was feasible also in the hard X-ray regime [36]. By using X-rays produced at the Stanford Positron Electron Accelerator Ring (SPEAR) facility in combination with a double-pass cylindrical mirror analyser, these authors obtained the Au $4f$ spectrum with electrons of kinetic energy around 8 keV, retaining an energy resolution (combining the contribution of the electron energy analyser and the photon bandwidth) of about 320 meV. On the other hand the count rate was extremely low, i.e., around 25 counts/s on the $4f_{7/2}$ peak; since usually in the valence band the count rate is significantly smaller than for core levels, it was immediately clear that it was not possible to measure valence bands with this technique retaining an adequate energy resolution (in general by properly choosing the settings of the electron analyser, higher count rates can be achieved at the expenses of energy resolution). This strong reduction of count rate with respect to conventional XPS based on Al Kα or Mg Kα sources is due to the decrease of the photoionisation cross-section upon increasing the photon energy as it can be seen in Fig. 1.12. Here the photon energy dependence of the total atomic photoionisation cross-section for three transition metal elements, namely Ti, Mn and Ru is reported; it can be seen how the cross-section decreases by at least one order of magnitude when passing from $\hbar\omega = 1$ keV to $\hbar\omega = 10$ keV. The sharp jumps visible at certain photon energies correspond to the absorption edges of elements. Interest towards high kinetic energy photoelectron spectroscopy was renewed after Köver *et al.* demonstrated, by using a Mo Kα source in combination with a new high resolution spectrometer, the feasibility of high resolution Auger electron spectroscopy (AES) with a significant increase of intensity with respect to previous results [38]. As we will be showing later in this section, one of the main reasons hard X-ray photoelectron spectroscopy is used, is that it allows to retain a much higher bulk sensitivity with respect to conventional XPS. So, in order to unravel the true bulk properties of materials and highlight differences with respect to the surface, several groups attempted to perform

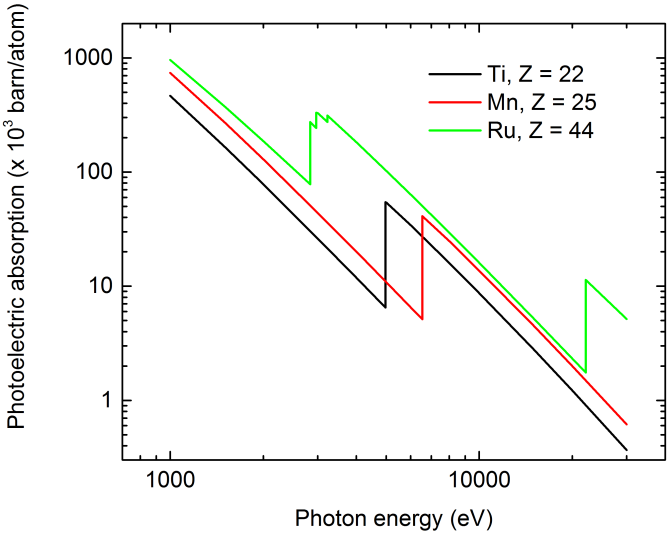


FIGURE 1.12: Total photoelectric cross-section for three transition-metal elements (Ti, Mn and Ru) in the 1-30 keV photon energy range. A log-log scale is used. Data obtained from [37].

high kinetic energy photoelectron spectroscopy, trying at the same time to retain a good energy resolution (few hundreds of meV) from both core levels and valence band. One of the first groups to report on the subject was the group of Suga, which measured the valence band of $CeRu_2Si_2$ and $CeRu_2$ compounds with an energy resolution of $\sim$ 200 meV using relatively high photon energy ($\sim$ 800 eV) [39]. Despite the fact that the photon energy was not so high with respect for example to the energy of Al Kα sources, it is however quite larger than the photon energy used in ultraviolet photoelectron spectroscopy (UPS), which is a well-established technique to study valence band using helium discharge lamps as photon sources ($\hbar\omega = 21.2$ eV). Furthermore, this was the first time in which a group attempted to increase the bulk sensitivity in valence band measurements by increasing the photon energy, while trying to maintain an adequate energy resolution. Some years later, the group of Kobayashi used a modified version of Gammadata Scienta SES2002 electron energy analyser to perform hard X-ray photoemission ($\hbar\omega = 5.95$ keV) at the SPring-8 synchrotron [40]. These results paved the way for dedicated experimental stations in some undulator based beamlines of synchrotron radiation sources: one typical example is the VOlume sensitive PhotoEmission (VOLPE) project at the undulator based ID16 beamline of the ESRF facility, which was based on the development of a custom electron energy analyser able to reach a resolution of about 70 meV [41]. A number of technical difficulties had to be overcome to develop this instrument, such as the electrical isolation of components working at high voltages (several kV) and the realisation of low noise and very stable power supplies. So, it was only thanks to the combination of high intensity sources such as undulators at third generation synchrotron radiation facilities and high efficiency electron energy analysers that HAXPES became feasible.

As reported by Fadley [35], the intensity of a photoelectron line of a given component of a spin-orbit doublet identified by the quantum numbers nlj, associated to an atom Q in a homogeneous polycrystalline sample can be written as a product of terms related to the source, the sample and the analyser:

$$I(Qnlj) = I_0(\hbar\omega) \times A_0 \times \frac{d\sigma_{Qnlj}}{d\Omega}(\hbar\omega) \times \Omega_0 \times \rho_Q \times \Lambda_{MED}(E_{kin}) \times D_0, \tag{1.2}$$

where

- $I_0(\hbar\omega)$ is the incident X-ray flux;
- A_0 is the illuminated sample area which is seen by the analyser;
- $d\sigma_{Qnlj}(\hbar\omega)/d\Omega$ is the differential photoionisation cross-section;
- Ω_0 is the solid angle accepted by the analyser;
- ρ_Q is the density of atoms Q;
- $\Lambda_{MED}(E_{kin})$ is the mean photoelectron escape depth;
- D_0 is the overall detection efficiency.

High intensity sources such as undulators at third generation synchrotron light source in combination with hard X-ray monochromators provides hard X-ray photon beams as intense as $\sim 10^{11} - 10^{12}$ photons/s and as monochromatic as $\Delta(\hbar\omega) \leq 0.1$ eV. With the proper set of optics, such beams can be focussed on spot sizes at the sample position as small as few tens of µm, which is well matched to the acceptance area A_0 of the current class of electron spectrometers. Due to the strong suppression of the photoionisation cross-section at high photon energies as suggested in Fig. 1.12, it is important that as many photons as possible fall inside the analyser field of view. It can be demonstrated that if A_0 is sufficiently small, with a proper set of electron optics able to retain sufficiently large values of retardation R (ratio between the photoelectron kinetic energy and the pass energy of the dispersive element of the analyser) and magnification M (ratio between the area of the photoelectron beam at the entrance of the dispersive element and A_0), then a quite large value of Ω_0 can be achieved along with an adequate energy resolution [35].

If a sufficiently focussed spot is achieved, a grazing incidence of photons can be used in order to irradiate the widest possible sample area without degrading the energy resolution. Such a geometry is already used in conventional XPS, because it is known to significantly suppress the inelastic background of the spectra, in particular for angles smaller than the critical angle for X-ray total reflection [42]. In this condition, the mean excitation depth of photons is reduced to values comparable with the mean escape depth of photoelectrons; however, in order to retain a sufficiently high bulk sensitivity (which is one of the main reasons for which HAXPES is performed), it would be desirable to work at angle slightly larger than the critical angle, in such a way that the mean excitation depth would be still higher (ten times or more) than the photoelectron mean

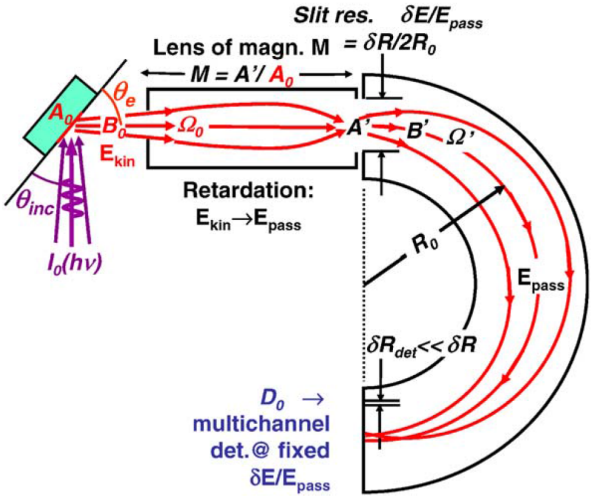


FIGURE 1.13: Sketch of a photoemission experiment in the case of a solid sample and an hemispherical electrostatic analyser: electrons from the sample are sent into the analyser by a retarding, imaging lens. The red arrows represent photoelectron trajectories. The fundamental parameters related to the final photoelectron intensity (as discussed in the text) are also indicated. Adapted from [35].

escape depth. This configuration in principle allows to collect bulk sensitive spectra with a suppressed inelastic background.

The last important point concerns the ability to detect multiple energies in the final focal plane of the analyser; in fact this increases sensibly the D_0 factor introduced in Eq. 1.2. Nowadays this is made possible thanks to several approaches, such as microchannel plates (MCPs) coupled with resistive anodes or charged-coupled device (CCD) detectors.

Thus, thanks to the availability of third-generation synchrotron radiation sources, together with retarding energy analysers designed to take advantage of the small spot sizes which can be achieved at synchrotron beamlines, coupled to suitable detectors for parallel acquisition, adequate data acquisition rates and good energy resolution can be achieved in spite of the decrease of photoionisation cross-section when going into the hard X-ray regime.

1.3.1 Information depth in HAXPES

Standard PES has helped tremendously in the investigation of the electronic properties of matter over the last decades, also thanks to its intrinsic surface sensitivity (probing depth of $0.5-2$ nm in the typical PES analysed electron kinetic energy range $20-1500$ eV), which makes it a technique a choice for the characterisation of the topmost atomic layers of a solid. This is mainly due to the fact that photoelectrons must travel in the solid, where they can interact with other electrons and various degree of freedom of the material, losing then energy. The distance from the surface from which photoelectrons can be obtained is usually quantified in terms of the so-called *inelastic mean free path* (IMFP), whose dependence from the photoelectron kinetic energy is reported in Fig.

1.14 for 41 elemental solids, as calculated by means of the TPP-2M algorithm [43]. We can see that in the 100-1000 eV range. accessible with conventional XPS, the IMFP is less than 10 Å. This intrinsic surface sensitivity of XPS can sometimes be a limitation, for

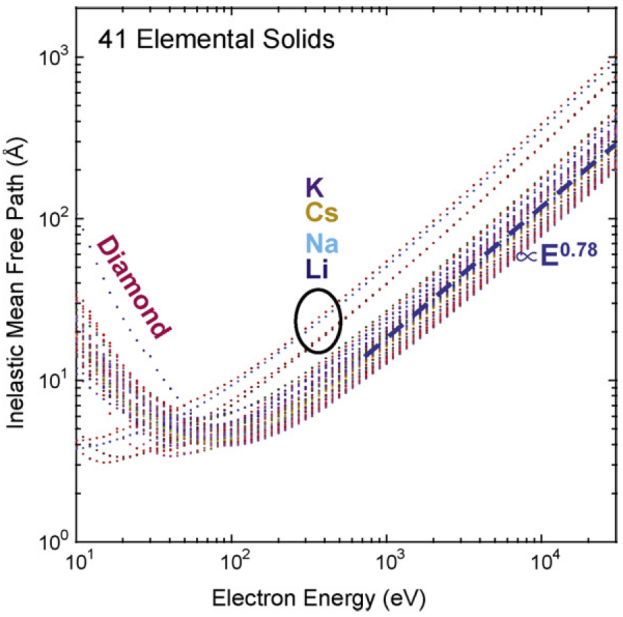


FIGURE 1.14: Calculations of inelastic mean free paths (IMFPs, Λ_2) for 41 elemental solids, using the TPP-2M algorithm [43]: Li, Be, three C allotropes, Na, Mg, Al, Si, K, Sc, Ti, V, Cr, Fe, Co, Ni, Cu, Ge, Y, Nb, Mo, Ru, Rh, Pd, Ag, In, Sn, Cs, Gd, Tb, Dy, Hf, Ta, W, Re, Os, Ir, Pt, Au and Bi. Diamonds and the alkali metals are explicitly indicated to show what electronic structure behaviour can induce deviations from the "general behaviour". The dashed line indicates the first approximation $\Lambda \propto E_{kin}^{0.78}$ behaviour at high kinetic energies. Adapted from [44].

example when wanting to investigate true bulk properties with negligible contribution from the surface or access buried interfaces [45]. However, by looking again at Fig. 1.14, we can see that the IMFP increases roughly as $E_{kin}^{0.75-0.10}$ for energies above 1 keV. It becomes immediately clear then that HAXPES offers a significant increase in the bulk sensitivity with respect to standard XPS. For example, in the case of metallic Au and a kinetic energy of 10 keV, the value of Λ_e can be estimated to be as high as $\sim$ 70 Å [35]. A more systematic study for high energy electrons ($4-6$ keV), on wedge-shaped samples of different class of materials, ranging from noble metals (Cu), open $3d$ shell metals (Co), semiconductors (Ge) and an open $4f$ shell strongly correlated oxide (Ge_2O_3), has confirmed that HAXPES "has the necessary probing depth to be considered a volume sensitive technique" [46]. To be more quantitative, the authors reported values of experimental attenuation lengths (EALs) ranging from $45-50$ Å at 4 keV and $60-65$ Å at 6 keV for Co, Cu and Ge, in fair agreement with theoretical calculations [47]. This also proved how elemental depth profiles can be obtained by changing the excitation photon energy. Furthermore, they were able to estimate the contribution of the surface layer to the total intensity: in the case of Cu, it resulted that for 6 keV electrons, the contribution of a 5 Å surface layer was around 7%, while at 600 eV it was about 46%.

1.3.2 Bulk-only well-screened peaks in HAXPES

It turned out that HAXPES experiments not only are able to access information from a larger probing depth with respect to standard XPS, but also have revealed the presence of "bulk-only" features in core-level and valence band spectra, which are not visible with more surface sensitive PES. The first study where, to our knowledge, this was shown, is a paper of 2004 by Horiba *et al.* on $La_{1-x}Sr_xMnO_3$ [6]. A very detailed experimental and theoretical study of core-level lineshapes measured by HAXPES on one Mott-Hubbard (MH) system, namely $V_{1.98}Cr_{0.02}O_3$ and one charge-transfer (CT) system, namely the optimally doped high-T_C cuprate $Bi_2Sr_2CaCu_2O_{8+\delta}$ crossing the metal-insulator transition, has been presented by Taguchi et al. [48]. They showed

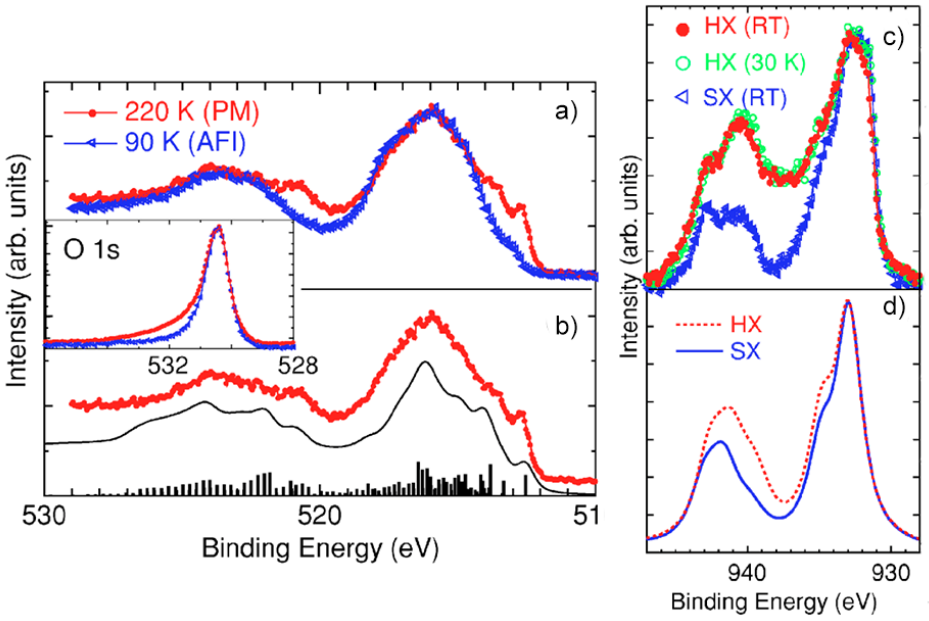


FIGURE 1.15: **a)** V $2p$ HAXPES spectra from $V_{1.98}Cr_{0.02}O_3$ in the paramagnetic metallic (PM) phase (red circles, $T = 220$ K) and antiferromagnetic insulating (AFI) phase (blue triangles, $T = 90$ K). **b)** Comparison of the experimental result in the PM phase with configuration-interaction cluster model calculations. In the inset, the O $1s$ spectrum is showed. **c)** Comparison between the Cu $2p$ spectra from $Bi_2Sr_2CaCu_2O_{8+\delta}$ in the hard (5.95 keV) and soft (1.5 keV) X-ray regime (filled red circles and blue open triangles, respectively) at room temperature and HAXPES spectrum at $T = 30$ K. **d)** Results of cluster calculations of the hard (red dashed line) and soft X-ray (blue solid line) Cu $2p$ spectra. Adapted from [48].

how the spectral features of V $2p$ and O $1s$ in $V_{1.98}Cr_{0.02}O_3$ are modified upon crossing the metal-insulator transition, in particular a low binding energy structure at 512.5 eV in the V $2p$ spectrum is visible only in the paramagnetic metallic (PM) phase. This *well-screened* peak had been seen in earlier soft X-ray studies, but appeared only as a weak shoulder and had been attributed to changes in the core-hole screening in the metallic and insulating phase [49]. The possibility to measure valence band on V_2O_3 with "high" photon energy (700 eV) with a good overall energy resolution (< 200 meV) had previously allowed to identify the presence of an intense coherent peak at the Fermi

level (E_F) in the PM phase which disappears in the antiferromagnetic insulator (AFI) phase [50]. It was then suggested that the feature we described above in the V $2p$ HAXPES spectrum was related to screening by states at E_F. Simply by adding charge transfer from a coherent band (approximated like a level) at E_F in a cluster model, the authors were able to reproduce the spectrum, as it can be seen by the theoretical curve (solid line) in panel b) of Fig. 1.15. It must be noticed that this mechanism is analogue to the one which is obtained by applying DMFT, as discussed in Sec. 1.2.4. A following paper by Panaccione *et al.*, where the authors applied HAXPES to study of both core-level and valence band of V_2O_3, confirmed the correlation between the low binding energy satellites observed in the V $2p$ and V $3p$ spectra and the coherent peak at the Fermi level in the metallic phase [22]. As screening from states at E_F implies nonlocal (long-range) screening of the core-hole, Taguchi *et al.* compared their results on V_2O_3 to the case of $Bi_2Sr_2CaCu_2O_{8+\delta}$, whose Cu $2p$ spectra in the soft X-ray range had been explained in terms of the competition between local and nonlocal screening channel [51]. It resulted that in both cases, the lowest binding energy feature, could be assigned to bulk screening by part of a coherent band. On the other hand, some questions arise when looking more carefully to panel c) of Fig. 1.15. Here the HAXPES spectra at room temperature (filled red circles) and at $T = 30$ K (empty green circles) are compared, but they do not show many differences; however, comparing the HAXPES with the soft X-ray spectrum (blue triangles), it can be seen that the high-binding energy satellites increases significantly when bulk sensitivity is achieved. In this case with the soft X-ray an escape depth of about 10 Å is achieved, which allows to probe only the top two Cu−O layers, while in the HAXPES regime, at least 2-3 unit cells are probed. The high binding energy satellite is usually described in terms of the transition to the $2p^5 3d^9$ state, so the large increase in the total area of the spectrum in HAXPES compared to soft X-rays can be naively attributed to an increase of $3d^9$ weight in the bulk. On the other hand, the theoretical calculations reported by authors seemed to indicate that the hybridisation between the Cu $3d$ states and the O $2p$ ligand, as well as the hybridisation between the Cu $3d$ states and the coherent band at the Fermi level, were reduced in the bulk with respect to the surface. In general it is in the surface that the overlap is expected to be diminished, due the different atomic environment and the reduced coordination between the atoms. This observation highlighted the importance of further experimental and theoretical effort aimed to the explanation of screening phenomena in photoemission and how they can be different in the bulk with respect to the surface of a solid.

In another experiment on electron doped $Nd_{2-x}Ce_xCuO_4$ cuprate [52], the depth dependence of the bulk peak in the Cu $2p$ spectrum was studied in order to shed light on the competition between screening channels in the bulk and the surface. The Cu $2p_{3/2}$ spectra measured in the hard ($\hbar\omega = 5.93$ keV, open circles) and soft X-rays ($\hbar\omega = 1.3$ keV, filled circles) at 70 K in normal emission on a $Nd_{1.85}Ce_{0.15}CuO_4$ sample are shown in Fig. 1.16. Both spectra present a broad structure around 945 - 940 eV binding energy which is recognised as a poorly screened satellite with a $2p^5 3d^9$ character, while the main structure consists of a broad peak (which is called main peak, M) associated to a $2p^5 3d^{10}\underline{L}$ electronic configuration (where $\underline{L}$ indicates a hole in the ligand) and an additional feature on the low binding energy side (which the authors refer to a satellite, S). It can be noticed that this structure evolves from a weak shoulder to a well defined

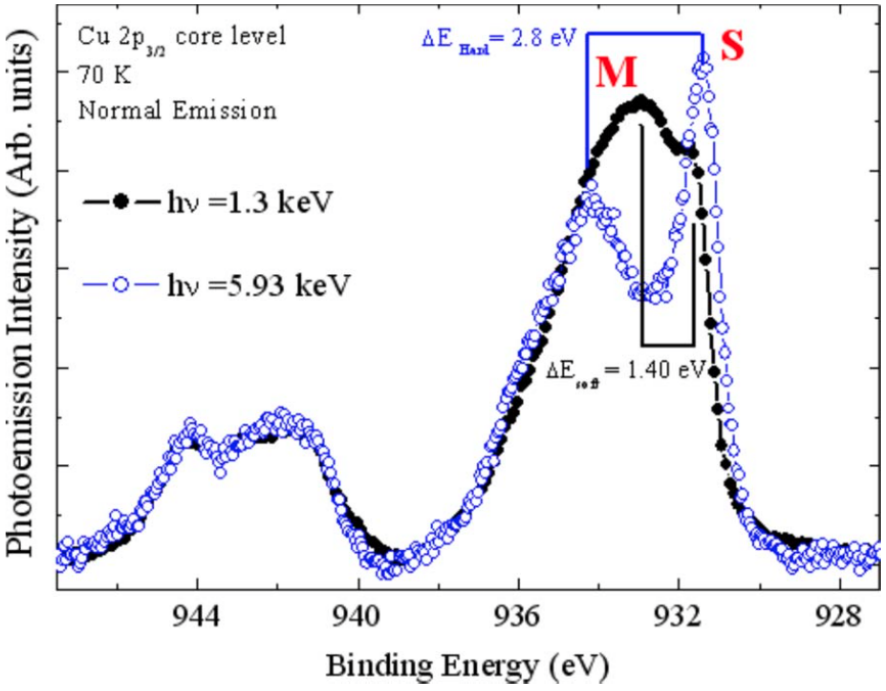


FIGURE 1.16: Comparison of soft and hard X-ray Cu $2p_{3/2}$ spectra measured at 70 K in normal emission on a $Nd_{1.85}Ce_{0.15}CuO_4$ sample. Details about the M and S peak along with the broad satellite structure around 945 - 940 eV binding energy are given in the text. Adapted from [52].

peak when passing from the soft to the hard X-rays and furthermore the energy separation between M and S passes from $\Delta E_{soft} = 1.4 \pm 0.2$ eV to $\Delta E_{hard} = 2.8 \pm 0.1$ eV, mainly due to the energy location of the M peak. To ascertain the nature of the S peak, the authors measured the valence band, but were not able to identify any quasiparticle feature as in the case of V_2O_3, which led them to postulate the existence of "a competition between surface and bulk characters within the Cu - O planes, involving the oxygen ligand". As mentioned earlier, in order to elucidate the modification of the electronic structure when passing from the bulk to the surface, the angular dependence of the Cu $2p_{3/2}$ spectrum was measured at a photon energy of $\hbar\omega = 5.99$ keV; when passing from normal emission to a more grazing emission, the surface contribution is enhanced and accordingly the intensity of the S peak is seen to reduce and the separation with the M peak to decrease. By assuming an exponential attenuation of a bulk peak covered by an overlayer with no S peak, the thickness of such overlayer was found to be $t = 15 \pm 5$ Å, corresponding to less than two unit cells of the sample.

Many other examples can be brought to the attention of the reader, in which well-screened peaks have been identified thanks to the bulk sensitivity of HAXPES in a number of $3d$ transition metal oxides, such as $La_{1-x}Sr_xMnO_3$ and $La_{1-x}Ba_xMnO_3$ (manganites) [6, 53], $La_{2-x}Sr_xCuO_4$ and $Nd_{2-x}Ce_xCuO_4$ (cuprates) [21, 52]. More recently, a similar feature was also identified in a different type of material, namely the dilute magnetic semiconductor (DMS) $Ga_{1-x}Mn_xAs$, where it has been related to the ferromagnetic properties of the compound below the transition temperature [7]. At the present, it is

still not clear the evolution of these structures as a function of the probing depth in photoemission and whether they appear suddenly beyond a certain critical thickness or more gradually.

1.3.3 Local and nonlocal screening channels

We have seen in the previous section, that the presence of low binding energy satellites in the HAXPES core-level spectrum of materials based on transition metal elements, such as cuprates and manganites, can be ascribed to screening of the core-hole by electrons deriving from quasiparticle states at the Fermi level [6, 48]. These findings, suggested the failure of another theoretical framework which had been used to describe the photoemission process from this type of materials in more conventional ranges of excitation energies, which includes nonlocal screening effects involving several metallic sites [30]. However, in 2006 van Veenendal claimed that these previous results did not prove the failure of the local/nonlocal formalism in describing features in HAXPES spectra, but that indeed nonlocal screening is sufficient to explain the presence of low binding energy peaks [33]. For example, in the case of the Mn $2p$ HAXPES spectrum of $La_{1-x}Sr_xMnO_3$, instead of a single MnO_6 cluster, the solid was described in terms of eight MnO_6 octahedra (i. e., involving then more than one metallic site, one of which is where the core-hole is formed during the photoemission process). Periodic boundary conditions were imposed in order to retain the local cubic symmetry as in Fig. 1.17(a). Of course such a "macrocluster" is computationally quite heavy, so in order to reduce the number of calculations needed, each MnO_6 cluster has been effectively represented with a basis set of e_g orbitals. As it will be shown later on, the e_g levels are formed by the crystal field splitting of the Mn $3d$ orbitals (see Sec. 1.4.2). Some of the results of these calculations can be seen in Fig. 1.17(b), where the doping dependence of the Mn $2p_{3/2}$ photoemission peak for $La_{1-x}Sr_xMnO_3$ in the ferromagnetic phase is reported. Three main features can be distinguished:

- starting from high binding energies, around 644 eV a feature can be seen which is related to a unscreened final state: this structure is more prominent for high hole doping, which leads to the absence of e_g electrons on the site hosting the core hole;
- around 641 eV we see the peak which is identified as due to a local screened final state, where there is one e_g electron on the MnO_6 effective unit;
- finally around 639 eV we can see a peak which is associated to nonlocal screened final state, which is characterised by the transfer of screening electrons from neighbouring MnO_6 clusters.

At different doping values correspond a different number of e_g electrons in the whole Mn_8 cluster, as it is illustrated in Tab. 1.1. It can be noticed in Fig. 1.17(b) that the feature associated to a nonlocal screened final state becomes less intense as the hole doping increases: indeed hole doping induces a larger concentration of Mn^{4+} cations (for $x = 0$ there are only Mn^{3+} ions), which happen to have the e_g states unoccupied.

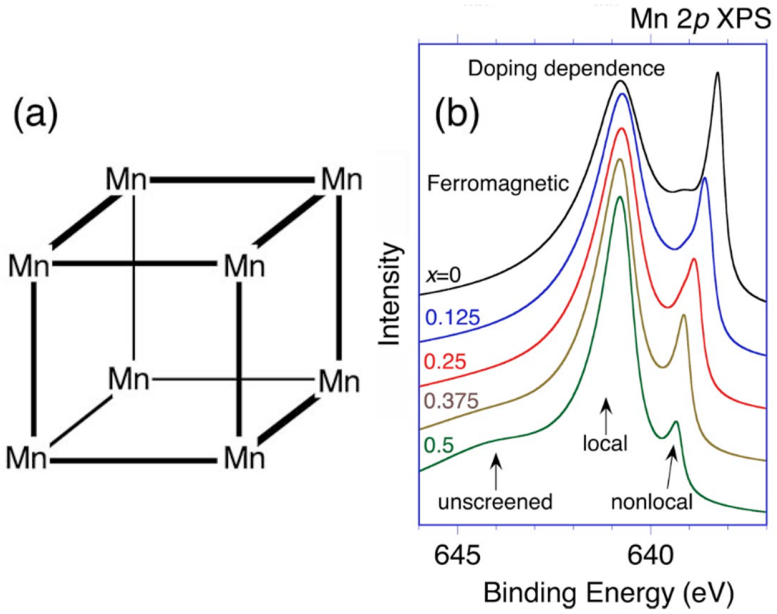


FIGURE 1.17: (a) Mn_8 cluster with cubic symmetry used for the calculations of the Mn $2p$ core level in $La_{1-x}Sr_xMnO_3$. (b) Mn $2p_{3/2}$ spectrum from $La_{1-x}Sr_xMnO_3$ in the ferromagnetic phase as a function of the Sr concentration and then of the number of e_g electrons in the Mn_8 cluster. Adapted from [33].

Hole doping (x)	e_g electrons
0	8
0.125	7
0.25	6
0.375	5
0.5	4

TABLE 1.1: Number of e_g electrons in a Mn_8 cluster with effective MnO_6 units for different hole doping. Values taken from [33].

As the hole doping increments then there are less e_g electrons in the systems and it becomes less probable to create a e_g^2 site. On the other hand, for larger x values it becomes possible to access unscreened final states, where there are no e_g electrons on the site with the core-hole, which is reflected by an increase if intensity around 644 eV. The decrease of intensity of the low binding energy feature as a function of the increased hole doping can be seen also in experimental Mn $2p$ HAXPES spectra on $La_{1-x}Sr_xMnO_3$ for $x > 0.2$. However, for $x = 0$, instead of becoming more intense as in the calculations, the data show that it decreases: since it is known that in manganites the interplay between electronic and magnetic degrees of freedom is crucial in determining the macroscopic properties of these compounds (for more details refer to Sec. 1.4.2), the magnetic structure of $La_{1-x}Sr_xMnO_3$ must be accounted for in the calculations. In particular if a A-type magnetic structure - ferromagnetic planes coupled antiferromagnetically - is considered, it can be shown that the nonlocal screening between such planes is strongly suppressed. Another properties which contributes in reducing the intensity of the low

binding energy feature in the undoped system is the ordering of the $3d$ orbitals, which induces anisotropies in the electron transfer interaction. So we have seen that by combining the competition between local and nonlocal screening processes with structural and magnetic properties of manganites, a satisfactory description of the Mn $2p$ HAXPES core level spectrum can be obtained. This has been proved the case also for other systems, such as cuprates and ruthenates [33].

1.4 Investigated systems

1.4.1 $Ga_{1-x}Mn_xAs$

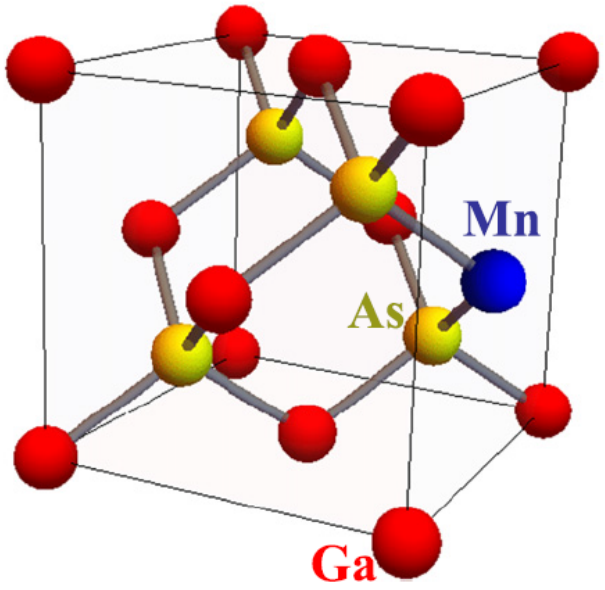


FIGURE 1.18: Zinc-blende crystal structure of GaAs with a random substitutional Mn ion in a Ga site. Adapted from [54].

$Ga_{1-x}Mn_xAs$ (manganese doped gallium arsenide) belongs to the category of III-V diluted magnetic semiconductors (DMSs), which express ferromagnetism upon Mn doping, as first demonstrated on InAs [55]. It has been widely studied for possible applications in spintronics, because displays a Curie temperature T_C which increases with increasing Mn doping and can reach values as high as 180 K for a substitutional Mn concentration $x \simeq 0.07$ (which is achieved for a nominal concentration $x = 0.12$) [54]. Mn acts as an acceptor when it is substituted to Ga, providing holes as charge carriers and has an un-filled d-electron band with a net magnetic moment. Ferromagnetism results from the exchange interaction between the Mn $3d$ magnetic moments mediated by the holes, suggesting a deep relationship between the magnetic and electrical properties of the material [56]. The growth of $Ga_{1-x}Mn_xAs$ films, which is usually done on a GaAs substrate, is a delicate process if the ferromagnetic properties are to be retained. In fact it is known that the minimum Mn density for ferromagnetism is more than an order of magnitude

higher than the equilibrium solubility limit. Growth techniques such as molecular beam epitaxy (MBE) can be used, keeping the substrate temperature below 580 K, as compared with the usual 820 - 920 K range for growing optoelectronic GaAs/(Al,Ga)As heterostructures. Furthermore, for high Mn concentration, Mn can be incorporated not only in place of Ga in the GaAs zinc-blende lattice (see Fig. 1.18), but also between the other atoms of the lattice, in which case is called *interstitial*. These loosely bound atoms are known to diffuse even at temperatures lower than the growth temperature, segregating at the surface and forming an oxide layer. The study of the properties of $Ga_{1-x}Mn_xAs$ through electron spectroscopies can be then seriously hampered by the presence of these defects and in fact has led over the years to a number of contradictory results [57, 58]. It is now clear that the surface oxide layer can be removed by chemical etching with HCl, which also yields a stable long-range ferromagnetic order [58].

Interesting results on the true bulk electronic properties of $Ga_{1-x}Mn_xAs$ thin films and on the way they are modified at the surface have been obtained by means of core-level HAXPES, investigating in particular the Mn $2p$ photoemission spectrum, as displayed in Fig. 1.19. In the panel (a), Mn $2p$ spectra from a $Ga_{0.95}Mn_{0.05}As$ sample measured with hard (black squares) and soft X-ray (empty red circles) after HCl chemical etching are compared. The striking difference is the sharp low binding energy feature which is clearly visible in the hard X-ray spectrum and completely absent in the soft X-ray one. To interpret the spectra, cluster calculations based on an Anderson impurity model taking also into account configuration interaction in the initial and final states have been carried out. A particular Mn site in a cluster of other atoms is considered with a basis set of states $3d^n$ (n = 3, 4, 5, 6 e 7) and holes (h); an appropriate combination of symmetry of states is chosen to reproduce a As $4p$ - Mn $3d$ hybridised valence band hole. The initial state of the photoemission process (i. e., the ground state of the Mn atom), is taken as the mixture of the various d^n configuration; in a similar way, the final state is taken as the result of hybridisation between different $\underline{c}d^n\varepsilon$, where ε represent the the continuum state to which the electron is photoexcited. The parameters of the cluster are the charge-transfer energy Δ, the intra-atomic Coulomb interaction U, the core-valence Coulomb interaction Q and the hybridisation V. The results for different values of hybridisation are illustrated in the panel (b) of Fig. 1.19, along with an inset where the energy levels in the initial and final states are reported before considering hybridisation and without multiplet structure and crystal-field symmetry effects (it is like all the levels associated to the same oxidation state, but with different energies due to effects such as multiplet structure and crystal-field splitting have been averaged to yield a single level). It can be seen in the inset of Fig. 1.19 that in the initial state the lowest energy configuration is the one with five electrons in the d levels and a hole in the valence band near the Fermi level $d^5\underline{h}$, while in the final state the $\underline{c}d^6\underline{h}^2$ is pulled below the $\underline{c}d^5\underline{h}$ configuration by an energy amount equal to Q. On the basis of these calculations, the low binding energy peak can be attributed to the $\underline{c}d^6\underline{h}^2$ final state, which has en electron more in the d levels with respect to the $\underline{c}d^5\underline{h}$ state, so corresponds to a *well-screened* peak. The absence of this peak in the soft X-ray spectrum suggests the bulk nature of the screening channel which is suppressed in the surface region. In [7], as best agreement between HAXPES spectrum and calculations was indicated the case of $V \simeq 2.5$, suggesting a more delocalised nature of the electrons in the bulk with respect

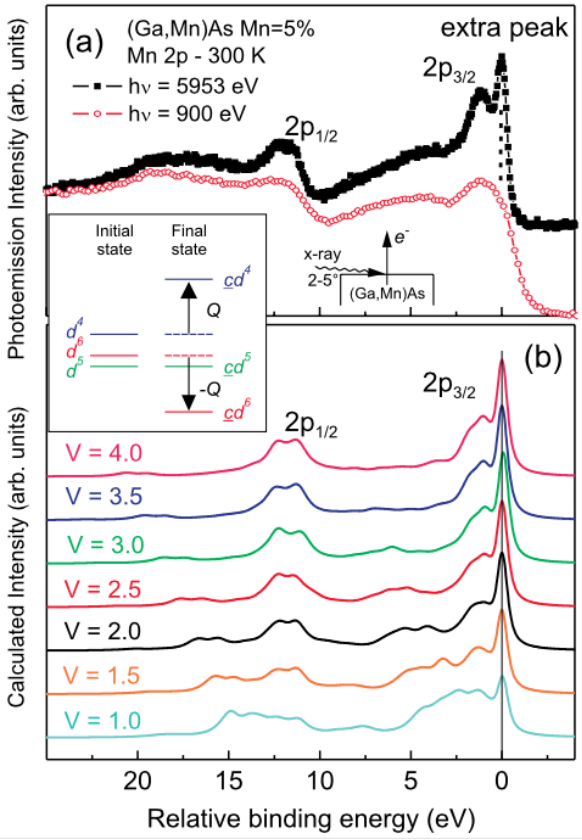


FIGURE 1.19: (a) Photoemission spectra of Mn $2p$ from a $Ga_{0.95}Mn_{0.05}As$ sample etched in HCl at a photon energy $\hbar\omega = 5953$ eV (black filled squares) and $\hbar\omega = 900$ eV (red open circles). The experimental resolution is 250 meV and 400 meV, respectively. (b) Calculated spectra as a function of the hybridisation parameter V between the different d^n configurations. In the inset the energy diagram of the d levels in the initial and final state without multiplet and crystal-field splitting and before hybridisation is showed. Q is the Coulomb interaction between the core hole and the valence levels. Adapted from [7].

to the surface. Further experimental and theoretical study confirmed two important points:

- the reversible variation of the well-screened peak intensity as a function of the temperature (i. e., crossing the magnetic transition temperature), which suggests an increase in the hybridisation when the ferromagnetic order is achieved [7];
- the mixed character of the Mn $3d$ electrons of substitutional Mn in $Ga_{1-x}Mn_xAs$, which form states which are not either purely atomiclike or itinerant [59].

1.4.2 $La_{1-x}Sr_xMnO_3$

Ferromagnetic hole doped manganese perovskite materials $L_{1-x}B_xMnO_3$ (where L is a trivalent rare-earth ion, such as La, Nd and Pr, while B is a divalent alkaline-earth ion, such as Ca, Sr, Ba and Pb) have been subject to intensive studies since the observation

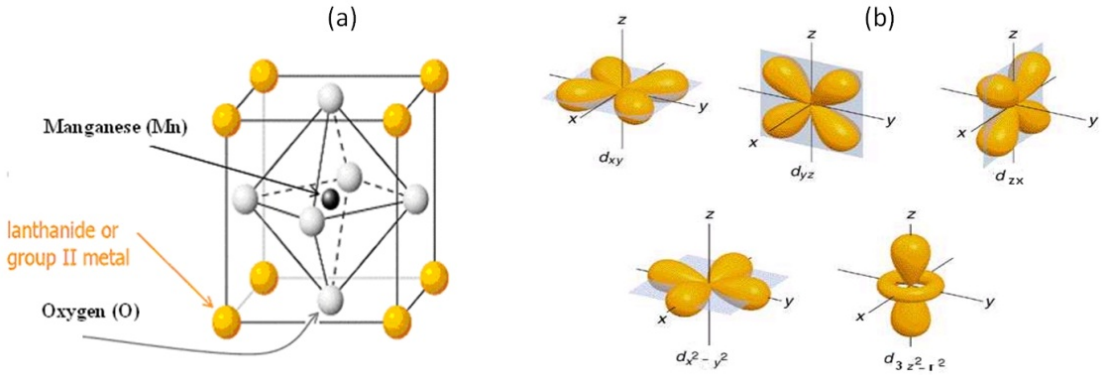


FIGURE 1.20: (a) Arrangements of ions in a perovskite-type structure of manganites and (b) shape of the five different d orbitals. Adapted from [60].

of *colossal magnetoresistance* (CMR) in $La_{1-x}Pb_xMnO_3$ films [61]. This effect consists in a decrease of the resistivity upon application of an external magnetic field, which is especially intense around the Curie temperature. Other interesting properties displayed by this class of systems is perfect spin polarisation and a metal-insulator transition above room temperature (Mn oxides are classified as charge-transfer insulators). Among these systems, possibly the most studied is $La_{1-x}Sr_xMnO_3$, which has been indicated as an optimal choice for spintronic applications, since it displays the higher Curie temperature ($T_C \simeq 330-340$ K upon optimal doping) along with a high carrier spin polarisation and a low carrier density [62]. In general, the electronic properties of $La_{1-x}Sr_xMnO_3$ are strongly related to the crystal structure, whose unit cell is shown in Fig. 1.20 (a). The lattice is approximated as a face-centered-cubic (fcc) with a Mn ion at the centre and La/Sr cations at the corners of the cube; each Mn ion is surrounded by six O ions, forming a MnO_6 octahedron. Due to the mismatch between the radii of the cations, the unit cells of the compounds becomes distorted, resulting a in-plane contraction and an out-of-plane elongation of the octahedron, which results in a rhombohedral crystal structure (as shown in the panel (a) of Fig. 1.21). How this affects the electronic structure can be better understood by looking at Fig. 1.21 where a schematic representation of the valence energy level diagram and of the density of states of $La_{1-x}Sr_xMnO_3$ is shown. The five Mn $3d$ levels for an isolated Mn ion in a ideal perovskite structure are split in a e_g doublet (derived from $d_{x^2-y^2}$ and $d_{3z^2-r^2}$ orbitals) and a t_{2g} triplet (d_{xy}, d_{xz} and d_{yz} orbitals) due to crystal-field effects; the t_{2g} have lower energy because their orbital lobes are directed between two O^{2-} ions, while the orbital lobes of the e_g levels are directed towards the O^{2-}, hence strong Coulomb repulsion (see Fig. 1.20 (b)). The degeneracy between the levels in the e_g and t_{2g} is then removed by the distortion of the MnO_6 octahedron. The parent compound $LaMnO_3$ has a $t_{2g}^3 e_g^1$ configuration of the Mn^{3+} ion and displays the ordering of the two e_g orbitals, which are arranged in a *antiferro-orbital* fashion on neighbouring sites of the (001) plane. This orbital ordering is responsible for ferromagnetic spin ordering in the (001) plane and ferromagnetic coupling along the crystallographic c-axis (*A-type* ordering). The valence state of the Mn ions in manganites is mixed between Mn^{3+} and Mn^{4+} and depends from the hole concentration; it is known that a doping concentration $x = 0.3 - 0.4$ induces a roughly equal number

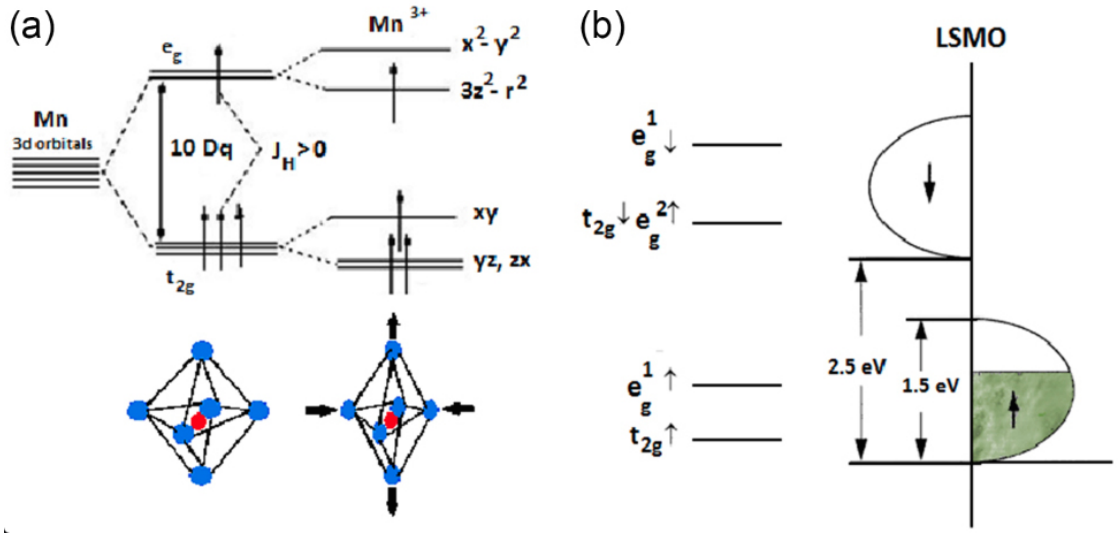


FIGURE 1.21: (a) Crystal field splitting of the Mn ion d-levels and removal of the degeneration in the e_g and t_{2g} levels due to the lattice distortion. (b) Schematic illustration of the density of states of $La_{2/3}Sr_{1/3}MnO_3$. The Hund's energy $J_H \simeq 2.5$ eV and the crystal field splitting $10Dq \simeq 1.5$ eV are also indicated. Adapted from [62].

of Mn^{3+} and Mn^{4+}. For the latter, the low energy t_{2g} states are occupied by three electrons with parallel spin, while in the case of Mn^{3+} the additional electron occupies a higher energy e_g state with the same spin as in the e_g levels. For $x < 0.5$ these states result to be separated from the empty minority band by a quantity which is called the Hund energy, $J_H \simeq 2.5$ eV. Of course also the O $2p$ levels contribute to the electronic structure: in $La_{1-x}Sr_xMnO_3$ they are completely occupied for both spin orientations, so that around the Fermi level the density of states will be the result of the hybridisation between the Mn-e_g and O-p majority spin states. Since the O $2p$ band is separated by the minority spin states from a band gap only majority carriers are present at the Fermi level, i. e. a 100% spin polarisation is achieved as shown in the (b) panel of Fig 1.21. The physical properties of $La_{1-x}Sr_xMnO_3$ are then related to a delicate interplay between charge, spin and lattice: changes in parameters such as doping, oxygen stoichiometry and (for thin films) substrate induced strain give rise to complicate phase diagrams. For example about the hole doping, when $x < 0.1$ $La_{1-x}Sr_xMnO_3$ is an antiferromagnetic insulator, but on increasing the Sr concentration the material displays first a ferromagnetic insulating phase ($x < 0.2$) and then a ferromagnetic metallic phase ($0.2 < x < 0.4$). Also for values of x around 0.3 a metal-insulator transition is observed at temperature T_{MI} which can coincide with the magnetic ordering temperature T_C. The magnetic and transport properties are usually explained in terms of the double-exchange mechanism [63] between localised $3d$ moments with strong intra-atomic exchange. e_g electrons can *hop* between adjacent Mn^{3+} and Mn^{4+} ions along the Mn-O-Mn chains, with the hopping probability being higher when the spins on neighbouring Mn ions are aligned parallel. This means that charge carriers can move easily in the presence of ferromagnetic order, while they get localised when the spins are randomly oriented and the material is paramagnetic.

In the case of thin films, since we have seen that the distortion of the unit cell plays a central role in determining the properties of the material, variations in strain due to lattice mismatch with different substrates can induce changes in the macroscopic properties. The lattice mismatch along the film/substrate interface is described as $\delta = (a_{sub} - a_{bulk})/a_{sub}$, where a_{sub} are the cell parameter, along the interface, of the substrate and of the films, respectively:

- $\delta > 0$ means that the unit cell of the film is elongated in the plane of the film and compressed along the growth direction, a situation which is called *tensile strain*;
- $\delta < 0$ corresponds to the situation in which the unit cell is compressed in the plane of the film and elongated along the growth direction, *compressive strain*;
- the case $\delta = 0$ is called *strain relaxed*.

These three cases are pictorially represented in Fig. 1.22, where the blue rectangle (cube) is the unit cell of the substrate and the yellow rectangle (cube) is the unit cell of the film. For $La_{1-x}Sr_xMnO_3$ the growth is very "simple": whatever the substrate the

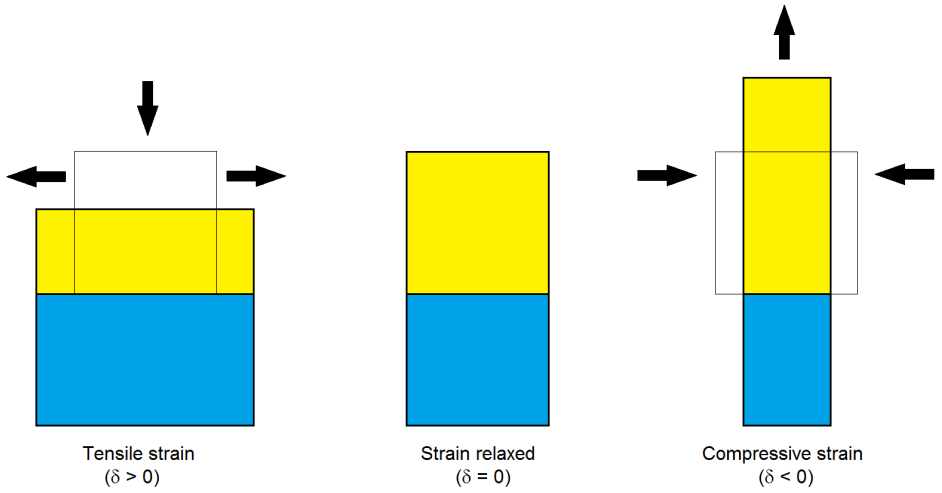


FIGURE 1.22: Pictorial representation of tensile strain ($\delta > 0$), strain relaxation ($\delta = 0$) and compressive strain ($\delta < 0$) in epitaxial growth. The blue rectangle (cube) is the unit cell of a substrate, the yellow rectangle (cube) is the unit cell of the film and the transparent cube is the unit cell in absence of strain. The black arrows indicate the direction in which the film unit cell expands or contracts to adapt to the substrate. Adapted from [64].

films are always oriented in the [001] crystallographic direction and grow epitaxially in a perfect "cube-on-cube" fashion, with the strain which does not relax for films which are thinner than 100 nm [64].

As in the case of the diluted magnetic semiconductor $Ga_{1-x}Mn_xAs$, HAXPES measurements on thin films of $La_{1-x}Sr_xMnO_3$ have highlighted the presence of low binding energy features in the core-level spectra of Mn $2p$ below the metal-insulator transition temperature which are not observed in the soft X-ray regime [6]. In Fig. 1.23 four Mn

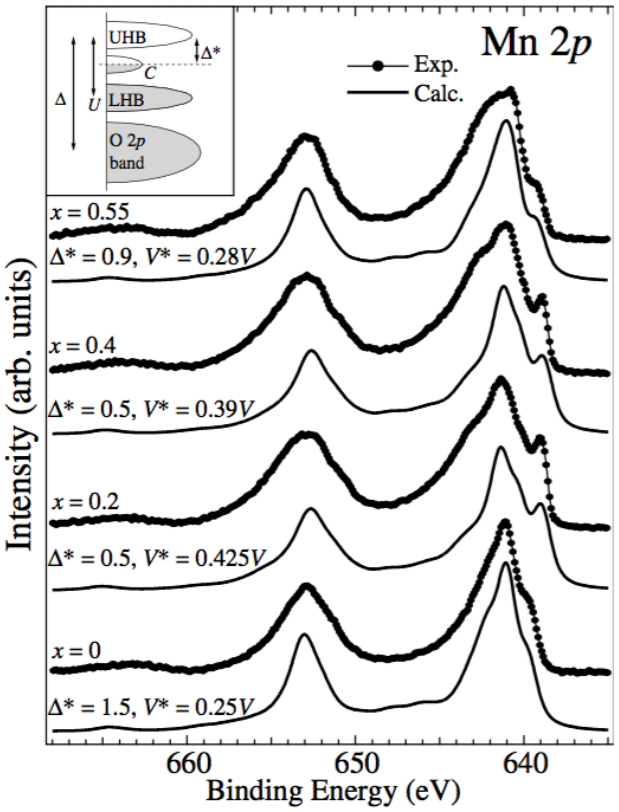


FIGURE 1.23: Doping dependence of the Mn $2p$ spectrum from $La_{1-x}Sr_xMnO_3$ measured at 40 K compared to MnO_6 cluster calculation results which include a coherent state at the Fermi level (as shown in the inset). Adapted from [6].

$2p$ spectra measured on $La_{1-x}Sr_xMnO_3/SrTiO_3$ thin films with different hole doping x at 40 K are shown, compared with calculations based on a MnO_6 cluster model which includes doping induced coherent states at the Fermi level (C in the inset of Fig. 1.23) along with the Mn $3d$ and O $2p$ states [6], in analogy to dynamical field theory. In the picture the low binding energy peak is very sharp in the case of $x = 0.2$ and $x = 0.4$, which are known to be metallic at 40 K (actually $x = 0.2$ has a metal-insulator transition just below room temperature, while $x = 0.4$ is metallic all the way to room temperature, but metallicity increases at low temperatures). The $x = 0$ sample is expected to be insulating, but hole doping can occur due to excess oxygen which can be introduced during the growth process, while $x = 0.55$ is an antiferromagnet and a conductor. Since in these two last samples the peak is less pronounced, it was assumed that this feature is related to the doping induced density of states at the Fermi level responsible for the magnetic and electrical properties of the material. In the calculations showed in Fig. 1.23 four configurations were used for the initial state, $3d^4$, $3d^5\underline{L}$, $3d^3C$ and $3d^5\underline{C}$, where $\underline{L}$ represent a hole in the O $2p$ ligand levels. Only two parameters were varied in the fit procedure, namely Δ^* and V^*, which represent the charge-transfer energy between the Mn $3d$ and the C levels and the hybridisation between the Mn $3d$ and C levels, respectively. The low binding energy features is associated by the calculations to the $2p^53d^5\underline{C}$ final state and is observed to increase as the hybridisation is turned on. These results suggest that the hybridisation with the coherent states (i.e., the degree of delocalisation

of d electrons) is higher for ferromagnetic compositions ($x = 0.2$ and $x = 0.4$) than for antiferromagnetic ($x = 0$ and $x = 0.55$).

A different explanation which does not require the presence of a coherent state at the Fermi level has been given following multi-cluster calculations by van Veenendaal [33], as described in Sec. 1.3.3. The changes in the intensity of the low binding energy feature can be ascribed to changes in the relative efficiency between local and nonlocal screening channels; to explain the decrease of the low binding energy feature in the case of $x = 0$, the presence of ferromagnetic planes coupled antiferromagnetically must be taken into account, because it reduces the hopping probability.

1.4.3 RuO_2

RuO_2 (ruthenium dioxide) is the only $4d$ system which has been studied in the framework of this thesis work. It has been identified as a promising candidate for several applications, ranging from electrical contact material, electrode contact in integrated circuits, electrocatalyst in chlor-alkali industry, optical thin film, ceramic resistor and catalyst for photodecomposition of water [65]. RuO_2 has a rutile crystal structure and its unit

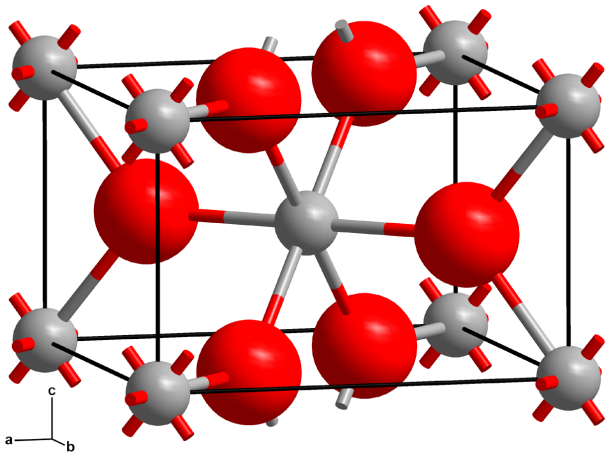


FIGURE 1.24: Rutile unit cell for RuO_2: the Ru atoms are in grey and the O atoms are in red. The three main crystallographic directions (a, b, c) are indicated. Adapted from [66].

cell is shown in Fig. 1.24 as a stick-and-ball model: the unit cell contains two formula units, with the Ru atoms (grey spheres) forming a body-centered tetragonal (bct) lattice and surrounded by a slightly distorted octahedron of O atoms (red spheres). Differently from all the other systems we have shown so far, it is a good metal at room temperature, due to the partially filled band which originates from the Ru $4d$ levels [67]. Because of the delocalised nature of the Ru $4d$ electrons, it was expected that correlation effects in $4d$ transition metal compounds are not so pronounced as in $3d$ systems. However, it has been pointed out that some class of systems such as ruthenium oxides with pyrochlore structure ($Y_{2-x}Bi_xRu_2O_7$) [68] and other ruthenates such as $Ca_{2-x}Sr_xRuO_4$ [69], exhibit macroscopic properties which arise as a consequence of the correlation between the

Ru 4*d* electrons. The correlated nature of such electrons is showed in some degree by the features of the Ru 3*d* photoemission spectra which have been observed in various ruthenates including RuO_2, as those which have been shown in Fig. 1.10 and discussed in paragraph 1.2.4. For the most insulating of the systems presented in that figure, namely $Y_2Ru_2O_7$, the Ru 3*d* spectrum is dominated by two broad peaks, which make up the spin-orbit doublet: for more metallic ruthenates a low binding energy feature appears for each of the spin-orbit components, which becomes more intense when passing to more conductive materials. In the case of the most metallic system of the series, namely RuO_2, it has become the dominant feature of the spectrum. It must be noted that the low binding energy feature has been first observed with conventional x-ray source such as an anode Al Kα lamp [70], so not strictly in the hard X-ray regime. A charge-transfer mechanism from the ligand to the metallic atom, such as in the case of 3*d* transition metal oxides such as $SrTiO_3$ [71], is not sufficient to explain these structures, because the ~ 2 eV separation between main and satellite peak is lower than expected from the chemical trend [29]. Similarly to the case of manganites, two explanations have been offered in order to justify the presence of these structures:

- screening of the core hole by quasiparticles at the Fermi surface [34];
- screening of the core hole by charge moving in from other metallic sites (nonlocal screening) [33].

The spectra calculated using the two different approaches are reported in Fig. 1.25. In

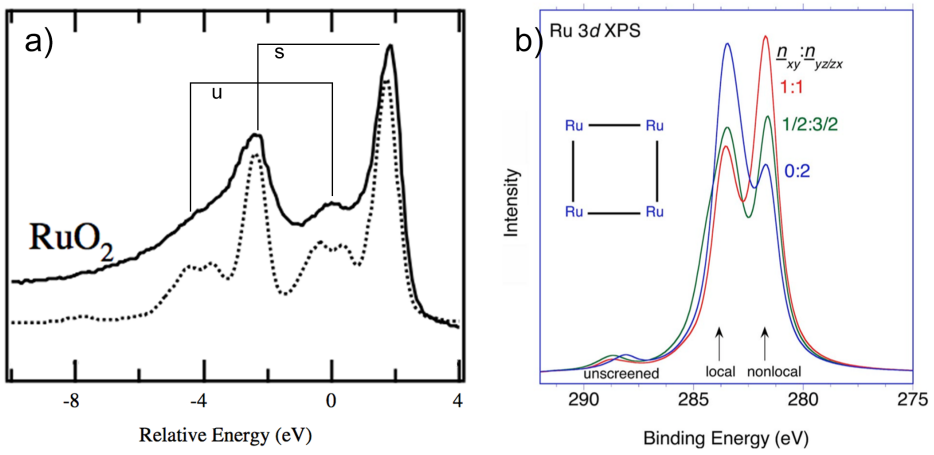


FIGURE 1.25: (a) Comparison of experimental (solid lines) and theoretical (dotted lines) Ru 3*d* spectrum of RuO_2, where calculations are performed considering screening from quasiparticle levels at E_F. Screened and unscreened peaks are indicated by the letters "s" and "u", respectively. Adapted from [34]. (b) Calculated Ru 3*d* spectra for a Ru_4 cluster (shown in the inset) for three different orbital occupations, considering both local and nonlocal screening mechanism. These spectra are obtained without considering spin-orbit coupling (see text). Adapted from [33].

the panel (a) of Fig. 1.25, the fitting of the Ru 3*d* spectrum of RuO_2 is shown (after subtraction of the peak associated with C 1*s* and of a inelastic background), within the model involving screening of the core hole by quasiparticles at E_F mediated by O

$2p$ orbitals, which we have seen in some details in section 1.2.4. For each spin-orbit component, in the theoretical spectra (dotted lines) three peaks can be seen, which are associated to three different final state configurations. As in Fig. 1.10 (also adapted from [34]), the main features of the experimental spectra have been indicated by the letters "u" as unscreened and "s" as screened. In particular, the low binding energy feature is the one related to the final state where the core hole is screened by charge moving in from the quasiparticle states at the Fermi level. It is interesting to note that, although RuO_2 had always been classified as a band metal, the results of the fitting as in Fig. 1.25(b) suggest that it should be reconsidered as a strongly correlated $4d$ metal, with the ratio between bandwidth and Coulomb interaction between electrons $W/U = 2.0$ [34]. The other proposed model, is the one we discussed in section 1.3.3, whose results for ruthenats are presented in Fig. 1.25(b). A Ru_4 cluster is here employed (see inset of Fig. 1.25(b)), along with a reduces basis set of t_{2g} orbitals in order to effectively represent a RuO_6 cluster in each of the four sites and four t_{2g} electrons are considered in each of the four sites. Three different curves are presented, each with a different ratio of number of holes per site between the xy orbital (which is directed in the plane of the Ru_4 cluster) and the yz and zx orbitals. $\underline{n}_{xy} : \underline{n}_{yz/zx} = 1 : 1$ means that there is one hole per site in a xy orbital for each hole per site in a yz and zx orbitals. Each spectrum presents three peaks: the one at the lowest binding energy is associated to a nonlocal screening process, involving an electron moving to the site where the core hole from a neighbouring site, in order to screen the potential induced by the core hole. The intensity of this process is higher in the case of xy orbitals, which have a higher strong coupling between RuO_6 units in the plane. By decreasing the $\underline{n}_{xy} : \underline{n}_{yz/zx}$ ratio, what happens is that there are less holes in the xy orbitals which can be filled by electrons moving in from neighbouring sites, leading to a gradual suppression of the nonlocal screening channel. Going towards higher binding energies, the other two peaks are related to local screening from the ligand around the metal site where the core hole has been formed and to a final state where the core hole is not screened. Although the author does not discuss this issue in its article, in our interpretation of these theoretical data these three peaks are all related to the Ru $3d_{5/2}$ spin-orbit component. The nonlocal screened Ru $3d_{3/2}$, should be found around 285 eV, which means very close to the local screened 5/2 peak. We assume that in order to avoid complications in the interpretation of the lineshapes, the author deliberately neglected the spin-orbit splitting of this core level in his calculations. From a qualitative point of view, the experimental spectrum of RuO_2 as reported in Fig. 1.25(a) seems more similar to the $\underline{n}_{xy} : \underline{n}_{yz/zx} = 1 : 1$ case of Fig. 1.25(b), with a strong nonlocal peak. It must be noticed that the peak which is associated to a locally screened final state in Fig. 1.25(b), seems to correspond in position to the peak which is indicated as unscreened in Fig. 1.25(a).

1.4.4 TiO_2

We have seen how one of the advantages of performing photoelectron spectroscopy with high photon energy is the enhancement of the probing depth. This has led to the identification of so-called bulk-only features in the spectra of core levels from a number of compounds based on transition metal elements. However, HAXPES makes also possible

to access a class of deep core-levels such as the 1s of transition metal elements, whose spectra can display chemical shifts, multiplets, satellites and other fine structures which can give additional information to those which can be obtained by means of valence and/or shallow core level photoemission.

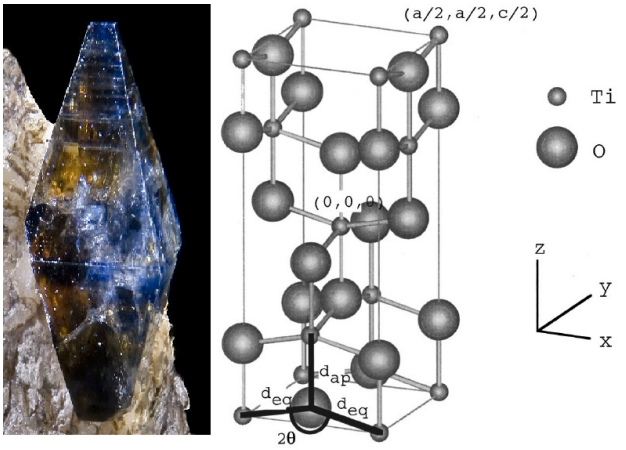


FIGURE 1.26: Anatase TiO_2 crystal and body-centered-tetragonal (BCT) lattice structure. d_{ap} and d_{eq} represent the apical and equatorial length of the bond between O and Ti atoms. The coordinate system (x, y, z) and the position of the Ti atom at the centre of the cuboid $(0, 0, 0)$ and at the vertex $(a/2, a/2, c/2)$ are also shown. Adapted from [72, 73].

Among the materials which display photocatalytic properties, titanium oxide, TiO_2, has been long considered one of the most promising due to its high efficiency, chemical stability, nontoxicity and low cost of production [74]. Photocatalysis is a reaction in which photons in the visible/ultraviolet range are used to activate a substance (the catalyst) which modifies the rate of a chemical reaction without being involved in it. It occurs when an electron-hole pair is generated upon absorption of a photon: since electrons are reductants and holes are oxidants, redox reactions can be started at the surface of the catalyst. TiO_2 exists in nature as a mineral mainly in three different forms (*polymorphs*), each displaying a different crystal structure, namely rutile, anatase and brookite. At the moment, to the extent of our knowledge, only rutile and anatase have been exploited in application based on TiO_2. Rutile is the most abundant form of TiO_2 and has been extensively studied over the course of the years. It has been found out however that concerning photocatalysis, anatase displays superior properties with respect to rutile [75]. A crystal of anatase, along with its primitive cell are showed in Fig. 1.26. The crystal lattice is body-centered tetragonal (BCT), with each Ti^{4+} cation in octahedral coordination with six O^{2-} anions and each O^{2-} anion is in planar coordination with three Ti^{4+} cation, two equatorials (the relative bond is identified as d_{eq} in Fig. 1.26) and one apical (d_{ap} in Fig. 1.26). The lattice constants a and c which characterise the lattice (a is the side of the square and c is the height of the cuboid) are 3.78 Å and 9.52 Å, respectively [76]. When stoichiometric, anatase is insulating (Mott-Hubbard insulator), with a band gap of 3.2 eV [77]; however this situation changes in the presence of a significant concentration of oxygen vacancies ($TiO_{2-\delta}$). Calculations have showed that the oxygen vacancies act like donors in a n-type semiconductor, which results in

the formation of Ti^{3+} states in the band-gap, which can overlap with the states at the conduction band minimum, reducing the value of the gap [78]. Furthermore, the presence of oxygen vacancies seems to have an impact on the nanostructure of anatase TiO_2 thin films, as it has been observed by high-resolution transmission electron microscope (HRTEM) in the case of TiO_2 thin films grown on $LaAlO_3$ [79]. The presence of crystallographic shear planes of oxygen vacancies with preferred orientations (101) and (103) has been reported, where (101) orientation is predominant close to the interface with the substrate, while (103) is more present in the body of the film. This is similar to what observed in the well studied Ti_nO_{2n-1} Magnéli phases of rutile, where crystallographic shear planes are related to a resistive switching phenomenon [80].

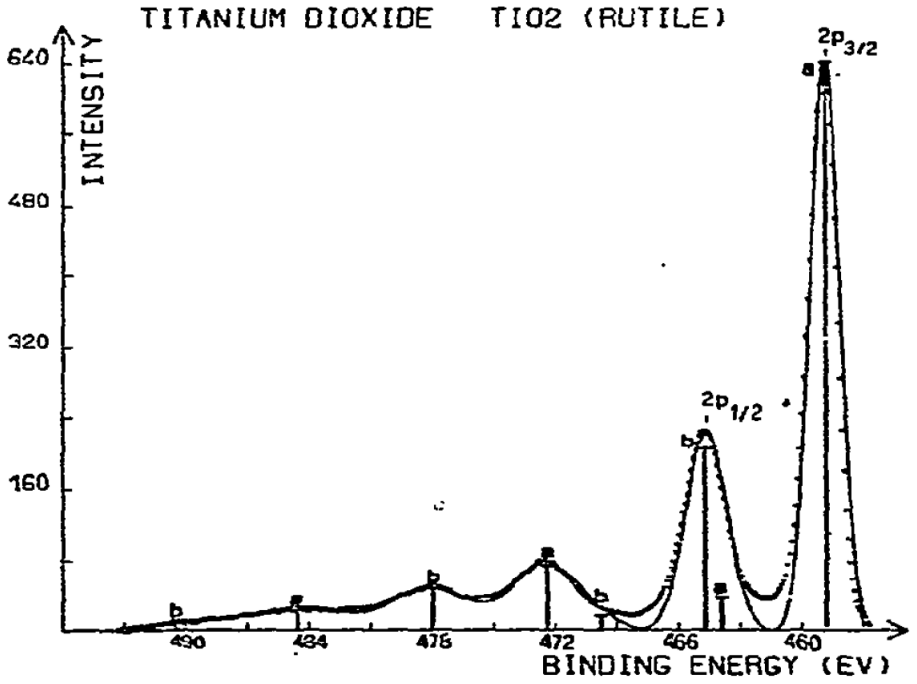


FIGURE 1.27: Photoemission spectrum of the Ti $2p$ core level from rutile TiO_2 and results of fitting with six Gaussians. The main peak and the associated satellites are indicated by the letters a for the $2p_{3/2}$ and b for the $2p_{1/2}$. Adapted from [81].

The lineshape of Ti $2p$ in TiO_2 rutile has been extensively studied since the 1970's. In an experiment performed on finely ground powders pressed on a gold substrate, eight satellites have been identified, four for each spin-orbit component, six of which are shown in Fig. 1.27 (the satellites of the $2p_{3/2}$ are indicated by the letter a in Fig. 1.27 and those of the $2p_{1/2}$ by the letter b) [81]. The first satellite is found at about 5 eV from the main peak (so for the $2p_{3/2}$ it falls under the $2p_{1/2}$ peak) and it was associated to monopole charge-transfer excitations $1t_{2g} \Rightarrow 2t_{2g}$, while the second at about 13 eV is related to $2e_g \Rightarrow 3e_g$ transitions. The other less intense satellite features at 26 and 47 (this one not shown) eV were identified as loss peaks. While the 13 eV satellite is immediately recognisable, the 5 eV structure could only be identified by performing the second derivative of the spectrum. A very similar study was performed in 1999 on TiO_2 single crystal fractured *in situ*, where two satellite features at 3 and 13 eV were identified in the Ti $2p$ spectrum following a fitting procedures with Voigt profiles [82].

The authors claimed to be the first to observe the feature at 3 eV, although we have seen that a very similar feature (at 5 eV) had been already identified in [81], a paper which incidentally, the authors have cited. The discrepancy between the energy position of the satellite may be attributed to the different fitting procedure or to the fact that they are two different features.

By using higher excitation energies such as the Cu Kα_1 line ($\hbar\omega$ = 8048 eV), it is possible to measure the Ti 1s photoline. Since in this case the spin-orbit coupling is absent, it should be easier to identify satellite structures, in particular the one around 5 or 3 eV from the main peak identified in [81] and [82], respectively. From measurements performed on TiO_2 powders, a satellite at 13.5 eV with respect to the main peak, same as observed in the case of Ti 2p was found and also a plasmon-like peak at 26 eV from the main line [83]. However, due to the intrinsic width of the Cu Kα_1 line ($\sim$ 2.3 eV), it was not possible resolve any structure close to the main line. It was only recently that Woicick *et al.* were able to identify a 5 eV satellite (along with the well known 13 eV satellite) in higher resolution measurements of the Ti 1s core level spectrum from a cubic system, namely a $SrTiO_3$ single crystal [71]. The results are shown in Fig. 1.28, where the Ti 1s and Ti 2p core level spectrum, recorded respectively with photon energy $\hbar\omega$ = 5597 eV and $\hbar\omega$ = 4967 eV, are reported. The authors were able to give direct

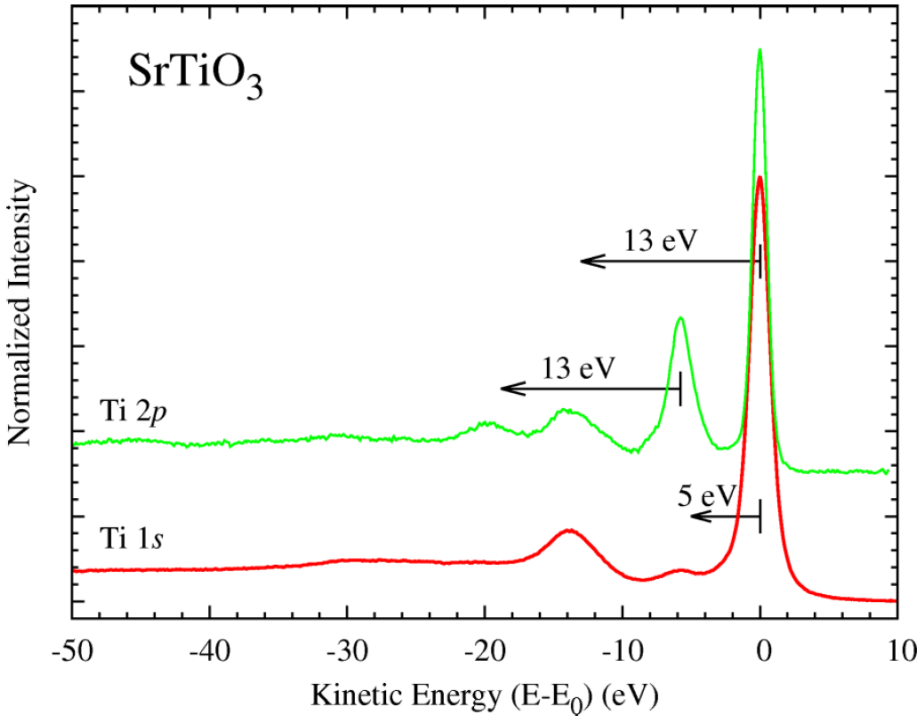


FIGURE 1.28: Ti 1s and Ti 2p core level photoemission spectra in the hard X-ray regime. The 5 and 13 eV satellite structures are indicated by arrows. Adapted from [71].

experimental evidence through the combination of resonant photoelectron and Auger

spectroscopy in the hard X-ray regime, that the two satellites originate from the crystal-field splitting of the Ti $3d$ states in t_2g and e_g levels. In particular, they are associated to charge-transfer monopole excitations:

- 5 eV satellite $\Rightarrow$ ligand $2p$ $t_{2g} \rightarrow$ metal $3d$ t_{2g};
- 13 eV satellite $\Rightarrow$ ligand $2p$ $e_g \rightarrow$ metal $3d$ e_g.

The overlap of the metal $3d$ e_g and ligand $2p$ e_g orbitals is greater than that between the metal $3d$ t_{2g} and ligand $2p$ t_{2g} overlap: this is due to the fact that the e_g orbitals are directed along the Ti-O axis, while the t_{2g} orbitals are perpendicular to it. This difference is the reason why the 13 eV satellite (e_g transitions) is more intense than the 5 eV peak (t_{2g} transitions).

It would be interesting to verify whether similar features can be identified in the case of anatase TiO_2 and whether they are affected by the changing of the conduction properties induced by a different level of oxygen vacancy concentration.

Chapter 2

Experimental methods

In this thesis work we have studied the role of correlation between d electrons in transition metal compounds by means of HAXPES, which can help highlight differences between bulk and surface properties. As we have seen in the previous chapter, high resolution HAXPES with reasonable count rate can only be performed at dedicated beamlines of third generation synchrotron radiation facilities. We consider then important to give some description of synchrotron radiation and how high intensity beam can be produced for spectroscopy: this will be done in section 2.1. In section 2.2 will focus on the facilities where the experiments related to this thesis work have been carried out, namely the GALAXIES beamline of the SOLEIL synchrotron and the I09 beamline of the Diamond light source.

2.1 Synchrotron radiation

In the previous chapter, it has been pointed out the importance of third generation synchrotron radiation sources in performing HAXPES experiments. The photon fluxes which can be achieved at these types of machines, have helped to balance out the effect of diminishing photoionisation cross-section in the hard X-ray regime, yielding adequate counting rates [35]. We will now briefly discuss the properties of third generation synchrotron radiation sources and of the light they produce, following the considerations reported in [84].

When a charged particle, such as en electron, is submitted to acceleration by a magnetic field, loses energy emitting electromagnetic radiation, the so-called *synchrotron radiation*.[1] The power radiated by a particle with energy E (and speed v) in this field is significantly higher for particles with higher energies and scales as $B^2\gamma^2$, where B is the value of the magnetic field and

$$\gamma = \frac{1}{\sqrt{1-\beta^2}} = \frac{1}{\sqrt{1-v^2/c^2}} \tag{2.1}$$

[1] If the accelerating field is electric, then the emitted radiation is called *bremsstrahlung*.

is the Einstein relativistic factor (β is the electron velocity in units of light velocity, c). Initially seen as an un-desired by-product of high-energy experiments, nowadays it is exploited in a number of facilities around the world, in fields including material science, physics, chemistry and biology [84].

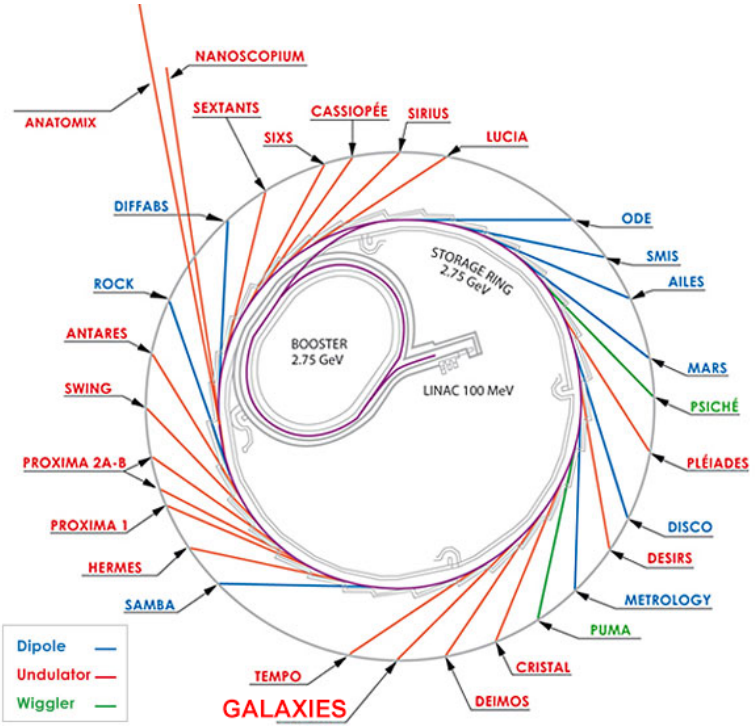


FIGURE 2.1: Schematic map of the third generation synchrotron radiation facility SOLEIL, showing the linac, the booster, the storage ring and the beamlines; for each beamline is indicated whether the light is produced by a bending magnet or an insertion device (wiggler or undulator). Adapted from [85].

In third generation synchrotron radiation sources, such as that schematically shown in Fig. 2.1 electrons are generated by a linear accelerator (linac) and injected in a circular accelerator, called *booster*, which in principle constitutes the "real" synchrotron. Here the electrons are accelerated through radio-frequency (RF) cavities to a given energy and then are sent into a *storage ring*, which is a structure made to circulate electrons for as many turns as possible keeping the energy (and the current) stable. The synchrotron light is produced when electrons pass through conventional *bending magnets*, which curve the electron trajectories and also in so-called *insertion devices*, which are installed in the straight sections of the storage rings. The energy lost by the electrons when they emit radiation is recovered making the particles pass into RF cavities. Insertion devices, such as the one schematically reported in Fig. 2.2, are periodic magnetic structures several meters long in which a sinusoidal magnetic field perpendicular to the electron direction with spatial period λ_0 and peak magnitude $\hat{B}$, forces electrons to move in a sine-like fashion around their initial velocity (as shown in Fig. 2.2) and then emit synchrotron radiation. An exact derivation of the wavelength λ of the radiation emitted in a similar magnetic array is outside the scope of this thesis work; it requires the application of spatial and electromagnetic field transformation from the observer frame reference to

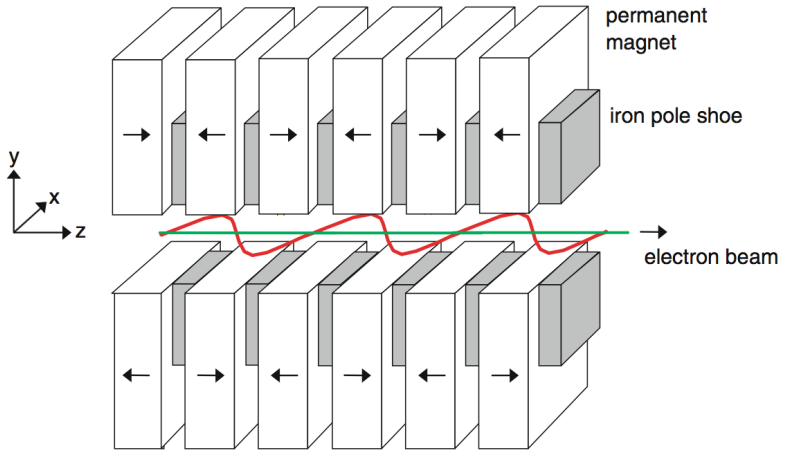


FIGURE 2.2: Schematic representation of an electron trajectory between the magnetic poles of an insertion device. The polarity of the permanent magnets is indicated by the arrows. Adapted from [86].

the electron frame reference in the framework of the Einstein special relativity theory [84, 86, and references therein]. Here we will limit ourselves to discuss only the final result

$$\lambda = \frac{\lambda_0}{2n\gamma^2}\left(1 + \frac{e^2\hat{B}^2\lambda_0^2}{8\pi^2 m^2 c^2} + \gamma^2\theta^2\right), \tag{2.2}$$

where n is the integer which represent the higher harmonics of the electron oscillating frequency induced by the field, θ is the angle between the photon emission direction and the electron propagation direction, e is the fundamental electric charge and m is the electron mass (this result is valid for small θ values). The θ angle can be defined as

$$\theta = \frac{1}{\beta\gamma}, \tag{2.3}$$

which for ultra-relativistic particles ($\beta \simeq 1$, $\gamma \gg 1$), results to be very small: for example in the case of electrons with 2.75 GeV kinetic energy, the resulting angle is $\theta \simeq 0.01°$. The fractional bandwidth of the harmonics emitted in the direction parallel to the insertion device axis ($\theta = 0$) is given by

$$\frac{\Delta\lambda}{\lambda} = \frac{1}{nN}, \tag{2.4}$$

where N is the number of periods of the magnet.

The second term of Eq. 2.2 is usually written in terms of a dimensionless parameter K, called the *undulator parameter* and it is defined as

$$K = \frac{e\hat{B}\lambda_0}{2\pi mc}. \tag{2.5}$$

If a weak field is applied ($K \ll 1$), the insertion device is usually called *undulator* and it can be shown that the emitted radiation spectrum is composed practically only by the

fundamental harmonic, whose wavelength (along the undulator axis) is given by

$$\lambda = \frac{\lambda_0}{2\gamma^2}. \tag{2.6}$$

The value of the fundamental harmonic can be selected by changing mechanically the distance between the magnetic poles of the undulator, the so-called *gap*, because by changing the gap the value of the magnetic field is varied. For a *U20* undulator, such as those used at the HAXPES beamline GALAXIES of the French synchrotron SOLEIL [87], the period of the magnetic array is $\lambda_0 = 20$ mm; with an electron beam energy of 2.75 GeV [88], by applying Eq. 2.6 we obtain a value of $\lambda \simeq 3.5$ Å. This corresponds to a photon energy of around 3600 eV.

We have seen that for ultra-relativistic particles most of the radiation is emitted in a cone with a small aperture θ around the electron velocity. As a consequence, it occurs that the radiation emitted by the same electron in different points of the wiggling trajectory inside the undulator interferes constructively. This means that the radiation intensity grows as the square of the number of periods, N^2.

In order to quantify the efficiency of radiation production by an undulator, it is convenient to define a figure of merit, the so-called *brilliance*.[2] Brilliance corresponds to the number of photons emitted per second, per a photon energy bandwidth defined as the 0.1% of the photon energy, per solid angle and per unit source size [ph s^{-1} $(0.1\%BW)^{-1}$ mm^{-2} $mrad^{-2}$]. "It determines how efficiently an intense flux of photons can be refocused to a small spot size and a small divergence" [84]. In Fig. 2.3, the brilliance for

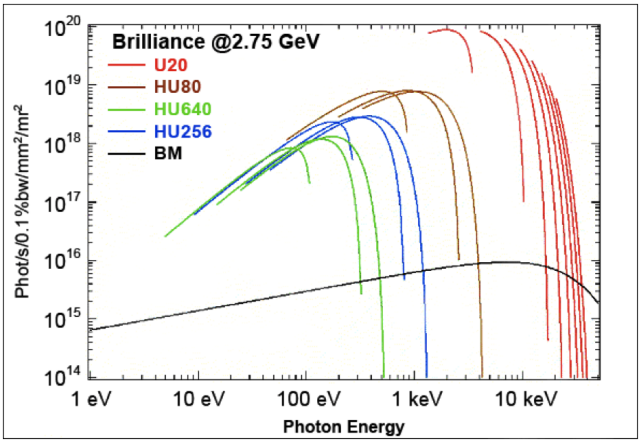


FIGURE 2.3: Calculated brilliance for different types of undulators (U20, HU80, HU640 and HU256) used at the SOLEIL synchrotron compared with the brilliance of a bending magnet (BM). Adapted from [89].

the various types of undulators used at the beamlines of the SOLEIL synchrotron is reported, compared with the brilliance for a conventional bending magnet. It can be seen that the peak brilliance for undulators is at least two orders of magnitude higher than the one for a bending magnet. It has to be noted however, that while emission

[2]Brilliance is one among the many figures of merit which characterise large scale facilities such as third generation synchrotron radiation sources.

from a bending magnet covers the whole energetic range illustrated in the graph, the undulators curves are sharper.

The radiation emitted from undulators is naturally linearly polarised when observed in the orbital plane, with the electric field lying in the plane of the wiggling electron trajectory. This is consequence of the symmetry of the electron trajectory within each period of the insertion device.

2.2 Experimental setups for HAXPES at synchrotrons

The HAXPES experiments which will be discussed in the next chapter of this thesis, have been carried out at two different beamlines, namely the GALAXIES beamline at the SOLEIL synchrotron and the ID09 beamline at the Diamond light source. While GALAXIES is strictly dedicated to spectroscopies employing photon energies > 2 keV, I09 offers a broader energy range which extends also in the soft X-ray regime, thank to the use of two separated undulators. In the following we will briefly review the characteristics of both beamlines.

2.2.1 GALAXIES beamline

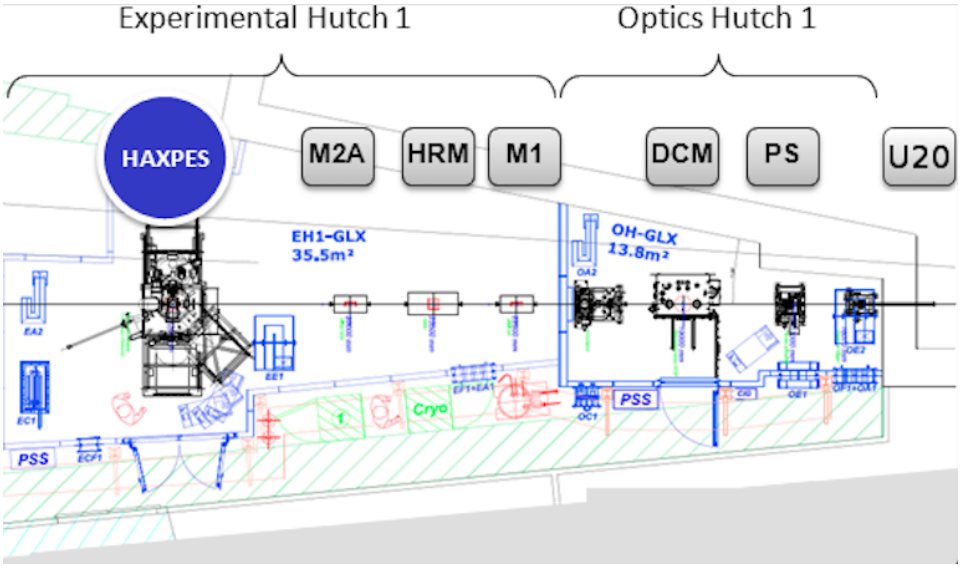


FIGURE 2.4: Layout of the GALAXIES beamline, where the light transport and monochromatisation elements are explicitly indicated (PS for the primary slits, DCM for double-crystal pre-monochromator, M1 for the collimating mirror, HRM for the high resolution monochromator and M2A for the toroidal mirror. HAXPES indicates the experimental chamber). Adapted from [90].

GALAXIES is a beamline of the French synchrotron SOLEIL which is equipped with two experimental stations, one dedicated to HAXPES, the other to resonant inelastic X-ray scattering (RIXS). The layout of the beamline is illustrated in Fig. 2.4; the RIXS hutch

which is found further downstream (i. e. on the left side of the HAXPES end station in Fig. 2.4) is not shown. The light source is an U20 undulator with 98 magnets made from $Nd_2Fe_{14}B$ with a period of 20 mm and a maximum 1.25 T magnetic field [91]. It can provide photons in an energy range spanning from 2.3 to 12 keV; this spectral interval is covered by a number of harmonics, which can be selected by properly choosing the value of the gap of the undulator. The optical section is composed by a set of primary slits (both vertical and horizontal, indicated as PS in Fig. 2.4) and a fixed-exit Si (111) double-crystal monochromator (DCM) which makes a first energy selection. This pre-monochromator is liquid nitrogen cooled, and its main function consists in reducing the heat load which the actual monochromator crystals will be subject to, as this can induce thermal distortions in the crystal structure which degrade the energy resolution. The next optical element is placed inside the experimental hutch and it is a collimating mirror (M1), which has two possible coating, depending on the photon energy range. For photon energies below 6 keV, a C coating is used, which rejects the higher order harmonics at the output of the DCM, while for energies above 6 keV a Pd coating is used. After this mirror, a four-bounce high-resolution monochromator (HRM) is placed, which houses a certain number of Si crystals, both symmetric and asymmetric, which can deliver radiation in a bandwidth which ranges from 100 to 400 meV over the whole photon energy range. The four-bounce geometry, which is schematically represented in Fig. 2.5 allows to maintain a constant beam height when scanning the photon energy. Thanks to the presence of the pre-monochromator, the heat load on the HRM crystal is reduced to a power of a few mW/mm^2, which means that no cooling is required [92]. The photons emerging from the HRM are reflected on the sample position by a

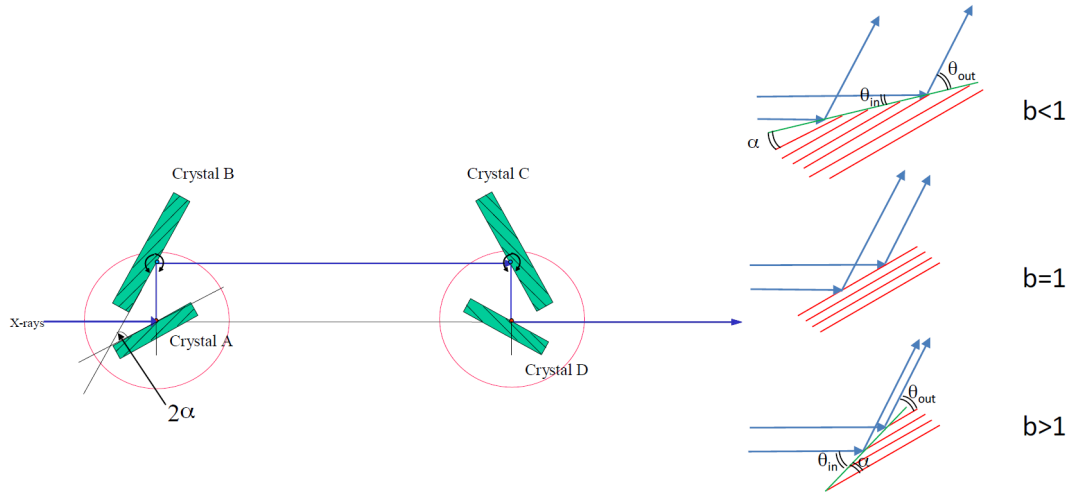


FIGURE 2.5: Geometry of a four-bounce crystal monochromator; on the right three different orientation of the crystal surface with respect to the Bragg planes are showed. $b = 1$ is the case for which the crystal surface is parallel to the Bragg planes; $b < 1$ and $b > 1$ are the case in which the bandwidth of the outgoing radiation is decreased and increased, respectively. α is the asymmetry angle, θ_{in} and θ_{out} are the incident and exit angles, respectively. Adapted from [92].

toroidal mirror (M2A), which is Pd coated and has a focal length of 3.2 m: the size of the spot at the sample position is 30 µm × 100 µm (vertical × horizontal). The

experimental chamber is constituted by a mu-metal shielded ultra-high-vacuum (UHV) vessel with a base pressure which is of the order of 10^{-8} Pa. The chamber hosts a four-axes manipulator for sample positioning and a EW4000 VG Scienta hemispherical electron energy analyser with a mean radius of 200 mm, mounted at a 90° angle with respect to the photon beam direction, as schematically illustrated in Fig. 2.7. As we have seen in the section regarding synchrotron radiation, the X-rays produced by undulators are linearly polarised with the electric field vector lying in the orbital plane. This means that the electric field is parallel to the lens axis, which allows to increase the detected photoelectron intensity. In fact it is known [93] that if the case of photoemission from free atoms with linearly polarised light, the photoionisation differential cross-section of a given subshell identified by the principal quantum number n and the orbital quantum number l can be approximated as

$$\frac{d\sigma_{nl}(\hbar\omega)}{d\Omega} = \frac{\sigma_{nl}(\hbar\omega)}{4\pi}\left[1 + \beta_{nl}(\hbar\omega)P_2(\cos\gamma)\right]. \tag{2.7}$$

In Eq. 2.7 σ_{nl} is the cross-section for the subshell nl, Ω is the solid angle, $\beta_{nl}(\hbar\omega)$ is the photon energy dependent asymmetry parameter for the subshell nl and $P_2(\cos\gamma) = (1/2)(3\cos^2\gamma - 1)$ is the second order Legendre polynomial, with γ defined as the angle between the polarisation vector and the photoelectron direction. In the case of HAXPES, for most subshells the value of $\beta_{nl}(\hbar\omega)$ is positive, which means that the associated differential cross-sections have a maximum in the direction parallel to the polarisation vector ($\gamma = 0$), as it can be seen in Fig. 2.6, which reports the polar plot of the term in the square brackets of Eq. 2.7 as a function of γ. The EW4000 analyser is equipped with a wide angle lens, which combined with a 2D detection system formed by a microchannel plate (MCP) and a charged-coupled device (CCD), in principle allows a 60° parallel detection. The same lens can be operated in a intensity optimised transmission mode, where all the information regarding the initial angular distribution of the photoelectrons is lost. In picture 2.7, also the four degrees of freedom of the manipulator are indicated:

- ts, translation along the photon beam direction;
- tx, translation along the spectrometer axis;
- tz, translation along the normal to the plane formed by the photon beam direction and the spectrometer axis;
- rz, rotation around the tz axis.

Using low rz values allows to maximise the photon flux on the sample (because of the grazing incidence) and to work in almost normal emission geometry, which maximise the information depth at a given photon energy. A configuration such as that shown in Fig. 2.7 allows to vary the information depth by changing the angle while keeping the photon energy fixed, a procedure which has been already used to analyse the competition between screening-channels in the bulk with respect to the surface in cuprates [52].

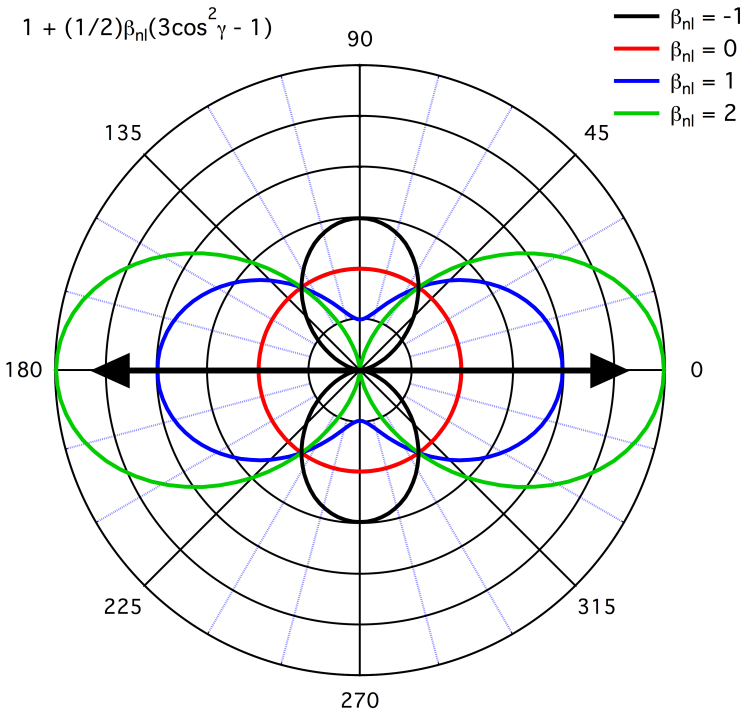


FIGURE 2.6: Polar plot of the term is square backets of Eq. 2.7, which is proportional to the angular distribution of photoelectrons from free atoms for different values of the asymmetry parameter $\beta_{nl}(\hbar\omega)$. The black line with arrow at both ends identifies the vector of the electric field of the radiation.

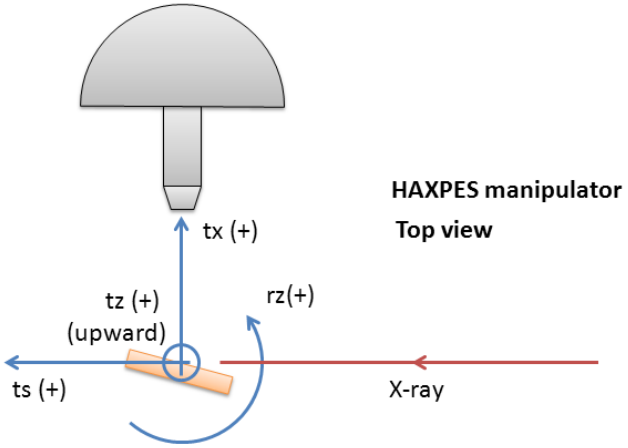


FIGURE 2.7: Experimental HAXPES geometry at the GALAXIES beamline. Adapted from [90].

2.2.2 I09 beamline

The I09 beamline operated at the Diamond Light Source Ltd. (Didcot, United Kingdom) is dedicated to the analysis of the electronic and atomic structure of surfaces and interfaces. The beamline offers the unique possibility to use both a hard and a soft X-ray beam on the same sample. Due to the wide energy range, a multitude of experimental techniques can be exploited, including X-ray photoelectron spectroscopy (both in the soft and hard X-ray regime), near edge X-ray absorption fine structure (EXAFS), X-ray standing waves (XSW) and photoelectron diffraction (PED) [94].

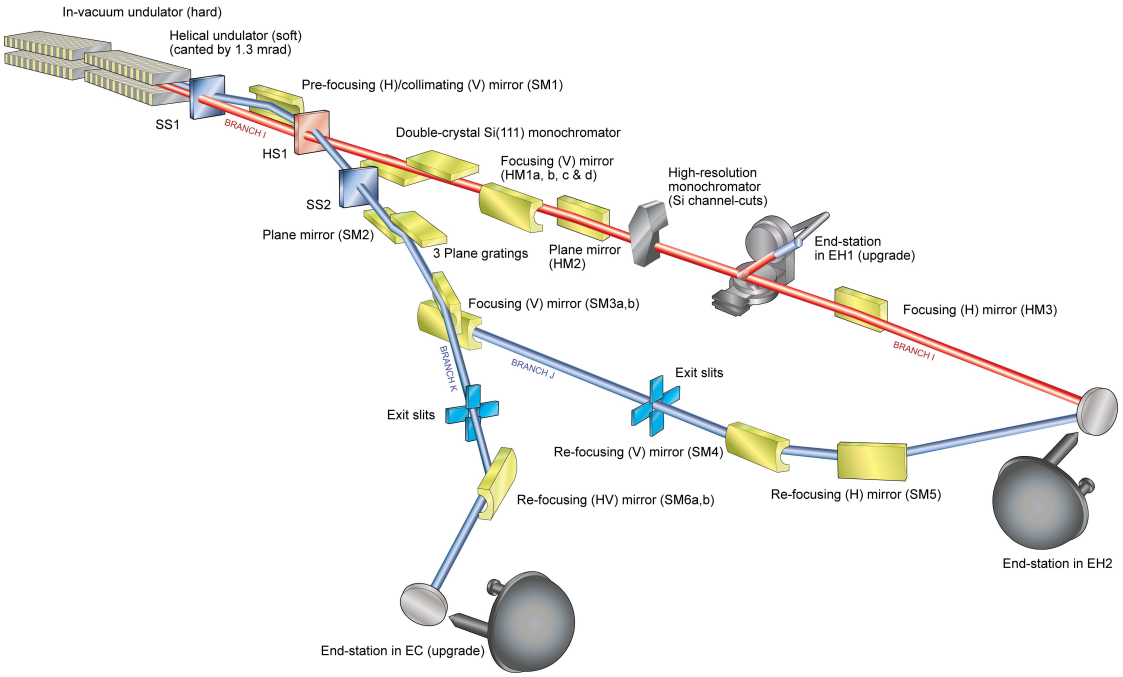


FIGURE 2.8: Schematic layout of the I09 beamline of the Diamond synchrotron. Two undulators produce photons in the soft and hard X-ray regimes, which follow different optical paths (branch I for the hard X-rays, branch J and K for the soft X-rays). Soft X-rays in the branch J are directed to the experimental station EH2 along with the hard X-rays. Adapted from [95].

The layout of the beamline is represented schematically in Fig. 2.8. It is divided in two branches, each one disposing of its own undulator, one for the hard X-rays and the other for the soft X-rays. The undulator for the soft X-rays (a 2.3 m modified APPLE II) is canted by 1.3 mrad with respect to the other (a 2 m in-vacuum U27), so that the light produced by the two insertion devices follows different optical paths. The hard X-rays travel in the so-called *branch I* to the experimental station in the second experimental hutch (EH2). They are monochromatised with a Si (111) double-crystal monochromator, which has a resolving power $E/\Delta E \simeq 10000$; this results in ~ 250 meV at $\hbar\omega = 2500$ eV, but at higher energies, as 6000 eV for example, the photon energy width is expected to be around 600 meV, which limits the overall energy resolution for an HAXPES experiment. The light can then be further monochromatised by using a channel cut Si (004) crystal, which should yield a resolution of about 250 meV. The energy range in the branch I

is 2.1 - 18 keV, with the lower limit imposed by the monochromator. The soft X-rays are deflected in a different branch by a pre-focusing/collimating mirror (SM1). At some point along this branch the light can be deflected by means of two focusing mirrors (SM3 a and b) in two different directions, namely branch J and K, which take the light to two different experimental stations: in particular, the branch J forces the soft X-rays in EH2 (almost collinearly with the hard X-rays), so that here one can dispose of the entire energetic range of the two branches. The soft X-ray energy is selected by a plane grating monochromator, using one of the different gratings with 300, 400 and 800 line/mm and the resolution can be further tuned by selecting the correct size for the exit slits (see Fig. 2.8). During our experiment, when using the light from the soft X-ray branch, we used the 300 line/mm grating in combination with a 20 µm slit size. Thanks to a series of focussing mirrors, both beams can be focussed to 15 µm × 30 µm (vertical × horizontal) spot size at the sample position in the experimental chamber of EH2. The branch J can cover the photon energy interval between 0.1 and 2 keV.

The experimental chamber is a UHV mu-metal shielded vessel with a base pressure of 10^{-8} Pa, which hosts a motorised five-axes manipulator (three translational and two rotational degrees of freedom, namely X, Y, Z, polar and azimuthal) and a VG Scienta EW4000 electron energy analyser (same as in the GALAXIES beamline). The inside of this chamber can be seen in Fig. 2.9. A $Ga_{0.87}Mn_{0.13}As$ sample, Au polycrystalline reference on the sample plate mounted on the manipulator, and the *nose* of the analyser lens are indicated. As in the case of the GALAXIES beamline, the axis of the spectrometer forms a 90° angle with the direction of the incoming photons.

2.3 Experimental aspects

In this section, some details regarding the samples studied for this thesis work and the characterisation of their core levels by means of both hard and soft X-ray photoelectron spectroscopy.

Exploiting the high photon energy available at the GALAXIES beamline (see paragraph 2.2.1), we have characterised the core levels of two different 38 nm (40 unit cells) anatase $TiO_{2-\delta}$ thin films grown on the same (001) of a $LaAlO_3$ (LAO) substrate by pulsed laser deposition (PLD) at the CNR - SPIN institute in Naples, Italy [79]. $LaAlO_3$ has been selected because of the small lattice mismatch with respect to TiO_2 (0.1%), which allows to grow thin films with a better crystallinity with respect to other substrates like $SrTiO_3$ [96]. The main difference between the two films is the O_2 partial pressure at which the substrate has been kept during deposition, as reported in Tab. 2.1, which results in different oxygen vacancy concentration, hence different electrical conductivity properties. From what we discussed in section 1.4.4, it is expected that due to the lower concentration of oxygen vacancies, S14-139 is more insulating than S14-140. In the graphs which will be shown in the following chapters, the labels which identify each sample will be the nominal oxygen pressure during the growth, i. e. S14-139 will have the label $P(O_2) = 10$ Pa.

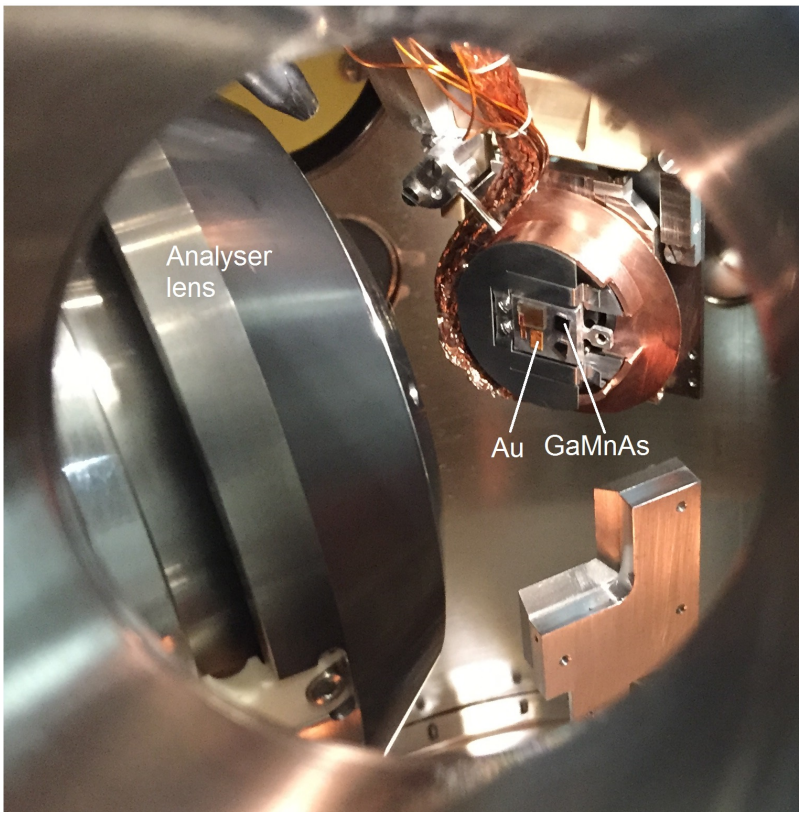


FIGURE 2.9: Inside of the I09 UHV chamber as photographed from a viewport. The sample holder mounted at the end of the manipulator is shown and the GaMnAs and Au samples are indicated by the white lines. On the left side the nose of the electron energy analyser lens can be seen. Picture courtesy of dr. A. Regoutz.

Sample	O_2 partial pressure (Pa)
S14-139	10
S14-140	10^{-3}

TABLE 2.1: Values of O_2 partial pressure during deposition of the two TiO_2 samples. A lower values of pressure implies a higher concentration of oxygen vacancies, which act as charge carriers.

Two photon energies have been selected for the measurements in order to change the inelastic mean free path of the photoelectrons, with a nominal value of 6900 eV using the symmetric Si (333) crystal of the high resolution monochromator and 2500 eV using the asymmetric Si (111) crystal. In both cases in the analyser the slits have been set to 0.3 mm and the pass-energy to 100 eV, conditions which correspond to a theoretical resolution of the analyser of 75 meV, while the lens mode has been set to *Angular 45*, which allows to work with an angular acceptance of $\pm 22.5°$ around the spectrometer axis. The angle between the photon direction and the sample surface is 5°, while the angle between the photoelectron direction and the surface is 85° (i. e. almost normal emission). The measurement have been performed at room temperature, with the samples undergoing no surface preparation, either in air or *in-situ*. The overall energy resolution at 6900 eV (analyser + beamline + thermal broadening) has been estimated by fitting the Au $4f$

lineshape from a polycrystalline gold sample mounted on the same plate which hosted the two anatase TiO_2 samples. Two Voigt profiles have been used in order to reproduce

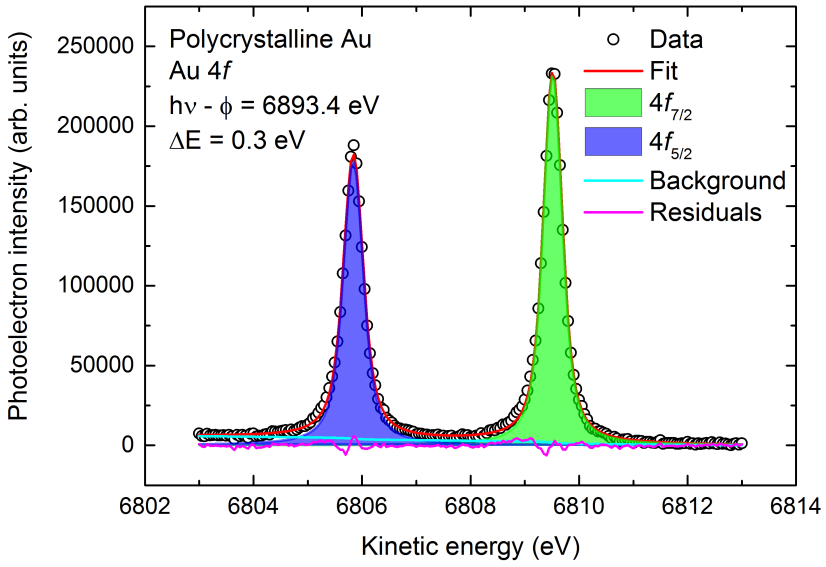


FIGURE 2.10: Fitting of the Au $4f$ photoemission line from a polycrystalline Au sample in electrical contact with the anatase TiO_2 samples. A Shirley background (pale blue line) and two Voigt profiles (green for the $4f_{7/2}$ and blue for the $4f_{5/2}$ component, respectively) have been used. The $h\nu - \phi$ (where $h\nu$ is the photon energy and ϕ is the work function of the analyser) value has been obtained by imposing that the binding energy for the $4f_{7/2}$ peak is 83. 9 eV [97].

the $4f_{5/2}$ and the $4f_{7/2}$ spin-orbit doublet components as shown in Fig. 2.10 (blue and green curve respectively), where the Gaussian FWHM, which represents the estimation of the overall energy resolution, is 0.3 eV.

In a different experiment we have exploited the unique capability of the I09 beamline to offer a broad range of photon energies, spanning both the soft and hard X-ray regime, while maintaining a comparable energy resolution, to investigate the depth dependence of the well-screened peak in the Mn $2p$ spectrum of $Ga_{1-x}Mn_xAs$ and $La_{1-x}Sr_xMnO_3$ samples, two $3d$ compounds, as well as in the case of the Ru $3d$ line in the case of rutile RuO_2, a $4d$ material.

In particular we have measured a $Ga_{1-x}Mn_xAs$ thin film grown on GaAs (001) substrate by low-temperature molecular beam epitaxy (LTMBE), with a nominal Mn acceptor concetration $x = 0.13$. Prior to measurements the sample has undergone a three minutes ultrasonic bath in isopropanol, followed by a one minute and a half rinsing in 37% diluted HCl and another rinsing in isopropanol, a procedure which is known to remove the surface oxide layer [58]. *In-situ* surface preparation such as annealing has not been performed in order to avoid effects such as the segregation of MnAs clusters at the surface [7]. For the photoemission measurements, four photon energies have been selected, two in the hard X-ray regime and two in the soft X-ray, namely 5940 and 2500 eV, and

1000 and 800 eV, respectively. All the measurements which we will be presenting in the following chapters have been performed at room temperature. For the spectra which

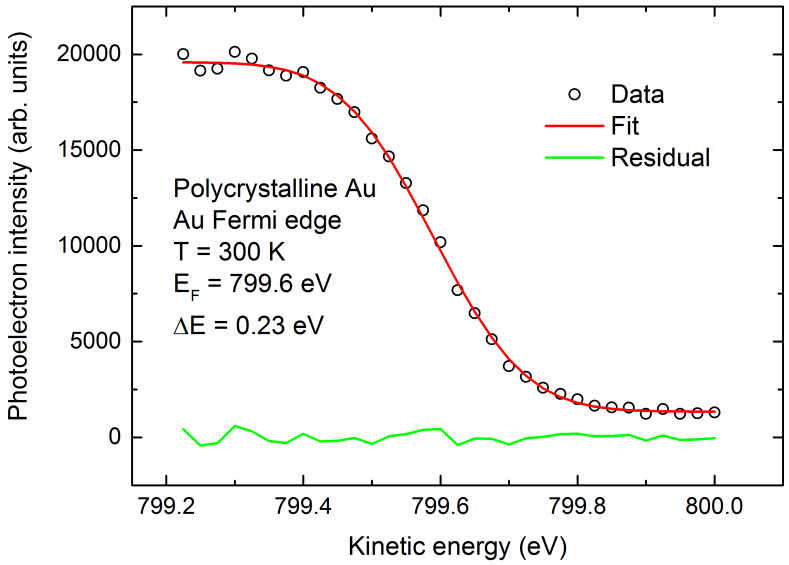


FIGURE 2.11: Example of the Fermi edge of the polycrystalline Au sample in electrical contact with the $Ga_{0.87}Mn_{0.13}As$ sample at a nominal photon energy of 800 eV. The open circles are the experimental data, the red curve is the fit with a function which is the convolution between the Fermi-Dirac function and a Gaussian and the green line is the residual.

we will be showing, the binding energy scale has been calibrated by measuring before and after each of the spectra of interest the Fermi edge of a polycrystalline Au sample which is mounted on the same plate next to the sample (see Fig. 2.9). By fitting the data with a Fermi-Dirac function at a temperature T convoluted with a Gaussian, it was possible to retrieve the value of the Fermi cutoff as well as the full width at half maximum (FWHM) of the Gaussian, which we will be using as an estimation of the overall experimental resolution. An example of such a fit is shown in Fig. 2.11 for the nominal photon energy of 800 eV, where the empty circles are the experimental data, the red line is the fit and the green curve is the residual. We can see that an overall energy resolution of about $\Delta E = 230$ meV is retained. Similar fittings have been carried out at all the used photon energies, confirming an overall experimental energy resolution below 300 meV over the whole $\hbar\omega$ range.

In the case of $La_{1-x}Sr_xMnO_3$, three 100 unit cells (about 40 nm) thick thin films grown on three different substrates have been studied. The samples have been grown by molecular beam epitaxy (MBE) at a dedicated chamber [98] located at the APE beamline of the Elettra synchrotron radiation source (Basovizza, Italy) and have the same nominal Sr concentration, $x = 0.35$, so they are expected to exhibit ferromagnetic ordering and metallicity below the metal-insulator transition temperature (which corresponds to the magnetic ordering temperature). Different substrates correspond to different values of

lattice mismatch, δ as it is reported in Tab. 2.2. The acronyms in parentheses in the first column of Tab. 2.2 will used as tags in the next chapter to indicate the results obtained from different samples. The depositions have been performed by keeping the substrates at a given temperature in a O_3 environment: the values of O_3 pressure and substrate temperature for the three samples which have been studied are reported in the last two columns of Tab. 2.2. They have been measured at the I09 beamline of the

Substrate	Lattice mismatch, (%)	Temperature, (K)	O_3 pressure, (Pa)
$SrTiO_3$ (STO)	1.0 (tensile)	1013	$5 \cdot 10^{-5}$
$La_{0.18}Sr_{0.82}Al_{0.59}Ta_{0.41}O_3$ (LSAT)	0.0 (relaxed)	998	$5 \cdot 10^{-5}$
$SrLaAlO_4$ (SLAO)	-3.0 (compressive)	1003	$5 \cdot 10^{-5}$

TABLE 2.2: Substrate, lattice mismatch (and associated strain type), substrate temperature and O_3 pressure during deposition of the three $La_{0.65}Sr_{0.35}MnO_3$ samples which have been studied in this thesis work.

Diamond light source in nearly normal emission geometry at a temperature of 200 K (in the ferromagnetic and metallic phase), which is achieved by flowing liquid nitrogen in a open circuit cryostat and then heating with a Lakeshore 336 cryogenic temperature controller. Also in this case we have studied the photon energy dependence of the well-screened peak in the Mn $2p$ photoemission line, to see how its contribution to the total lineshape changes as a function of the probed film thickness. The binding energy scale has been calibrated by measuring before and after each spectra of interest the Fermi edge of a gold polycrystalline foil mounted on the same plate of the samples. From a fitting procedure similar to that shown in Fig. 2.11 we found out that an overall energy resolution between 250 meV and 300 meV is retained at the various used photon energies.

Finally, two RuO_2 rutile samples, in the form of thin films with a thickness of 25 nm and a surface roughness < 1 nm have also been measured at different photon energies. The films have been grown on two different substrates, in order to retain a different crystallographic orientation of the surface, as reported in Tab. 2.3. The samples have

Substrate	Lattice plane
TiO_2	(111)
$SrTiO_3$	(100)

TABLE 2.3: Substrate and crystallographic orientation of the two RuO_2 thin films under investigation.

been inserted in the UHV chamber without sample preparation *ex-situ* or *in-situ*. The Ru $3d$ peak has been studied at three different photon energies, in order to see the variation in relative weight of the screened and unscreened peak, as well as the valence band as a function of the kinetic energy of the photoelectrons. All the measurements have been performed in nearly normal emission. As in the previous case, from the fitting of the Fermi edge measured from a polycrystalline Au foil in thermal and electrical contact with

the samples, as in Fig. 2.11, we were able to estimate that the overall energy resolution at the three used photon energies is in the 250-300 meV range and to calibrate the binding energy scale.

Chapter 3

Experimental results

In this chapter we will focus on the experimental results which have been obtained by applying HAXPES to the study of the core level spectra of three different $3d$ transition metal compounds along with with one $4d$ system. One of the main objectives of such study is the identification and characterisation of low binding energy satellites associated to bulk screening channels which are suppressed at the surface, revealing a different degree of correlation between electrons. In section 3.1 and 3.2, the photon energy dependence of the low binding energy nonlocal satellite in the Mn $2p$ spectrum of two different Mn based compounds, namely diluted magnetic semiconductor $Ga_{1-x}Mn_xAs$ and ferromagnetic perovskite $La_{1-x}Sr_xMnO_3$, is studied in order to estimate the critical thickness at which the screening channel associated to the peak "sets in". These results have been compared with those obtained from a representative of a different class of materials, namely the $4d$ rutile oxide RuO_2, which is known to display a intense well-screened peak in the Ru $3d$ spectrum already in the soft X-ray range. The data regarding RuO_2 are presented in section 3.3. In section 3.4, the satellite structure of Ti $1s$ and Ti $2p$ photolines from anatase TiO_2 thin films with different conduction properties has been characterised using two different photon energies, in order to evaluate differences between bulk and surface properties.

3.1 $Ga_{0.87}Mn_{0.13}As$

We will now introduce the spectra which have been collected on a diluted magnetic semiconductor $Ga_{1-x}Mn_xAs$ sample at different photon energies, ranging from 800 to almost 6000 eV. In Fig. 3.1 we present the survey spectra measured at 800 and 5940 eV nominal photon energy (black and red curve, respectively) normalised at the height of the Ga $3p$ peak, in order to show how the change of the photoionisation cross-section as a function of photon energy influences the relative weight of the various photoemission lines. In particular we can notice that the C $1s$ and O $1s$ significantly increase when lowering photon energy: although it is true that for $\hbar\omega = 800$ eV we are more surface sensitive so that an increase of contamination can be expected, this may not be the case for our sample as we will now discuss. In Fig. 3.2, the spectra measured at different

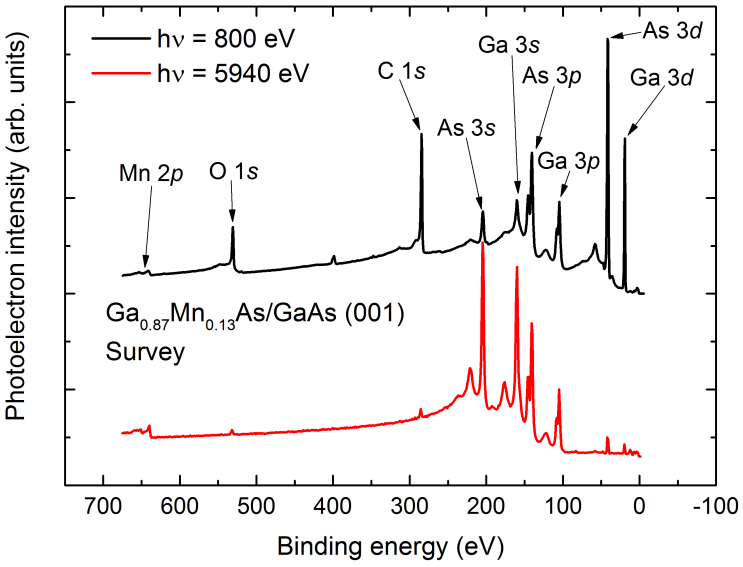


FIGURE 3.1: Survey spectra of the $Ga_{0.87}Mn_{0.13}As$ sample acquired at 800 and 5940 eV nominal photon energy (black and red curve, respectively). The main photoemission lines are marked by the arrows.

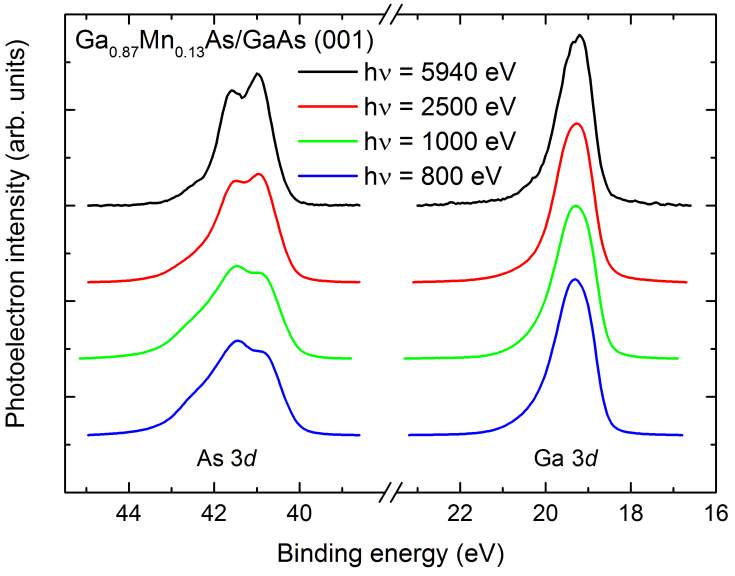


FIGURE 3.2: Comparison of the As 3*d* (high binding energy side) and Ga 3*d* (low binding energy side) spectra measured on $Ga_{0.87}Mn_{0.13}As$ as a function of the photon energy. The spectra have been normalised to the same area after a Tougaard background subtraction, while a vertical offset has been added for clarity.

photon energies of the shallow core levels As $3d$ and Ga $3d$ are displayed. The two sets of spectra are presented after an integral background subtraction and subsequent normalisation to the same area. The bottom axis has been split in order to . It is known that in the presence of an oxide layer, both peaks should present high binding energy structures typical of untreated $Ga_{1-x}Mn_xAs$, associated to As_2O_x ($x = 3, 5$) and Ga_2O_x ($x = 1, 3$) [99]. Such features are not visible in the data reported in Fig. 3.2 not even at 800 eV photon energy. The increase of the high binding energy feature in the spectra of As $3d$ at lower photon energies is probably due to the increase of elemental As, since it is known that the etching procedure is preferential for Ga [99, 100].

In Fig. 3.3 a), the spectra of Mn $2p$ core level from the $Ga_{0.87}Mn_{0.13}As$ thin film at the four different photon energies are presented. The curves have been normalised to the same total area after a Tougaard background subtraction and a vertical offset has been added for clarity. We see how the spectrum at the maximum photon energy, apart from the main peak, displays a clear feature at lower binding energies, labelled extra-peak (in Fig. 3.3 a) a relative binding energy scale is used, taking as zero the position of the extra-peak, in order to facilitate the comparison with the theoretical calculations in the bottom panel) which, as we discussed earlier, is interpreted as a well-screened satellite, due to a nonlocal screening channel typical of the bulk [54]. We can follow its evolution as a function of the photon energy and we can see how its contribution to the total area of the Mn $2p_{3/2}$ line diminishes steadily when the photon energy is reduced, i. e. as the surface sensitivity increases. On the high binding energy side with respect to the main peak, other features can clearly be seen, which are attributed to charge-transfer and multiplet contributions. The experimental spectra are compared with theoretical calculations [7] as a function of the hybridisation V among d^n configurations reported in Fig. 3.3 b): we note that for $V \geq 3$ the "valley" between Mn $2p_{3/2}$ and $2p_{1/2}$ has quite a low intensity, while the experimental spectra measured at photon energies higher than 1000 eV are quite structured. We can then qualitatively assign (as in [7]) the HAXPES spectrum at 5940 eV to a hybridisation $V = 2.5$; it can be seen that by lowering the V value, the high binding energy features increase with respect to the extra peak, as it is the case for the experimental data when lowering the photon energy. On the other hand, the calculated extra peak remains always a prominent feature in the spectrum, while in the measured spectra it becomes less and less intense, since it appears as a little more than a shoulder at 800 eV photon energy. We can then notice that the suppression of the hybridisation shows the same behaviour as the decrease of the photon energy, suggesting that when the surface has a strong contribution, the hybridisation between the d^n configurations is quite reduced.

To explain the decrease of the low binding energy feature in the Mn $2p$ spectra when decreasing the photon energy, it can be assumed the presence of a layer of a given thickness at the surface where the screening channel associated to the peak is suppressed, as in the case of the electron doped $Nd_{2-x}Ce_xCuO_4$ cuprate [52]. In order to give an estimate of the thickness of this layer, we have to evaluate the contribution of the low binding energy peak at each photon energy. For this reason, we performed a fitting of the Mn $2p_{3/2}$ spin-orbit component (because here the well-screened peak is much more visible with respect to the Mn $2p_{1/2}$) of the four spectra shown in Fig. 3.3 a). In Fig. 3.4

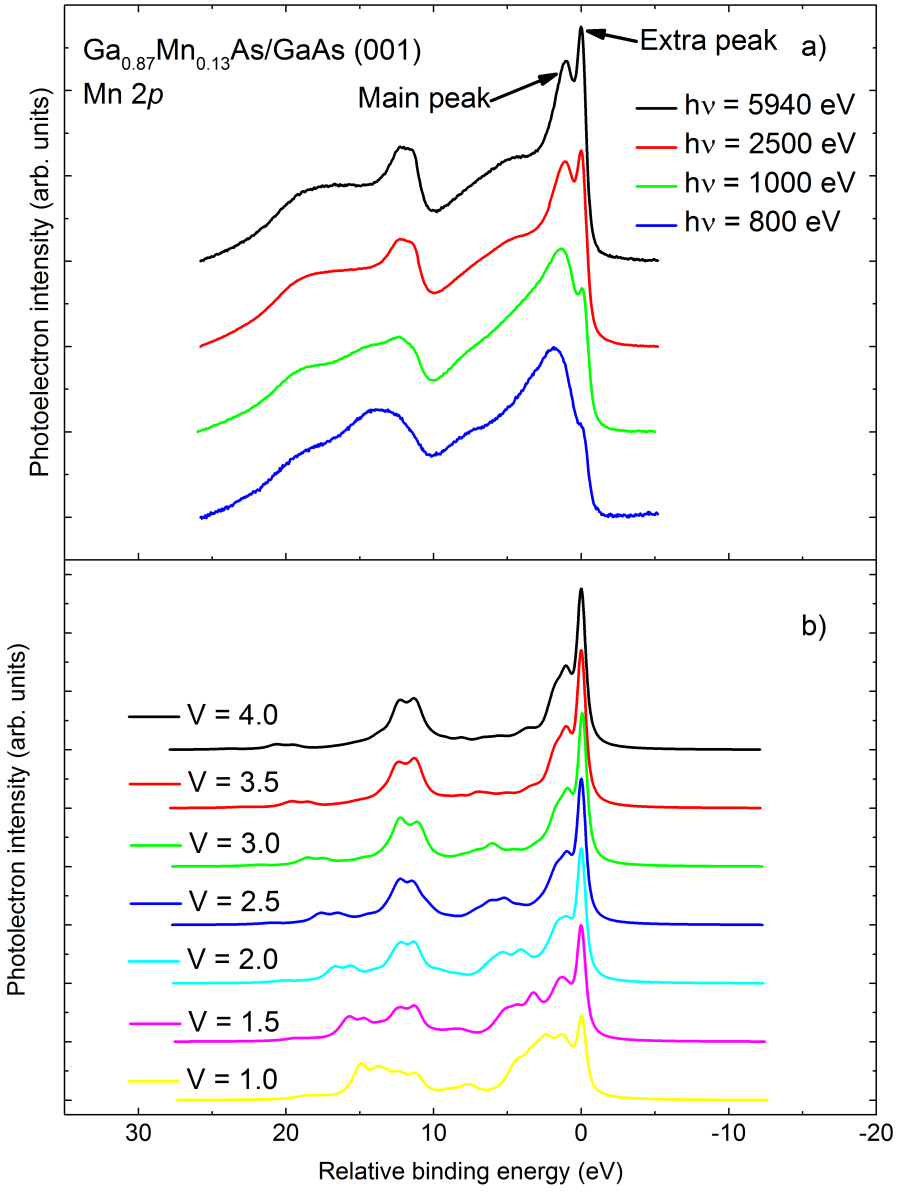


FIGURE 3.3: a) Comparison of the Mn $2p$ spectra from $Ga_{0.87}Mn_{0.13}As$ thin film measured at four different photon energies; the spectra have been normalised to the same total area after the subtraction of a Tougaard background. The main and extra peak of the $2p_{3/2}$ component are indicated by arrows. b) Theoretical spectrum as a function of the hybridisation parameter V among d^n levels as adapted from [7].

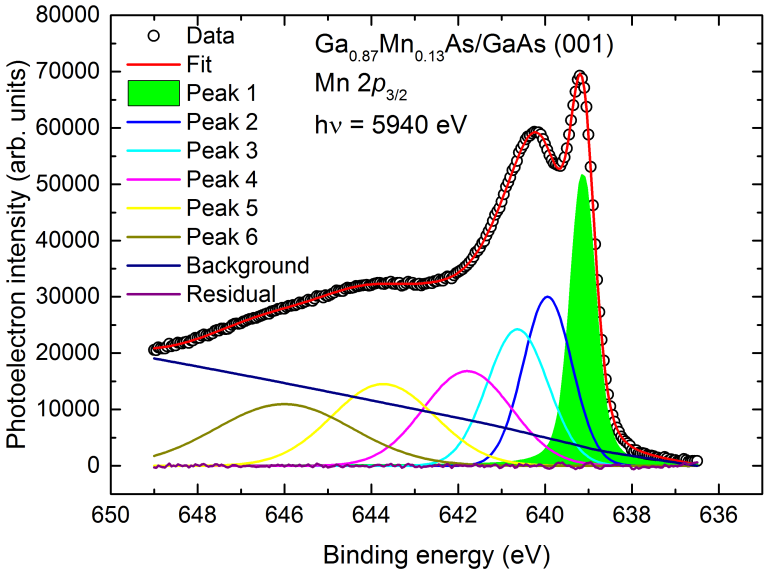


FIGURE 3.4: Fitting of the Mn $2p_{3/2}$ of the $Ga_{0.87}Mn_{0.13}As$ sample measured at a photon energy of $\hbar\omega = 5940$ eV. Six peaks have been used, a Voigt for the extra peak and five Gaussians to reproduce the remaining area.

it is reported the example of the fitting for the spectrum measured at the highest photon energy ($\hbar\omega = 5940$ eV). Six components have been used, a Voigt (Peak 1, with filled area) which represents the well-screened peak and five Gaussians, which is the minimum number of components which allowed to reproduce the lineshape, after the subtraction of an integral background. In particular Peak 2 and Peak 3 reproduce the main peak. The values of the ratio between the area of Peak 1 and the total area have been plotted as black spheres in Fig. 3.5 (left axis) as a function of the mean escape depth at the different kinetic energies of the $2p_{3/2}$ photoelectrons, which have been calculated simply as the product of the inelastic mean free path obtained from the TPP-2M formula for GaAs [43] and the cosine of the angle between the normal to the sample surface and the photoelectron direction ($\theta \simeq 3°$). To each point it has been associated an error bar corresponding to the $\pm 5\%$ of the value of the ratio. The experimental data have been fitted with an exponential attenuation curve of the form

$$I(\lambda) = A \exp(-B/\lambda), \tag{3.1}$$

where λ is the mean escape depth of the photoelectrons, while A ad B are fit parameters whose meaning will be explained briefly. As we have introduced earlier, one way to interpret these data is to assume that exists a layer of thickness B close to the surface where the screening channel which is associated to the extra peak is absent. This layer will then attenuate the signal coming from the "bulk", i. e. from the region of the sample where the screening channel associated to the extra peak is active (because of the higher delocalisation of the $3d$ electrons). The open triangles (right axis) in Fig. 3.5 represent the value of the contribution of a layer of thickness B (as obtained from

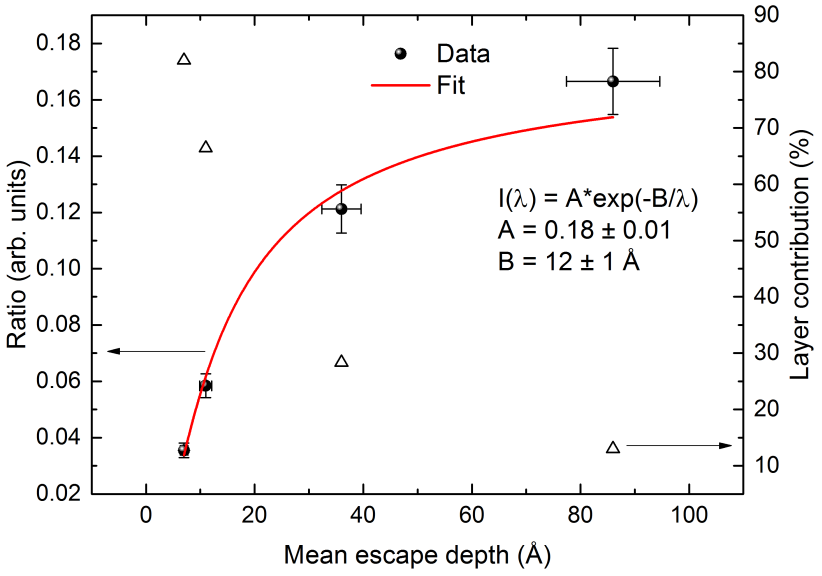


FIGURE 3.5: Weight of the well screened peak (Peak 1 in Fig. 3.4) to the total area of the Mn $2p_{3/2}$ line (filled squares, left axis) as a function of the mean escape depth of photoelectrons fitted with an exponential law (see text for details) and contribution of a layer of thickness 12 to the photoemission signal (open triangles, right axis).

the fitting) to the total photoemission signal. The more the thickness of the layer is similar to the information depth at a given photon energy, the higher the contribution of the surface layer to the total photoemission signal will be, corresponding to a more significant suppression of the extra peak. Increasing the photon energy and hence the information depth, the peak will be less and less attenuated, because the layer will be a small fraction of the information depth. The parameter A of the fit indicates which is the value of the contribution of the extra peak to the total area of the Mn $2p$ spectrum when the thickness of the attenuating layer is negligible with respect to the information depth. From the fitting shown in Fig. 3.1, we obtained as values $A = 0.18 \pm 0.01$ arb. units and $B = 12 \pm 1$ Å; we notice that B is quite close to the 15 ± 5 Å found in the case of the electron doped $Nd_{2-x}Ce_xCuO_4$ cuprate [52].

In Fig. 3.6 the energy separation between the main and extra peak of the Mn $2p_{3/2}$ core level as a function of the photon energy is reported, showing a decrease when increasing the photon energy, until a sort of saturation is reached at energies higher than 2500 eV. The values in Fig. 3.6 have been calculated assuming that the main peak can be reproduced by the sum of Peak 2 and 3 and taking the maximum of the resulting curve as position of the main peak. The solid line is only a guide for the eye.

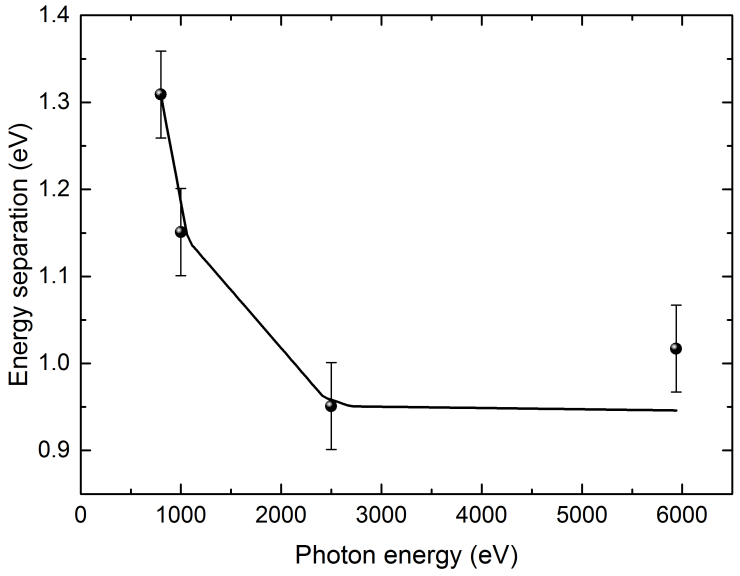


FIGURE 3.6: Energy separation between extra and main peak (obtained as the sum of Peak 2 and 3) as a function of the photon energy. The solid line is a only guide for the eye.

3.2 $La_{0.65}Sr_{0.35}MnO_3$

$La_{1-x}Sr_xMnO_3$ is the first $3d$ systems where a low binding energy satellite in the $2p$ HAXPES spectrum of a transition metal element has been reported [6]. The survey spectra measured at 5940 eV photon energy of the three manganite thin films grown with different tensile condition are presented in the left panel of Fig. 3.7. The main photoemission lines have been indicated by the arrows and the curves have been normalised to the intensity of the O $1s$ core level. In the right panel of Fig. 3.7, the expanded view of the spectral region between 300 and 250 eV binding energy is presented, to compare the C $1s$ peak to the La $4s$ and Sr $3p$ photolines, showing that the contribution of surface contamination is negligible in HAXPES spectra. In Fig. 3.8 we show the results of the photon energy dependence of the Mn $2p$ spectrum measured on the manganites. In the panel a) we can see the Mn $2p$ lineshapes acquired at a photon energy $\hbar\omega = 5940$ eV on all three the samples; we can immediately recognise the presence of a well-screened feature around 639 eV binding energy for all the three spectra. Similarly, around 651 eV, the well-screened peak of the Mn $2p_{1/2}$ line can be seen as a small bump. Also, around 665 eV we can recognise the charge-transfer satellites of the $2p_{1/2}$ (the equivalent satellites for the $2p_{3/2}$ peak are superimposed to the $2p_{1/2}$ main peak) [101]. Another feature is visible around 643 eV, which is usually attributed to a Mn^{4+} derived state [6]. The curves have been normalised to the same area after the subtraction of a Tougaard background to account for electron energy-loss; a vertical offset has been added for clarity. In panel b) the photon energy dependence of the Mn $2p$ photoemission line from the strain-relaxed sample (grown on LSAT substrate) is presented. It can be immediately

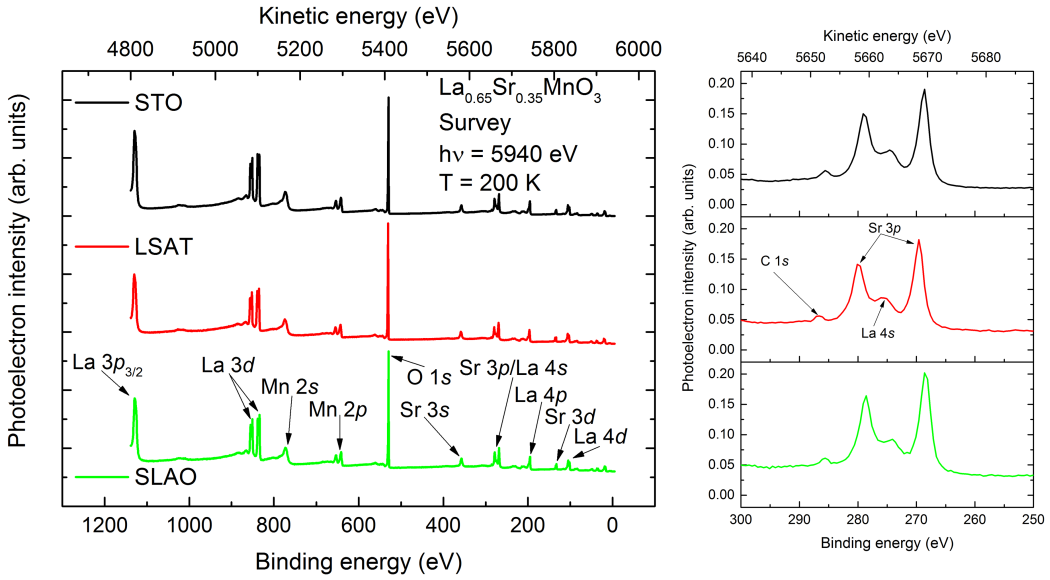


FIGURE 3.7: Survey spectra acquired from the three manganite thin films at a photon energy $\hbar\omega = 5940$ eV and a temperature $T = 200$ K. The main core levels have been indicated by arrows and the curves have been normalised to the intensity of the O $1s$ photoline. (Right panel) Expanded view of the spectral region of the C $1s$, to show the negligible contribution of surface contamination to the HAXPES spectra.

seen how, at least from a qualitative point of view, these results are different from what we observed for the $Ga_{1-x}Mn_xAs$ sample. In this case even at the highest used photon energy the extra-peak has a small intensity with respect to the main peak and also seems to disappear completely already at a photon energy $\hbar\omega = 1000$ eV. For these curves the same normalisation as in the graph of panel a) has been performed. A very similar photon energy dependence (not shown) is seen in the case of the sample with tensile strain (grown on SLAO substrate), except for the fact the intensity of the low binding energy peak seems to be lower. This is better underlined in Fig. 3.9, where the Mn $2p_{3/2}$ spectra at $\hbar\omega = 5940$ eV of the three samples are shown. These spectra are a "cut" from the complete curves which are reported in Fig. 3.8 a), meaning that they are normalised to the intensity of the whole Mn $2p$ line (of course in this case no vertical offset has been applied). We can see that when going from tensile to compressed strain the intensity of the well-screened peak is progressively reduced, especially when passing from relaxed to compressive, while the difference between tensile and relaxed seems to be very small as it can expected since the lattice mismatch for the tensile strained film is only $\delta = +0.01$. On the tensile and relaxed sample we tried to perform the same analysis as in the case of the $Ga_{1-x}Mn_xAs$ compound we showed in the previous section, fitting the Mn $2p_{3/2}$ lineshape and extracting the contribution of the well screened peak to the total area. In this case we used six Gaussians and a integral background to reproduce the spectrum as showed in Fig. 3.10 in the case of the strain relaxed sample, where the extra peak is the one with the filled area and is labelled as Peak 1. In Fig. 3.11 the mean escape depth dependence of the well screened peak is reported for the relaxed (black squares) and strain compressed sample (red circles) along with fitting using an exponential function as that reported in Eq. 3.1. The values of the A and B parameters as extracted from

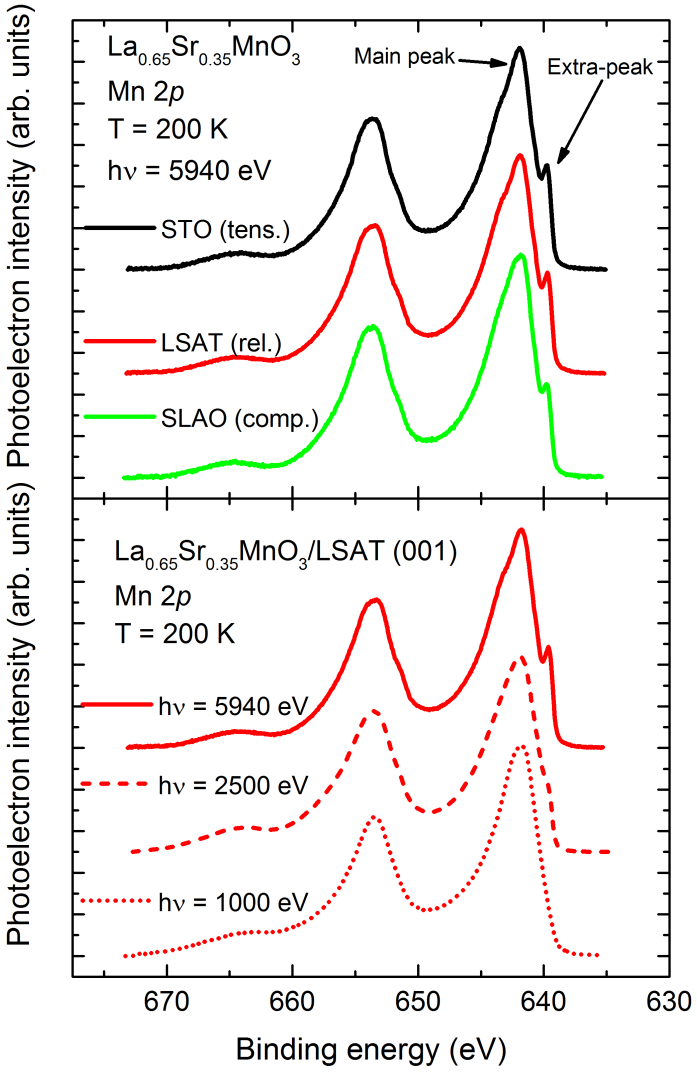


FIGURE 3.8: a) Comparison of the Mn 2*p* photoemission spectra from the three manganite samples measured at the highest photon energy achievable $\hbar\omega = 5940$ eV. b) Photon energy dependence of the Mn 2*p* photoemission line from the sample grown on LSAT (strain relaxed). In both graphs the curves have been normalised to the same area after subtraction of a Tougaard background.

the fit are reported both in Fig. 3.11 and Tab. 3.1; it can be seen that for both films $B \simeq 40$ Å. Although there seems to be a small difference between the absolute values for the thickness of the attenuating layer of the two samples (specifically it is smaller in the case of the strain relaxed specimen), the two numbers are practically identical within the associated uncertainty. The main sources of uncertainty in this analysis are related to the subtracted integral background and to the determination of the area of the extra peak at the lower available photon energy where, as it can be seen in Fig. 3.8 b), the peak is practically not visible. From these data it seems that even at the highest photon energy the feature is still strongly attenuated from the layer where the screening channel is absent. In fact, as it can be seen by the open triangles in Fig. 3.11, the contribution

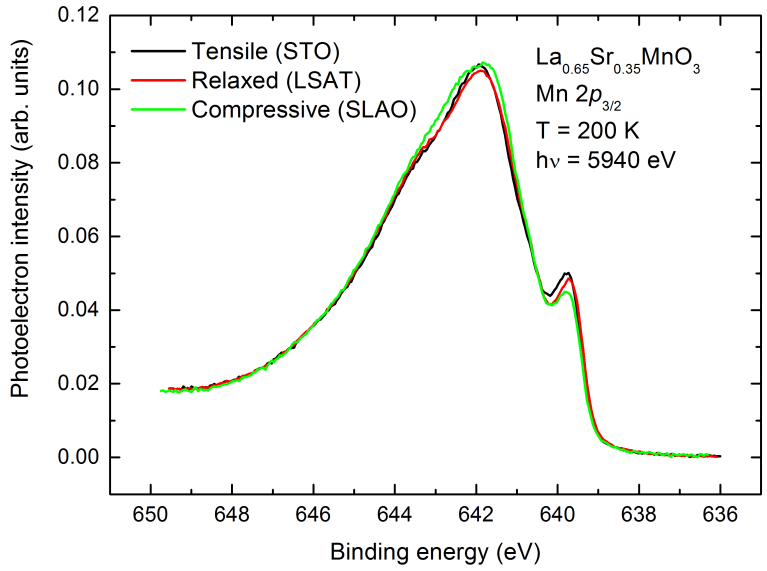


FIGURE 3.9: Comparison of the Mn $2p_{3/2}$ spectra measured at $\hbar\omega = 5940$ eV for tensile strained (STO substrate), strain-relaxed (LSAT substrate) and compressive strained (SLAO substrate) $La_{0.65}Mn_{0.35}MnO_3$ thin films. The curves have been normalised to the area of the total Mn $2p$ photoemission line after a Tougaard background subtraction.

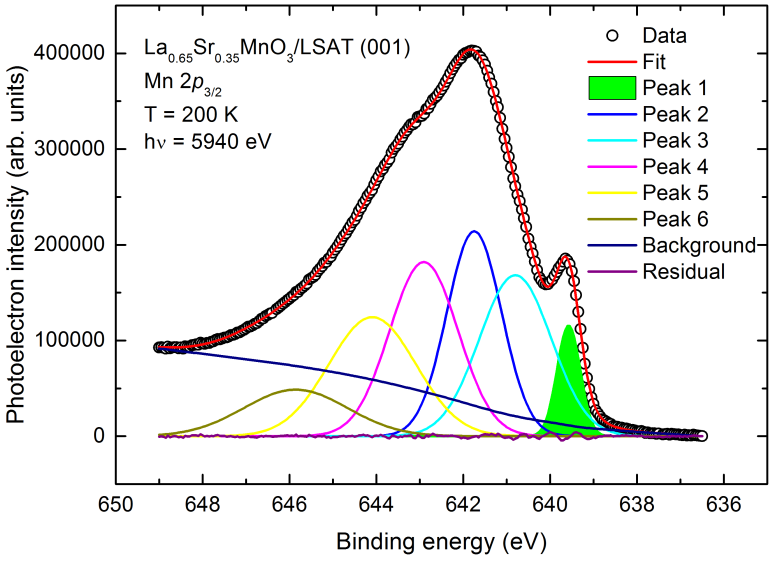


FIGURE 3.10: Fitting of the Mn $2p_{3/2}$ spectrum from the strain relaxed sample measured at $T = 200$ K with a photon energy of $\hbar\omega = 5940$ eV. Six Gaussian and a integral background have been used to reproduce the lineshape.

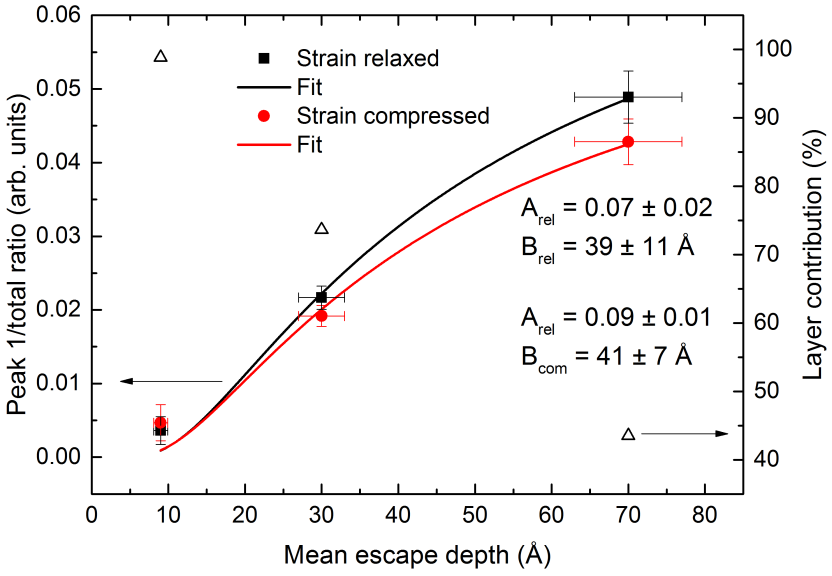


FIGURE 3.11: Contribution of the extra peak to the total area of the Mn $2p_{3/2}$ lineshape for the strain relaxed (black squares) and the strain compressed sample (red circles) as a function of the mean escape depth of photoelectrons at different photon energies (left axis). An exponential attenuation law has been used to fit the experimental points and the values of the parameters as extracted from the fit are reported in the graph. The open triangles represent the value of the contribution of a layer of thickness 40 Å to the photoemission signal (right axis) as a function of the mean escape depth of photoelectrons.

Strain, δ (%)	A (arb. units)	B (Å)
Compressive, -3	0.09 ± 0.01	41 ± 7
Relaxed, 0	0.07 ± 0.02	39 ± 11

TABLE 3.1: Values of the fitting parameters A and B for the attenuation of the Mn $2p_{3/2}$ extra-peak of relaxed and compressive strained manganite samples.

of a layer with thickness 40 Å to the total photoemission intensity is already $\sim 43\%$ at $\hbar\omega = 5940$ eV.

On these samples we have also measured the Mn $3s$ core level: the spectra acquired at the maximum used photon energy (~ 5940 eV) are shown in Fig. 3.12: the splitting which can be seen is not due to spin-orbit, but to the interaction between the spin of the $3s$ core hole and the uncoupled spin of the $3d$ band (this effect is known as *multiplet splitting*) [102]. The lower binding energy peak corresponds to a high-spin state, while the higher binding energy line is related to a low-spin configuration (the small vertical lines indicate the position of the low-spin component at all photon energies). On mixed-valence manganites, an empirical linear relation has been found between the value of the exchange splitting and the formal valence of the Mn ions in these oxides [103]. It is also interesting to note how on the low binding energy side of the high spin component, a

small shoulder can be seen, which in a previous work has been identified as an extra-peak, completely equivalent to the case of Mn $2p_{3/2}$ [104].

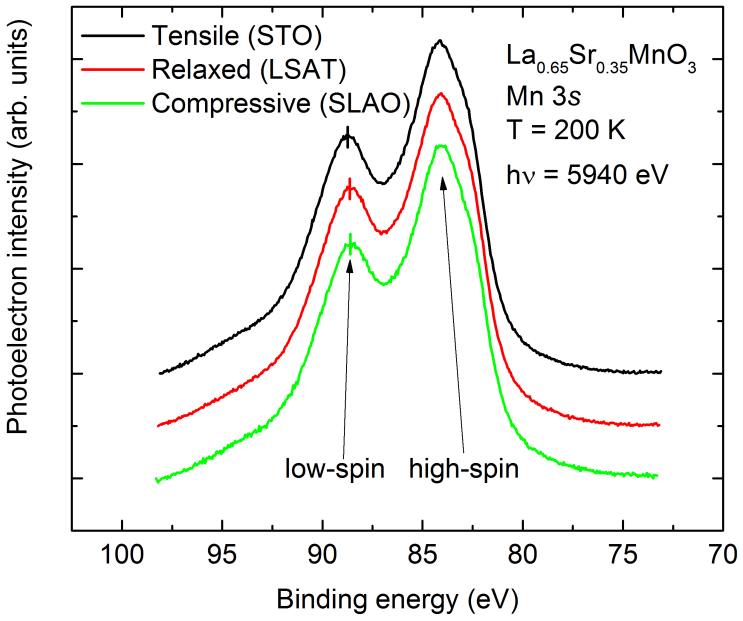


FIGURE 3.12: Comparison of the Mn $3s$ spectra measured on the three samples with different strain conditions (tensile black, relaxed red and compressive green) at $T = 200$ K and $\hbar\omega = 5940$ eV photon energy. The curves have been normalised to the same area after the subtraction of a Tougaard background and a vertical shift has been applied for clarity. The position of the low-spin component is indicated by a small vertical line.

Mn $3s$ spectra at different photon energies for the relaxed and compressive strained samples are shown in Fig. 3.13 a) and b) respectively. All the curves have been normalised to unit area after a Tougaard background has been subtracted. We can see that in the case of strain relaxed sample (Fig. 3.13 a)), both the separation between the high and low-spin peaks and the relative weight of the high-spin feature increase when lowering the photon energy; both effects, only less pronounced, can also be seen in the compressive strained sample (Fig. 3.13 b)). A more quantitative analysis is made by fitting the Mn $3s$ spectra with five Voigt profiles and a integral background, as it can be seen in Fig. 3.14 where the fitted spectrum at 2500 eV photon energy from the strain relaxed sample is shown as example. The difference between the position of the features labelled as Peak 1 and Peak 2 has been used to evaluate the exchange splitting and the following empirical linear formula

$$v_{Mn} = 9.67 - 1.27\Delta E_{3s}/eV \tag{3.2}$$

as reported in [105], has been used to calculate the Mn valence v_{Mn}, as shown in Tab. 3.2.

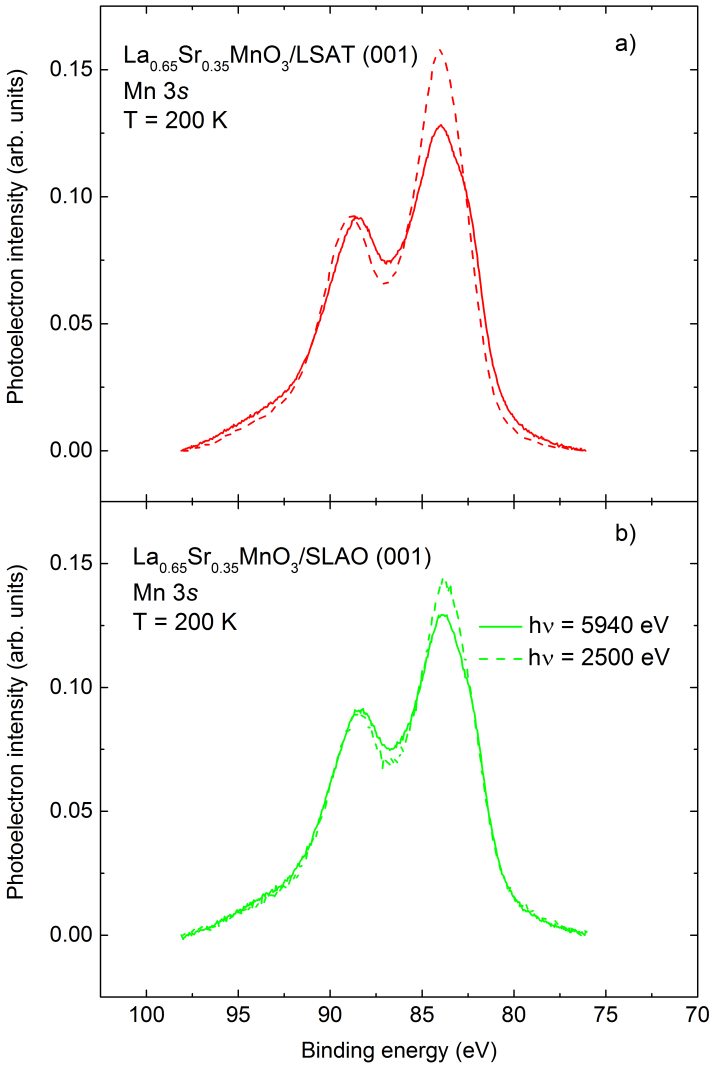


FIGURE 3.13: Mn 3*s* spectra from the strain relaxed (a) and compressive strained (b) sample at two different photon energies, $\hbar\omega = 5940$ eV (solid line) and $\hbar\omega = 2500$ eV (dashed line). A Tougaard background has been subtracted and a normalisation to the same total area has been performed.

	ΔE_{3s} (eV)		Mn valence	
Strain, δ(%)	$\hbar\omega = 2500$ eV	$\hbar\omega = 5940$ eV	$\hbar\omega = 2500$ eV	$\hbar\omega = 5940$ eV
Compressive, -3	4.7	4.4	3.7	4.1
Relaxed, 0	4.8	4.4	3.6	4.1
Tensile, +1	–	4.5	–	4.0

TABLE 3.2: Values of exchange splitting ΔE_{3s} obtained from the fitting of the Mn 3*s* spectra and of the Mn valence as calculated using Eq. 3.2.

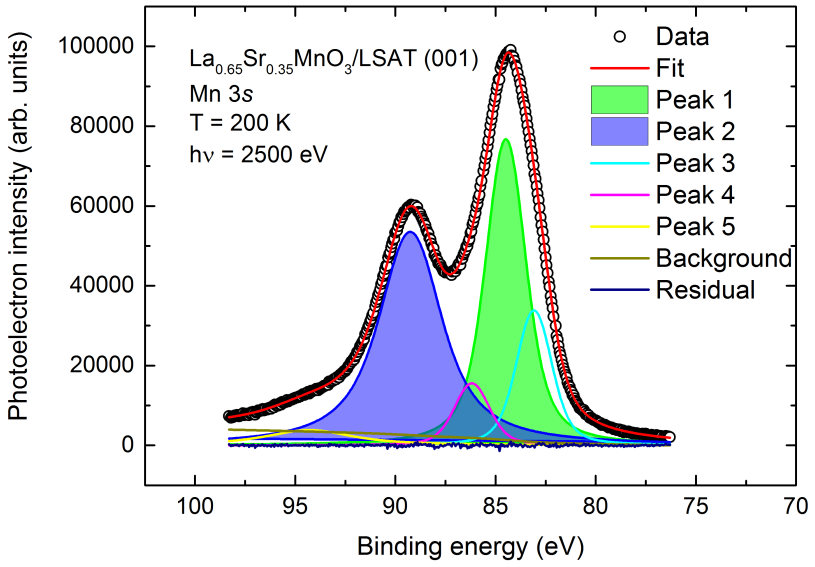


FIGURE 3.14: Fitting of the Mn 3*s* spectrum from the strain relaxed sample at 2500 eV photon energy with five Voigt profiles and a integral background.

We have also measured the valence band spectra of the three manganites as reported in Fig. 3.15 a) for $\hbar\omega = 5940$ eV and $T = 200$ K. Five main structures can be seen, which can be identified as in [106, 107]:

- around 7.5 eV, there is a structure assigned to hybridisation between O and Mn derived states (actually this structure is not reproduced in the calculations showed in [106], authors did this assignment without elaborating on it, while in [107], which cites the previous paper among the references, the structure is labelled as O $2p^*$ in the pictures, but is not referred to in the text);
- at about 6 eV, we have the O $2p$ band;
- at about 4 and 2.5 eV, there are O $2p$−Mn $3d$ t_{2g} hybridised states;
- close to the Fermi level, there is the small band associated to the Mn $3d$ e_g levels.

In Fig. 3.15 b), the valence band photoemission spectrum for three different photon energies measured on the strain relaxed film is shown: we can see that decreasing the photon energy, the structure around 7.5 eV binding energy seems to be suppressed, while one of the two bands associated to O $2p$−Mn $3d$ t_{2g} hybridised states (the one with lowest binding energy) significantly increases in intensity, as well the Mn $3d$ e_g derived band. The same measurements have been performed on the compressive strained sample (not shown), displaying a very similar behaviour to what reported in Fig. 3.15.

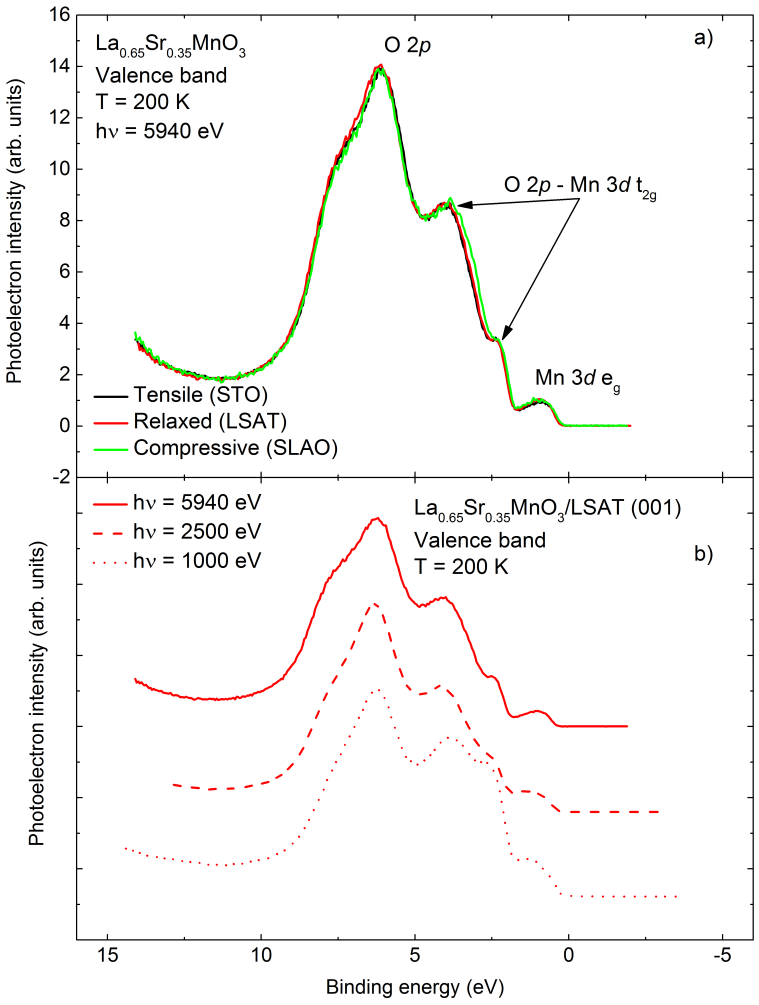


FIGURE 3.15: a) Comparison of the valence band photoemission spectrum acquired on the three different manganite thin films (black tensile strain, red strain relaxed and green compressive strain) at $T = 200$ K and a photon energy $\hbar\omega = 5940$ eV. The main features are labelled as in [106, 107]. b) Evolution of the valence band photoemission spectrum from the strain relaxed sample (a very similar behaviour is seen for the compressive strained film, not shown).

3.3 A 4*d* system: RuO_2

We will now present a HAXPES study performed on two rutile RuO_2 thin films grown on two different substrates with distinct crystallographic orientations. An example of survey spectra measured on the two samples at 5940 eV photon energy is presented in Fig. 3.16. We have indicated by arrows the main photolines (including the Sr 3*s* from the substrate in the case of the sample grown on $SrTiO_3$) and the curves have been normalised to the intensity of the O 1*s* peak. It can be noticed that the Ru peaks seem more intense in the spectrum measured on the sample grown on the $SrTiO_3$ substrate.

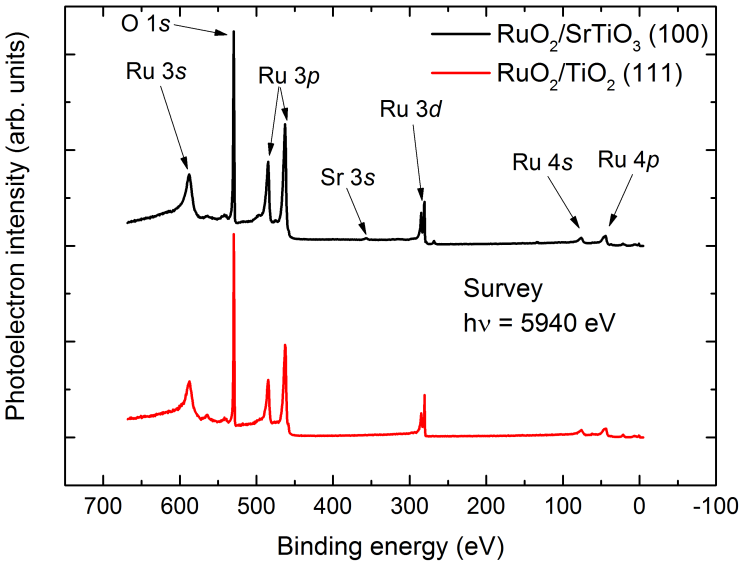


FIGURE 3.16: Comparison of the survey spectrum measured at 5940 eV photon energy on the two ruthenates. The curves have been normalised to the intensity of the O 1*s* peak.

In Fig. 3.17, the photon energy dependence of the Ru 3*d* core level spectrum is reported: starting from the curve measured at 5940 eV on the sample grown on TiO_2, we can identify at least four features, two for each component of the spin-orbit doublet. In the analogue spectrum acquired on the other sample, the small peak around 279 eV is the Sr $3p_{3/2}$ photoline from the substrate ($SrTiO_3$). The peak at the lowest binding energy is considered the screened peak, although there is still debate whether the screening is due to electrons from a quasiparticle states at the Fermi level [34] or from a neighbouring metallic site (nonlocal screening) [33].[1] The curves have been normalised to the intensity of the screened Ru $3d_{3/2}$ peak after the subtraction of a Tougaard background; also an offset has been added for the sake of clarity. it can be seen that by changing the photon energy, the ratio between the screened and unscreened peak 5/2 peaks varies. In particular, the screened peak increases with respect to the unscreened one.

We have also measured the evolution of the valence band spectrum for both samples, which is shown in Fig. 3.18. Three main feature can be seen and the spectra have been normalised to the intensity of the big component close to the Fermi level. In analogy with another rutile oxide, namely IrO_2, whose valence band displays three structures similar to those reported in Fig. 3.18 [108], the peaks can be considered the result of photoemission from states deriving from the overlap of the metal (Ru in our case) *d* and oxygen 2*p* levels namely, starting from lower binding energy, π antibonding, π bonding

[1] In Fig. 3.17, we have indicated the four most visible features, dividing between screened and unscreened. This is what is done in the article by Kim *et al.* [34], but has we have shown previously, the peak around 282 eV which we indicate as unscreeened, in the work of van Veenendal [33] is associated to a local screening. The use of the notation as in Fig. 3.17 is made only for the sake of simplicity, not because we are leaning more towards the quasiparticle screening model.

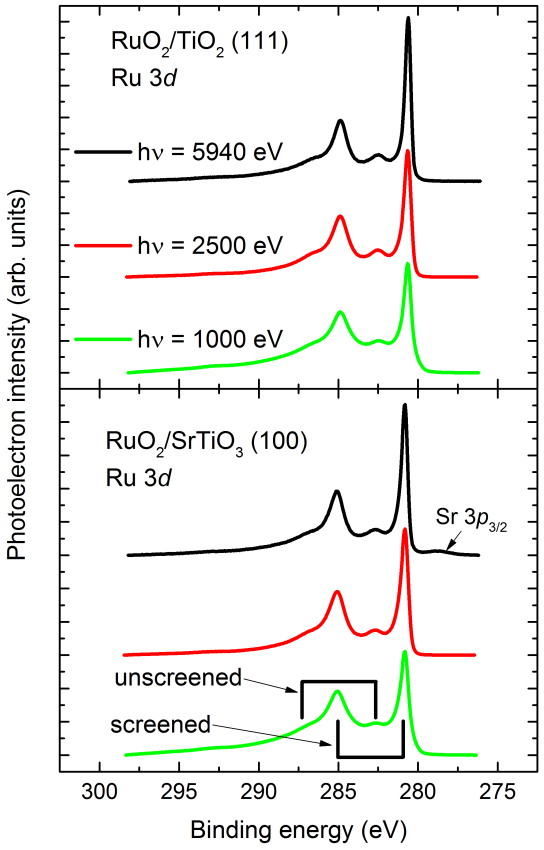


FIGURE 3.17: Photon energy dependence of the Ru $3d$ core level spectrum measured on the two ruthenates. The curves have been normalised to the intensity of the screened Ru $3d_{3/2}$ line after subtraction of a Tougaard background.

and σ bonding states. However, the main contribution to the spectra is given by the Ru $4d$ states, since at the used photon energies the photoionisation cross-section for Ru $4d$ electrons is significantly larger than the one for O $2p$ electrons [109].

3.4 $TiO_{2-\delta}$

We present now the results obtained on two different anatase TiO_2 samples, presenting different conduction properties as a consequence of the different oxygen vacancy concentration induced by growing the films at different O_2 pressures (see Tab. 2.1). Survey spectra at 6900 eV and 2500 eV have been acquired and are reported in Fig. 3.19 and 3.20, respectively, after being normalised to the O $1s$ peak, and given a vertical offset for the sake of clarity. Both graphs are displayed with the binding energy scale (bottom axis) and the corresponding kinetic energy scale (top axis). C $1s$ peak due to surface contamination can be seen in the spectra of both samples at both energies, although it seems more pronounced in the case of the $P(O_2) = 10$ Pa spectra. Since we have not measured some Au $4f$ photoemission peak at 2500 eV, we have aligned the spectra at

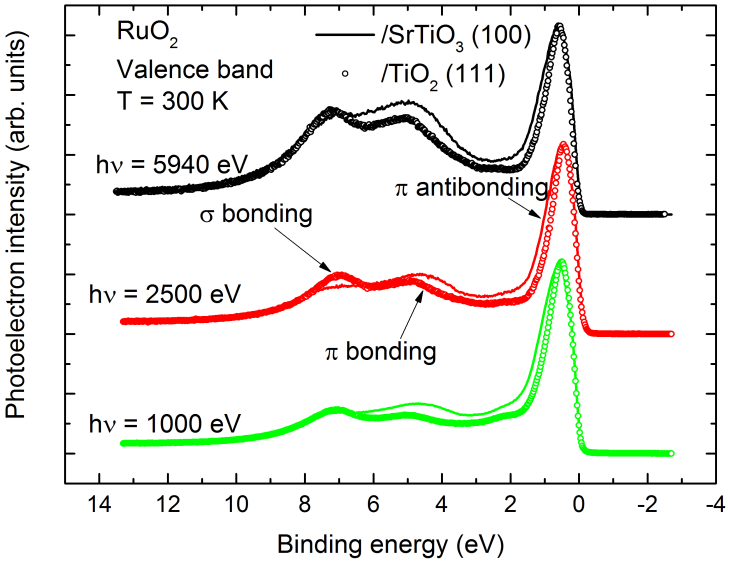


FIGURE 3.18: Photon energy dependence of the valence band measured on the two ruthenates. The solid line curves are the spectra acquired on the sample grown on $SrTiO_3$, while for the specimen grown on TiO_2, small open circles are used.

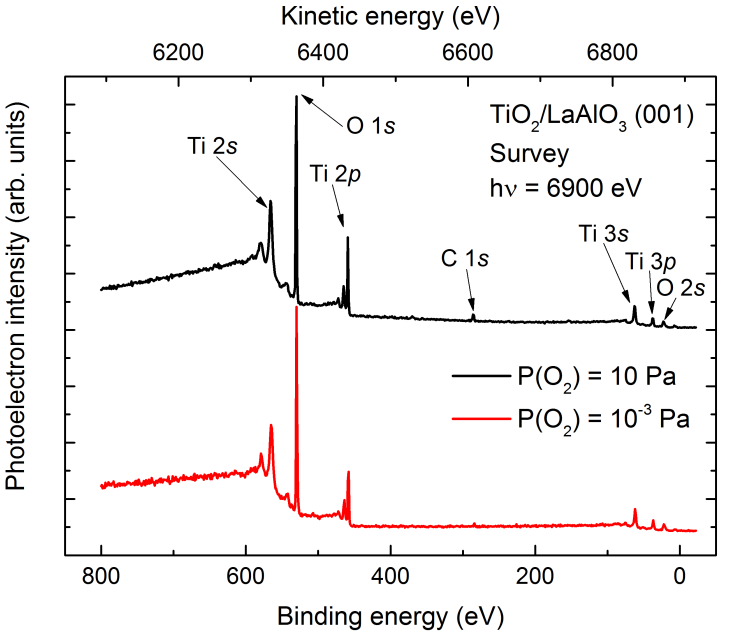


FIGURE 3.19: Survey spectra from the $P(O_2) = 10$ Pa sample (black curve) and the $P(O_2) = 10^{-3}$ Pa sample (red curve), normalised to O 1*s* peak at 6900 eV photon energy. The main peaks have been labelled in the figure.

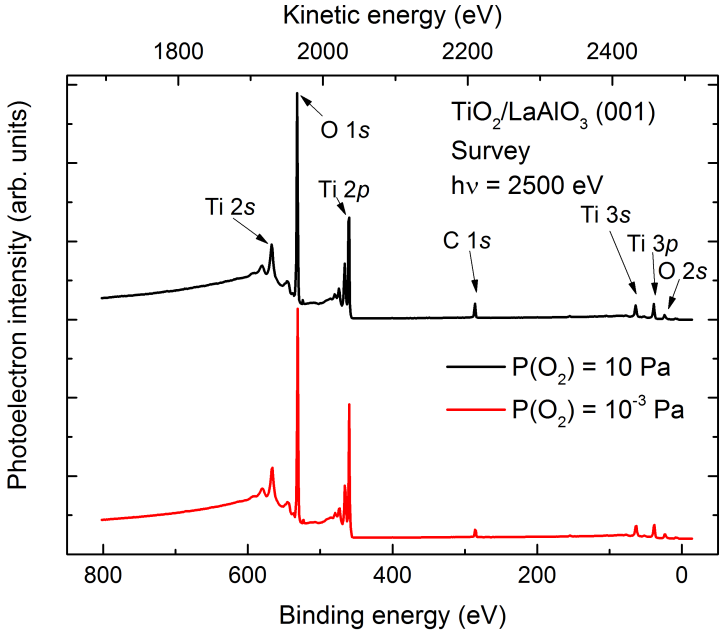


FIGURE 3.20: Survey spectra from the $P(O_2) = 10$ Pa sample (black curve) and the $P(O_2) = 10^{-3}$ Pa sample, normalised to O 1*s* peak at 2500 eV photon energy. The main peaks have been labelled in the figure.

this photon energy by assuming that the binding energy of the C 1*s* peak is the same as in the spectra at 6900 eV photon energy. From a qualitative point of view, by comparing the ratio of the Ti 2*p* peaks of the two samples at 6900 eV photon energy with the correspondent ratio at 2500 eV photon energy, we can see that at 6900 eV there is more Ti in the $P(O_2) = 10$ Pa sample (which means less O), while at 2500 eV the situation is inverted. Generally one would expect the $P(O_2) = 10^{-3}$ Pa to have a lower O concentration, which is what we see at 2500 eV but not at 6900 eV. Since the spectra at 2500 eV are surely more surface sensitive than those at 6900 eV (inelastic mean free path of 35 Å and 94 Å at the kinetic energy of the O 1*s* photoelectrons at the two different photon energies [43]), maybe this is due to the fact that O diffuses toward the surface (more "efficiently" in the sample with a lower concentration of oxygen vacancies, $P(O_2) = 10$ Pa).

We can clearly see in all the spectra reported in Fig. 3.19 and 3.20, that both the spectra of the Ti 2*s* and 2*p* core levels display a rich variety of features at higher binding energies with respect to the main peak. With a photon energy of 6900 eV we can also measure a core level as deep as the Ti 1*s* (binding energy of 4966 eV for atomic Ti [110], not shown in the survey), which is expected to have the simplest shape, since it has no spin-orbit splitting and also the exchange-splitting is expected to be small, because the overlap of the 1*s* core level with the 3*d* valence levels should be negligible. It can help us to identify features which could be hidden in more complicated spectra of photolines such as Ti 2*p*. By using two different photon energies, we can probe whether there are any difference between bulk and surface. Of course at 2500 eV photon energy it will not be possible to measure the Ti 1*s*. In Fig. 3.21 the comparison between the Ti 1*s*

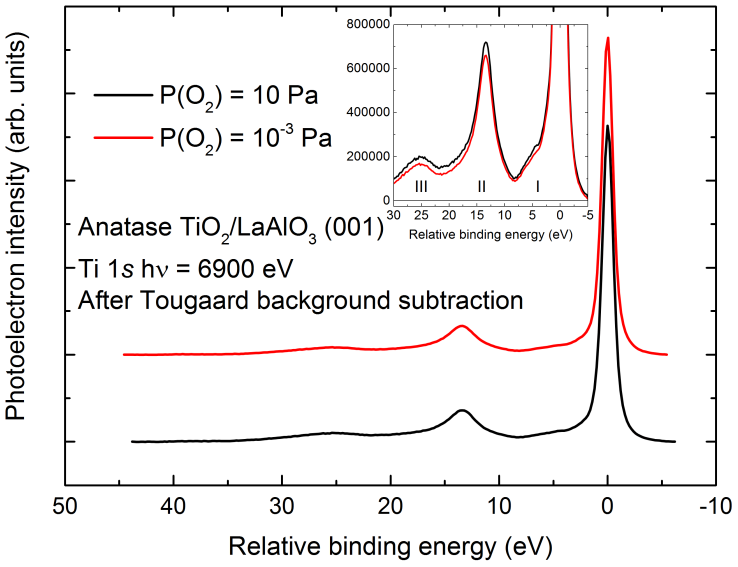


FIGURE 3.21: Comparison of the Ti 1*s* acquired at 6900 eV photon energy from sample $P(O_2) = 10$ Pa (black curve) and $P(O_2) = 10^{-3}$ Pa (red curve). The peaks have been normalised to the height of the main peak and a vertical offset has been added for clarity. In the inset, the vertical scale has been expanded and the vertical offset has been removed, in order to show the three satellites, indicated by Roman numerals, I, II and III.

spectra acquired from the two sample is presented; the curves have been normalised to the height of the main peak after the subtraction of a Tougaard background [111] and a vertical offset has been applied to facilitate the comparison. In the inset the same two curves are reported (without vertical offset this time), but the vertical scale has been expanded in order to emphasise the weak satellites features. We can identify, beside the main peak, at least three features, at about 5, 13 and 25 eV higher binding energies with respect to the main peak, whose positions have been marked by the Roman numerals I, II and III, respectively. From now these we will use these labels when referring to the three satellites peaks. In Fig. 3.22 a), we show a comparison of the Ti 1*s* and Ti 2*p* lineshape measured on the $P(O_2) = 10^{-3}$ Pa sample. To facilitate the comparison, the spectra have been arbitrary aligned to the energy of the main peak, which in the case of the Ti 2*p* spectra is the $2p_{3/2}$ and the position of the satellites which have been seen in Fig. 3.21 are indicated by the dashed lines. The $2p_{1/2}$ peak can be seen at around 5 eV from the $2p_{3/2}$ and it is quite broad, which means that it sits right on top of the satellite I which we had identified in the Ti 1*s* spectra of Fig. 3.21. Satellite II is easily recognisable at about 13 eV, along with its spin-orbit doublet "companion" around 18 eV, while the presence of satellite III can be guessed as a small bump around 25 eV (also its spin-orbit doublet companion should be present, but it is very difficult to clearly see it with this scale). In the panel b) of Fig. 3.22, we report the Ti 2*p* spectra acquired at the two different photon energies of 6900 and 2500 eV: they have been normalised to the intensity of the Ti $2p_{3/2}$ peak after the subtraction of a Tougaard background and

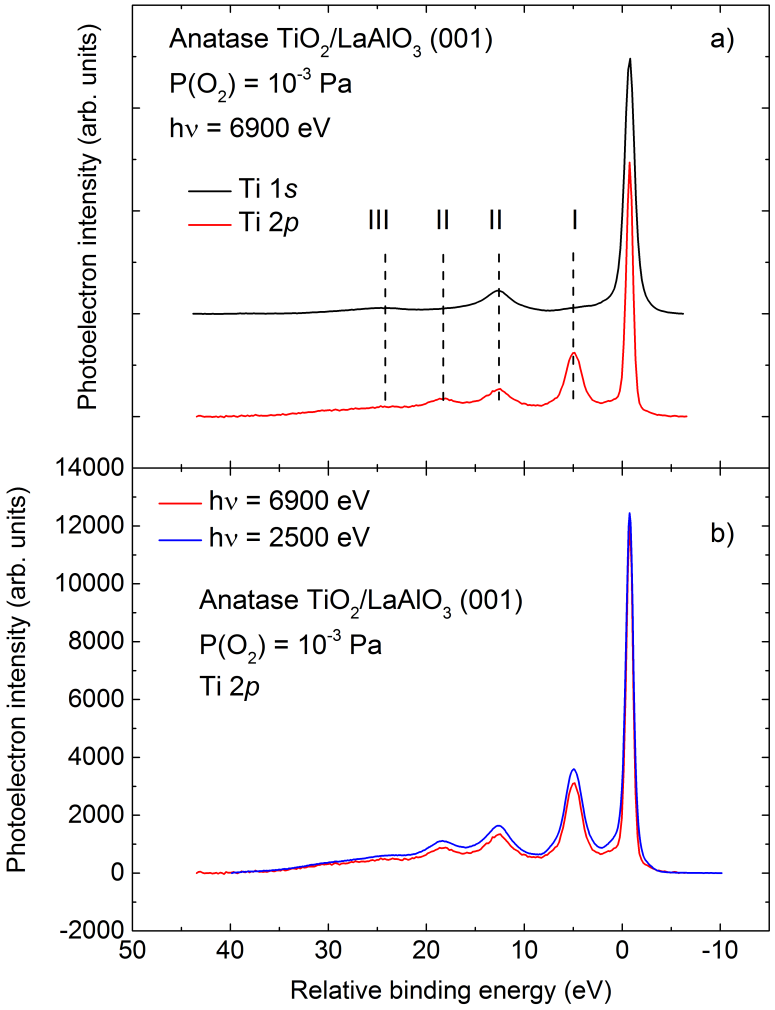


FIGURE 3.22: a) Comparison of the experimental spectrum of Ti 1*s* (black curve) with those of Ti 2*p* at 6900 and 2500 eV photon energies (red and green curve, respectively) from the $P(O_2) = 10^{-3}$ Pa sample. The spectra have been normalised to the intensity of the main peak after subtraction of a Tougaard background. A vertical offset has been added for the sake of clarity. Three different satellites are indicated as I, II and III. b) Comparison of the Ti 2*p* spectra acquired on the same sample at two different photon energies (6900 and 2500 eV): the curves have been normalised to the intensity of the Ti $2p_{3/2}$ main peak after the subtraction of a Tougaard background.

we can immediately notice how the intensity of Satellite II and III with respect to that of the main line increases when passing to a lower photon energy. Furthermore, also the intensity of the Ti $2p_{1/2}$ is higher at $\hbar\omega = 2500$ eV: this may be due to the presence of Satellite I. In the case of the $P(O_2) = 10$ Pa specimen (graph not shown), the differences between the spectra acquired at different photon energies are less pronounced. In order

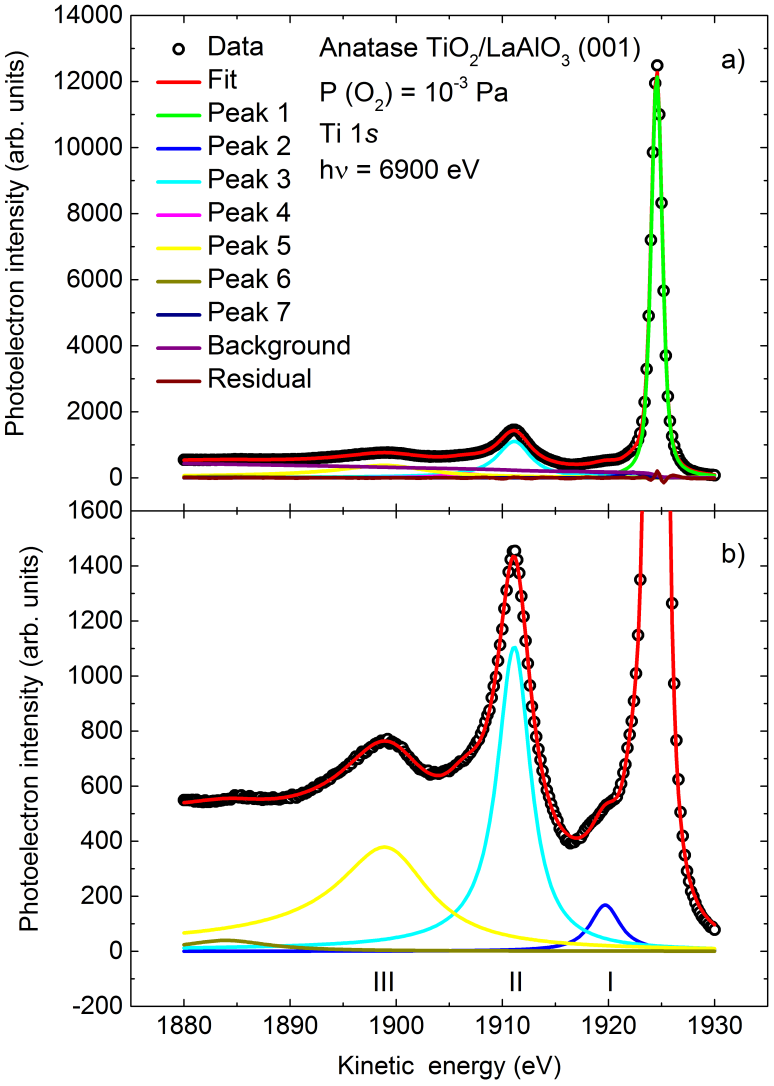


FIGURE 3.23: a) Fitting of the Ti 1*s* lineshape acquired at 6900 eV photon energy from the $P(O_2) = 10^{-3}$ Pa sample. b) Same curve as in panel a) with an expanded y-scale in order to show the small satellite around 5 eV from the main line.

to try to disentangle the various contributions to the lineshapes, we performed a fitting procedure of the spectra, as it is shown in Fig. 3.23 a) for the Ti 1*s* photoline measured from the $P(O_2) = 10^{-3}$ Pa specimen. Since the main line is much more intense than the satellites, in Fig. 3.23 b) we reported the experimental curve and its fit along with the peak associated to the satellites on an expanded y-scale. By looking more closely, we can see that along with the peaks associated to Satellite I, II and III, (Peak 2, 3 and 5, respectively) there is also a small satellite around 1884 eV, about 40 eV from the main line, labelled as Peak 6 in the fitting. The sum of seven peaks and an integral

background has been used to replicate the experimental spectrum; in particular, the peaks associated to the main line (Peak 1 in Fig. 3.23), to Satellite II (Peak 3) and to Satellite III (Peak 5) have an asymmetric line shape. Furthermore, in order to reproduce the low kinetic energy side of the main line and of Satellite II, along with Peak 1 and 3, another component is necessary, Peak 7 and 4, respectively. Since the curves of the

Sample	Respect to main line	Satellite I	Satellite II	Satellite III
$P(O_2) = 10^{-3}$ Pa	Distance (eV)	4.9	13.4	25.1
	Amplitude	0.08	1.07	1.28
$P(O_2) = 10$ Pa	Distance (eV)	4.8	13.4	25.1
	Amplitude	0.11	1.03	1.52

TABLE 3.3: Values of the energy separation and area ratio between the satellites and the main line for both anatase specimens as obtained from the fitting of the Ti 1*s* spectra.

$P(O_2) = 10$ Pa sample are very similar to what reported in Fig. 3.23 for the other specimen, the related picture will not be shown. However, we report in Tab. 3.3 the values of energy distance and the amplitude ratio of Satellite I, II and III with respect to the main line for both samples as obtained from the fitting procedure. We notice immediately that the differences, if any, are very small.

A similar analysis was performed on the Ti 2*p* spectra for both samples and two photon energies (2500 and 6900 eV). In Fig. 3.24 and 3.25, the curves obtained by the fitting procedure are shown for the $P(O_2) = 10^{-3}$ Pa sample, at 6900 and 2500 eV photon energies, respectively.

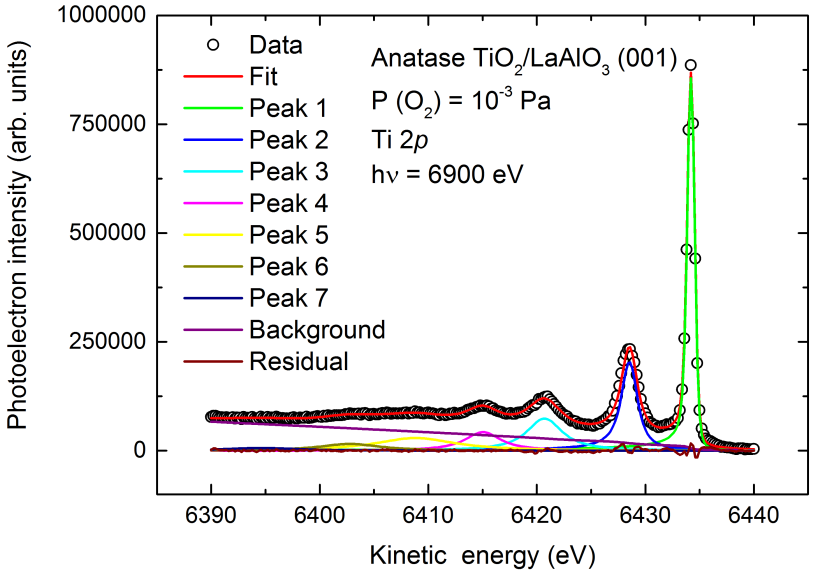


FIGURE 3.24: Fitting of the Ti 2*p* lineshape acquired at 6900 eV photon energy from the $P(O_2) = 10^{-3}$ Pa sample.

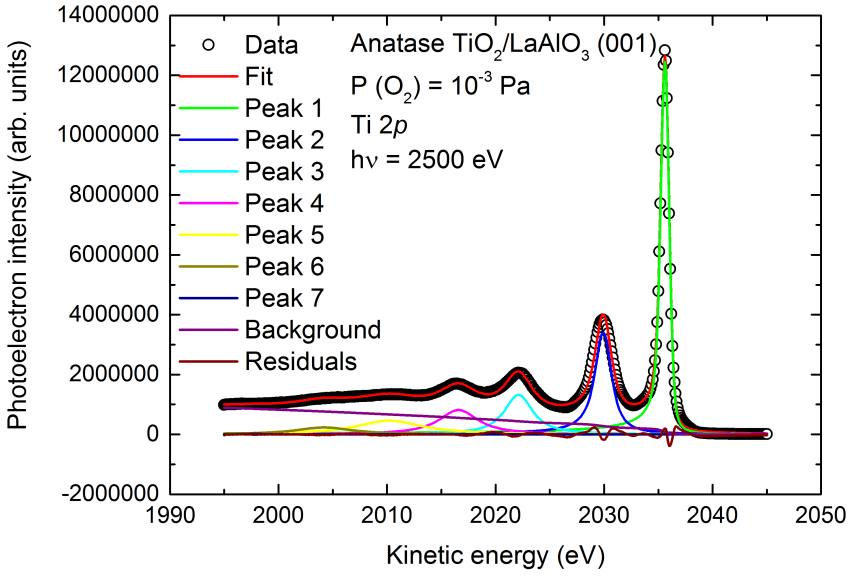


FIGURE 3.25: Fitting of the Ti $2p$ lineshape acquired at 2500 eV photon energy from the $P(O_2) = 10^{-3}$ Pa sample

Finally valence band spectra for the two specimens at the two different photon energies were measured: the data for the $P(O_2) = 10^{-3}$ Pa sample are shown in Fig. 3.26, compared with the molecular-orbital bonding structure for anatase TiO_2 (based on a TiO_6 cluster) [73]. Since no binding energy calibration is available for both energies, the

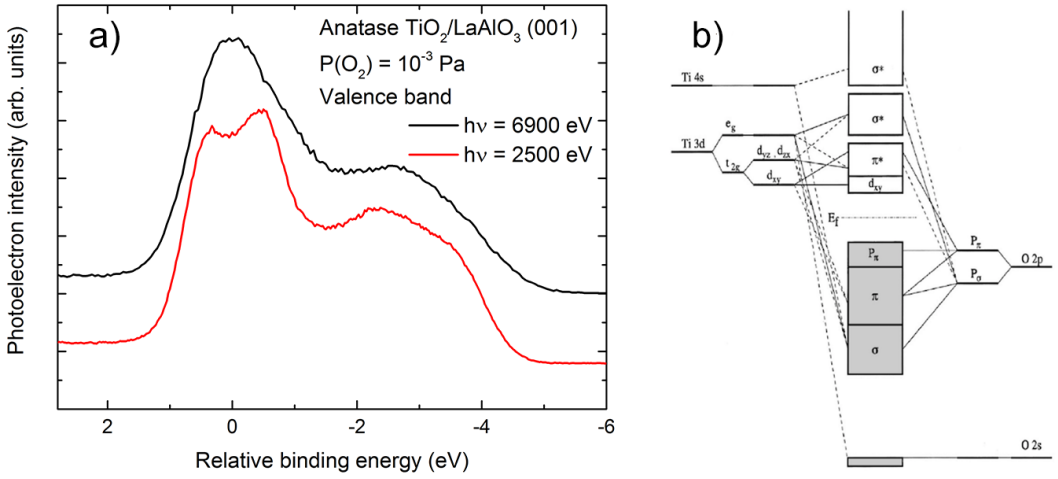


FIGURE 3.26: a) Valence band photoemission spectra of the anatase TiO_2 sample grown with $P(O_2) = 10^{-3}$ Pa at 6900 and 2500 eV photon energy. In this graph the binding energy scale has been aligned to the maximum of the $\hbar\omega = 6900eV$ spectrum. b) Molecular-orbital bonding structure for anatase TiO_2; the dashed and solid lines represent a weak and intense contribution of the orbital to the levels, respectively. Adapted from [73].

spectra have been aligned to the most intense feature of the 6900 eV curve, which means that 0 is not the Fermi level. The valence band of anatase TiO_2 is usually decomposed into three contributions [73], which are represented by the grey rectangles in Fig. 3.26 b):

- in the upper region (i. e., closer to the Fermi level) there are P_π nonbonding states derived from the O $2p$ levels;
- in the middle energy region, π bonding states formed by Ti t_{2g} and O $2p$ levels are found;
- in the lower region, σ bonding states originated from Ti e_g and O $2p_\sigma$ levels are present.

σ and π identify covalent bonds that are formed when atomic orbitals overlap "head-on" and when two lobes on one orbital overlap two lobes of the other orbital, respectively.

The most significant modification of the spectra of Fig. 3.26 a) upon changing the photon energy from 6900 to 2500 eV is the apparent splitting of the feature in the upper region.

Chapter 4

Discussion

The possibility to measure with high resolution core level spectra on strongly correlated $3d$ systems with bulk sensitivity offered by performing HAXPES at undulator based beamlines of third generation synchrotron radiation facilities, has put in evidence the presence of structures which were not seen in spectra acquired at lower photon energies, which have been called extra-peaks. They are a spectral evidence of the strong electron correlation between the $3d$ electrons, which is also the basis of the many macroscopic properties that this class of materials in known to show. Before the advent of HAXPES, these features were known only in the spectra measured at lower photon energies, in strongly correlated systems based on $4d$ and $4f$ elements. For example, in the case of Ce-based compounds, the initial core-hole could be screened in two ways, namely by a delocalised conduction electron or a localised $4f$ electron. These different screening channels would give rise to a poorly and a well screened feature, respectively, the second having a lower binding energy than the first [28]. This phenomenological model was put on a more quantitative ground by Gunnarssonn and Schönhammer, which developed a model based on the single impurity Anderson Hamiltonian [27], which allowed to calculate all the possible configurations of the $4f$ levels in the final state. Despite well established, this model proved to be inadequate to describe the presence of well screened features observed by HAXPES in $3d$ based transition metal compounds, like manganites.

The first interpretation of these "new" well screened features was given by introducing in the Anderson Hamiltonian another term due to the presence of an additional state, usually called coherent state, close to the Fermi level, which opens a new screening channel [6]. A different explanation has been given on the base of a competition between local and nonlocal screening channels, as obtained by using a bigger cluster with respect to the one used in the previous model, involving more than one metallic site [33]. In this case the presence of the extra peak is associated to a nonlocal screening channel, with the charge screening the core hole moving in from another metallic site. The debate is still open as to which approach is more adequate to explain this class of features as well as the question whether it is possible to effectively map these two models one into the other or not. Since then, extra peaks in strongly correlated $3d$ systems such as vanadates, manganites and cuprates have been widely studied, and have been connected to both metallic and ferromagnetic properties. It has been highlighted that these features are

visible for the materials in the metallic phase and are suppressed when the systems enter the insulating phase. This can be expected, since it is known that the character of the valence or conduction electrons is different between a metal and an insulator, which means that also the screening processes will be different. Furthermore, extra-peaks in the core levels of $3d$ based transition metals have not been detected at low excitation energies, which hints to a different screening behaviour of the surface with respect to the bulk. Despite the extensive experimental [7, 52, 104] and theoretical [6, 33] work carried out with HAXPES on strongly correlated $3d$ materials, there are issues which must be addressed. For example, it would be useful to evaluate the critical thickness at which well-screened structures appear in the core-level spectra of different materials. Once such values are known, by tuning the photon energy in such a way to obtain the desired information depth, one could for example use the presence or absence of these features as a benchmark of magnetism and/or metallicity in samples produced for device applications. In this chapter we will make some considerations regarding the experimental results which have been previously presented. In particular we have measured the photon energy dependence of the so-called extra-peak in the Mn $2p$ core level spectrum of two different Mn compounds, namely $Ga_{0.87}Mn_{0.13}As$ and $La_{0.65}Sr_{0.35}MnO_3$. In the case of the latter, three different samples grown on different substrates have been investigated, each with a different lattice mismatch at the interface which propagates to the surface without relaxing. In section 4.1 we will address the characterisation of the surface of $Ga_{1-x}Mn_xAs$, which can be a delicate issue since a chemical etching procedure is performed to remove an oxide layer. In section 4.2, we will examine the photon energy dependence of the low binding energy nonlocal satellite in $Ga_{0.87}Mn_{0.13}As$ and $La_{0.65}Sr_{0.35}MnO_3$ thin films, which highlights a different evolution of the feature as a function of the probing depth for the two materials. Assuming that for both compounds this feature arises from a screening channel which is suppressed in a layer of given thickness close to the surface of the films, it results that the thickness of this layer is larger in the case of the $La_{0.65}Sr_{0.35}MnO_3$ samples. While well-screened peaks have been identified in the $3d$ based materials only with the help of HAXPES, similar structures had already been identified in the core level spectra measured with soft X-rays in another class of systems, namely the $4d$ transition metal compounds, such as RuO_2 [34]. In this case, well screened peaks are the dominant features of Ru $3d$ spectra; by measuring the photon energy dependence of this core level, we have been able to show how the ratio between well screened and unscreened features increases when using higher photon energies, as discussed in 4.2.

A separated section is devoted to the study of Mn $3s$ and valence band spectra (4.3). In particular, we have evaluated how the exchange splitting in the Mn $3s$ spectrum changes as a function of the photon energy, which in turn can be related via an empirical formula to the valence state of the Mn ions [**?**]. We have found out that in both the strain relaxed and compressed samples the valence on the ions increases when passing at lower photon energies, suggesting an increase in the electron population on the atoms. This evidence is supported also by the photon energy dependence of the valence band spectrum, were a significantly large increase of the feature associated to the eg levels close to the Fermi level is registered upon lowering the photon energy.

Another interesting class of satellite peaks which appear in the core level spectra of $3d$ based oxides, even at more conventional photon energies, are the high binding energy charge-transfer satellites, which are related to the screening of the core hole on the metal site by charge moving in from the ligand. In particular, electrons are transferred from the $2p$ ligand levels to the $3d$ metal states, who are responsible for the screening [71]. In this field, one of the most widely studied systems is the rutile TiO_2, whose Ti $2p$ spectrum presents many interesting features. However, the interpretation of such structures is hampered by the presence of the spin-orbit Ti $2p_{1/2}$, which may be superimposed to one of the satellites [81, 82]. The less investigated, but potentially more interesting, due to the enhanced photocatalytic properties, counterpart of rutile TiO_2 is one of its polymorph, anatase TiO_2 [77]. In section 4.4 the high binding energy satellite structure due to charge-transfer observed in the Ti $1s$ and Ti $2p$ photoemission spectra of anatase TiO_2 thin films with different conduction properties will be discussed.

4.1 Surface characterisation

One of the main advantages in performing HAXPES experiment is that true bulk sensitivity can be achieved, which in turn allows to relax the serious constraints on the surface quality which are necessary to obtain reliable information at more conventional lower photon energy ranges. On the other hand, prior to HAXPES measurements the $Ga_{1-x}Mn_xAs$ sample underwent a chemical etching procedure to remove the superficial oxide layer and no further *in-situ* was performed. By measuring at each used photon energy the Ga and As $3d$ core levels which have been shown in Fig. 3.2, we were able to establish that the procedure was successful in getting rid of the surface oxide layer. This can be seen by the lineshapes of Ga and As $3d$, which do not present the high binding energy feature which is associated to the presence of oxidised species [99], even at the most surface sensitive photon energy. Atomic force microscopy (AFM) images have been acquired both on the as-received and etched sample, as shown in Fig. 4.1 on a $10 \times 10\,\mu m^2$ area. The image of the as-received sample (Fig. 4.1 (a)), shows the

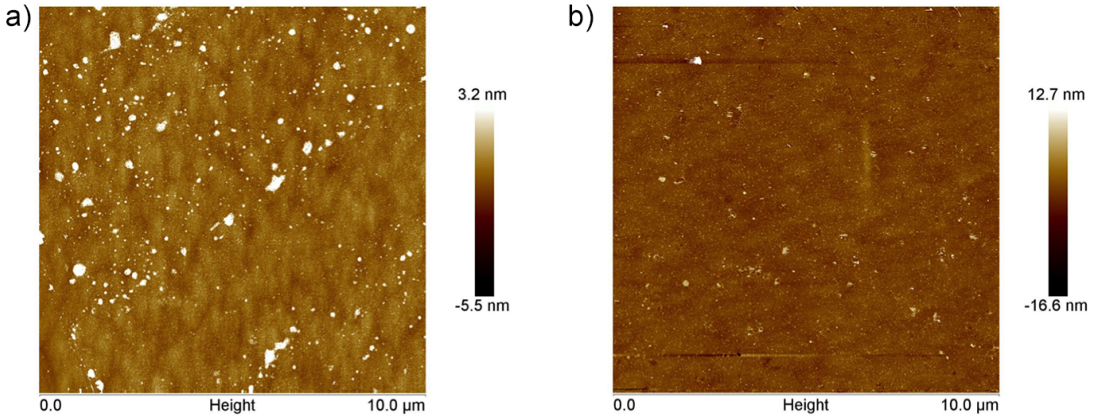


FIGURE 4.1: $10 \times 10\,\mu m^2$ AFM images of the $Ga_{1-x}Mn_xAs$ sample surface of the (a) as-received and (b) etched sample. Figures courtesy of dr. M. Cavallini.

presence of outgrowths (structures with lateral size ranging between 100 and 500 nm and thickness between 3 and 12 nm) on the surface: the value of root mean squared roughness is 1.1 ± 0.2 nm (if the measure is made in the space between the outgrowths, it reduces to 0.4 ± 0.1 nm). After the etching procedure, a reduction of the number of outgrowths can be seen (those remaining have a lateral size ranging between 100 and 200 nm and a thickness between 3 and 10 nm), while the roughness increases, passing to 1.5 ± 0.3 nm (1.2 ± 0.2 nm, if measured between the outgrowths), as it can be seen in Fig. 4.1 (b) [112].

On the other hand, by estimating the area of the Mn $2p$, Ga and As $3d$ core level peaks shown in the previous chapter at each used photon energy and taking into account the photoionisation cross-section for these photolines [109], we made a semiquantitative assessment of the surface composition. The results of such analysis are reported in

$Ga_{1-x}Mn_xAs$	Atomic concentration		
	Ga	Mn	As
Nominal	0.87	0.13	1.00
$\hbar\omega = 800$ eV	0.96	0.04	1.00
$\hbar\omega = 1000$ eV	0.93	0.07	1.00
$\hbar\omega = 2500$ eV	0.90	0.10	1.00
$\hbar\omega = 5940$ eV	0.92	0.08	1.00

$La_{1-x}Sr_xMnO_3$	Atomic concentration			
	La	Sr	Mn	O
Nominal	0.65	0.35	1	3
–	–	–	–	–
$\hbar\omega = 1000$ eV	0.40	0.60	0.09	3.91
$\hbar\omega = 2500$ eV	0.51	0.49	1.06	2.94
$\hbar\omega = 5940$ eV	0.54	0.46	0.55	3.45

TABLE 4.1: Elemental composition of the etched $Ga_{1-x}Mn_xAs$ and the strain relaxed $La_{1-x}Sr_xMnO_3$ samples as a function of the photon energy compared with the nominal stoichiometry.

Tab. 4.1. We can immediately see that at the lowest available photon energy, the concentration of Mn appears to be lower with respect to the bulk, suggesting the presence of a Mn depletion region at the surface. On the other hand the bulk values, i. e. for energies larger than $\hbar\omega = 2500$ eV, are closer to the expected value of substitutional Mn, which is around 7% with a nominal doping of 13% [54].

For $La_{1-x}Sr_xMnO_3$, in Tab. 4.1 we report a similar semiquantitative analysis made for the strain relaxed sample: by using the La $4d$, Sr $3d$, Mn $2p$ and O $1s$ core level peaks, we notice that at the surface the atomic concentration of Mn is quite lower than the nominal value, suggesting also in this case a depletion of Mn in the surface region.

4.2 Well-screened satellites in $3d$ and $4d$ compounds

In section 3.1 and 3.2 we have seen how the Mn $2p$ spectra of $Ga_{0.87}Mn_{0.13}As$ and $La_{0.65}Sr_{0.35}MnO_3$ thin films display a low binding energy satellite structure which has a different evolution as a function of the used photon energy for the two compounds. This is particularly evident for the satellite structure of the Mn $2p_{3/2}$. Incidentally we note that the relative satellite of the Mn $2p_{1/2}$ component is less pronounced, appearing at most as a broad shoulder. In the case of $La_{0.65}Sr_{0.35}MnO_3$, calculations have indeed suggested that the $2p_{1/2}$ satellite should be broader than the $2p_{3/2}$ one, making it more

difficult to discriminate from the $2p_{1/2}$ main peak, which is in turn is quite broad, being the result of the convolution of many multiplet structures [113].

In the case of $Ga_{0.87}Mn_{0.13}As$, a diluted magnetic semiconductor, which is known to exhibit ferromagnetism below $T_C \simeq 180$ K due to net magnetic moment of the unfilled d band of the substitutional Mn ions, the spectrum of the Mn $2p$ core level at room temperature with a photon energy of 5940 eV reveals a very intense extra-peak on the low binding energy side of the Mn $2p_{3/2}$ peak. From the photon energy dependence we have presented in the previous chapter (see Fig. 3.3), we can clearly see how the intensity of this feature changes drastically with respect to the main peak when lowering the photon energy. For example, it is interesting to notice how, despite being only a shoulder, in our data the peak it is still visible at a photon energy as low as 800 eV, while until now reports of photoemission spectroscopy on $Ga_{1-x}Mn_xAs$, and more in general on $3d$ transition metal compounds, have pointed out that such satellites were not visible in the soft X-ray regime. For example in the measurements at ESRF performed by Fujii *et al.*, the spectrum measured at 900 eV photon energy showed a large bump in the region of the Mn $2p_{3/2}$ line, with no evident structures [7] (see also Fig. 1.19). One may be tempted to ascribe these discrepancies to the different energy resolution; however this may not be the case, since the spectrum at $\hbar\omega = 900$ eV in Ref. [7] was measured with an overall energy resolution of 250 meV, which is compatible with what we obtained at the I09 beamline (between 230 and 310 meV over the whole exploited photon energy range). Furthermore, the extra-peak in their HAXPES spectrum is visible already with a resolution of 400 meV. So other explanations must be taken into consideration. One aspect which must be carefully taken into account when measuring core level spectra with soft X-rays is the quality of the surface. For example, it must be recalled that before being inserted inside the load-lock of the I09 experimental chamber, the sample has undergone an etching procedure, in order to remove the surface oxide layer which is formed during the deposition of the film [54]. Our PES measurements of the Ga and As $3d$ lineshapes (see Fig. 3.2), where there is no trace of the peaks associated to the oxide layer [99], suggest that the procedure was successful. Furthermore, AFM images of the sample surface acquired before and after etching, have proved that the procedure reduces the number of outgrowths, while maintaining the surface roughness between $1 - 2$ nm. So our data suggest that with an adequate *ex-situ* surface preparation and a spot size of few tens of microns, the extra-peak of $Ga_{1-x}Mn_xAs$ can be observed also in the soft X-ray regime. An inadequate surface preparation could be responsible for the absence of the extra-peak in the $\hbar\omega = 900$ eV spectra in Ref. [7].

By a comparison with the calculations as in Fig. 3.3 this suggests that a certain degree of hybridisation between the d^n configurations is retained also close to the surface (the information depth of Mn $2p$ photoelectrons for $\hbar\omega = 800$ eV is about 21 Å). However, although the peak is visible at all the used photon energies, it is evident from our spectra that the ratio with respect to the total area of the whole Mn $2p_{3/2}$ changes sensibly. Our hypothesis is that exists a layer with a certain thickness close to the surface, where the nonlocal screening channel associated to the extra-peak is suppressed with respect to the bulk of the film. This should in turn be related to the different degree of localisation of the Mn $3d$ orbitals which are involved in the screening of the core-hole. By acquiring

spectra at different photon energies, i. e. different information depths, it can be expected that the signal coming from the bulk (the extra-peak) will be more attenuated by this layer when the information depth has a similar value to the thickness of such slab. By plotting the value of the ratio of the well-screened peak with respect to the total area of the peak as a function of the mean escape depth of Mn $2p$ photoelectrons and fitting the points with an exponential attenuation law, an estimation of the thickness of the attenuating layer can be obtained.

In order to estimate the contribution of the extra-peak to the total photoemission signal, a fitting procedure of the lineshapes is required: since the extra-peak in the Mn $2p_{1/2}$ component is not very well resolved, we restricted our analysis to the case of the Mn $2p_{3/2}$. Of course the photoline is the result of the superposition of various peaks associated to different oxidation states as shown in Chapter 1 ($\underline{c}^4$, $\underline{c}^5$ and $\underline{c}^6$ are the most important, with the latter associated to the well-screened peak), which in turn are mixed by hybridisation and display a multiplet structure, which in the experimental spectra is not resolved. We started our analysis from the spectrum acquired at 5940 eV which displays the most intense extra-peak which we tried to reproduced such peak with a Voigt profile: we succeeded only by using a Gaussian FWHM which is double (0.52 eV) of what we expected from the estimation of the energy resolution by the Fermi edge fitting. We managed to account for the rest of the lineshape by using five Gaussian lines (see Fig. 3.4). As a first attempt we left the parameters of the peaks free when passing from a photon energy to another as reported in Tab. 4.2. As detailed in Fig. 3.4, Peak 1 represents the extra-peak, while Peak $2-6$ mimic the rest of the Mn $2p_{3/2}$ lineshape. We also performed another attempt and blocked the values of the Gaussian FWHM for the spectra at 2500, 1000 and 800 eV to the values obtained for 5940 eV. Only the Gaussian FHWM of Peak 1 was left free to account for small differences in energy resolution upon changing photon energy. This approach resulted in a different estimation of the integral background parameters (which are fitted as well) at the two lowest photon energies. As a consequence the experimental values of the ratio between area of Peak 1 (satellite) and the total area of the Mn $2p_{3/2}$ peak proved to be different as shown in Fig. 4.2. Since the value of the χ^2 for the case of blocked parameters is more than twice that of the free parameters case, so we decided to stick with the latter. The error bar of the mean escape depth is mostly due to the uncertainty on the values of the inelastic mean free path as calculated with the TPP-2M algorithm [43]. On the other hand, regarding the uncertainty on the value of the ratio of Peak 1 with respect to total area, the main contribution derives from the determination of the background, which can drastically change the estimation of the peak areas at the two lowest photon energies used, as we have shown in Fig. 4.2.

From the fitting procedure we just illustrated we obtained a value of 12 ± 1 Å as estimation of the thickness of a layer where we have assumed that the degree of localisation of the Mn $3d$ orbitals is different with respect to the bulk. As shown in Fig. 4.3, assuming that we are probing in the direction of the z axis, this corresponds to slightly more than two unit cells of $Ga_{1-x}Mn_xAs$, which has a zinc blende structure with a cell parameter of $a = 5.7$ Å [114]. It must be noted that at all the used photon energies the information depth, which is the distance normal from the surface from which the 95% of the

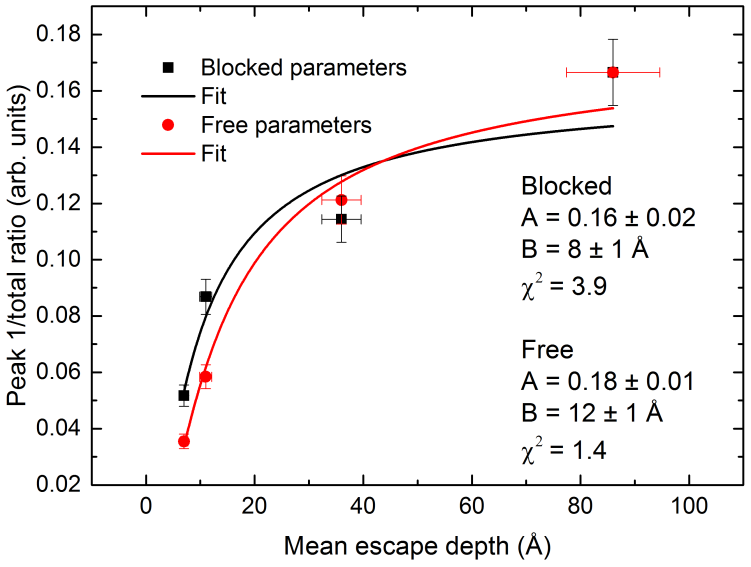


FIGURE 4.2: Comparison of the attenuation of the extra-peak as a function of the photon energy as obtained by two different fitting procedures of the Mn $2p_{3/2}$ spectra from $Ga_{0.87}Mn_{0.13}As$, with blocked (black squares) and free Gaussian FHWM of the five components representing the main peak (see text for details).

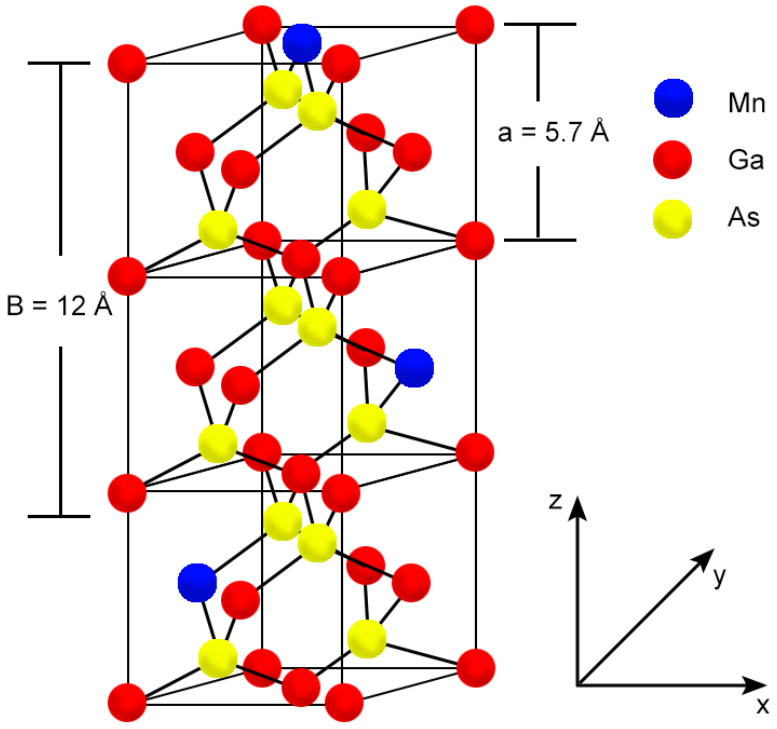


FIGURE 4.3: Crystal structure of $Ga_{0.87}Mn_{0.13}As$ and schematic of the thickness of the attenuating layer. For the sake of simplicity, only substitutional Mn atoms have been considered (it is known the incorporation of interstitial Mn atoms in $Ga_{1-x}Mn_xAs$ thin films).

$Ga_{0.87}Mn_{0.13}As$, Mn $2p_{3/2}$					
Ph. en. (eV)	Peak	Pos. (eV)	Amplitude	Gaus. FWHM (eV)	Lor. FWHM (eV)
800	1	638.99	1.00	0.52	0.20
	2	639.68	2.26	1.42	0
	3	640.60	3.38	1.61	
	4	641.55	7.56	2.55	
	5	643.31	6.38	3.24	
	6	646.28	7.60	4.75	
1000	1.00	638.80	1	0.57	0.15
	2	639.50	1.11	1.604	0
	3	640.36	1.28	1.77	
	4	641.38	1.45	2.59	
	5	643.24	1.63	3.13	
	6	645.89	1.78	4.09	
2500	1	639.10	1.00	0.52	0.27
	2	639.91	2.18	1.53	0
	3	640.44	2.47	1.96	
	4	641.39	4.16	2.59	
	5	643.34	3.79	3.19	
	6	645.84	3.52	4.33	
5940	1	639.13	1.00	0.52	0.25
	2	639.95	0.98	1.32	0
	3	640.64	1.00	1.65	
	4	641.79	1.00	2.39	
	5	643.72	1.01	2.80	
	6	646.00	1.01	3.70	

TABLE 4.2: Fitting parameters of the four Mn $2p_{3/2}$ spectra from $Ga_{0.87}Mn_{0.13}As$. Peak 1 represents the low binding energy satellite feature.

photoemission signal is obtained is always larger than the thickness of the attenuating layer: for example at $\hbar\omega = 800$ eV is around 21 Å and at $\hbar\omega = 5940$ eV is about 260 Å. This means that at all photon energies we can expect to have a contribution to the photoemission signal from the "bulk" of the film where the nonlocal screening channel is present, and this is the reason why also at $\hbar\omega = 800$ eV we can see an extra-peak in the Mn $2p_{3/2}$ spectra. Of course in order to observe an extra-peak with this photon energies an adequate surface preparation is needed, which is our case as we have confirmed by AFM and PES measurements. We can then affirm that in the case of $Ga_{0.87}Mn_{0.13}As$ thin films, the electronic properties are compatible with the one of the bulk when there are at least three unit cells.

We applied a similar approach to the case of the fitting of the Mn $2p_{3/2}$ measured from the $La_{0.65}Sr_{0.35}MnO_3$ spectra in the metallic phase ($T = 200$ K). We can notice by looking at Fig. 4.4 how the extra-peak in these Mn $2p$ spectra seems to have a different dynamics with respect to the case of $Ga_{0.87}Mn_{0.13}As$. In fact while for $Ga_{0.87}Mn_{0.13}As$ we can identify a low binding energy satellite all the used photon energies, for $La_{0.65}Sr_{0.35}MnO_3$ at the lowest used photon energy (1000 eV in this case) we can no longer see the peak. The data presented in Fig. 4.4 are those regarding the strain relaxed sample (grown on a

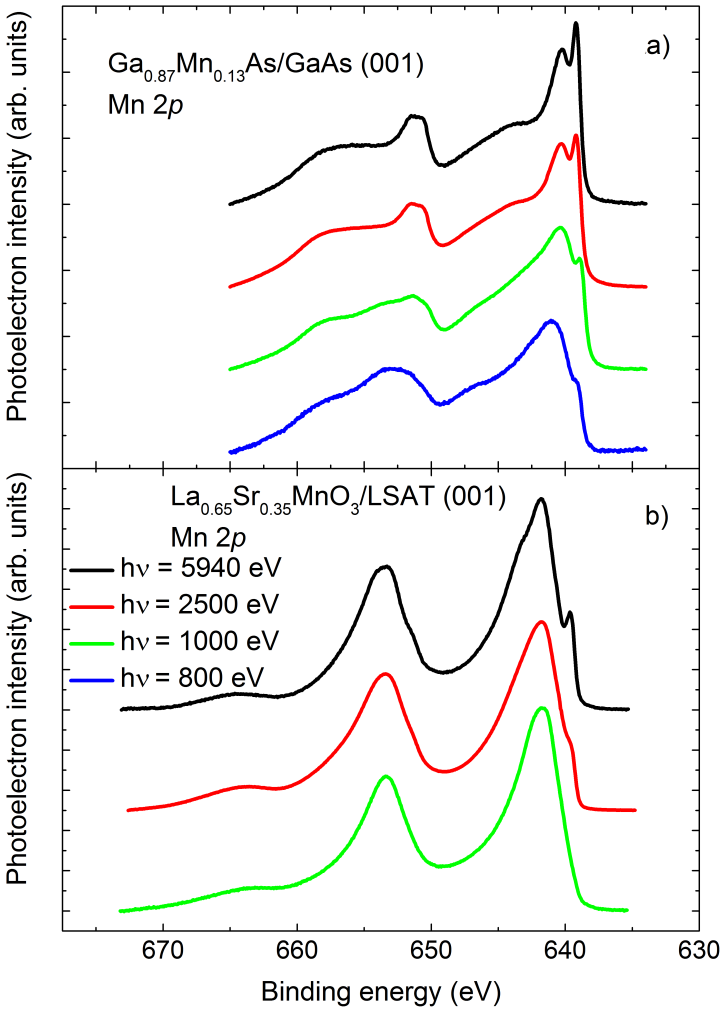


FIGURE 4.4: Comparison of the photon energy dependence of the Mn $2p$ spectrum measured on the a) $Ga_{0.87}Mn_{0.13}As$ and b) $La_{0.65}Sr_{0.35}MnO_3$ strain relaxed sample.

LSAT substrate), but for the strain compressed sample (grown on a SLAO substrate) we have a very similar behaviour. For these samples we have measured the Mn $2p$ spectrum only at three photon energies, because due to the "disappearance" of the well-screened peak it would have been useless to further lower the photon energy. In this case when fitting the lineshapes, other than the evaluation of the integral background, a major source of uncertainty derived from the determination of the area of the satellite peak at 1000 eV, where the feature it is not resolved. As for the case of $Ga_{1-x}Mn_xAs$ sample, the fitting parameters have been left free to move. The parameters obtained from the fitting procedure are shown in Tab. 4.3, 4.4 and 4.5 for the tensile (for which only one photon energy has been measured), relaxed and compressive strained sample, respectively. The values of the area of the extra-peak with respect to the total Mn $2p_{3/2}$ have been plotted with respect to the mean escape depth and fitted with an exponential attenuation curve such as shown in Fig. 4.5 both for the strain relaxed and compressed sample, where

the blue triangle represents the value for the spectrum measured on the tensile strained specimen at $\hbar\omega = 5940$ eV. It turned out that, with a small difference between the two

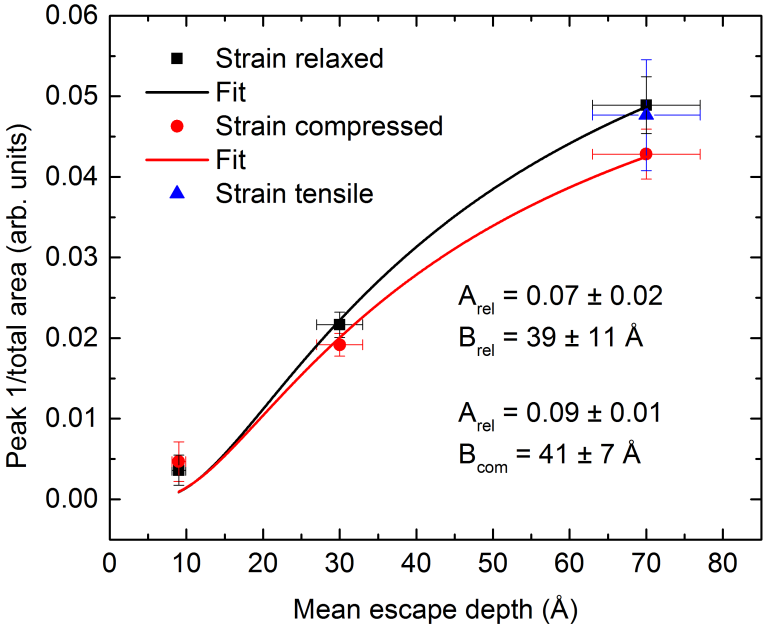


FIGURE 4.5: Attenuation of the extra-peak of the Mn $2p_{3/2}$ line for strain relaxed (black squares) and strain compressed (red circles) $La_{1-x}Sr_xMnO_3$ thin films. For the strain tensile sample, only the value corresponding to an excitation energy of $\hbar\omega = 5940$ eV is shown (blue triangles). The exponential fitting and the resulting parameters for the strain relaxed and strain compressed specimens are also displayed.

samples, the thickness of the attenuating layer results to be around 40 Å, significantly larger than for the $Ga_{0.87}Mn_{0.13}As$ and corresponding to about ten unit cells. This could be due to the presence of the so-called *dead-layer*, a interfacial layer showing insulating and nonmagnetic behaviour at all temperatures without a metal-insulator transition [115, 116]. X-ray magnetic scattering in resonant conditions (XRMS) measurements on $La_{0.67}Sr_{0.33}MnO_3$ thin films on TiO_2-terminated $SrTiO_3$ have revealed the presence of a ~ 17 Å dead layer when measured at a temperature $T = 200$ K [116], which is the same measurement at which our HAXPES measurements have been carried out.

The role of electron correlation in $4d$ oxide rutile RuO_2 was considered negligible and the compounds was defined as a band metal [117]. However, Ru $3d$ spectra, already in the soft X-ray range, show some hints of the strongly correlated character of $4d$ electrons in this compound [33, 34]. As we have shown in Fig. 3.17, Ru $3d$ spectrum shows at least four features, that can be divided into two screened peaks around 281 and 285 eV binding energy and two unscreened peaks around 282 and 287 eV binding energy as in [34]. In this interpretation the screened peaks correspond to a final state where the core hole is screened by quasiparticles at the Fermi surface. On the other hand, another possible explanation is a nonlocal screening mechanism, with electrons coming from a neighbouring metallic site: in this case the feature a 282 eV, which in

$La_{0.65}Sr_{0.35}MnO_3$/STO, Mn $2p_{3/2}$				
Ph. en. (eV)	Peak	Pos. (eV)	Amplitude	Gaus. FWHM (eV)
5940	1	639.71	1	0.62
	2	641.72	4.2	1.41
	3	640.57	3.1	1.62
	4	642.57	4.0	2.02
	5	643.60	6.0	2.64
	6	645.60	2.6	3.14

TABLE 4.3: Fitting parameters for the Mn $2p_{3/2}$ spectrum measured at $T = 200$ K on the $La_{0.65}Sr_{0.35}MnO_3$ tensile strained sample. Peak 1 identifies the well-screened satellite.

$La_{0.65}Sr_{0.35}MnO_3$/LSAT, Mn $2p_{3/2}$				
Ph. en. (eV)	Peak	Pos. (eV)	Amplitude	Gaus. FWHM (eV)
1000	1	639.43	1	0.66
	2	641.37	65	1.50
	3	640.38	53	1.73
	4	642.42	73	1.73
	5	643.77	52	2.21
	6	645.57	32	3.07
2500	1	640.01	1	0.57
	2	641.83	9.3	1.48
	3	640.75	6.1	1.47
	4	642.83	14	1.95
	5	644.21	10	2.31
	6	645.85	6.5	3.08
5940	1	639.58	1	0.63
	2	641.75	4.4	1.48
	3	640.80	4.5	1.95
	4	642.91	4.7	1.85
	5	644.09	4.0	2.36
	6	645.86	1.9	2.81

TABLE 4.4: Fitting parameters for the Mn $2p_{3/2}$ spectra measured at $T = 200$ K on the $La_{0.65}Sr_{0.35}MnO_3$ strain relaxed sample. Peak 1 identifies the well-screened satellite.

the previous case was seen as the unscreened Ru $3d_{5/2}$ would be associated to a final state where the core hole is screened by charge moving from the ligand around the metallic site (local screening). The same holds for the structure around 287 eV, which is then the local screened Ru $3d_{3/2}$ peak [33][1]. The unscreened peaks for both spin-orbit components would be at higher binding energies, not discriminated by the background in the experimental spectrum.

It is interesting to notice that the low binding energy feature of the two spin-orbit components, are the dominant structures of the Ru $3d$ spectra reported in Fig. 3.17

[1]The author of [33] seems to not include spin-orbit splitting in his calculations, he just presents calculated spectra with three components, which we interpret as those of the Ru $3d_{5/2}$.

$La_{0.65}Sr_{0.35}MnO_3$/SLAO, Mn $2p_{3/2}$				
Ph. en. (eV)	Peak	Pos. (eV)	Amplitude	Gaus. FWHM (eV)
1000	1	639.47	1	0.66
	2	641.17	52	1.50
	3	640.24	29	1.73
	4	642.26	61	1.73
	5	643.56	44	2.21
	6	645.28	27	3.07
2500	1	639.65	1	0.57
	2	641.41	13	1.48
	3	640.25	4.5	1.47
	4	642.48	17	1.95
	5	643.82	11	2.31
	6	645.43	6.4	3.08
5940	1	639.42	1.0	0.63
	2	641.40	4.4	1.48
	3	640.60	4.6	1.95
	4	642.43	5.5	1.85
	5	643.67	5.6	2.36
	6	645.52	2.4	2.81

TABLE 4.5: Fitting parameters for the Mn $2p_{3/2}$ spectra measured at $T = 200$ K on the $La_{0.65}Sr_{0.35}MnO_3$ strain compressed sample. Peak 1 identifies the well-screened satellite.

already in the soft X-ray regime. This is different from what observed in $3d$ systems such as $Ga_{1-x}Mn_xAs$ and $La_{1-x}Sr_xMnO_3$, where for excitation energies lower than 1 keV the extra-peak is only a small shoulder or is not visible at all, respectively.

4.3 Depth dependent valence change and metallicity in manganites

In manganites compounds in the metallic phase, the conduction is ascribed to the hopping of electron occupying the e_g level on a Mn 3^+ ion to a similar unoccupied level on a Mn 4^+ ion separated by an oxygen ion (double exchange). The measurements we performed on the valence band for the strain relaxed and compressed sample as illustrated in Fig. 4.6 for the case of the strain relaxed sample, but a similar behaviour can be observed for the compressive strained film, show a feature close to the Fermi level that in the literature is associated to the e_g band. It is interesting to notice how decreasing the photon energy there is an increase in the intensity of this feature, which may suggest a higher occupation of the e_g levels, which in turn could imply a reduction of the hopping probability and hence a reduction of the metallicity. The fact that the electron population on the Mn atoms becomes higher when more surface sensitivity is achieved is suggested also from the Mn $3s$ spectra. This core level in fact, due to a strong superposition with the valence $3d$ orbitals, displays an exchange splitting of few

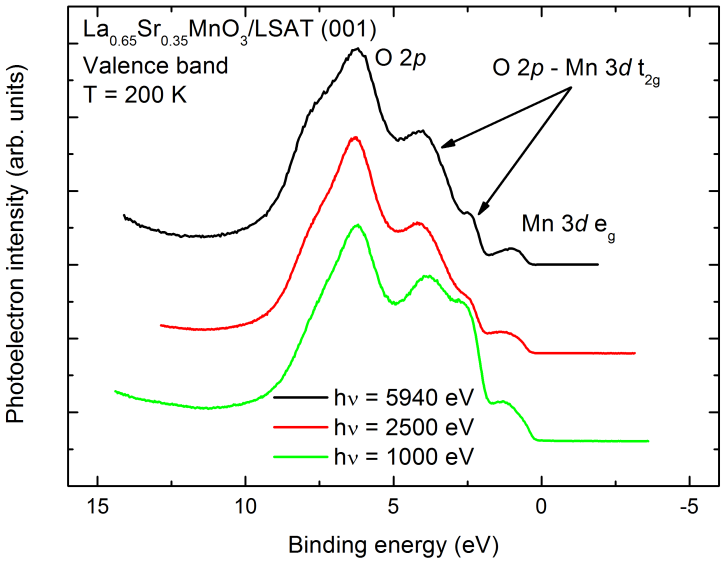


FIGURE 4.6: Photon energy dependence of the valence band of the strain relaxed manganite film.

eV, which can be used to evaluate the oxidation state of the Mn atoms. We measured two photon energies (5940 and 2500 eV) apiece for the strain relaxed and compressed specimen and one (5940 eV) for the tensile strained specimen. From the results of a fitting procedure of these spectra (see Fig. 3.14) we were able to show that the valence of the Mn ions increases when lowering the photon energy for both samples, as reported in Tab. 3.2, which suggests an increase of the electron population on the Mn ions (a higher ion valence implies that the ion is more positively charged). The fitting parameters we obtained for the Mn 3*s* spectra are reported in Tab. 4.6, 4.7 and 4.8 for the tensile strained, strain relaxed and compressive strained samples, respectively; the peaks are those displayed in Fig. 3.14. By looking the Mn 3*s* spectra measured at the

$La_{0.65}Sr_{0.35}MnO_3$/STO, Mn 3*s*					
Ph. en. (eV)	Peak	Pos. (eV)	Amplitude	Gaus. FWHM (eV)	Lor. FWHM (eV)
5940	1	84.34	1.00	1.54	1.21
	2	88.82	1.94		3.60
	3	82.73	0.71		1.09
	4	85.93	0.23		0.71
	5	95.005	0.76		9.26

TABLE 4.6: Fitting parameters for the Mn 3*s* spectrum measured at $T = 200$ K on the $La_{0.65}Sr_{0.35}MnO_3$ tensile strained sample. The energy positions of Peak 1 and Peak 2 have been used to calculate the exchange splitting ΔE_{3s}.

highest used photon energy of 5940 eV (see Fig. 3.12), we can identify as shoulder on the low binding energy side of the high spin component. This feature has already been seen in previous HAXPES measurements [104], also in the case of the Mn 3*p* line, and

$La_{0.65}Sr_{0.35}MnO_3$/LSAT, Mn 3s					
Ph. en. (eV)	Peak	Pos. (eV)	Amplitude	Gaus. FWHM (eV)	Lor. FWHM (eV)
2500	1	84.49	1.00	1.65	1.23
	2	89.25	1.21		2.98
	3	83.08	0.37		0.80
	4	86.18	0.17		0.76
	5	94.29	0.13		4.68
5940	1	84.17	1.00	1.53	1.01
	2	88.60	2.28		3.61
	3	82.59	0.91		1.17
	4	85.66	0.37		0.93
	5	94.67	0.88		10.27

TABLE 4.7: Fitting parameters for the Mn 3s spectrum measured at $T = 200$ K on the $La_{0.65}Sr_{0.35}MnO_3$ strain relaxed sample. The energy positions of Peak 1 and Peak 2 have been used to calculate the exchange splitting ΔE_{3s}.

$La_{0.65}Sr_{0.35}MnO_3$/SLAO, Mn 3s					
Ph. en. (eV)	Peak	Pos. (eV)	Amplitude	Gaus. FWHM (eV)	Lor. FWHM (eV)
2500	1	84.13	1.00	1.65	1.23
	2	88.87	0.80		2.98
	3	82.57	0.22		0.80
	4	85.88	0.14		0.76
	5	93.48	0.08		4.68
5940	1	83.99	1.00	1.54	1.21
	2	88.44	1.83		3.60
	3	82.37	0.63		1.09
	4	85.61	0.23		0.71
	5	94.38	0.51		9.26

TABLE 4.8: Fitting parameters for the Mn 3s spectrum measured at $T = 200$ K on the $La_{0.65}Sr_{0.35}MnO_3$ strain compressed sample. The energy positions of Peak 1 and Peak 2 have been used to calculate the exchange splitting ΔE_{3s}.

has been interpreted as a well screened satellite as in the case of the Mn 2p. The Mn 3s lineshape is more spread out in energy with respect to the 2p as due to multiplet effects and this makes more difficult to resolve the extra-peak. A similar effect has been found in another 3d systems, namely V_2O_3, whose V 2p peak presents a well-resolved low binding energy satellite for both 3/2 and 1/2 spin-orbit component and a similar but less resolved feature can also be seen in the spectra of the shallower core level V 3p [22]. So both in manganites and vadanates, low binding energy satellites in the metal 2p HAXPES spectra have been identified, as well as for less bound core level, where on the other hand they appear less intense and display a different energy distance from the main line. These differences can be induced by the different degree of overlap between the core levels and the valence orbitals involved in the screening of the core hole [45].

The decrease of the Mn ion valence when lowering the photon energy as suggested by the results of the fitting of the Mn 3s spectra, along with the observation of an increase in

the structure associated to photoemission from the e_g band in the valence band spectra, suggest that the relative concentration of Mn^{3+} and Mn^{4+} changes with the probing depth. A lower valence implies that the ions are less positively charged and there are then more electrons on the ions, which can be hosted only in the e_g levels. However, if these states are already filled, it is not possible to fill them with electrons coming from a neighbouring ion, as in the double-exchange mechanism, which is the base of the electrical conduction mechanism in manganites. One could then suggest that the system is less metallic at smaller probing depth, but this is also what one observe with the photon energy dependence of the extra-peak in the Mn $2p_{3/2}$ spectrum, which decreases when the photon energy is decremented.

4.4 Charge-transfer satellites in TiO_2

In section 3.4 we have characterised the core level spectra of two anatase TiO_2 thin films grown with two different oxygen vacancy concentration, which yields different conduction properties. A different oxygen concentration is induced by the growth conditions of the films, in particular by the oxygen pressure in the deposition chamber. TiO_2 core levels, especially the Ti $2p$ have been extensively studied over the years especially for the rutile polymorph, which is the most stable form of titania. However, the interpretation of the Ti $2p$ spectrum can be made difficult by the spin-orbit splitting, which can hide some small feature, such as a 5 eV satellite which should fall directly below the Ti $2p_{1/2}$. Thanks to the high photon energy achievable at the GALAXIES beamline ($\hbar\omega = 6900$ eV) it was also possible to investigate a deeper but simpler core level, namely the Ti $1s$, which however is quite rich in features on the high binding energy side as shown in Fig. 3.21. By looking at the two spectra reported in that picture, it can immediately be noticed, by a comparison with similar data presented on $SrTiO_3$ by Woicick *et al.* [71] (see also section 1.4.4), the intensity of Satellite I with respect to the main line in our data is quite smaller, appearing as a small bump while in the data by Woicick the peak is well defined. $SrTiO_3$ belongs to the class of perovskites and at room temperature exhibits a cubic unit cell with a lattice constant $a = 3.905$ Å [118], which corresponds (in the absence of distortions) to a metal-oxygen distance $d_{Ti-O} = 1.9525$ Å (it is half the lattice constant). On the other hand, in anatase TiO_2 we have that the metal-metal distance is reported to be 5.35 Å [73], which results in $d_{Ti-O} = 2.675$ Å (also in the case of anatase TiO_2 six oxygen ions are octahedrally coordinated to a central Ti ion). So the overlap between orbitals is expected to be smaller in the case of anatase TiO_2, meaning that the transitions between t_{2g} orbitals associated to Satellite I, already not very intense in the case of $SrTiO_3$, will be further suppressed. In Tab. 4.9 and 4.10 we report the parameters of the fitting of the Ti $1s$ lineshape for the $P(O_2) = 10$ Pa and $P(O_2) = 10^{-3}$ Pa sample, respectively, while in Tab. 4.11 and 4.12 are shown the parameters for the fitting of the Ti $2p$ spectra, two photon energies for each specimen. The values reported in the amplitude (area of the peak) column have been normalised to that of the main peak (Peak 1). The fitting of the Ti $1s$ on both samples have been performed by imposing a slight asymmetry on the peaks reproducing Satellite II and III (Peak 3 and Peak 5, respectively). Peak 2 reproduces the small bump close to the main

TiO_2/LAO, $P(O_2) = 10$ Pa, Ti 1s, $\hbar\omega = 6900$ eV					
Peak	Asym.	Pos. (eV)	Amplitude	Gaus. FWHM (eV)	Lor. FWHM (eV)
1	0	1923.83	1.00	0.36	0.34
2		1918.99	0.11		1.93
3	0.04	1910.48	1.03		1.71
4	0	1905.91	0.26		2.64
5	0.14	1898.76	1.52		5.17
6	0	1883.61	0.39		4.85
7		1921.75	0.05		1.06

TABLE 4.9: Fitting parameters for the Ti 1s spectrum measured on the $P(O_2) = 10$ Pa sample at $\hbar\omega = 6900$ eV.

TiO_2/LAO, $P(O_2) = 10^{-3}$ Pa, Ti 1s, $\hbar\omega = 6900$ eV					
Peak	Asym.	Pos. (eV)	Amplitude	Gaus. FWHM (eV)	Lor. FWHM (eV)
1	0	1924.55	1.00	0.36	0.32
2		1919.69	0.11		1.56
3	0.04	1911.17	1.07		1.73
4	0	1906.47	0.19		2.17
5	0.14	1899.48	1.28		4.68
6	0	1883.95	0.26		4.91
7		1922.23	0.03		0.74

TABLE 4.10: Fitting parameters for the Ti 1s spectrum measured on the $P(O_2) = 10^{-3}$ Pa sample at $\hbar\omega = 6900$ eV.

TiO_2/LAO, $P(O_2) = 10$ Pa, Ti 2p					
$\hbar\omega = 2500$ eV					
Peak	Asym.	Pos. (eV)	Amplitude	Gaus. FWHM (eV)	Lor. FWHM (eV)
1	0.07	2035.07	1	0.35	0.09
2	0.07	2029.33	1.04		0.72
3	0	2021.55	1.12		1.51
4		2015.94	1.12		2.06
5		2009.40	1.44		3.86
6		2003.49	0.56		2.91
7		1996.37	0.02		3.80
$\hbar\omega = 6900$ eV					
Peak	Asym.	Pos. (eV)	Amplitude	Gaus. FWHM (eV)	Lor. FWHM (eV)
1	0.06	6433.59	1.00	0.31	0.09
2	0.04	6427.88	1.22		0.73
3	0	6420.12	1.80		1.97
4		6414.30	1.45		2.01
5		6407.61	2.86		4.49
6		6401.34	1.13		4.49
7		6394.20	0.86		3.70

TABLE 4.11: Fitting parameters for the Ti 2p spectrum measured on the $P(O_2) = 10$ Pa sample at 2500 and 6900 eV photon energy.

TiO_2/LAO, $P(O_2) = 10^{-3}$ Pa, Ti $2p$					
$\hbar\omega = 2500$ eV					
Peak	Asym.	Pos. (eV)	Amplitude	Gaus. FWHM (eV)	Lor. FWHM (eV)
1	0.08	2035.65	1.00	0.32	0.13
2	0.04	2029.96	1.00		0.72
3	0	2022.11	1.08		1.47
4		2016.59	1.16		2.10
5		2010.23	1.38		3.69
6		2004.22	0.70		3.14
7		1997.88	0.02		1.01
$\hbar\omega = 6900$ eV					
Peak	Asym.	Pos. (eV)	Amplitude	Gaus. FWHM (eV)	Lor. FWHM (eV)
1	0.06	6434.23	1.00	0.30	0.08
2	0.03	6428.56	1.23		0.70
3	0	6420.71	1.80		1.90
4		6415.03	1.37		1.92
5		6408.84	2.63		4.43
6		6402.76	1.30		3.41
7		6394.66	0.79		4.25

TABLE 4.12: Fitting parameters for the Ti $2p$ spectrum measured on the $P(O_2) = 10^{-3}$ Pa sample at 2500 and 6900 eV photon energy.

peak, at a distance of about 4.8 eV for both samples. In the case of Ti $2p$ spectra for both excitation energies of 6900 and 2500 eV, the 3/2 and 1/2 main peaks are reproduced using asymmetric lineshapes, Peak 1 and 2, respectively. While Satellite II and III are reproduced in the fitting for both spin-orbit components, 3 and 5 for the $2p_{3/2}$ and 4 and 6 for the $2p_{1/2}$, respectively, we were not able to introduce a component to reproduce a satellite between the 3/2 and 1/2 main peaks, (corresponding to Satellite I in the case of the Ti $1s$) as suggested by [81] in the case of rutile TiO_2.

Chapter 5

Perspectives

In the last ten years, HAXPES has been established as a technique of choice for the study of the electronic properties of materials, exploiting the enhancement in probing depth due to the increase in the kinetic energy of the analysed electrons in order to obtain information about the electronic structure of materials with true bulk sensitivity. However, a deeper insight into the physical properties of solid state materials, can be gained only when information about electronic structure is combined with the investigation of elementary processes such as collective excitations. Phenomena like electron-electron interactions, electron-coherent phonon coupling and electron-phonon coupling, take place on the so-called *ultrafast* time scale, usually less than 1 ps [119]. On the other hand

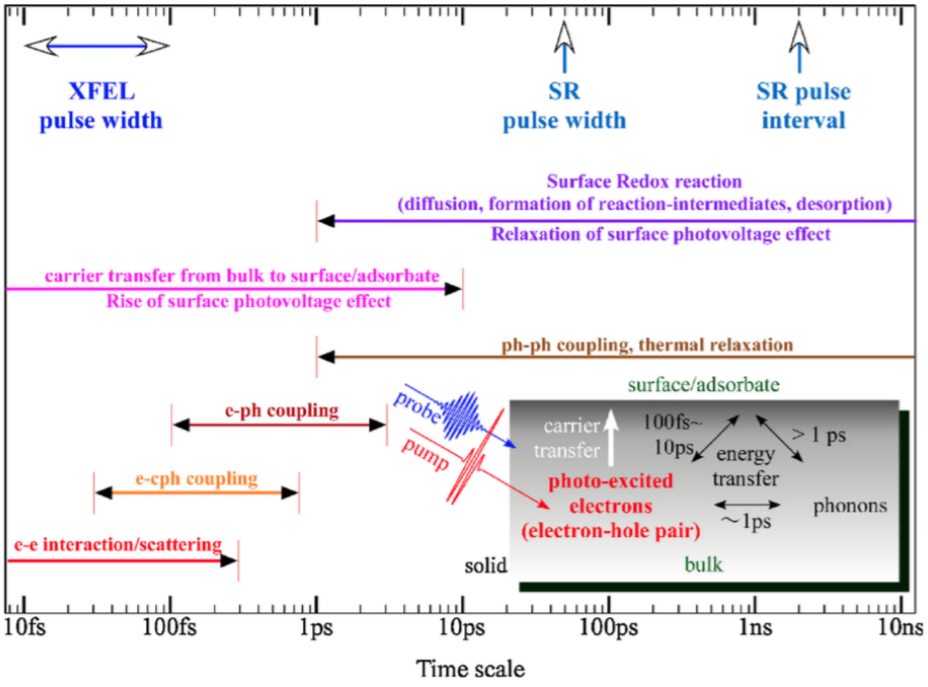


FIGURE 5.1: Time scale of some chemical and physical processes compared with the typical time scales of XFEL and third generation light sources. Adapted from [119].

chemical reactions are the results of various elementary processes that occur over a wide

range of time scales. Indeed while bod-breaking and bond-making take place in the fs regime, there are other aspect such as surface diffusion, formation of reaction intermediates and desorption which take place on time scales longer than ps. In Fig. 5.1 are reported the time scales typical of some physical and chemical processes, compared with the temporal properties of the radiation generated at third generation light sources and at new fourth generation facilities, the so-called X-ray Free Electron Lasers (XFELs). It becomes clear that to investigate thoroughly chemical reaction, time-resolved spectroscopies over a time window spanning from fs to ms are required. Time-resolved photoelectron spectroscopy (tr-PES) has been developing in recent years especially in the soft X-ray regime, thanks to advance in the design and realisation of novel light sources, allowing to study various phenomena, ranging from ultrafast demagnetisation process in magnetic samples [120], ultrafast melting of charge density waves in Mott insulators [8], relaxation of surface photovoltage effect on semiconductor surfaces [121], to the dynamics of surface reactions [122, 123]. These experiments are performed in the so-called pump-and-probe configuration, which is schematically represented in Fig. 5.2 compared with conventional "static" PES: two radiation pulses are used, one at the time $t = 0$ which "pumps" energy into the system (which for example in a metal can allow electronic transition at levels above the Fermi level) and the other at a given delay Δt which probes the properties of the excited material. On the base of these considerations,

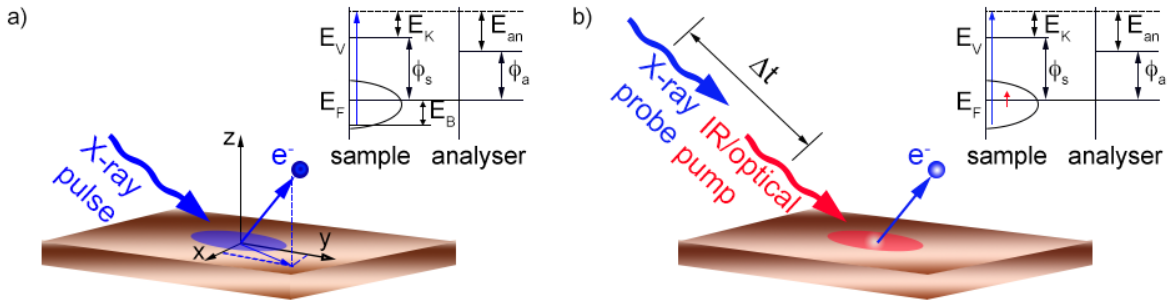


FIGURE 5.2: Schematic representation of a conventional a) and time-resolved b) photoelectron spectroscopy experiment. In the inset the energy level diagram of sample and analyser is shown.

it seems only fit to give some indications on the possible future developments of HAXPES with time resolution, by presenting an example of experiment on one of the same $La_{1-x}Sr_xMnO_3$ thin films which have been previously discussed and by discussing the properties of some instruments for the realisation of dedicated electron energy analysers.

5.1 Time-resolved HAXPES on $La_{1-x}Sr_xMnO_3$

A first example of Tr-HAXPES experiment with synchrotron radiation has been performed at the BL19LXU beamline of the SPring-8 light source (Hyougo, Japan) on one of the $La_{1-x}Sr_xMnO_3$ samples which have been discussed earlier, namely the strain relaxed one (grown on LSAT). We have tried to measure the evolution of the extra-peak in the Mn $2p_{3/2}$ as a function of the delay between pump and probe pulse. The pump

pulse is given by a 1.5 eV laser, with a repetition rate of 1 kHz; on the other hand the X-ray probing pulses have a repetition rate of about 208 kHz, which means that in order to match the lower value of 1 kHz of the pump laser a chopper must be used. In this way, we are selecting only a small part of the available X-ray intensity, which means that when collecting spectra in time-resolved mode, longer counting times with respect to conventional HAXPES are needed. In Fig. 5.3, we show the comparison between the

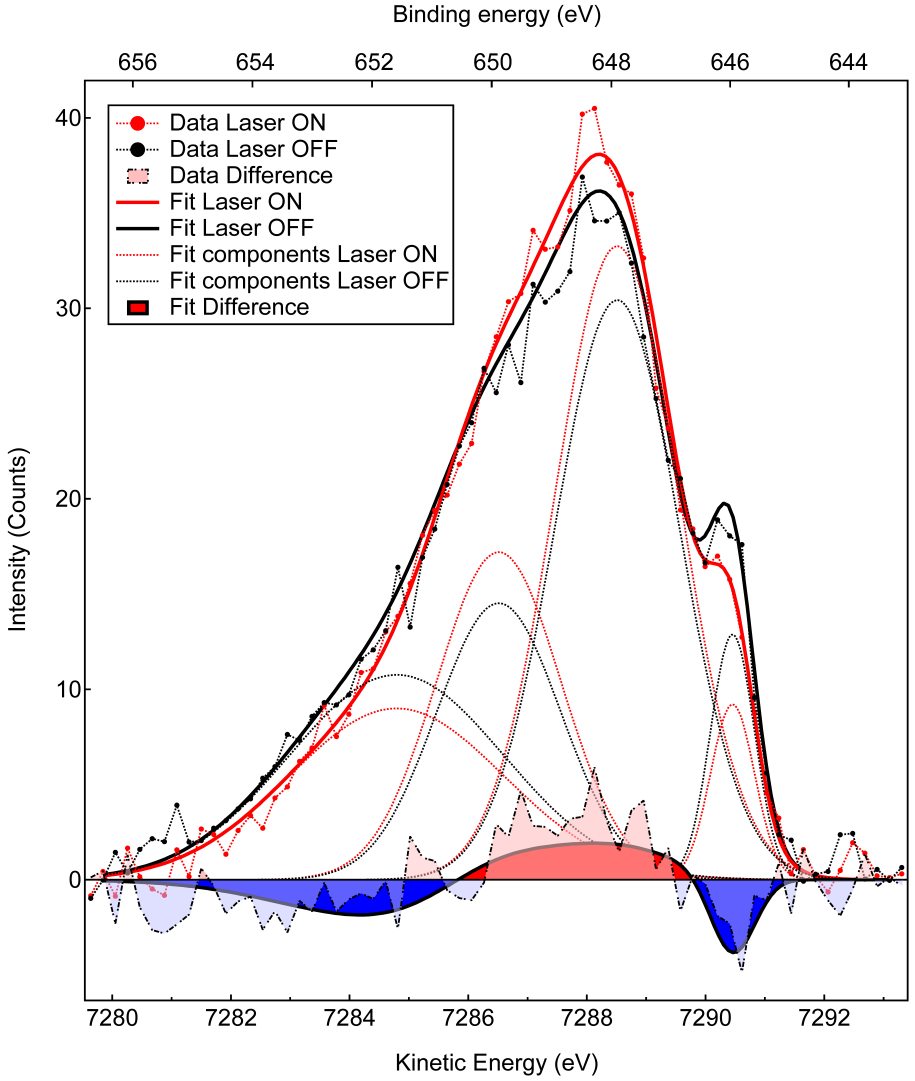


FIGURE 5.3: Comparison of the Mn $2p_{3/2}$ spectra from strain relaxed $La_{0.65}Sr_{0.35}MnO_3$ thin film measured at a 100 ps delay from the pump pulse (red curve) and without laser pumping (black curve). Each experimental spectra, has been reproduced as the sum of four Gaussian profiles. At the bottom the difference between both the experimental and fitting curves is shown.

Mn $2p_{3/2}$ spectrum measured at a delay $\Delta t = 100$ ps between pump and probe (red curve) and the one measured in the absence of the pump pulse (blue curve). The difference between the two spectra is also plotted, showing a spectral weight transfer between the case of "hot" (the pumped one) and "cold" sample. Spectra have been collected at five different delays between pump and probe pulses; for each "pumped" spectrum a corresponding one measured without pump pulse has also been acquired. By fitting these

curves with four Gaussians as shown in Fig. 5.3 and plotting the value of the intensity of the extra-peak (the width of the peak is the same in all the fittings and plotting the intensity is equivalent to plotting the area) as a function of the delay, a curve as the one reported in Fig. 5.4 is obtained. The blue stripe represents the value of the intensity

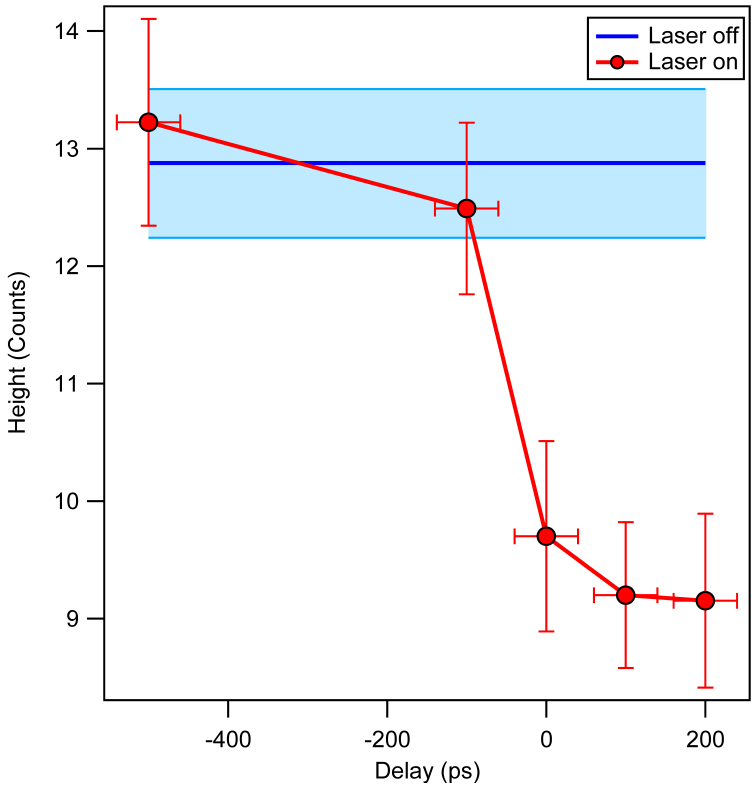


FIGURE 5.4: Intensity of the extra-peak of the Mn $2p_{3/2}$ spectrum from a strain relaxed $La_{0.65}Sr_{0.35}MnO_3$ sample as a function of the delay between pump and probe pulses. The blue stripe indicates the value of the intensity of the extra-peak for the spectra measured without pump.

of the extra-peak for the spectra measured without pumping. The detailed analysis of the lineshapes of the Mn $2p_{3/2}$ is still undergoing and the full comprehension of the behaviour shown in Fig. 5.4 requires sophisticated modelling of the laser/sample interaction, which is outside the scope of this thesis work. These measurements however show that the extra-peak can be used as a fingerprint to follow the dynamics of the system following laser illumination. On the other hand, details regarding the screening process associated to the peak occur faster time scales (fs) and cannot be investigated with time resolved HAXPES using synchrotron radiation, due to the intrinsic time duration of the X-ray pulses, around 40 ps. Such a study could only be undertaken by exploiting the characteristics of the radiation at the new XFEL, which have been discussed earlier in this paragraph.

5.2 TOF spectrometers for time-resolved HAXPES

Tr-PES could receive an additional boost from the advent of XFELs, which can provide pulses in the soft and hard X-ray regime, with a time duration inferior than 1 ps. However, a new effort in the design and realisation of dedicated electron spectrometers in order to take advantage of the properties of these light source is mandatory, exactly how happened in the early 2000's in the case of static HAXPES [41]. The pulsed structure of these light sources is particularly adapted to be used in combination with time-of-flight (TOF) spectrometers, which require a time reference. In this class of analysers the energy selection is performed by measuring the flight time of particles between a sample and a detector, which is a known function of the particle kinetic energy, $t(E)$. The simplest design, a drift tube where electrons fly in a field-free space, is unfortunately not suitable for use at high electron kinetic energies, due to the severe degradation of the energy resolution. In first approximation, the energy resolution ΔE of a TOF spectrometer can be simply written as the product

$$\Delta E = |F(E)|\Delta t, \tag{5.1}$$

where Δt is the overall time resolution (pulse duration, time resolution of the detector, time spread of monochromatic electrons) and $F(E)$ is the so-called *differential energy resolution* of the analyser, defined as $F(E) = (dt/dE)^{-1}$, whose inverse, the *time-energy dispersion*, quantifies the difference in flight time for electron with different kinetic energies. For non-relativistic electrons the kinetic energy is written as $E = mv^2/2$, where m is the electron mass and v its velocity: in the case of a drift tube of length L, v is the ratio between the length of the tube and the time necessary to cover a distance equal to L, which implies $E = m(L/t)^2$. By inverting this relation we can write t as a function of the kinetic energy E and calculate the time-energy dispersion as dt/dE, whose inverse yields the differential energy resolution, which in the case of the drift tube results

$$F(E) = -\left(\frac{8}{m}\right)^{1/2} \frac{E^{3/2}}{L}. \tag{5.2}$$

Since we have seen in Eq. 5.1 that the energy resolution is proportional to the modulus of $F(E)$ and from Eq. 5.2 results that $F(E)$ increases going to higher electron kinetic energies, it is clear that in the HAXPES regime the energy resolution of a drift tube deteriorates with respect to the soft X-ray range. To give some order of magnitude, we consider an overall time resolution $\Delta t = 0.1$ ns and invert Eq. 5.2 to calculate the length necessary to retain an energy resolution of 100 meV with electrons of 10000 eV kinetic energy. The result is $L \simeq 1.2$ km, which does not require further discussion. One thing that must be noted, is that in this simple treatment, we have assumed as overall time resolution a value which is the typical time resolution which can be expected for detectors based on delay anodes. We will call Δt_1 the time resolution of the detector. However, in general the overall time resolution may be limited by another factor, which is the time spread of electrons with the same energy which follow different trajectories inside the drift tube: we will define this value as Δt_2. So in first approximation, the

overall time resolution of a time-of-flight spectrometer should be written as

$$\Delta t = \sqrt{{\Delta t_1}^2 + {\Delta t_2}^2}. \tag{5.3}$$

On the other hand, energy resolution is not the only problem of simple drift tubes: since there is no retarding of the electrons, it is clear that all the particles which are emitted in the acceptance cone of a drift tube are able to reach the detector: this may result in saturation problems at high intensity light sources such as XFELs.

In this chapter we want to present two alternative approaches of a TOF spectrometer suitable for core levels HAXPES experiments at pulsed X-ray sources, based on the two designs:

- a retarding cylindrical lens;
- a spherical mirror.

In both systems, voltages are applied to create a retarding field in the path of electrons, which helps in improving the energy resolution; on the other hand, the chromaticity in the case of the lens and the dispersive power in the case of the spherical mirror, allow to select only a part of the kinetic energy spectrum (i. e., a defined window of flight times). Both spectrometers are optimised in such a way to be compatible with the time structure of a source such as the European X-Ray Free Electron Laser (EXFEL), which is currently under construction in Hamburg. It is expected to deliver 27000 pulses/s with a duration of 2 - 100 fs also in the hard X-ray photon energy range [124]. Due to the particular time structure of the electron bunches in the linear accelerator of EXFEL, shown in Fig. 5.5, although there 27000 pulses/s, it does not mean that there is a pulse each 1/27000 s. Indeed, in a second 10 bunch trains are produced, each with a

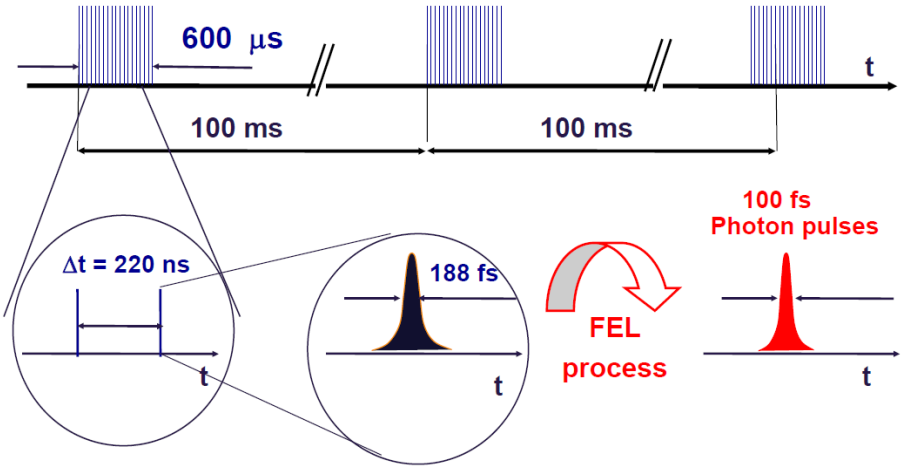


FIGURE 5.5: Projected time structure of the electron bunches and radiation pulses at the EXFEL. Adapted from [125].

duration of 600 µs and containing 2700 electron bunches. In each of this bunch trains,

the separation between bunches is around 220 ns, which corresponds to a repetition rate of 4.5 MHz.

Both spectrometers have been characterised by means of electron trajectory simulations using the SIMION® software package: given a certain electrode configuration, on the basis of the applied potentials the program calculates the electric field in the space. At this point it is possible to "fly" beams of charged particles with the possibility to control the initial configuration (kinetic energy, take-off angle, extension of the source...).

5.2.1 Linear time-of-flight spectrometer

The first system we propose is based on a cylindrical retarding electron lens shown in Fig. 5.6: it is composed by six electrodes with a total length of 100 cm and a inner diameter of 10 cm. By properly biasing the electrodes, it is possible to make the transit

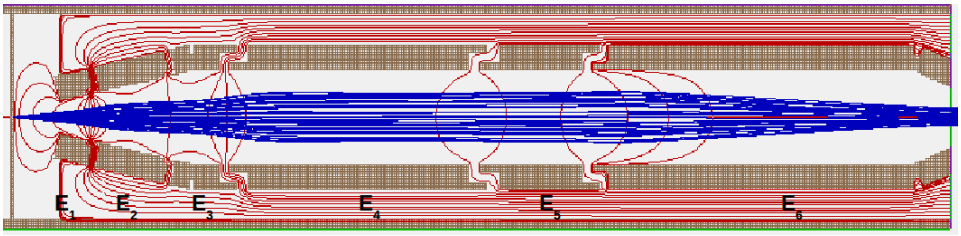


FIGURE 5.6: Schematic cross-section of the cylindrical retarding lens showing electron trajectories and potential contour lines. The six electrodes are labelled as E_1, E_2, ..., E_6. Figure courtesy of dr. G. Greco.

time of electrons much longer with respect to the case of a drift tube with the same length. Of course this implies retarding electron to lower kinetic energies, but due to the chromaticity of the lens, it means that only a set of kinetic energies could be acquired in parallel. In order to acquire a wider kinetic energy range it will be necessary to scan the potential of the electrodes, as it is done in conventional hemispherical electron energy analysers.

We have studied this system for electrons with kinetic energy around 10000 eV. At first we have chosen a point-like source and evaluated the best potential configuration by measuring at each iteration the transmission curve as a function of the kinetic energy for the accepted angle of ~ 50 msr. We have selected the set of potentials which allowed us to retain a transmission of 100% in the widest possible kinetic energy range, which resulted to be as wide as ~ 110 eV. The values of the potentials for the six electrodes are reported in Tab. 5.1. At this point we have tried to evaluate the properties of

Electrode	E_1	E_2	E_3	E_4	E_5	E_6
Potential (kV)	0.0	-7.3	-5.0	-9.0	-9.5	-9.9

TABLE 5.1: Values of the optimised potentials of the six electrodes of the cylindrical lens for analysing electron kinetic energies around 10000 eV.

the spectrometer with initial conditions as close as possible to a real photoelectron spectroscopy experiment at a source like EXFEL. We have chosen a disk source of 0.5 mm radius (to simulate a beam with finite spot size), from which 50000 electrons are emitted in a cone of aperture $\pm 7^\circ$ (corresponds to a solid angle of ~ 50 msr) with the axis around the normal to the disk. The starting position on the disk and the emission angles of each of the 50000 electrons are randomly chosen. The 50000 value was selected because it was the highest number which allowed to provide a statistically significant result while maintaining a reasonable computation time. On the other hand, the source size was chosen higher than what expected for the EXFEL (radius between 15 and 30 µm), because it is known that by increasing the spot size is possible to reduce the energy broadening of features in photoemission spectra due to space-charge effects, which can be a serious issue at high intensity light sources [126, 127]. In Fig. 5.7 a) we show

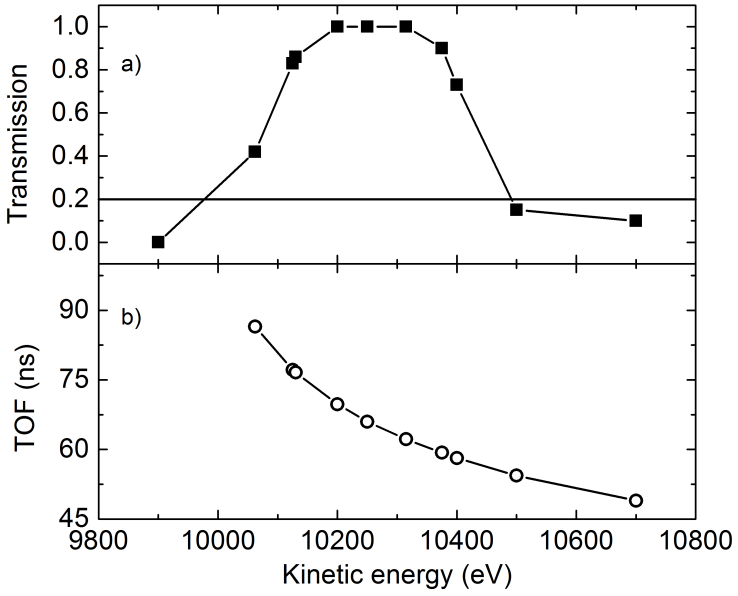


FIGURE 5.7: a) Transmission curve and b) average time-of-flight as a function of the electron kinetic energy for the cylindrical lens. The horizontal black line in panel a) represent the 20% threshold below which we arbitrary assume that the signal cannot be distinguished from the instrumental noise. The solid lines between the points are just a guide for the eye. Adapted from [128].

the transmission curve of the cylindrical lens as a function of the electron kinetic energy: the most prominent feature is the plateau of constant 100% transmission of ~ 110 eV around a central energy of about 10260 eV. In Fig. 5.7 b) we report the dependence of the transit time of electrons from the source to a 25 mm radius detector: it must be noticed that the value reported in this curve are average value over all the electrons which have reached the detector. In principle electrons with the same energy which have followed different trajectories will have a different time-of-flight. We arbitrary define as *effective kinetic energy band-pass*, the energy interval for which a transmission above 20% is retained (represented by the black horizontal line in Fig. 5.7 a)): the energy range for which this is verified corresponds to a time-of-flight range of about 30 ns. We will use only this range for calculating from the time-of-flight curve $t(E)$ the differential

energy resolution $F(E)$ by numerically evaluating the first derivative of $t(E)$ and taking the inverse. From the product between $F(E)$ and the time resolution Δt (see Eq. 5.2) one can then obtain the energy resolution and so the resolving power $E/\Delta E$, which is reported in Fig. 5.8 as a function of the initial kinetic energy of the detected electrons. The difference between the curves in the graph must be ascribed to the value of overall

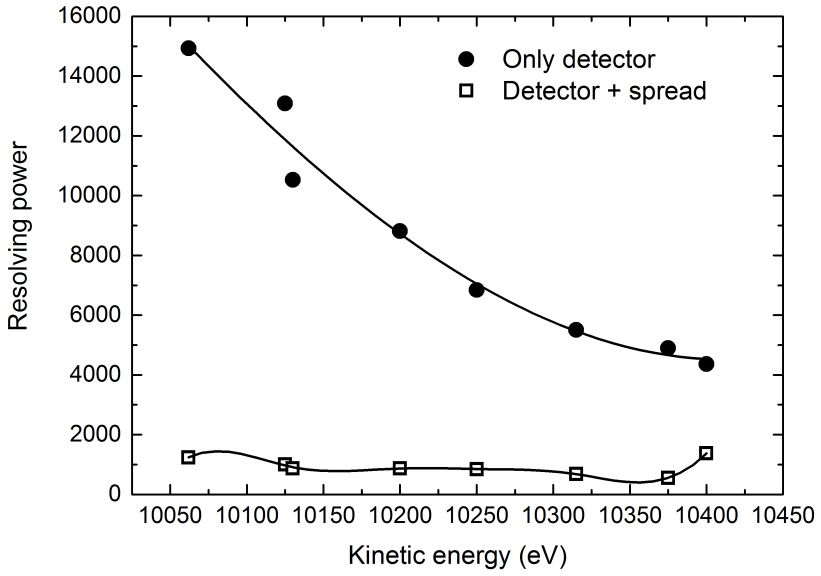


FIGURE 5.8: Values of resolving power of the cylindrical lens as a function of the electron initial kinetic energy in the case of overall time resolution equal to the detector time resolution (filled circles) and when considering also the time spread of monochromatic electrons following different trajectories (open squares).

time resolution Δt which has been considered:

- for the filled circles in Fig. 5.8 (*Only detector*), we have taken $\Delta t = \Delta t_1 = 0.1$ ns, considering then only the time resolution of the detector (Δt_1);
- for the open squares in Fig. 5.8 (*Detector + spread*), $\Delta t = \sqrt{{\Delta t_1}^2 + {\Delta t_2}^2}$, also the contribution of the time spread for monochromatic electrons (Δt_2) has been taken into account.

When considering only the time resolution of the detector, we see that the resolving power monotonically decrease at higher kinetic energy, due to the fact that the time-of-flight of the photoelectrons increases as a function of the electron kinetic energy. At 10250 eV, which is an energy in the center of the transmission plateau, the resolving power has a value of ~ 6800. Since $\Delta t_2 > \Delta t_1$ for all the considered initial electron kinetic energy, it is more correct to take also Δt_2 into account when evaluating the resolving power of the instrument. Δt_2 is calculated as the standard deviation of the time-of-flight distribution of electrons with the same energy which have reached the detector. We notice that in this case the resolving power shows practically no dependence

from the kinetic energy, although the value is quite less than the previous case: at 10250 eV we retain [inserire valore]. However, if one could use a position sensitive detectors, with a suitable matrix correlating time-of-flight and impact position to the trajectory of electrons with given kinetic energy and emission angle it should be possible to calculate a correction on the time-of-flight and reduce Δt_2 to a value comparable or inferior to Δt_1.

We now briefly recap the main results obtained for the cylindrical lens and kinetic energies around 10000 eV:

- accepted solid angle of ~ 50 msr;
- plateau of 100% transmission in a range of ~ 110 eV around a ~ 10260 eV central energy;
- 30 ns time interval of the electron bunch with a transmission $> 20\%$;
- resolving power of ~ 6800 at kinetic energy of 10250 eV in the best case scenario where the overall time resolution is equal to the detector time resolution.

With a plateau of accepted kinetic energy of more than 100 eV it is possible to acquire in parallel with constant transmission the full lineshape of core level spectra, without having to scan the potentials of the electrodes. 30 ns can be interpreted as the duration of the electron bunch which is produced by a single XFEL photon pulse: this value makes the analyser suitable for measurement at EXFEL where the time separation between two consecutive X-ray pulses is expected to be ~ 220 ns. On the other hand, a resolving power of 6800 at a kinetic energy of 10250 eV corresponds to a energy resolution of about 1.5 eV, which is about one order of magnitude worse than what can be achieved nowadays at synchrotron based HAXPES beamlines.

5.2.2 Spherical reflector based time-of-flight spectrometer

Although very attractive due to mechanical simplicity with respect to other spectrometer designs, we have seen that a cylindrical lens such as the one we have presented in the previous section offers a poor energy resolution. We now present a different type of TOF analyser which exploits the capability of a spherical electron mirror to separate the trajectories for electrons with different kinetic energy. One of the most interesting properties of a spherical geometry is that it allows the analytical calculations of the electron trajectories [129, 130]. It is formed by two concentric spherical segments, the inner one with radius R_1 and the outer with radius R_2 between which a potential difference $-U_r$ is applied ($U_r > 0$, it is also called the *retarding potential*) and a series of guard rings set to a certain tension as shown in Fig. 5.9. The outer hemispheres R_2 has a radius of 2000 mm and the ratio between the radii of outer and inner electrode is $R_2/R_1 = 20$: as we will be showing briefly, the size of the spectrometer is directly related to the achievable energy resolution in a given range of electron kinetic energies, so we chose this dimensions in order to retain an energy resolution around 100 meV for

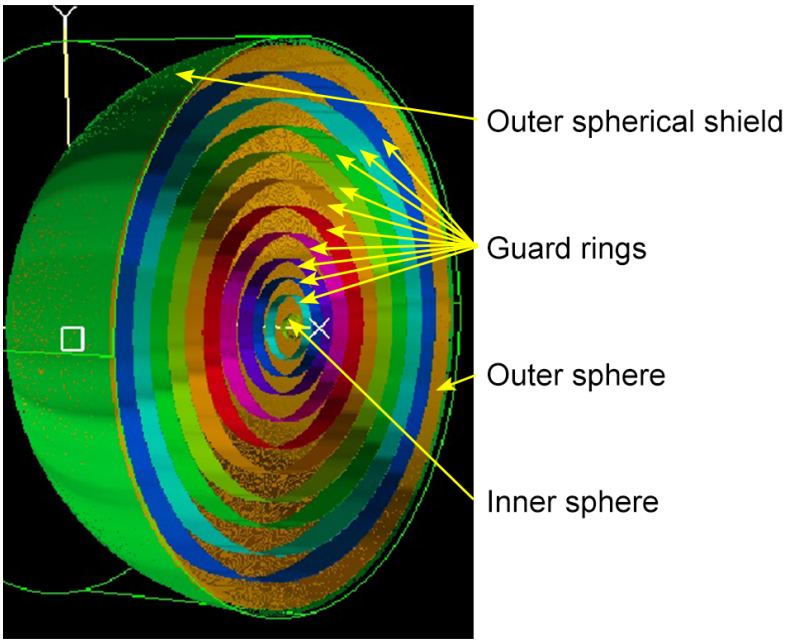


FIGURE 5.9: 3D view of the spherical mirror showing the main features of the spectrometer: the outer and inner hemispheres, the guard rings and the external hemispherical shield.

electron kinetic energies around 5000 eV (a resolving power of 50000). Thanks to the presence of the rings, in the space between the two hemispheres it can be established an electric central field equivalent to that induced between two concentric whole spheres of equal dimensions. Meanwhile the volume delimited by the inner surface of the inner electrode is field-free; in fact, although it cannot be seen from the picture, the inner sphere is a grid (i. e., it allows particles to pass through it), which for a sake of simplicity is considered to have 100% transmission for all electron kinetic energies. It must be noticed that the complete spectrometer includes also a hemispherical shield (grounded) and a planar shield in front, which in the picture has been removed in order to show the elements within, as well as a detector with a pupil in front of it (not shown in Fig. 5.9). The shields are used to limit stray fields which could affect the electron trajectories, while the pupil is used to reduce the transmitted band-pass, as we will be discussing later.

It can be shown that in order to retain a good energy resolution at high kinetic energies (around 5 keV), it is necessary to have both a large outer electrode and radii ratio as it can be seen in Fig. 5.10, where the calculated values of differential energy resolution (left axis) and energy resolution (right axis) for a value of retarding potential $U_r = 5037$ V are shown as a function of the radius of the outer sphere for different ratios between the radii of the two concentric electrodes. The values are calculated for a point-like source and a single trajectory with a starting angle for which the trajectory results to be symmetric with respect to the axis of the analyser. The energy resolution ΔE is calculated considering only the detector time resolution. The value of the potential has been chosen following theoretical considerations by Artamonov *et al.*, which showed that for a spectrometer with large radii ratio, the energy resolution can be optimised by

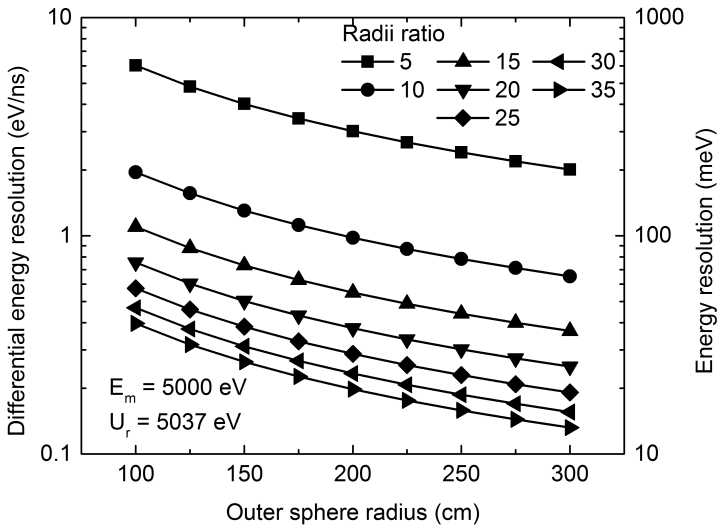


FIGURE 5.10: Values of differential energy resolution (F, left axis) and energy resolution (ΔE, right axis) as a function of the outer electrode radius for different values of the ratio between the radii of the hemispheres. Adapted from [128].

choosing as ratio between the central transmitted energy and the retarding potential, a value $m = 0.943$. From the calculations reported in Fig. 5.10 we understood that in order to retain an energy resolution around 100 meV, it was necessary to have a large outer electrode and a large radii ratio.

The choice of the shape and size of the pupil proved to be a very delicate issue, since it plays a fundamental role in determining the energy band-pass of the spectrometer. As we have seen in the previous section, a given energy window corresponds to a certain time-of-flight range, which must be shorter than the separation between two consecutive EXFEL photon pulses ($\sim$ 220 ns) to perform measurements in a pulse-by-pulse fashion. To achieve this goal, we had to fine tune the characteristics of the pupil, until a configuration was found with a rectangular 3.20×0.86 mm^2 for a 0.5 mm source radius and an accepted solid angle of ~ 4 msr, which allowed to retain a time range of about 200 ns for electron with a transmission $> 20\%$. The choice of such a small solid angle was once again dictated by the constraints on the accepted time-of-flight range: with a larger accepted solid angle a larger range of electron time-of-flight would be transmitted, because the beam waists would become so large that at different energies they would be practically superimposed, making the pupil ineffective. Although such as a reduction of the accepted solid angle from a certain point of view is a limitation, it can however help in some measure to reduce space-charge effects [127]. In Fig. 5.11, the trajectories of 1000 monochromatic 5020 eV electrons are shown in the azimuthal plane of the spectrometer, with a zoom of the region of the detector and the pupil. The electrons start from a source which is located at a distance $R_1/2$ from the centre of the hemispheres and travel freely until they cross the surface of the inner hemisphere. Once inside the volume between the two electrodes, the particles experience the central field and are reflected back until they

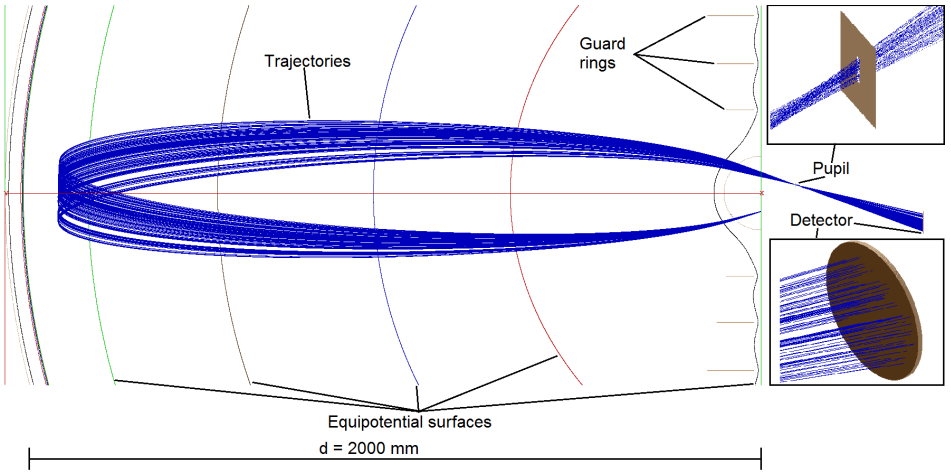


FIGURE 5.11: Cross section of the spherical mirror showing trajectories for 5020 eV kinetic energy electrons and a zoom of the region of the pupil and detector.

pass again through the inner electrode. At this point they propagate freely until impact on the detector or are intercepted by the pupil. The pupil is placed in proximity of what is called the *waist* of the electron beam: in general the pupil is effective because the position of the beam waist changes depending on the energy of the electron beam. Fig.

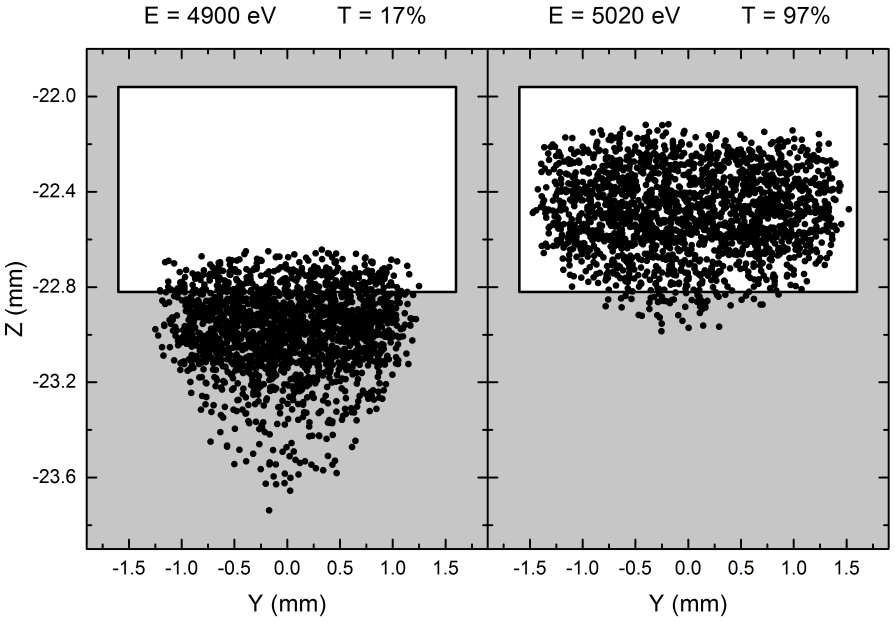


FIGURE 5.12: Position of 1000 electrons at the pupil plane at 4900 (left panel) and 5020 eV (right panel) kinetic energy: the value of the transmission is also indicated. Y and Z are the axes in the SIMION® workbench. Adapted from [128].

5.12 shows the position of 1000 electrons (black fots) on the pupil plane (the pupil is the white rectangle) at 4900 and 5020 eV kinetic energy for a 3.20×0.86 mm^2 rectangular pupil. At 5020 eV, most of the electrons (97%) are transmitted through the aperture;

at 4900 eV, the position of the beam waist moves to more negative z values and only a fraction of the electrons ($1sim17\%$) pass through the pupil. The transmission and

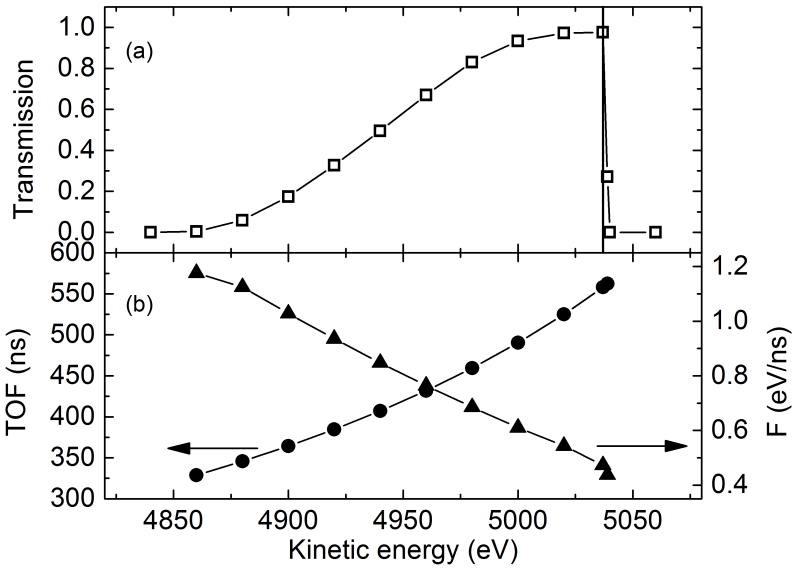


FIGURE 5.13: a) Transmission and b) average time-of-flight (left axis) and differential energy resolution (right axis) as a function of the electron kinetic energy for the spherical mirror in the case of a 0.5 mm radius source and 4 msr accepted solid angle.

the average time-of-flight curve for electrons flying in a spherical mirror from a 0.5 mm radius source in a 4 msr solid angle are shown in Fig. 5.13 a) and b), respectively. Their shapes are quite different from what we have seen in Fig. 5.7 a) and b) in the case of the cylindrical lens. In particular, the transmission curve presents a very sharp fall on the high kinetic energy side: this is due to the fact that when the energy is higher than a certain threshold value, the electrons are not reflected back before they hit the inner surface of the outer electrode. In Fig. 5.13, along with time-of-flight curve (circles, left axis), it is shown the differential energy resolution $F(E)$ (triangles, right axis). We see that the time-of-flight *increases* when the electron kinetic energy is higher: this is due to the fact that electrons with higher kinetic energy will penetrate more in the retarding field region, so that the time necessary to reflect them back will be longer. By using the values of $F(E)$ obtained from the derivative of the time-of-flight we can evaluate the energy resolution, again in the two cases where only the time resolution of the detector ($\Delta t_1 = 0.1$ ns) is considered and when also the time spread (Δt_2) of monochromatic electrons is accounted for. From our calculations it turns out that we have a resolution of ~ 70 and ~ 200 meV at a 4980 eV kinetic energy in the first and second case, respectively.

The results obtained from the simulation of electrons with kinetic energies around 5000 eV flying in a spherical mirror with inner sphere radius $R_1 = 10$ cm and radii ratio $R_2/R_1 = 20$ are hereby reported:

- accepted solid angle of ~ 4 msr;

- $> 90\%$ transmission in a range of ~ 40 eV around a ~ 5020 eV central energy;
- 200 ns time interval of the electron bunch with a transmission $> 20\%$;
- resolving power of ~ 71000 at kinetic energy of 4980 eV in the best case scenario where the overall time resolution is equal to the detector time resolution.

In the 40 eV plateau the transmission value changes from $\sim 98\%$ to $\sim 93\%$ (from the high to the low kinetic energy side): the analyser can then be exploited to acquire in parallel core level spectra from most elements, without modifying the applied potential between the hemispheres. By properly tuning the characteristics of the pupil, the energy range of electrons with a transmission higher than 20% corresponds to a time-of-flight interval of ~ 200 ns, which is less than the separation between photon pulses at EXFEL. A resolving power of 71000 at 4980 eV kinetic energy, corresponds to a energy resolution of ~ 70 meV: for comparison, the Scienta EW4000 hemispherical analyser used at the GALAXIES beamline of the SOLEIL synchrotron, which is dedicated to HAXPES, offers a theoretical resolution of 75 meV with 100 eV pass energy and a circular slit with diameter 0.3 mm [87].

5.2.3 Comparison

We now briefly compare the characteristics which have been obtained from the SIMION® simulations of two different TOF spectrometers, one based on a cylindrical lens and the other on a spherical mirror.

Starting from the transmission properties, the cylindrical lens offers a larger accepted solid angle of ~ 50 msr with respect to the ~ 4 msr of a spherical mirror. In order to increase this value for the latter, one could try to reduce the size of the analysers, which of course will cause the energy resolution to degrade. In both cases these values are small with respect to the maximum of ~ 308 msr which is the number quoted for a commercial system like the ArTOF, however for a maximum electron kinetic energy of 1 keV [131]. However, this may prove not to be a limitation, since it has been reported that a small accepted solid angle may help in reducing the energy spread due to space-charge effect [127]. From the transmission curves 5.7 a) and 5.13 a), it can be seen that while for the cylindrical lens there is a plateau of 100% transmission which extend for 110 eV, for the spherical mirror there is a 40 eV interval where the transmission varies from $\sim 98\%$ to $\sim 93\%$. In both cases, these characteristics make the spectrometers compatible with the measurement in parallel of core level spectra from most elements. However, the spherical reflector appears to be more efficient in suppressing undesired kinetic energies, especially on the high energy side, where it exhibits a sharp cut-off.

If we calculate the resolving power for the two analysers taking into consideration only the time resolution of the detector ($\Delta t_1 = 0.1$ ns) we obtain a resolving power of 6800 and 71000 at the central transmitted energy for the cylindrical lens and the spherical mirror, respectively. This can be a realistic case only if the analysers are used in combination with a position sensitive detector, because then it would be possible to reconstruct a

matrix which correlates the measured parameters (time-of-flight and impact position) to the trajectory of electrons with given kinetic energy and emission angle [132]. With this matrix it would be possible to evaluate a correction to the measured time-of-flights and reduce Δt_2 to a value comparable or lower than Δt_1.

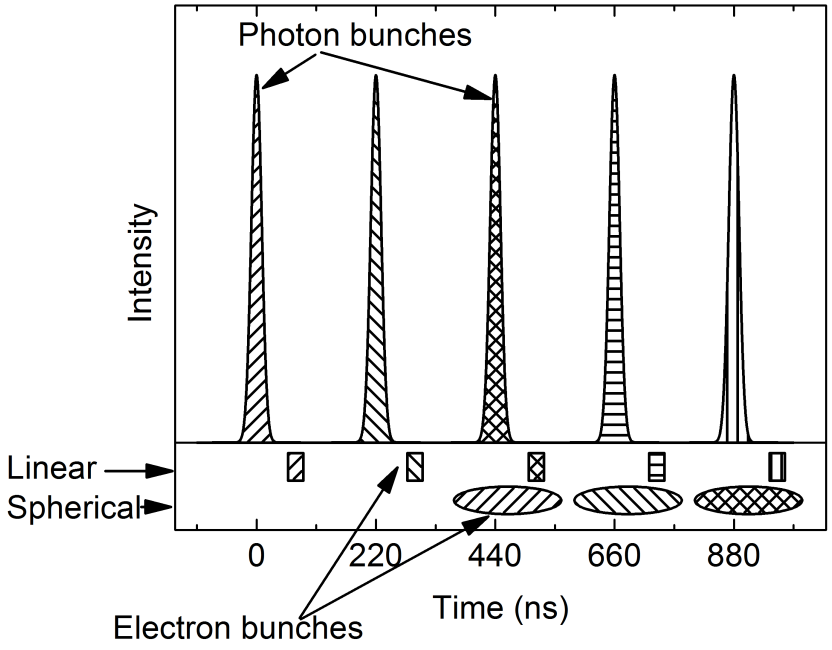


FIGURE 5.14: Time structure of the photoelectron pulses generated by the photon bunches in one of the bunch trains at EXFEL which are transmitted in the TOF analysers. The photon bunches are represented as Gaussian curves (whose width is not to real scale) and the correspondent electron pulses are depicted as rectangles for the cylindrical lens and ellipses for the spherical mirror with the same pattern.

From the time-of-flight curves 5.7 b) and 5.13 b), it was possible to evaluate the compatibility of the spectrometers for shot-to-shot measurements at a pulsed X-ray source like EXFEL. We will explain this with the help of Fig. 5.14, where some of the X-ray pulses contained in one of the bunch trains of EXFEL are schematically represented as a sequence of Gaussian curves with a time separation of 220 ns (note that the width of the Gaussians is not to scale). For each photon pulse there are two photoelectron packets, which are represented by rectangle and ellipse for the cylindrical lens and the spherical mirror, respectively, having the same pattern as the corresponding Gaussian. The size of the rectangles and ellipses corresponds to the time-of-flight range of electrons with a transmission larger than 20%. For the cylindrical lens the value is 30 ns and 200 ns for the spherical mirror: in both cases the electron pulses are well separated and there is enough time after one pulses has been detected for the detector to get ready to accept a new one. Of course the detector must have a sampling speed of about 4.5 MHz.

Conclusions

The core of this thesis work consists in the application of hard X-ray photoelectron spectroscopy (HAXPES) to investigate the satellite structure in the core level spectra of different $3d$ strongly correlated materials, whose behaviour is dictated by the localised nature of the $3d$ electrons of the transition metal element.

It is known that from the study of such satellite features, which arise from the screening of the core hole by part of the valence or conduction electrons, it is possible to extrapolate information about the correlation between electrons. In particular, HAXPES has proved capable of revealing in $3d$ transition metal compounds such as oxides and diluted magnetic semiconductors, a class of bulk-only features which are particularly intense and well resolved in the $2p$ spectra of the transition metal elements [6, 7] and are not visible at surface sensitive excitation energies. These well screened satellites have been related to both metallicity and ferromagnetism; they have been observed to disappear when a system passes into the insulating phase and are not detected when low kinetic energy electrons are employed. This suggests that in the bulk and surface of materials, the screening of the core holes behaves differently. The description of these peaks required a new theoretical framework, which includes an additional screening mechanism from coherent or doping induced states which are at and near the Fermi level [21]. On the other hand, a different class of calculations based on a multi-site cluster model involving a nonlocal screening channel, have offered a alternative way to interpret these spectra [33]. It is still not clear which of these two models is best suited to explain the observed extra features and whether they could be mapped one into the other or not. From the experimental point of view, it would be interesting to understand whether the presence or absence of these features could be used to reveal through spectroscopy the presence of metallicity in materials at conditions close to the metal to insulator transition. On the other hand, since it is now clear that these features appear only when a determined set of conditions are met, it could be possible to use them as a fingerprint of good quality of samples produced for device applications [5]. Of course, before this approach can be considered to be reliable, it must be established the value of the critical probing depth at which these feature are revealed in different materials and if they appear suddenly or in a more gradual way.

Performing HAXPES at different photon energies while maintaining a comparable energy resolution, allows to probe the evolution of well screened peaks as a function of the probing depth. A broad photon energy range must be exploited from more than 6000 eV

to less than 1000 eV, retaining a energy resolution as good as 300 meV, which at the moment is currently possible at few synchrotron based beamlines all over the world, such as the I09 beamline of the Diamond synchrotron radiation facility. Here we have measured the Mn $2p$ spectra of a diluted magnetic semiconductor $Ga_{1-x}Mn_xAs$ in the paramagnetic phase (room temperature) and of two perovskite manganites $La_{1-x}Sr_xMnO_3$ thin films with different strain conditions in the ferromagnetic and metallic phase ($T = 200$ K).

The Mn $2p$ spectra of both materials shows a well-screened feature on the low binding energy side which is more intense and well resolved for the Mn $2p_{3/2}$ peak. For $Ga_{1-x}Mn_xAs$, in the spectrum measured at $\hbar\omega = 5940$ eV the peak is the predominant structure: lowering the photon energy it becomes smaller with respect to the rest of the $2p_{3/2}$ spin-orbit component, but it does not disappear even at $\hbar\omega = 800$ eV. This was the first time that the extra-peak in $Ga_{1-x}Mn_xAs$ was observed in a soft X-ray Mn $2p$ spectrum. In the case of the $La_{1-x}Sr_x$ films, at a 5940 eV photon energy, the $2p_{3/2}$ well screened peak can be seen as a well resolved but low intensity feature with respect to the main line. The difference with respect to the previous case, is that already at 1000 eV photon energy, the structure has become so small that it is longer visible in the spectrum without a fitting procedure. This is verified for both the strain relaxed and the compressive strained sample. For both classes of samples a fitting procedure of the Mn $2p_{3/2}$ spectra at the different photon energies has been performed. The ratio of area of the extra-peak respect to the total area of the photoline has been plotted as a function of the mean escape depth at the different photon energies. From the fitting of these dependences with with an exponential attenuation curve, we estimated the value of the thickness of an attenuating layer in which the screening channel associated to the extra-peak is absent, obtaining in the case of $Ga_{0.87}Mn_{0.13}As$ dependence a thickness of the layer a value of 12 ± 1 Å which corresponds to a little more than two unit cells. In the case $La_{0.65}Sr_{0.35}MnO_3$ from a very similar analysis we obtained a higher value of 40 ± 9 Å, which corresponds to about ten unit cells.On the other hand, on the $4d$ system RuO_2 which is a more metallic system with respect to $Ga_{1-x}Mn_xAs$ and $La_{1-x}Sr_xMnO_3$, whose electrical conductivity is related to hole doping with Mn ions, the Ru $3d$ spectra present a well-screened peak which is the dominant structure for both spin-orbit components, already at an excitation energy of 1000 eV. By increasing the photon energy, the ratio between this feature and the unscreened peak increments. This is quite different from what has been observed in the case of $La_{1-x}Sr_xMnO_3$, where the well-screened peak on the low binding energy side of the Mn $2p_{3/2}$ photoline becomes less intense as the excitation energy is decreased, resulting no longer visible at $\hbar\omega = 1000$ eV. It is also different from the case of $Ga_{1-x}Mn_xAs$, which however seems a intermediate situation between ruthenates and manganites, since the extra-peak is quite intense in the HAXPES spectra and decreases in intensity when lowering the photon energy, although it remains visible also at the lowest used photon energy of 800 eV. From these observations, one can conclude that the depth of the surface layer in which electronic properties are different with respect to the bulk depends on the materials. The different evolution with photon energy of the well screened peaks in various materials can be ascribed to both intrinsic and extrinsic properties of the systems. For example, surface preparation plays a major role at the low photon energies, as it suggested by the fact

that in $Ga_{1-x}Mn_xAs$ we are able to see the extra-peak at photon energies lower than former studies [7]. On the other hand, if one compares the surface layer with different properties with respect to the bulk to space-charge depletion of semiconductors [133], different charge carrier density can be an additional parameter that may influence the probing depth dependence of well-screened features.

We have also applied HAXPES to the study of the satellite structure of the Ti $1s$ and $2p$ spectra in anatase TiO_2 thin films grown with different oxygen vacancy concentration, which should yield different conduction properties. In this case we were not looking for extra peaks on the low binding energy side, but more "conventional" satellites which have been observed in analogue HAXPES spectra from the $SrTiO_3$ compounds and have been associated to monopole charge-transfer transitions from the O $2p$ levels to the crystal-field split Ti $3d$ orbitals. These satellites are found in the Ti $1s$ spectrum at around 4.8 and 13.4 eV higher binding energy with respect to the main peak as resulted from a fitting procedure of the lineshapes, which is quite compatible with what reported in the case of $SrTiO_3$; however, due to the ~ 5 eV spin-orbit splitting in the Ti $2p$, we were to identify in the fitting of the spectra only the satellite at about 13 eV and not the one at 5 eV. Also, in the case of Ti $1s$ the ratio between the satellite at 5 eV and the main peak is quite smaller for anatase TiO_2 with respect to $SrTiO_3$, which is possibly due to the smaller overlap between the t_{2g} orbitals on Ti and O sites.

New possibilities for HAXPES appear with the development of fourth generation synchrotron radiation facilities, also called X-ray Free Electron Lasers (XFELs), able to provide short (few tens of fs) but intense (peak brilliance up to 8 order of magnitude higher with respect to third generation storage rings). With the radiation produced by this type of sources it could be possible to perform time-resolved experiments to study the ultrafast dynamics of processes such as chemical reactions or demagnetisation. Time-resolved photoelectron spectroscopy is already performed by exploiting the pulsed nature of the synchrotron radiation produced in third generation storage rings, although with a time resolution limited by the width of the pulses, which is some tens of ps. We have acquired time resolved Mn $2p_{3/2}$ spectra from the strain relaxed $La_{0.65}Sr_{0.35}MnO_3$ sample and have demonstrated that the extra-peak decreases when the measurements is made after a certain time interval from the laser pump pulse.

In order to perform time-resolved HAXPES at XFELs with a reasonable compromise between energy resolution and counting rates, it is necessary to design and build a new class of spectrometers. Due to the pulsed nature of the XFEL light sources, it could be appropriate to use time-of-flight electron energy analysers instead of conventional hemispherical spectrometers. Apart from a good energy resolution (i. e. few hundreds of meV for kinetic energies of several keV), it would also be desirable that such an analyser would be able to discriminate between electron bunches generated by different photon pulses. We have characterised by means of electron trajectory simulations two different TOF spectrometers for core level HAXPES at the European X-ray Free Electron Laser (EXFEL) light source which is currently under construction at Hamburg. Both are based on quite conventional designs, namely a cylindrical lens with six separately biased electrodes and a spherical reflector. Our results showed that the cylindrical lens can offer a wider angular acceptance with respect to the spherical mirror (more than three

times larger) and both systems present a transmission plateau wide and flat enough to record in parallel core level spectra from most atomic species. The one for the cylindrical lens is more than twice broader than the one of the spherical mirror, which means that the second can suppress undesired energies more efficiently. Furthermore, from the simulations it resulted that the resolving power of the spherical mirror is more than one order of magnitude larger than that of the cylindrical lens. Finally, both spectrometers result to be compatible with the time structure which is expected at a pulsed light source like the EXFEL, meaning that the duration of the single electron bunches which are transmitted to the detector is shorter than the time separation between consecutive photon pulses, so that the detector can unambiguously assign to each photon packets its correspondent electron bunch. This is true for both systems, but in the case of the spherical reflector this comes only if particular care is taken in choosing the size and position of the pupil.

Bibliography

[1] S. Hüfner. **Photoelectron Spectroscopy: Principles and Applications**. Springer, 1996.

[2] G. A. Sawatzky and J. W. Allen. **Magnitude and Origin of the Band Gap in NiO**. *Phys. Rev. Lett.*, 53:2339, 1984. doi:10.1103/PhysRevLett.53.2339.

[3] G. van der Laan, C. Westra, C. Haas and G. A. Sawatzky. **Satellite structure in photoelectron and Auger spectra of copper dihalides**. *Phys. Rev. B*, 23: 4369, 1981. doi:10.1103/PhysRevB.23.4369.

[4] C. S. Fadley. Basic Concepts of X-ray Photoelectron Spectroscopy. In **Electron Spectroscopy: Theory, Techniques and Applications**. Academic Press, 1978.

[5] J. Woicick. **Hard X-ray Photoelectron Spectroscopy (HAXPES)**. Springer, 2015.

[6] K. Horiba, M. Taguchi, A. Chainani, Y. Takata, E. Ikenaga, D. Miwa, Y. Nishino, K. Tamakasu, M. Awaji et al. **Nature of the Well-Screened State in Hard X-Ray Mn 2*p* Core-Level Photoemission Measurements of $\mathbf{La_{1-x}Sr_xMnO_3}$**. *Phys. Rev. Lett.*, 93:236401, 2004. doi:10.1103/PhysRevLett.93.236401.

[7] J. Fujii, M. Sperl, S. Ueda, K. Kobayashi, Y. Yamashita, M. Kobata, P. Torelli, F. Borgatti, M. Utz, C. S. Fadley, A. X. Gray, G. Monaco, C. H. Back, G. van der Laan and G. Panaccione. **Identification of Different Electron Screening Behavior Between the Bulk and Surface of (Ga,Mn)As**. *Phys. Rev. Lett.*, 107:187203, 2011. doi:10.1103/PhysRevLett.107.187203.

[8] S. Hellmann, M. Beye, C. Sohrt, T. Rohwer, F. Sorgenfrei, H. Redlin, M. Kalläne, M. Marczynski-Bühlow, F. Hennies, M. Bauer, A. Fölisch, L. Kipp, W. Wurth and K. Rossnagel. **Ultrafast Melting of a Charge-Density Wave in the Mott Insulator $1T$-$\mathbf{TaS_2}$**. *Phys. Rev. Lett.*, 105:187401, 2010. doi:10.1103/PhysRevLett.105.187401.

[9] H. a. Bethe. **Theorie der Beugung von Elektronen in Kristallen**. *Ann. Phys. (Leipzig)*, 87:55, 1928.

[10] A. Sommerfeld. **Zur Elektronentheorie der Metalle auf Grund der Fermischen Statistik**. *Z. Phys.*, 47:1, 1928. doi:10.1007/BF01391052.

[11] F. Bloch. **Bemerkungen zur Elektrontheorie des Ferromagnetismus und der elektrischen Leiftähigheit**. *Z. Phys.*, 57:545, 1929. doi:10.1007/BF01340281.

[12] J. H. de Boer and E. J. W. Verwey. **Semi-conductors with partially and with completely filled 3*d*-lattice bands**. *Proc. Phys. Soc.*, 49:59, 1937. URL `http://stacks.iop.org/0959-5309/49/i=4S/a=307`.

[13] M. Imada, A. Fujimori and Y. Tokura. **Metal-insulator transitions**. *Rev. Mod. Phys.*, 70:1039, 1998. doi:10.1103/RevModPhys.70.1039.

[14] N. F. Mott. **The basis of the electron theory of metals, with special reference to the transition metals**. *Proc. Phys. Soc. London, Ser. A*, 62:416, 1949. URL `http://stacks.iop.org/0370-1298/62/i=7/a=303`.

[15] N. F. Mott. **Metal-Insulator Transition**. *Rev. Mod. Phys.*, 40:677, 1968. doi:10.1103/RevModPhys.40.677.

[16] J. Hubbard. **Electron Correlations in Narrow Energy Bands**. *Proc. Phys. Soc. London, Ser. A*, 276:238, 1963. doi:10.1098/rspa.1963.0204.

[17] G. Kotliar and D. Vollhardt. **Strongly Correlated Materials: Insight From Dynamical Mean-Field Theory**. *Phys. Today*, 57(3):53, 2004. doi:10.1063/1.1712502.

[18] A. Fujimori, F. Minami and S. Sugano. **Multielectron satellites and spin polarization in photoemission from Ni compounds**. *Phys. Rev. B*, 29:5225, 1984. doi:10.1103/PhysRevB.29.5225.

[19] J. Zaanen, G. A. Sawatzky and J. W. Allen. **Band Gaps and Electronic Structure of Transition-Metal Compounds**. *Phys. Rev. Lett.*, 55:418, 1985. doi:10.1103/PhysRevLett.55.418.

[20] M. T. Greiner and Z. -H. Lu. **Thin-film metal oxides in organic semiconductor devices: their electronic structures, work functions and interfaces**. *NPG Asia Mater.*, 5:e55, 2013. doi:10.1038/am.2013.29.

[21] M. Taguchi, A. Chainani, K. Horiba, Y. Takata, M. Yabashi, K. Takamasu, Y. Nishino, D. Miwa, T. Ishikawa, T. Takeuchi, K. Yamamoto et al. **Evidence for Suppressed Screening on the Surface of High Temperature $La_{2-x}Sr_xCuO_4$ and $Nd_{2-x}Ce_xCuO_4$**. *Phys. Rev. Lett.*, 95:177002, 2005. doi:10.1103/PhysRevLett.95.177002.

[22] G. Panaccione, M. Altarelli, A. Fondacaro, A. Georges, S. Huotari, P. Lacovig, A. Lichtenstein, P. Metcalf, G. Monaco, F. Offi, L. Paolasini, A. Potaryaev, O. Tjernberg and M. Sacchi. **Coherent Peaks and Minimal Probing Depth in Photoemission Spectroscopy of Mott-Hubbard Systems**. *Phys. Rev. Lett.*, 97:116401, 2006. doi:10.1103/PhysRevLett.97.116401.

[23] A. Kotani and Y. Toyazawa. **Optical Spectra of Core Electrons in Metals with an Incomplete Shell. I. Analytic Features**. *J. Phys. Soc. Japan*, 35: 1073, 1973. doi:10.1143/JPSJ.35.1073.

[24] A. Kotani and Y. Toyazawa. **Photoelectron Spectra of Core Electrons in Metals with an Incomplete Shell**. *J. Phys. Soc. Japan*, 37:912, 1974. doi:10.1143/JPSJ.37.912.

[25] S. Hüfner and G. K. Wertheim. **Core-Electron Splittings and Hyperfine Fields in Transition-Metal Compounds**. *Phys. Rev. B*, 7:2333, 1973. doi:10.1103/PhysRevB.7.2333.

[26] S. Asada and S. Sugano. **Satellites in X-Ray photoelectron Spectra of Transition-Metal Compounds**. *J. Phys. Soc. Jpn.*, 41:1291, 1976. doi:10.1143/JPSJ.41.1291.

[27] O. Gunnarsson and K. Schönhammer. **Photoemission from Ce Compounds: Exact Model Calculation in the Limit of Large Degeneracy**. *Phys. Rev. Lett.*, 50:604, 1983. doi:10.1103/PhysRevLett.50.604.

[28] J. C. Fuggle, M. Campagna, Z. Zolnierek, R. Lässer and A. Platau. **Observation of a Relationship between Core-Level Line Shapes in Photoelectron Spectroscopy and the Localization of Screening Orbitals**. *Phys. Rev. Lett.*, 45:1597, 1980. doi:10.1103/PhysRevLett.45.1597.

[29] J. Zaanen, C. Westra and G. A. Sawatzky. **Determination of the electronic structure of transition-metal compounds: 2*p* x-ray photoemission spectroscopy of the nickel dihalides**. *Phys. Rev. B*, 33:8060, 1986. doi:10.1103/PhysRevB.33.8060.

[30] M. A. van Veenendaal and G. A. Sawatzky. **Nonlocal Screening Effects in 2*p* X-ray Photoemission Spectroscopy Core-Level Line Shapes of Transition Metal Compounds**. *Phys. Rev. Lett.*, 70:2459, 1993. doi:10.1103/PhysRevLett.70.2459.

[31] M. Tomellini. **X-Ray Photoelectron Spectra of Defective Nickel Oxide**. *J. Chem. Soc. Faraday Trans.*, 84:3501, 1988. doi:10.1039/F19888403501.

[32] K. Okada. **Multi-Site Effects on the Core-Level Photoemission of Sr_2RuO_4**. *Surf. Rev. Lett.*, 9:1023, 2002. doi:10.1142/S0218625X02003287.

[33] M. van Veenendaal. **Competition between screening channels in core-level x-ray photoemission as a probe of changes in the ground-state properties of transition-metal compounds**. *Phys. Rev. B*, 74:085118, 2006. doi:10.1103/PhysRevB.74.085118.

[34] H.-D. Kim, H.-J. Noh, K. H. Kim and S.-J. Oh. **Core-Level X-Ray Photoemission Satellites in Ruthenates: A New Mechanism Revealing The Mott Transition**. *Phys. Rev. Lett.*, 93:126404, 2004. doi:10.1103/PhysRevLett.93.126404.

[35] C. S. Fadley. **Hard X-ray photoelectron spectroscopy and diffraction in the hard X-ray regime: Fundamental considerations and future possibilities**. *Nucl. Instr. Meth. Phys. Res. A*, 547:24, 2005. doi:10.1016/j.nima.2005.05.009.

[36] P. Pianetta, I. Lindau, S. Doniach and W. E. Spicer. **X-ray photoemission spectroscopy**. *Nature*, 250:214, 1974. doi:10.1038/250214a0.

[37] **XCOM: Photon Cross Sections Database**. Accessed: 03/07/2015.

[38] L. Köver, D. Varga, I. Csenry, J. Tóth and K. Tökési. **Some Applications of High-energy, High resolution Auger Electron Spectroscopy Using Bremsstrahlung Radiation**. *Surf. Interface Anal.*, 15:9, 1992. doi:10.1002/sia.740190106.

[39] A. Sekiyama, T. Iwasaki, K. Matsuda, Y. Saitoh, Y. Ônuki and S. Suga. **Probing bulk states of correlated electron systems by high-resolution resonance photoemission**. *Nature*, 403:396, 2000. doi:10.1038/35000140.

[40] K. Kobayashi, M. Yabashi, Y. Takata, T. Tokushima, S. Shin, K. Tamasaku, D. Miwa, T. Ishikawa, H. Nohira, T. Hattori, Y. Sugita, O. Nakatsuka, A. Sakai and S. Zaima. **High resolution-high energy x-ray photoelectron spectroscopy using third-generation synchrotron radiation source, and its applicationto Si-high k insulator systems**. *Appl. Phys. Lett.*, 83:1005, 2003. doi:10.1063/1.1595714.

[41] P. Torelli, M. Sacchi, G. Cautero, M. Cautero, B. Krastanov, P. Lacovig, P. Pittana, A. Fondacaro, F. Offi, G. Paolicelli, G. Stefani, M. Grioni, R. Verbeni, G. Monaco and G. Panaccione. **Experimental setup for high energy photoemission using synchrotron radiation**. *Rev. Sci. Instrum.*, 76:023909, 2005. doi:10.1063/1.1852323.

[42] J. Kawai, M Takami, M. Fujinami, Y. Hashiguchi. S. Hayakawa, Y. Gonshi. **A numerical simulation of total reflection X-ray photoelectron spectroscopy (TRXPS)**. *Spectrochim. Acta B*, 47:983, 1992. doi:10.1016/0584-8547(92)80092-U.

[43] S. Tanuma, C. J. Powell and D. R. Penn. **Calculations of inelastic mean free paths. IX. Data for 41 elemental solids over the 50 eV to 30 keV range**. *Surf. Interface Anal.*, 43:689, 2010. doi:10.1002/sia.3522.

[44] C. S. Fadley. **X-ray photoelectron spectroscopy: Progress and perspectives**. *J. Electron Spectrosc. Relat. Phenom.*, 178–179:2, 2010. doi:10.1016/j.elspec.2010.01.006.

[45] F. Borgatti, F. Offi, P. Torelli, G. Monaco and G. Panaccione. **Interfacial and bulk electronic properties of complex oxides and buried interfaces as probed by HAXPES**. *J. Electron Spectrosc. Relat. Phenom.*, 190:228, 2013. doi:10.1016/j.elspec.2013.01.002.

[46] M. Sacchi, F. Offi, P. Torelli, A. Fondacaro, C. Spezzani, M. Cautero, G. Cautero, S. Huotari, M. Grioni, R. Delaunay, M. Fabrizioli, G. Vankó, G. Monaco, G. Paolicelli, G. Stefani and G. Panaccione. **Quantifying the effective attenuation length in high-energy photoemission experiments**. *Phys. Rev. B*, 71:155117, 2005. doi:10.1103/PhysRevB.71.155117.

[47] P. J. Cumpson and M. P. Seah. **Elastic Scattering Corrections in AES and XPS. II. Estimating Attenuation Lengths and Conditions Required for their Valid Use in Overlayer/Substrate Experiments**. *Surf. Interface Anal.*, 25:430, 1997. doi:10.1002/(SICI)1096-9918(199706)25:6<430::AID-SIA254>3.0.CO;2-7.

[48] M. Taguchi, A. Chainani, N. Kamakura, K. Horiba, Y. Takata, M. Yabashi, K. Takamasu, Y. Nishino, D. Miwa, T. Ishikawa, S. Shin, E. Ikenaga, T. Yokoya, K. Kobayashi, T. Mochiku, K. Hirata and K. Motoya. **Bulk screening in core-level photoemission from Mott-Hubbard and charge-transfer systems**. *Phys. Rev. B*, 71:155102, 2005. doi:10.1103/PhysRevB.71.155102.

[49] K. E. Smith and V. E. Henrich. **Photoemission study of composition- and temperature-induced metal-insulator transitions in Cr-doped V_2O_3**. *Phys. Rev. B*, 50:1382, 1994. doi:10.1103/PhysRevB.50.1382.

[50] S.-K. Mo, J. D. Denlinger, H.- D. Kim, J.-H. Park , J. W. Allen, A. Sekiyama, A. Yamasaki, K. Kadono, S. Suga, Y. Saitoh, T. Muro, P. Metcalf, G. Keller, K. Held, V. Eyert, V. I. Anisimov and D. Vollhardt. **Prominent Quasiparticle Peak in the Photoemission Spectrum of the Metallic Phase of V_2O_3**. *Phys. Rev. Lett.*, 90:186403, 2003. doi:10.1103/PhysRevLett.90.186403.

[51] M. A. van Veenendal, H. Eskes and G. A. Sawatzky. **Strong nonlocal contributions to Cu $2p$ photoelectron spectroscopy**. *Phys. Rev. B*, 47:11462, 1993. doi:10.1103/PhysRevB.47.11462.

[52] G. Panaccione, F. Offi, P. Torelli, G. Vanko, O. Tjernberg, P. Lacovig, A. Guarino, A. Fondacaro, A. Nigro, M. Sacchi, N. N. Brookes and G. Monaco. **Analysis of surface-bulk screening competition in the electron-doped $Nd_{2-x}Ce_xCuO_4$**. *Phys. Rev. B*, 77:125133, 2008. doi:10.1103/PhysRevB.77.125133.

[53] S. Ueda, H. Tanaka, E. Ikenaga, J. J. Kim, T. Ishikawa, T. Kawai and K. Kobayashi. **Competition between screening channels in core-level x-ray photoemission as a probe of changes in the ground-state properties of transition-metal compounds**. *Phys. Rev. B*, 80:092402, 2009. doi:10.1103/PhysRevB.80.092402.

[54] K. Edmonds, G. van der Laan and G. Panaccione. **Electronic structure of (Ga,Mn)As as seen by synchrotron radiation**. *Semicond. Sci. Technol.*, 30: 043001, 2015. URL `http://stacks.iop.org/0268-1242/30/i=4/a=043001`.

[55] H. Ohno, H. Munekata, T. Penney, S. von Molnár and L. L. Chang. **Magneto-transport properties of *p*-type (In,Mn)As diluted magnetic III-V semiconductors**. *Phys. Rev. Lett.*, 68:2664, 1992. doi:10.1103/PhysRevLett.68.2664.

[56] M. Wang, R. A. Marshall, K. W. Edmonds. A. W. Rushforth, R. P. Campion and B. L. Gallagher. **Determining Curie temperature in diluted ferromagnetic semiconductors: High Curie temperature (Ga,Mn)As**. *Appl. Phys. Lett.*, 104:132406, 2014. doi:10.1063/1.4870521.

[57] H. Åsklund, L. Ilver, J. Kanski, J. Sadowski and R. Mathieu. **Photoemission studies of $Ga_{1-x}Mn_xAs$: Mn concentration dependent properties**. *Phys. Rev. B*, 66:115319, 2002. doi:10.1103/PhysRevB.66.115319.

[58] F. Maccherozzi, G. Panaccione, G. Rossi, M. Hochstrasser, M. Sperl, M. Reinwald, G. Woltersdorf, W. Wegscheider and C. H. Back. **Influence of surface treatment on the magnetic properties of $Ga_{1-x}Mn_xAs$ thin films**. *Phys. Rev. B*, 74:104421, 2006. doi:10.1103/PhysRevB.74.104421.

[59] K. Edmonds, G. van der Laan, N. R. S. Farley, R. P. Campion, B. L. Gallagher, C. T. Foxon, B. C. C. Cowie, S. Warren and T. K. Johal. **Magnetic Linear Dichroism in the Angular Dependence of Core-Level Photoemission from (Ga,Mn)As Using Hard X Rays**. *Phys. Rev. Lett.*, 107:197601, 2011. doi:10.1103/PhysRevLett.107.197601.

[60] N. Panwar, I. Coondoo, V. Sen and S. K. Agarwal. *Advances in Ceramics - Electric and Magnetic Ceramics, Bioceramics, Ceramics and Environment*, chapter **Structural, Morphological, Magneto-Transport and Thermal Properties of Antinomy Substituted**. InTechOpen, 2011.

[61] C. W. Searle and S. T. Wang. **Studies of the ionic ferromagnet (LaPb)MnO_3 III. Ferromagnetic resonance studies**. *Can. J. Phys.*, 47:2703, 1969. doi:10.1139/p69-329.

[62] S. Majumdar and S. van Dijken. **Pulsed laser deposition of $La_{1-x}Sr_xMnO_3$**. *J. Phys. D: Appl. Phys.*, 47:034010, 2014. URL `http://stacks.iop.org/0022-3727/47/i=3/a=034010`.

[63] C. Zener. **Interaction between the *d*-Shells in the Transition Metals. II. Ferromagnetic compounds of Manganese with Perovskite Structure**. *Phys. Rev.*, 82:403, 1951. doi:10.1103/PhysRev.82.403.

[64] A.-M. Haghiri-Gosnet and J.-P. Renard. **CMR manganites: physics, thin films and devices**. *J. Phys. D: Appl. Phys.*, 36:R127, 2003. URL `http://stacks.iop.org/0022-3727/36/i=8/a=201`.

[65] N. Mehtougui, D. Rached, R. Khenata, H. Rached, M. Rabah and S. Bin-Omran. **Structural, electronic and mechanical properties of RuO_2 from first-principle calculations**. *Mater. Sci. Semicond. Process.*, 15:331, 2012. doi:10.1016/j.mssp.2012.02.001.

[66] **File:Rutile structure.png**. `https://commons.wikimedia.org/wiki/File:Rutile_structure.png`, 2012. Accessed: 27/07/2015.

[67] K. M. Glassford and J. R. Chelikowsky. **Electronic and structural properties of RuO_2**. *Phys. Rev. B*, 47:1732, 1993. doi:10.1103/PhysRevB.47.1732.

[68] S. Yoshii and M. Sato. **Studies of Metal-Insulator Transition of Pyrochlore Compound $Y_{2-x}Bi_xRu_2O_7$**. *J. Phys. Soc. Jpn.*, 68:3034, 1999. doi:10.1143/JPSJ.68.3034.

[69] S. Nakatsuji and Y. Maeno. **Quasi-Two Dimensional Mott Transition System $Ca_{2-x}Sr_xRuO_4$.** *Phys. Rev. Lett.*, 84:2666, 2000. doi:10.1103/PhysRevLett.84.2666.

[70] Y. J. Kim, Y. Gao and S. A. Chambers. **Core-level X-ray photoelectron spectra and X-ray photoelectron diffraction of RuO_2(110) grown by molecular beam epitaxy on TiO_2(110)**. *Appl. Surf. Sci.*, 120:250, 1997. doi:10.1016/S0169-4332(97)00233-X.

[71] J. C. Woicick, C. Weiland and A. K. Rumaiz. **Loss for photoemission versus gain for Auger: Direct experimental evidence of crystal-field splitting and charge-transfer in photoelectron spectroscopy**. *Phys. Rev. B*, 91: 201412(R), 2015. doi:10.1103/PhysRevB.91.201412.

[72] **Anatase - St Christophe-en-Oisans, Bourg d'Oisans, Isère, Rhône-Alpes, France - Topotype deposit-** 1.7×1.7 **cm**. `https://en.wikipedia.org/wiki/Anatase#/media/File:Anatase_Oisans.jpg`. Accessed: 16/07/2015.

[73] S. Asahi, Y. Taga, W. Mannstadt and A. J. Freeman. **Electronic and optical properties of anatase TiO_2.** *Phys. Rev. B*, 61:7459, 2000. doi:10.1103/PhysRevB.61.7459.

[74] J. H. Carey, J. Lawrence and H. M. Tosine. **Photodechlorination of PCB's in the presence of titanium dioxide in aqueous suspensions**. *Bull. Environ. Contam. Toxicol.*, 16:697, 1976. doi:10.1007/BF01685575.

[75] A. Fujishima and K. Honda. **Electrochemical photolysis of water at a semiconductor electrode**. *Nature*, 238:37, 1972. doi:10.1038/238037a0.

[76] R. Ciancio, E. Carlino, C. Aruta, D. Maccariello, F. Miletto Granozio and U. Scotti di Uccio. **Nanostructure of buried interface layers in TiO_2 anatase thin films grown on $LaAlO_3$ and $SrTiO_3$ substrates**. *Nanoscale*, 4:91, 2012. doi:10.1039/C1NR11015B.

[77] L. Kavan, M. Grätzel, S. E. Gilbert, C. Klemenz and H. J. Scheel. **Electrochemical and Photoelectrochemical Investigation of Single-Crystal Anatase**. *J. Am. Chem. Soc.*, 118:6716, 1996. doi:10.1021/ja954172l.

[78] N. S. Portillo-Vélez, O. Olvera-Neria, I. Hernández-Pérez and A. Rubio-Ponce. **Localized electronic states induced by oxygen vacancies on anatase TiO_2 (101) surface**. *Surf. Sci.*, 616:115, 2013. doi:10.1016/j.susc.2013.06.0061.

[79] R. Ciancio, E. Carlino, G. Rossi, C. Aruta, U. Scotti di Uccio, A. Vittadini and A. Selloni. **Magnèli-like phases in epitaxial anatase TiO_2 thin films**. *Phys. Rev. B*, 86:104110, 2012. doi:10.1103/PhysRevB.86.104110.

[80] R. Waser and M. Aono. **Nanoionics-based resistive switching**. *Nat. Mater.*, 6:833, 2007. doi:10.1038/nmat2023.

[81] S. K. Sen, J. Riga and J. Verbist. **$2s$ and $2p$ X-RAY PHOTOELECTRON SPECTRA OF Ti^{4+} ION IN TiO_2**. *Chem. Phys. Lett.*, 39:560, 1976. doi:10.1038/35000140.

[82] M. Oku, H. Matsuta, K. Wagatsuma, Y. Waseda and S. Kohiki. **Removal of inelastic scattering part from Ti2p XPS spectrum of TiO_2 by deconvolution method using O1s as response function**. *J. Electron Spectrosc. Relat. Phenom.*, 105:211, 1999. doi:10.1142/S0218625X02003287.

[83] N. Moslemzadeh, G. Beamson, P. Tsakiropoulos, J. F. Watts, S. R. Haines and P. Weightman. **Electronic structure of Ti metal and TiO_2 powder studied by hard and soft (Cu Kα_1 and Al Kα_1) X-ray photoelectron and Auger spectroscopy**. *J. Electron Spectrosc. Relat. Phenom.*, 152:148, 2006. doi:10.1016/j.elspec.2006.05.003.

[84] D. H. Bilderback, P. Elleaume and E. Weckert. **Review of third and next generation synchrotron light sources**. *J. Phys. B: At. Mol. Opt. Phys.*, 38: S773, 2005. doi:10.1088/0953-4075/38/9/022.

[85] **SOLEIL Synchrotron beamlines**. `http://www.synchrotron-soleil.fr/Recherche/LignesLumiere`, . Accessed: 02/09/2015.

[86] P. Schmüser, M. Dohlus, J. Rossbach and C. Behrens. **Free-Electron Lasers in the Ultraviolet and X-Ray Regime**. Springer Tracts in Modern Physics, 2014.

[87] **GALAXIES: Description de la ligne**. `http://www.synchrotron-soleil.fr/Recherche/LignesLumiere/GALAXIES/DescriptionLigne#DonneesTechniques`, . Accessed: 08/07/2015.

[88] **SOLEIL synchrotron: Storage ring main parameters**. `http://www.synchrotron-soleil.fr/portal/page/portal/SourceAccelerateur/ParametresPrincipaux`, 2012. Accessed: 08/07/2015.

[89] **Way for light: Synchrotron SOLEIL**. `http://www.wayforlight.eu/eng/synchrotrons/soleil.aspx`, . Accessed: 08/07/2015.

[90] **GALAXIES: User guide**. `http://www.synchrotron-soleil.fr/Recherche/LignesLumiere/GALAXIES/UserGuide#Hexapod`, . Accessed: 08/07/2015.

[91] J.-P. Rueff, J. M. Ablett, D. Céolin, Th. Moreno, V. Balédent, B. Lassalle-Kaiser, J. E. Rault, M. Simon and A. Shukla. **The GALAXIES beamline at the SOLEIL synchrotron: inelastic X-ray scattering and photoelectron spectroscopy in the hard X-ray range**. *J. Synchrotron Rad.*, 22:175, 2015. URL `10.1107/S160057751402102X`.

[92] J. M. Ablett, J.-M. Dubuisson, T. Moreno, D. Céolin, D. Prieur, E. Raimon, D. Corruble, J. Coquet, A. Lestrade, C. Bourgoin and J.-P. Rueff. **New Design Concept for a High-Resolution In-Vacuum 4-Bounce Hard X-Ray Monochromator at the GALAXIES Beamline at the SOLEIL Synchrotron**. *J. Phys.: Conf. Ser.*, 425:052007, 2013. URL `http://stacks.iop.org/1742-6596/425/i=5/a=052007`.

[93] J. J. Yeh and I. Lindau. **Atomic subshell photoionization cross sections and asymmetry parameters:** $1 \leq Z \leq 103$. *At. Data Nucl. Data Tables*, 32:1, 1985. doi:10.1016/0092-640X(85)90016-6.

[94] **I09 beamline**. `http://www.diamond.ac.uk/Beamlines/Surfaces-and-Interfaces/I09.html`, . Accessed: 18/08/2015.

[95] **I09 beamline layout**. `http://www.diamond.ac.uk/Beamlines/Surfaces-and-Interfaces/I09/Beamline-layout/base/0/text_files/file/document/SISA%20I09.jpg`, . Accessed: 07/08/2015.

[96] M. Emori, M. Sugita, K. Ozawa and H. Sakama. **Electronic structure of epitaxial anatase TiO_2 films: Angle-resolved photoelectron spectroscopy study**. *Phys. Rev. B*, 85:035129, 2012. doi:10.1103/PhysRevB.85.035129.

[97] **Electron binding energies**. `https://userweb.jlab.org/~gwyn/ebindene.html`. Accessed: 20/07/2015.

[98] A. Yu. Petrov, C. Aruta, S. Mercone, C. Adamo, I. Alessandri, and L. Maritato. **Room temperature metal-insulator transition in as grown $(La_{1-x}Sr_x)_yMnO_3$ thin films deposited by molecular beam epitaxy**. *Eur. Phys. J. B*, 40:11, 2004. doi:10.1140/epjb/e2004-00233-7.

[99] M. V. Lebedev, D. Ensling, R. Hunger, T. Mayer and W. Jaegermann. **Synchrotron photoemission spectroscopy study of ammonium hydroxide etching to prepare well-ordered GaAs(100) surfaces**. *Appl. Surf. Sci.*, 229: 226, 2004. doi:10.1002/sia.740190106.

[100] S. A. Hatfield, T. D. Veal, C. F. McConvill, G. R. Bell, K. W. Edmonds, R. P. Campion, C. T. Foxon and B. L. Gallagher. **Photoelectron spectroscopy study of $Ga_{1-x}Mn_xAs(001)$ surface oxide and low temperature cleaning**. *Surf. Sci.*, 585:66, 2005. doi:10.1016/j.susc.2005.04.012.

[101] T. Hishida, K. Ohbayashi and T. Saitoh. **Hidden relationship between the electrical conductivity and the Mn $2p$ core-level photoemission spectra in $La_{1-x}Sr_xMnO_3$**. *J. Appl. Phys.*, 113:043710, 2013. doi:10.1063/1.4789315.

[102] C. S. Fadley, D. A. Shirley, A. J. Freeman, P. S. Begus and J. V. Mallow. **Multiplet Splitting of Core-Electron Binding Energies in Transition-Metal Ions**. *Phys. Rev. Lett.*, 23:1397, 1969. doi:10.1103/PhysRevLett.23.1397.

[103] V. R. Galakhov, M. Demeter, S. Bartkowski, M. Neumann, N. A. Ovechkina, E. Z. Kurmaev, N. I. Lobachevskaya, Ya. M. Mukovskii, J. Mitchell and D. L. Ederer. **Mn $3s$ exchange splitting in mixed-valence manganites**. *Phys. Rev. B*, 65: 113102, 2002. doi:10.1103/PhysRevB.65.113102.

[104] F. Offi, N. Mannella, T. Pardini, G. Panaccione, A. Fondacaro, P. Torelli, M. W. West, J. F. Mitchell and C. S. Fadley. **Temperature-dependent electronic structure of the colossal magnetoresistive manganite $La_{0.7}Sr_{0.3}MnO_3$ from hard x-ray photoemission**. *Phys. Rev. B*, 77:174422, 2008. doi:10.1103/PhysRevB.77.174422.

[105] E. Beyreuther, S. Grafström, L. M. Eng, C. Thiele and K. Dörr. **XPS investigation of Mn valence in lanthanum manganite thin films under variation of oxygen content**. *Phys. Rev. B*, 73:155425, 2006. doi:10.1103/PhysRevB.73.155425.

[106] S. Picozzi, C. Ma, Z. Yang, R. Bertacco, M. Cantoni, A. Cattoni, D. Petti, S. Brivio and F. Ciccacci. **Oxygen vacancies and induced changes in the electronic and magnetic structures of $La_{0.66}Sr_{0.33}MnO_3$: A combined *ab initio* and photoemission study**. *Phys. Rev. B*, 75:094418, 2007. doi:10.1103/PhysRevB.75.094418.

[107] C. Schlueter, P. Orgiani, T.-L. Lee, A. Yu. Petrov, A. Galdi, B. A. Davidson. J. Zegenhagen and C. Aruta. **Evidence of electronic band redistribution in $La_{0.65}Sr_{0.35}MnO_{3-\delta}$ by hard X-ray photoelectron spectroscopy**. *Phys. Rev. B*, 86:155102, 2012. doi:10.1103/PhysRevB.86.155102.

[108] J. M. Kahk, C. G. Poll, F. E. Oropeza, J. M. Ablett, D. Céolin, J.-P. Rueff, S. Agrestini, Y. Utsumi, K. D. Tsuei, Y. F. Liao, F. Borgatti, G. Panaccione, A. Regoutz, R. G. Edgell, B. J. Morgan, D. O. Scanlon and D. J. Payne. **Understanding the electronic structure of IrO_2 Using Hard-X-ray Photoelectron Spectroscopy and Density-Functional-Theory**. *Phys. Rev. Lett.*, 112: 117601, 2014. doi:10.1103/PhysRevLett.112.117601.

[109] J. H. Scofield. Theoretical Photoionization Cross Sections from 1 to 1500 keV. Technical report, Lawrence Livermore National Laboratory, 1973.

[110] J. A. Bearden and A. F. Burr. **Reevaluation of X-Ray Atomic Energy Levels**. *Rev. Mod. Phys.*, 39:125, 1967. doi:10.1103/RevModPhys.39.125.

[111] S. Tougaard. **Formalism for quantitative surface analysis by electron spectroscopy**. *J. Vac. Sci. Technol. A*, 8:2197, 1990. doi:10.1116/1.577037.

[112] M. Cavallini. AFM investigation of (Ga,Mn)As. Technical report, CNR-ISMN, Bologna, 2015.

[113] H. Tanaka, Y. Takata, K. Horiba, M. Taguchi, A. Chainani, S. Shin, D. Miwa, K. Tamakasu, Y. Nishino, T. Ishikawa, E. Ikenaga, M. Awaji, A. Takeuchi, T. Kawai and K. Kobayashi. **Electronic structure of strained $(La_{0.85}Ba_{0.15})MnO_3$ thin films with room temperature ferromagnetism investigated by hard x-ray photoemission spectroscopy**. *Phys. Rev. B*, 73:094403, 2006. doi:10.1103/PhysRevB.73.094403.

[114] R. Singh. *Growth and Characterization of a diluted magnetic semiconductor: Gallium Manganese Arsenide*. PhD thesis, University of Arkansas, 2008.

[115] M. Huijben, L. W. Martin, Y.-H. Chu, M. B. Holcomb, P. Yu, G. Rijnders, D. H. A. Blank and R. Ramesh. **Critical thickness and orbital ordering in ultrathin $La_{0.7}Sr_{0.3}MnO_3$ films**. *Phys. Rev. B*, 78:094413, 2008. doi:10.1103/PhysRevB.78.094413.

[116] A. Verna, Bruce A. Davidson, Y. Szeto, A.Yu. Petrov, A. Mirone, A. Giglia, N. Mahne and S. Nannarone. **Measuring magnetic profiles at manganite surfaces with monolayer resolution**. *J. Magn. Magn. Mater.*, 322:1212, 2010. doi:10.1016/j.jmmm.2009.05.022.

[117] R. R. Daniels, G. Margaritondo, C.-A. Georg and F. Lévy. **Electronic states of rutile dioxides: $\mathbf{RuO_2}$, $\mathbf{IrO_2}$ and $\mathbf{Ru_xIr_{1-x}O_2}$**. *Phys. Rev. B*, 29:1813, 1984. doi:10.1103/PhysRevB.29.1813.

[118] S. Theiss. *Interface Structure and Electronic Properties of $SrTiO_3$ and $YBa_2Cu_3O_{7-\delta}$ Crystals and Thin Films*. PhD thesis, Universität Hamburg, 2007.

[119] S. Yamamoto and I. Matsuda. **Time-Resolved Photoelectron Spectroscopy Using Synchrotron Radiation: Past, Present and Future**. *J. Phys. Soc. Japan*, 82:021003, 2013. doi:10.7566/JPSJ.82.021003.

[120] M. Cinchetti, M. Sánchez Albaneda, D. Hoffmann, T. Roth, J.-P. Wüstenberg, M. Krauß, O. Andreyev, H. C. Schneider, M. Bauer and M. Aeschlimann. **Spin-Flip Processes and Ultrafast Magnetization Dynamics in Co: Unifying the Microscopic and Macroscopic View of Femtosecond Magnetism**. *Phys. Rev. Lett.*, 97:177201, 2006. doi:10.1103/PhysRevLett.97.177201.

[121] M. Ogawa, S. Yamamoto, K. Fujikawa, R. Hobara, R. Yukawa, Sh. Yamamoto, S. Kitagawa, D. Pierucci, M. G. Silly, C.-H. Lin, R.-Y. Liu, H. Daimon, F. Sirotti, S.-J. Tang and I. Matsuda. **Relaxations of the surface photovoltage effect on the atomically controlled semiconductor surfaces studied by time-resolved photoemission spectroscopy**. *Phys. Rev. B*, 88:165313, 2013. doi:10.1103/PhysRevB.88.165313.

[122] M. Dell'Angela, T. Anniyev, M. Beye, R. Coffee, A. Föhlisch, J. Gladh, T. Katayama, S. Kaya, O. Krupin, J. LaRue, A. Møgelhøj *et al.* **Real-Time Observation of Surface Bond Breaking with an X-ray Laser**. *Science*, 339: 1302, 2013. doi:10.1126/science.1231711.

[123] M. Dell'Angela, F. Hieke, F. Sorgenfrei, N. Gerken, M. Beye, N. Gerasimova, H. Redlin and W. Wurth. **Ultrafast surface dynamics probed with time resolved photoemission**. *In press - Surf. Sci.*, –:–, 2015. doi:10.1016/j.susc.2015.08.011.

[124] T. Tschentscher. The European X-Ray Free Electron Laser Technical design report. Technical report, European X-Ray Free Electron Laser GmbH, Hamburg, 2011.

[125] **European XFEL- Status of Technical Development**. `www.xfel.eu/sites/site_xfel-gmbh/content/e63594/.../altarelli_eng.pdf`. Accessed: 27/08/2015.

[126] L. P. Oloff, M. Oura, K. Rossnagel, A. Chainani, M. Matsunami, R. Eguchi, T. Kiss, Y. Nakatani, T. Yamaguchi, J. Miyawaki, M. Taguchi, K. Yamagami, T. Togashi, T. Katayama, K. Ogawa, M. Yabashi and T. Ishikawa. **Time-resolved**

HAXPES at SACLA: probe and pump pulse-induced space-charge effects. *New J. Phys.*, 16:123045, 2014. URL `http://stacks.iop.org/1367-2630/16/i=12/a=123045`.

[127] A. Verna, G. Greco, V. Lollobrigida, F. Offi, and G. Stefani. **Space-charge effects in high-energy photoemission**. *In preparation*, –:–, –.

[128] V. Lollobrigida, G. Greco, D. Simeone, F. Offi, A. Verna and G. Stefani. **Electron trajectory simulations of time-of-flight spectrometers for core level high-energy photoelectron spectroscopy at pulsed X-ray sources**. *J. Electron Spectrosc. Relat. Phenom.*, 205:98, 2015. doi:10.1016/j.elspec.2015.09.005.

[129] O. M. Artamonov, S. N. Samarin and A. O. Smirnov. **An application of the electron mirror in the time-of-flight spectrometer**. *J. Electron Spectrosc. Relat. Phenom.*, 120:11, 2001. doi:10.1016/S0368-2048(01)00279-1.

[130] O. M. Artamonov, S. N. Samarin, G. Paolicelli and G. Stefani. **The use of the time-energy dispersion in an electron energy analyzer**. *J. Electron Spectrosc. Relat. Phenom.*, 131-132:105, 2003. doi:10.1016/S0368-2048(03)00129-4.

[131] M. Ogawa, S. Yamamoto, Y. Kousa, F. Nakamura, R. Yukawa, A. Fukushima, A. Harasawa, H. Kondoh, Y. Tanaka, A. Kakizaki and I. Matsuda. **Development of soft x-ray time-resolved photoemission spectroscopy system with a two-dimensional angle-resolved time-of-flight analyzer at SPring-8 BL07LSU**. *Rev. Sci. Instrum.*, 83:023109, 2012. doi:10.1063/1.3687428.

[132] R. Ovsyannikov, P. Karlsson, M. Lundqvist, C. Lupulescu, W. Eberhardt, A. Fö. **Principles and operation of a new type of electron spectrometer - ArTOF**. *J. Electron Spectrosc. Relat. Phenom.*, 191:92, 2013. doi:10.1016/j.elspec.2013.08.005.

[133] H. Lüth. **Solid Surfaces, Interfaces and Thin Films**. Springer-Verlag Berlin Heidelberg, 2010.

Acknowledgements

Eccoci qui: io non l'avrei mai detto eppure sembra che sia vero. È stato un percorso molto intenso, con parecchie esperienze, alcune delle quali ho l'impressione che mi porterò dietro per tutta la vita. Non dirò se siano state belle o brutte perché, come mi è stato fatto notare saggiamente nel corso di questi tre anni, data la nostra visione limitata della realtà che ci circonda non siamo in grado di vedere tutte le possibili conseguenze di un'azione o evento. Quali che siano, queste esperienze fanno parte di un bagaglio molto ricco che mi porterò appresso lungo qualsiasi strada la vita mi riserverà. Ovviamente, la parte più preziosa è costituita da coloro i quali ho avuto l'occasione di incontrare.

Ho deciso che parlerò esplicitamente solo di poche persone in questo paragrafo, altrimenti verrebbe fuori un'altra tesi, sicuramente scritta meglio! Tutti gli altri sapranno perdonare questo mio piccolo capriccio, con la consapevolezza che quello che avete fatto per me resta, non può in alcun modo venire cancellato e che ve ne sarò per sempre grato. Grazie a chi mi ha detto di sì, ma grazie ancora di più a chi mi ha detto di no e forse mi ha fatto capire che dovevo cambiare qualcosa. Grazie a chi mi ha fatto ridere ed a chi mi ha fatto piangere, perché mi ha fatto trovare dentro di me la forza per andare avanti. Grazie a chi è stato lì a lungo e a chi è passato rapido come una stella cadente, lasciando come ricordo un sorriso ed un desiderio. Grazie a chi ha tratto beneficio dal mio aiuto e a chi ha saputo prendere i miei sbagli e trasformarli in qualcosa di bello. Grazie a chi ha illuminato la mia giornata con un sorriso e a chi mi ha rimesso in riga con un rimprovero. Grazie a chi mi ha parlato in italiano e a chi ha fatto in modo che la diversa lingua costituisse non un ostacolo, ma un punto di contatto tra realtà diverse. Grazie a chi mi ha mostrato come usare il cervello e a chi mi ha insegnato a seguire il mio cuore. A voi tutti, dal più profondo della mia anima, grazie.

Non posso non partire dal mio supervisore, il dr. Francesco Offi, che ha avuto l'ONERE (non vorrei che qualcuno per distrazione sbagliasse a leggere questa parola) di avermi come dottorando e che mi ha seguito passo per passo in questo percorso, neanche fosse il suo di dottorato. Sia facendo materialmente delle operazioni con me, che aiutandomi a trovare la strada da seguire per arrivare ad un certo risultato. Non credo di essere riuscito a ripagare appieno tutto quanto lui ha fatto per me, non certo per mancanza di voglia o di impegno quanto forse di capacità. Solo in italiano non è abbastanza, quindi lo ringrazierò in tutte le lingue dei paesi che mi ha dato l'occasione di visitare in questi tre anni: thank you very much, merci beaucoup, arigatou gozaimasu (chiedo scusa qui per l'uso di caratteri latini, decisamente inappropriato).

Approfitto di questa sezione anche per ringraziare tutti coloro che mi hanno aiutato nelle varie fasi della preparazione e realizzazione degli esperimenti che sono stati discussi in questa tesi e nella seguente fase di analisi dati: F. Borgatti, D. Ceolin, B. Gobaut, T.-L. Lee, P. Orgiani, G. Panaccione, A. Yu. Petrov, A. Regoutz, J.-P. Rueff, C. Schlueter e P. Torelli.

Ovviamente non posso esimermi dal citare il buon Marco. Grazie per avermi preso sotto la tua ala, per avermi mostrato (e provato ad insegnare) come fare molte cose, per aver posto rimedio ai miei errori, per avermi incoraggiato quando tutto sembrava aver perduto senso, per avermi spiegato la tua visione del mondo ed essere stato pronto ad ascoltare la mia, per avermi sostenuto anche a distanza, per avermi fatto entrare in quella realtà intima e colorata che è la tua famiglia. Se tutte le persone del mondo facessero per un altro metà di quello che tu hai fatto per me, probabilmente questo in cui viviamo sarebbe un posto molto diverso.

E poi ci siete voi, che costituite un pezzo insostituibile del mio cuore: sia quelli che sono rimasti, che coloro che hanno preso strade diverse. Forse nessuno di voi leggerà mai questo mio scritto, ma tutte queste pagine non avrebbero alcun senso se non parlassi di voi. Grazie per avermi accettato nonostante tutti i miei difetti e le nostre divergenze di opinioni (no no no no, come direi io). Grazie per avermi dato tutto ed aver chiesto in cambio solo che io fossi me stesso. Grazie per le serate passate a casa a giocare a carte, per i lunghi viaggi insieme, per le chiaccherate sotto la luna. Grazie a Bartolo, Claude, Claudio, Dabbe, Dablò, Derio, Flavio, Fra, Giò, Giulia, Guiniz, Naples, Pabbio, Pir, Rogo e Vinz, che avete fatto di me quello che sono e mi rendete felice sempre più felice di esserlo.

C'è poi tutto un gruppo di persone che ho avuto la fortuna di avere come mia famiglia: non li ho scelti io, ma grazie al cielo c'è stato chi ha scelto per me ed è qualcuno infinitamente più bravo di me a farlo. Come rappresentanti di tutto il gruppo, ovviamente non posso che nominare voi (l'elenco è in ordine alfabetico, così nessuno rompe che voglio più bene ad uno piuttosto che all'altro): Andrea, Damiano, Emanuele, mamma, Michele e papà. Se sono arrivato da qualche parte e mai arriverò da qualche altra è merito del vostro amore, che ognuno mi regala nella sua personalissima maniera che porta qualcosa di prezioso ed insostituibile alla mia vita.

Dio ci benedica tutti e ci porti tutti a casa, una volta che avremo contribuito con il nostro mattoncino alla ricostruzione di quel paradiso terrestre che costituiva il piano originale.